HIGH VALENT METAL-OXO CORROLAZINES: SYNTHESIS, CHARACTERIZATION, AND REACTIVITY

by Regina A. Baglia

A dissertation submitted to The Johns Hopkins University in conformity with the requirements for the degree of Doctor of Philosophy

Baltimore, Maryland, USA
November 18, 2016

Abstract

High-valent metal-oxo species are important intermediates in biological and synthetic systems and perform difficult oxidation reactions such as hydroxylation of unactivated C–H bonds. Due to the inherent instability of these intermediates, it remains challenging to study factors that control their reactivity. The corrolazine ligand, which is a modified porphyrinoid framework, is able to stabilize metal ions in high oxidation states. This has allowed for spectroscopic characterization and mechanistic study of high-valent metal-oxo complexes. This thesis is focused on the preparation and characterization of high-valent metal-oxo corrolazine complexes with an emphasis on reactivity in O–H or C–H bond cleavage reactions.

Chapter 1 provides an introduction to the importance of metal-oxo species in biology, valence tautomerism as a way to stabilize formally high oxidation states in oxo-metalloporphyrinoid complexes, Lewis acids as a way to control reactivity in biomimetic complexes, and a summary of previous work on the synthesis, characterization, and reactivity of high-valent metal-oxo corrolazines.

Chapter 2 describes the synthesis and characterization of two high-valent metal-oxo corrolazine complexes, $Mn^{V}(O)(TBP_8Cz)$ and $Cr^{V}(O)(TBP_8Cz)$. The H-atom abstraction reactivity of the two complexes were compared and the $Mn^{V}(O)$ was found to be more reactive than the $Cr^{V}(O)$ complex. The difference in H-atom abstraction reactivity was rationalized using thermodynamic arguments.

The formation of a valence tautomer of $Mn^{V}(O)(TBP_8Cz)$ with the nonmetallic Lewis acid $B(C_6F_5)_3$ to give $Mn^{IV}(O–B(C_6F_5)_3)(TBP_8Cz^{\bullet+})$ is described in Chapter 3. The

reactivity of $Mn^{IV}(O–B(C_6F_5)_3)(TBP_8Cz^{\bullet+})$ with H-atom donor substrates was tested and compared to the Zn^{II} adduct and the starting $Mn^{V}(O)$ complex.

In Chapter 4, the characterization of $Mn^{IV}(O–LA)(TBP_8Cz^{\bullet+})$ complexes (LA = $Zn(OTf)_2$ and $B(C_6F_5)_3$) by X-ray absorption spectroscopy (XAS) is described. An expanded reactivity study of $Mn^{IV}(O–LA)(TBP_8Cz^{\bullet+})$ complexes (LA = TFA, $Zn(OTf)_2$, $B(C_6F_5)_3$, and $HBAr^F$) with C–H bonds was undertaken, and the reaction rates were found to be entirely dependent on the strength of the Lewis acids.

In Chapter 5, a novel, electron-deficient high-valent manganese-arylimido corrolazine complex, $Mn^{V}(NC_6Cl_3H_2)(TBP_8Cz)$, is synthesized and characterized. The electronic structure and corresponding reactivity of this compound could be controlled by the addition of either a weak acid (TFA) or strong acid ($HBAr^F$).

In Chapter 6, the synthetic methodology of a new corrolazine ligand with para-isopropylphenyl substituents is described.

Committee members:

David P. Goldberg

Kenneth D. Karlin

V. Sara Thoi

Acknowledgements to Collaborators

I am grateful to the collaborators who contributed to the research in this thesis. The collaborators and their contributions are listed below:

1. Dr. Maxime Siegler at The Johns Hopkins University performed X-ray crystallographic data collection and structure determination for all crystal structures.
2. Prof. Ivana Ivanović-Burmazović and Maximilian Dürr from the Department of Chemistry and Pharmacy at Friedrich-Alexander Universität Erlangen-Nürnberg in Erlangen, Germany performed low-temperature mass spectrometry.
3. Dr. Courtney Krest-Roach at the SLAC National Accelerator Laboratory performed X-ray Absorption Spectroscopy.
4. Prof. Samuel P. De Visser from the University of Manchester and Nick Yang at University of Wisconsin-Madison performed computational studies.

Table of Contents

Index of Figures

Index of Schemes

Index of Tables

1. Chapter 1. Introduction

1.1. Metal-oxo species in biology

1.1.1. Iron-oxo species

Metal-oxo species are key intermediates in important oxidation reactions in biological and industrial processes. The Cytochrome P450 (Cyt-P450) class of heme enzymes is found in most tissues of the human body and plays important roles in hormone synthesis and breakdown, cholesterol synthesis, vitamin D metabolism, and also serves to metabolize potentially toxic compounds including drugs and metabolites produced in the body during endogenous metabolism.[1,2] The active site of Cyt-P450 contains a heme cofactor which is axially ligated by a thiolate derived from a cysteine residue. A main reaction that Cyt-P450 catalyzes is a monooxygenase reaction, in which dioxygen acts as the O-atom source in a hydroxylation reaction of relatively inert C–H bonds, as shown in Scheme 1.1.

Scheme 1.1. Overall reaction for hydroxylation by Cytochrome P450s

$$R\text{–}H + O_2 + 2H^+ + 2e^- \xrightarrow{\text{Cyt-P450}} R\text{–}OH + H_2O$$

The consensus catalytic cycle is shown in Scheme 1.2. The key C–H bond cleaving intermediate, Compound I (Cpd-I), is a formally iron(V)-oxo species, which has been characterized as an $Fe^{IV}(O)(por^{\bullet+})$ with an Fe^{IV} center ligated by a porphyrin π-radical-cation.[3] Cpd-I abstracts a hydrogen atom (H•) to initially form a carbon-centered radical (R•) and a putative Fe^{IV}–OH, which then homolytically cleaves to allow for radical "rebound" to give the hydroxylated product (R–OH) and the $Fe^{III}(por)$ resting catalytic state. In nature, hydroxylation of inert C–H bonds is unique to thiolate-ligated

enzymes such as Cyt-P450. Other heme enzymes with axial ligands such as peroxidases (axial histidine) or catalases (axial tyrosinate) are unable to activate inert C–H bonds. The large driving force for H-atom abstraction by P450 Cpd-I is partly due to the high basicity of the one-electron reduced $Fe^{IV}(O)(por)$,[4-6] which provides a thermodynamically controlled mechanism that can circumvent nonproductive oxidation of the surrounding amino acids and destruction of the enzyme.

Scheme 1.2. Consensus catalytic cycle for C–H hydroxylation by Cytochrome P450s

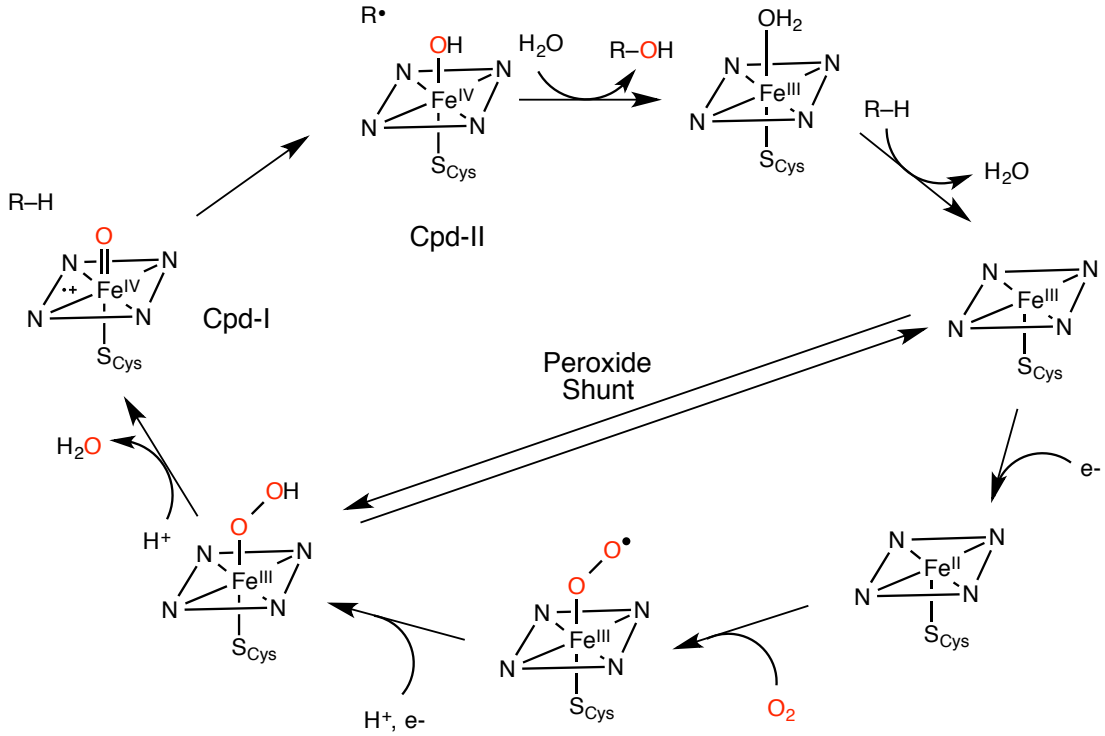

Chloroperoxidase (CPO) and aromatic peroxygenase (APO) are also in the thiolate-ligated class of heme enzymes.[1] Using hydrogen peroxide as the oxidant, CPO catalyzes the chlorination of a wide range of organic substrates. The proposed mechanism for CPO is the generalized mechanism for peroxidases, in which hydrogen peroxide binds to the ferric porphyrin, followed by heterolytic cleavage of the O–O bond to generate Cpd-I. APO catalyzes the hydroxylation of aromatic C–H substrates, among others. Like

CPO, hydrogen peroxide binds to the ferric enzyme and heterolytic cleavage generates Cpd-I. While Cpd-I is a common intermediate in both CPO and APO, the mechanistic steps following its formation and leading to oxidized product and the ferric resting state are still not clear. One clue to these mechanistic questions is that Cpd-II formation by one-electron transfer has been found to be a non-productive pathway, and that the high basicity of Cpd-II may prevent this mechanistic offshoot.[5,7]

Thus, there are several key questions that remain regarding thiolate-ligated heme enzyme mechanisms. The rebound step in Cyt-P450 remains unobserved because it occurs after the rate-determining C–H cleavage by Cpd-I. Thus, the factors that favor this rebound step (rather than further H• abstraction from the carbon radical, i.e. desaturation) remain to be determined. For CPO and APO, the exact role that Cpd-I plays in the mechanism is still not well understood. There is an opportunity for synthetic model systems to give insight into these mechanisms. Scheme 1.3 illustrates the diversity of reactivity by Cpd-I in thiolate-ligated heme enzymes.

Scheme 1.3. Diversity of reactivity of Cpd-I in thiolate ligated heme enzymes.

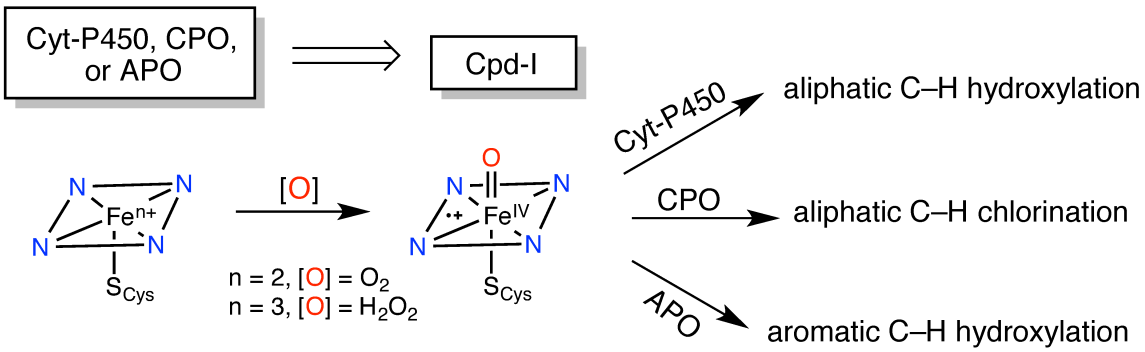

1.1.2. Manganese-oxo species

Photosynthesis is a multistep photo-induced process that consists of the oxidation of water to dioxygen by four electron and four protons. This process is coupled to the

reduction of CO_2 to sugars, which are used as fuel in photosynthetic organisms. Water oxidation is catalyzed by Photosystem II (PSII), an enzyme found in most green algae, cyanobacteria, and plants. The active site of PSII is a multimetallic cluster consisting of four Mn ions and one Ca ion, bridged by oxido ligands called the oxygen evolving complex (OEC) (Scheme 1.4).[8,9] The mechanism of water oxidation has been intensely debated in the literature.[8,10,11] Two of the most commonly considered mechanistic proposals for the key O–O bond forming step are shown in Scheme 1.5. One consists of the radical coupling of two Mn^{IV}–O• (manganese oxyl) units. Another proposal features a nucleophilic attack of a hydroxide or water ligand on an electrophilic Mn^{V}=O unit.

Scheme 1.4. Recent crystal structure of the OEC at 1.9 Å resolution.

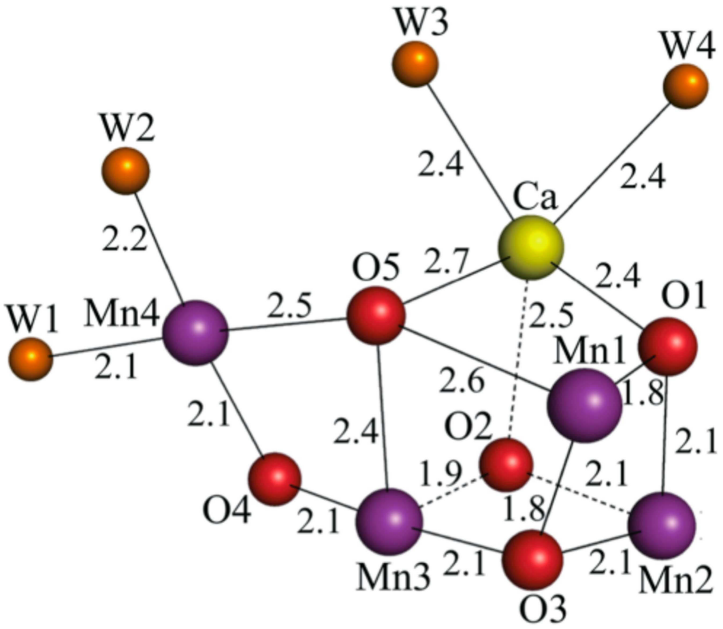

Scheme 1.5. Two common proposed mechanisms for the O–O bond formation step in photosynthetic water oxidation.

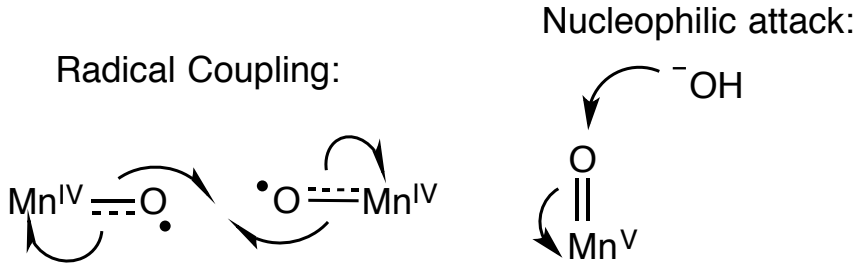

A common thread in these mechanistic proposals is the involvement of a high-valent manganese-oxo species. Furthermore, the role of the non-redox active Lewis acid Ca^{2+} is not well understood; however, it is essential for the catalytic function of the enzyme.

High-valent metal-oxo intermediates in the catalytic cycles of biological and industrial oxidation processes are very transient species. Therefore, it is difficult to study and determine the factors that control the reactivity of these species. The synthesis of thermally- and aerobically-stable metal-oxo complexes can provide a unique opportunity to study these types of species in a controlled setting. Our group has achieved the synthesis of these metal-oxo complexes by the use of the corrolazine ligand platform, which is a ring-contracted porphyrinoid ligand. One goal of this thesis is to determine the factors that control the intrinsic reactivity of stable metal-oxo complexes in fundamental reaction steps, such as hydrogen atom (H•) abstraction, by making carefully controlled changes to the chemical environment (such as adding Lewis acids in the secondary coordination sphere, Chapters 3, 4, and 5) or by changing the central metal ion (Chapter 2).

1.2. Porphyrinoid Family

1.2.1. Porphyrins

Porphyrins are aromatic, 18π-electron tetrapyrrolic macrocycles (Chart 1.1). Fully deprotonated, porphyrins have a 2– charge. They are important ligands in many biological systems, especially in the heme enzymes mentioned earlier. Porphyrinoid ligands are redox-active, and often play a role in the catalytic cycles of these enzymes by carrying an electron hole in the π-system as a porphyrin π-cation-radical. Therefore, these ligands are crucial to heme enzyme function. For example, the Cyt-P450 Cpd-I has an oxidizing equivalent that resides on the porphyrin ligand, allowing for access to a formally high oxidation state without having to generate an "$Fe^{V}(O)$" species.

Chart 1.1. Ligand frameworks of common members of the porphyrinoid family.

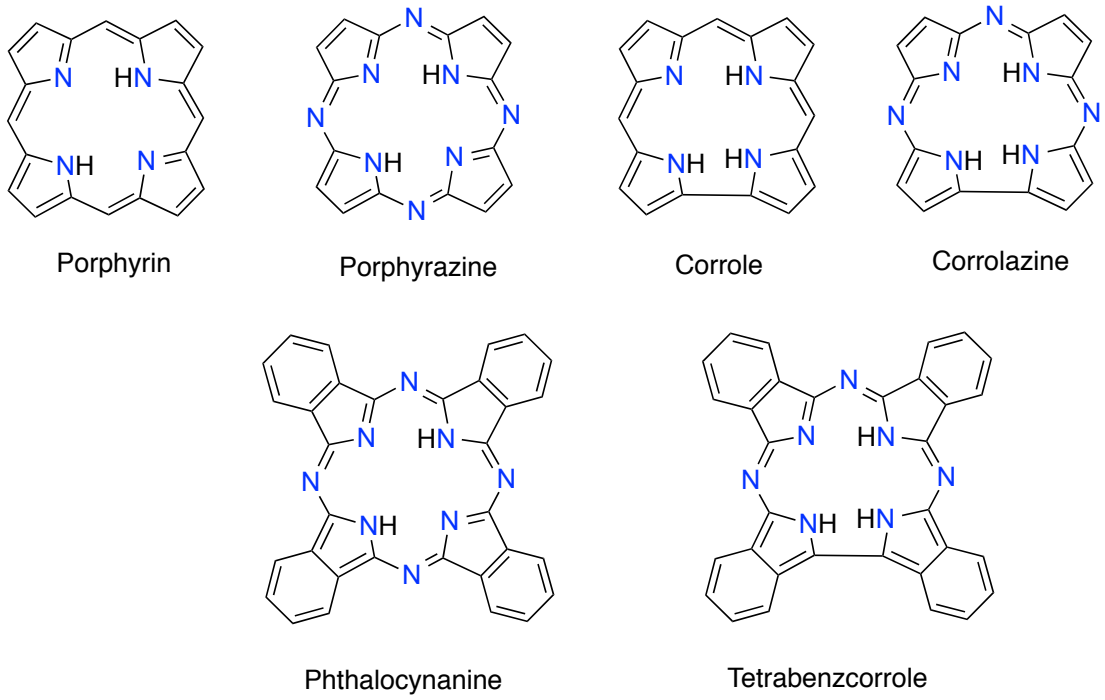

Synthetic metalloporphyrins have been used to generate high-valent metal-oxo complexes as models of mechanistic intermediates. In 1979, it was found that an iron(III) porphyrin complex, $Fe^{III}(Cl)(TPP)$ (TPP = tetraphenylporphyrinato^{2-}), catalyzed the

epoxidation of alkenes and hydroxylation of alkanes at room temperature.[12] While no intermediates could be observed at room temperature, the key oxidative intermediate was proposed to be a high-valent iron-oxo complex. A couple years later, an iron(IV)-oxo porphyrin π-cation-radical species was observed at −78 °C.[13] The $Fe^{IV}(O)(TMP^{\bullet+})$ complex was also capable of oxidizing alkenes to epoxides even at this low temperature, suggesting that this species was kinetically competent to catalyze the reaction at room temperature. Since these early reports, there have been many examples of high-valent iron-oxo porphyrin complexes, although these species are only stable at low temperatures and even then have short half-lives.

As close analogs of the iron-porphyrins, high-valent manganese-oxo species were targeted as synthetic models for iron-oxo reactivity studies. While $Mn^{IV}(O)$(porph) species could be generated at room temperature, the higher-valet $Mn^{V}(O)$(porph) species remained elusive until 1997. At that time, Groves et al were able to detect and characterize an $Mn^{V}(O)$-porphyrin at room temperature by rapid-mixing stopped-flow UV-vis spectroscopy.[14] This complex was an efficient O-atom transfer reagent, and was able to rapidly oxidize olefin substrates to epoxides. Since then, other $Mn^{V}(O)$ porphyrin complexes have been generated and characterized. These species were observable transiently at room temperature, which allowed for some reactivity to be determined.[15,16]

Historically, high-valent chromium-oxo porphyrins were some of the earliest well-characterized metal-oxo complexes that were studied in order to help understand oxygen transfer reactivity of the high-valent iron-oxo porphyrin species. The first synthesis of a high-valent chromium-oxo porphyrin was achieved by the addition of iodosylbenzene (PhIO) or *meta*-chloroperoxybenzoic acid (mCPBA) to Cr(III)(TPPCl)

(TPPCl = chlorotetraphenylporphyrinato^{2-}).[17] The product of these oxidation reactions was a chromium(V)-oxo species that was transiently observable in solution at room temperature. This complex had a room temperature EPR spectrum characteristic of chromium(V), and an ^{18}O-isotope sensitive stretching frequency in the IR of 972 cm^{-1}, which is indicative of a chromium-oxygen triple bond.[18] The autoreduction of $Cr^{V}(O)$ allowed for the isolation of a chromium(IV)-oxo complex, and the enhanced stability of this complex led to characterization by X-ray diffraction (XRD).[19,20] These Cr^{IV}/Cr^{V}-oxo complexes were also able to oxidize olefins to epoxides.

1.2.2. Corroles

Corroles are members of the porphyrinoid family that are missing a *meso*-carbon, i.e. contain a direct Cα–Cα bond between two of the pyrrole rings. They retain an 18π-aromatic system, but the contraction of the macrocyclic ring gives the fully-deprotonated corrole an overall 3– charge. The higher charge and smaller cavity size allows corroles to stabilize metal ions in higher oxidation states and makes them ideal ligands to characterize high-valent metal-oxo species and study the corresponding reactivity.

The synthesis of corroles was first reported in 1965 by Johnson and Kay.[21] However, the difficult preparation and multi-step syntheses were significant obstacles in the active research on metallocorroles. Some practical one-pot synthetic strategies for corrole syntheses were developed by Gross[22,23] and Paolesse[24] in 1999, and this allowed for rapid growth in this field. In 2006, Gryko published an updated corrole synthesis, which improved yields and gave a new synthetic route for asymmetric corroles.[25] A review article in *Chemical Reviews* in 2016 summarizes the history of corrole synthesis and provides modern synthetic routes, whose effectiveness depends on the electronic

properties of the desired substituents.[26] In 2000, Gross et al reported the first isolation of a high-valent Mn-oxo in the corrole system by oxidation with PhIO or ozone (O_3).[27] The $Mn^V(O)$(tpfc) (tpfc = *meso*-tris(pentafluorophenyl)corrole) complex was characterized by UV-vis, and gave diamagnetic ^1H- and ^{19}F-NMR spectra. Surprisingly, the complex was stable in solution over several hours, confirming the ability of corroles to stabilize metals in high oxidation states. The $Mn^V(O)$(tpfc) complex was able to oxidize triphenylphosphine, with concurrent formation of the reduced Mn^{III}(tpfc) complex. The chromium analogue of the tpfc complex, $Cr^V(O)$(tpfc), was reported only a year later.[28] As with the porphyrins, the $Cr^V(O)$(tpfc) complex was more stable than its manganese counterpart. The $Cr^V(O)$(tpfc) complex could oxidize triphenylphosphine at a very slow rate, but was not reported to oxidize other organic substrates. Since these first reports, corrole ligands have been used to make metal-ligand complexes with every first-row transition metal, and some 2nd- and 3rd- row metals, and these complexes have found wide use in many applications, including in the fields of renewable energy, anti-cancer therapy, and chemical sensing.[29-31]

1.2.3. Corrolazine

The corrolazine, first synthesized by our group in 2001,[32] is a *meso*-*N*-substituted corrole and can be viewed as a hybrid between a tetraazaporphyrin (porphyrazine) and a corrole. The corrolazine, like corroles, has a 3– charge when fully deprotonated, and a small cavity enforced by the direct pyrrole-pyrrole linkage. The synthesis of corrolazines was achieved by a ring contraction of β-aryl substituted porphyrazines with PBr_3 (Scheme 1.6).[33] Demetalation of the resulting P^V-corrolazine could be performed by treating with Na/NH_3 at –78 °C followed by protonation to give the metal-free

corrolazine TBP_8CzH_3 (octakis(4-*tert*-butylphenyl)corrolazine). The free-base corrolazine can then be metalated by a variety of metals including Mn,[33,34] Fe,[35] Cr,[36] and Re[37]. Furthermore, the synthesis of a high-valent $Mn^V(O)$ corrolazine was achieved by oxidation of the $Mn^{III}(TBP_8Cz)$ complex with iodosylbenzene, an oxygen atom donor reagent.[34] Recently, the $Mn^V(O)$ complex was crystallized and characterized by X-ray diffraction (XRD), whose structure confirmed all of the spectroscopic data on this complex for the past 15 years.[36]

Scheme 1.6. Synthesis of substituted corrolazines

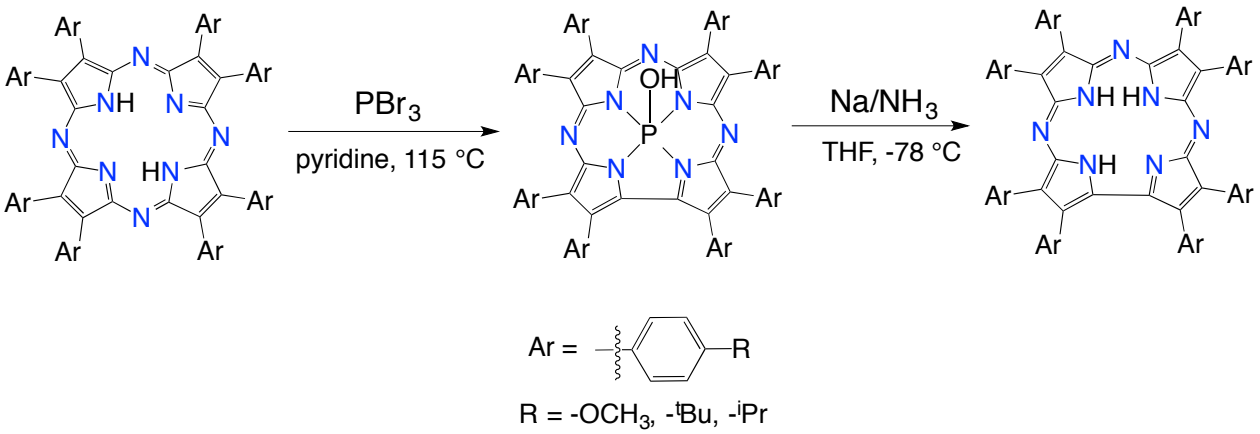

1.3. Valence Tautomerism

Valence tautomers are metal-ligand complexes that undergo stimulated intramolecular electron transfer between the redox-active ligand and the redox-active metal center (Scheme 1.7). Valence tautomers typically exhibit different optical, structural, and magnetic properties from each other, making them attractive targets for molecular switching materials and devices. Therefore, the design of valence tautomers that respond to stimuli *reversibly* is of significant interest. Valence tautomerism can be chemically induced, for example, by a pH change, or by nonchemical changes, such as irradiation, temperature, and pressure.[38] Common redox-active ligands include the

porphyrin family (Chart 1.1), the quinoid family, and the diothiolene family.[39,40] Cooperativity between redox-active ligands and abundant first-row transition metals has been highly sought after for catalytic applications, because of the possibility of undergoing multi-electron transformations without the need for expensive second or third row metals.[41]

Scheme 1.7 Valence Tautomerism by Intramolecular Electron Transfer

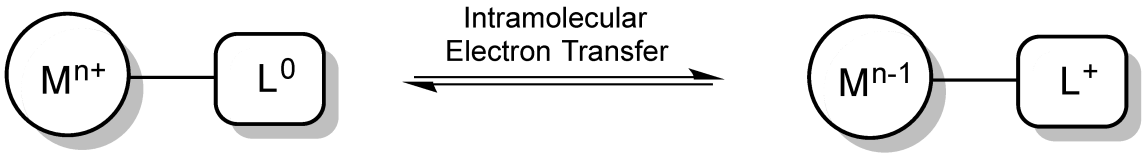

1.3.1. Valence Tautomerism in Metalloporphyrinoids

Some metalloporphyrins are known to exhibit chemically-induced valence tautomerism. The redox changes of synthetic metalloporphyrins have been studied extensively, because they serve as model systems for heme enzyme intermediates. For example, in cytochrome P450, Cpd-I exists as one of two possible valence tautomers, $Fe^{IV}(O)(por^{\bullet+})$ and $Fe^{V}(O)(porph)$. In synthetic high-valent metalloporphyrins, ligand properties often dictate which valence tautomer is favored. For example, ligand metathesis of $Fe^{III}(ClO_4)_2(tmp^{\bullet+})$ (tmp = tetramesitylporphyrinate^{2-}), which contains a π-radical-cation on the porphyrin ligand, with sodium methoxide resulted in formation of the valence tautomer $Fe^{IV}(OMe)_2(tmp)$, a bismethoxy complex.[42] Metal-centered oxidation of $Fe^{III}(ClO_4)_2(tpp)$ (tpp = tetraphenylporphyrinate^{2-}) could be achieved in the presence of excess fluoride ion to give the $Fe^{IV}(tpp)F_2$ valence tautomer, but in the presence of other halides such as Cl^-, Br^-, and I^-, the $Fe^{III}(tpp^{\bullet+})$ valence tautomer was generated.[43-45] This result can be rationalized by considering halide ligand donor properties on the hard/soft scale. For example, fluoride is a hard π-donor ligand, whereas

the other halides are softer π donors. Oxidation of Fe^{III}(tpp) in the presence of neutral ligands and water also result in the ferric-porphyrin π-cation radical tautomer.[45]

Scheme 1.8 Two Possible Valence Tautomers for Cpd-I in Cyt-P450

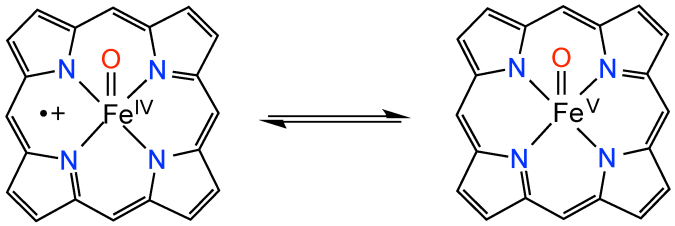

observed *not observed*

Valence tautomeric behavior has also been observed in manganese porphyrins.[38] As with iron porphyrins, the oxidation of Mn^{III} (por) can occur either at the metal or the porphyrin ligand to give either Mn^{IV}(por) or Mn^{III}($por^{•+}$), respectively, and the site of oxidation depends strongly on the axial ligands bound to the Mn^{III}(por) starting material, as shown in Scheme 1.9. For example, five-coordinate Mn^{III}(X)($tpp^{•+}$) where X = ClO_4^-, I^-, NCS^-, Br^-, Cl^-, and N_3^- can be generated from the Mn^{III}(X)(tpp) complexes.[46] The Mn^{IV}(por) tautomer could only be generated in the presence of axial ligands that are stronger π-donors and as a six-coordinate complex. The oxidation of Mn^{III}(tpp) in the presence of sodium methoxide allowed for the isolation of a Mn^{IV}(tpp)$(OMe)_2$ complex which was stable enough to crystallize and analyze by XRD.[47]

Scheme 1.9 Ligand-Controlled Valence Tautomerism in Manganese-Porphyrins

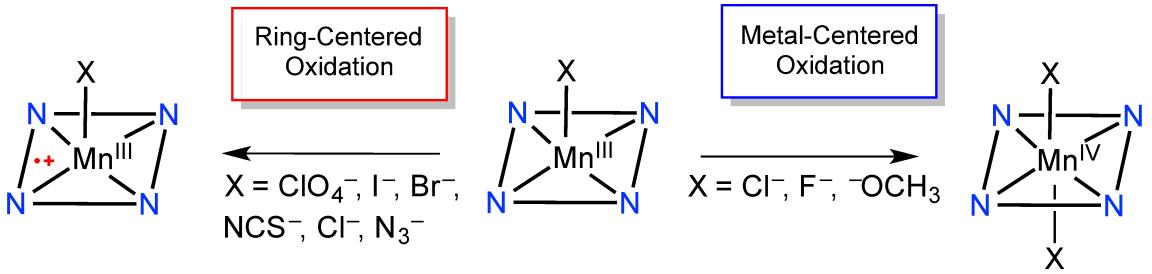

Mn and Fe porphyrins allowed for the isolation of either one of the valence tautomers, but examples of controlled switching between two valence tautomers in metal-porphyrin systems are still rare. An early example by Spreer and coworkers showed that the addition of methoxide to $Mn^{III}(Cl)(tpp^{\bullet+})$ generated the valence tautomer $Mn^{IV}(OMe)_2(tpp)$. A more recent example by Gross and coworkers was reported in 1997, in which $Mn^{III}(ClO_4)(tmp^{\bullet+})$ could be converted to its valence tautomer by the addition of chloride ion to generate an $Mn^{IV}(Cl)_2(tmp)$ complex.[48] Surprisingly, the $Mn^{IV}(Cl)_2(tmp)$ complex was able to chlorinate olefin substrates, which was one of the first synthetic examples of halogenation by a high-valent metalloporphyrin. Much more recently, $Mn^{III}(tmp)Cl$ was found to be a catalytic precursor for aliphatic fluorination in the presence of a fluoride source and PhIO, and the active catalytic species was characterized as an $Mn^{IV}(F)_2(tmp)$ complex.[49]

In the corrole framework, the location of oxidation of Fe^{III}corroles underwent intense debate.[50,51] High-valent chloroiron corroles can exist in one of two possible valence tautomers, either as an $Fe^{IV}Cl(cor)$ complex or as an $Fe^{III}Cl(cor^{\bullet+})$ complex, the latter having a π-radical-cation on the aromatic macrocyclic ligand. Ultimately, a consensus about the locus of oxidation was reached, and determined to be corrole-based.[52] However, the electronic structure of these complexes are still of interest for several research groups. In a recent report by Newcomb and coworkers, the $Fe^{IV}(X)(cor)$ tautomer could be observed before electronic rearrangement to the $Fe^{III}(X)(cor^{\bullet+})$ tautomer, and the thermal stability of the former tautomer was dependent on the identity of the axial ligand.[53]

1.3.2. Valence Tautomerism in Oxo-metalloporphyrinoids

High-valent metal-oxo porphyrinoid complexes can exist in one of several valence tautomers. However, there are few examples of metal-oxo complexes for which both valence tautomers are known. Our group has shown that addition of metallic and nonmetallic Lewis acids (LA = $Zn(OTf)_2$, $B(C_6F_5)_3$, H^+) to $Mn^V(O)(TBP_8Cz)$ stabilized the valence tautomer $Mn^{IV}(O–LA)(TBP_8Cz^{\bullet+})$, which contained an Mn^{IV} ion coupled to a π-radical-cation on the corrolazine ring and the Lewis or Brönsted acid bound at the terminal oxo ligand.[54-56] The two valence tautomers were reversible with the addition of an appropriate trapping reagent, and they also displayed significantly different reactivity from each other in both H-atom abstraction and O-atom transfer reactions. Acid-dependent valence tautomerism was observed in a high-valent Fe-oxo porphyrin when trifluoroacetic acid (TFA) was added to $Fe^{IV}(O)(tpfp^{\bullet+})(L)$ (tpfp = 5,10,15,20-tetrakis-(pentafluorophenyl)porphyrinato^{2-}) to transiently generate the $Fe^{III}(tpfp^{++})(L)_2$, an Fe-isoporphyrin complex (Scheme 1.10).[57] Addition of chloride to this species generated a potent halogenation oxidant that was able to chlorinate olefins and other substrates. An iron-porphyrin dication species, $Fe^{III}(tmp^{++})$, had also been observed in the reaction of Fe^{III}(tmp) *N*-oxide with TFA, but no other valence tautomers were observed in that case.[58] Recently, reversible valence tautomerism was observed for oxo-ferryl porphyrins by pH-jump stopped-flow UV-vis spectroscopy, where an $Fe^{IV}(O)$(por) complex was present at high pH, but an $Fe^{III}(OH_2)(por^{\bullet+})$ was the dominant species at low pH. In 2015, Abu-Omar showed that when TFA was added to the high-valent Mn-oxo corrole complex, $Mn^V(O)$(tpfc), the valence tautomer $Mn^{IV}(OH)(tpfc^{\bullet+})$ could be generated.

Scheme 1.10. Valence tautomerism in a Cpd-I analogue induced by addition of TFA

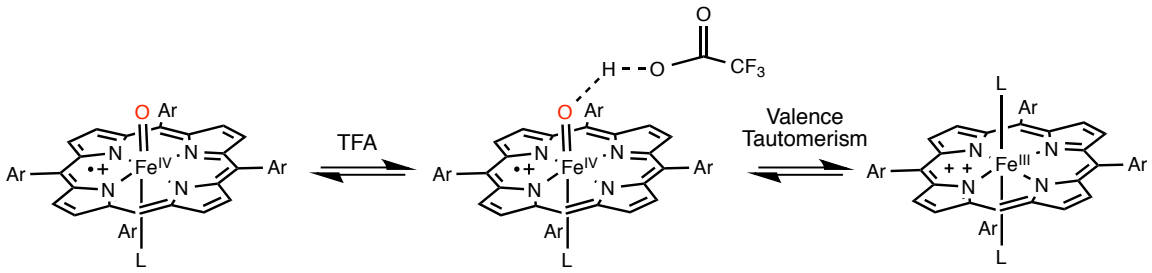

1.4. Lewis Acid Activation

Lewis and Brönsted acids are known to tune the reactivity of high-valent metal-oxo species in biological and synthetic systems. In the photosynthetic reaction center, the redox-inactive Lewis acid Ca^{2+} is known to play a critical role in water oxidation. One proposed function is to stabilize possible high-valent Mn-oxo intermediates, but its role during catalysis remains poorly understood.[59,60] Studies on the effect of Lewis acids on synthetic metal-oxo complexes have provided insights into this process, as well as how to control and modulate reactivity of metal-oxo species in other systems. In this section, we discuss the effects of Lewis acids on *reactivity* of mononuclear metal-oxo/-imido species, although there are several groups who study the structural and electronic effects of Lewis acids on multinuclear Mn–O cluster compounds.[61]

An early example of the influence of Lewis acids on an isolable, mononuclear high-valent metal-oxo complex was reported by Collins and coworkers.[62] The addition of redox-inactive metal ion LiOTf (OTf = trifluoromethanesulfonate^{1-}) to a non-heme $Mn^{V}(O)$(TAML) complex (TAML = tetraamido macrocyclic ligand) resulted in a change in the UV-visible spectrum to a new species, and gave a significantly different ^{1}H-NMR spectrum that remained diamagnetic. In the IR spectrum, a 15 cm^{-1} increase in frequency of the ν(Mn–^{18}O) band was observed. Based on these data, the authors concluded that the

Lewis acid was not bound to the oxo unit, but rather to the macrocyclic ligand at the bidentate pyridyl/carbonyl site (see Scheme 1.11). The Lewis acid/metal-oxo adduct exhibited enhanced rates of oxygen atom transfer to triphenylphosphine, which was attributed to an increased electrophilicity. Use of other Lewis acids, including Na^{+}, Zn^{2+}, and Sc^{3+}, resulted in a dependence of the rates on Lewis acid strength, with the more Lewis acidic metal ions giving faster rates of OAT. A very recent example using a similar $Mn^{V}(O)$(TAML) complex in the presence of Sc^{3+} confirmed the Mn^{5+} oxidation state of the Lewis acid/$Mn^{V}(O)$ adduct by XAS/EXAFS. The Lewis acid/$Mn^{V}(O)$ adduct showed similar reactivity to the earlier findings with enhanced OAT rates to triarylphosphines, which was attributed to the increased electrophilicity of the oxo unit due to Lewis acid binding at the remote site.[63]

Scheme 1.11. Secondary ion binding in a non-heme $Mn^{V}(O)$(TAML) complex

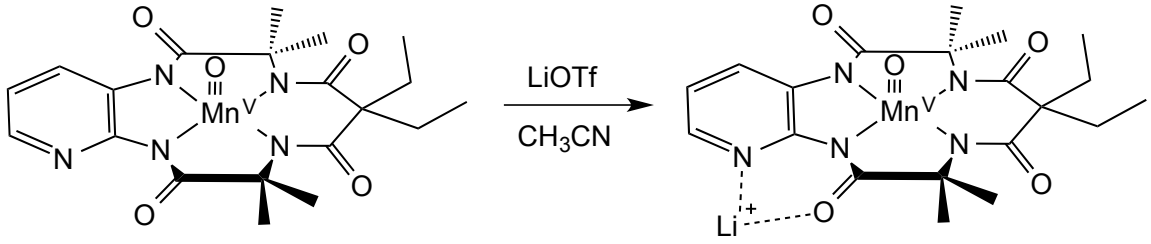

The influence of Lewis acids has been studied in other non-heme systems. Ten years ago, the versatile N4Py ligand system (N4Py = *N*,*N*-bis(2-pyridylmethyl)-*N*-bis(2-pyridyl)methylamine) allowed for the isolation of an air-stable, crystalline iron(IV)-oxo complex.[64] Recently, the manganese-oxo derivative $Mn^{IV}(O)$(N4Py) was synthesized independently by two different research groups.[65,66] Addition of the strong Lewis acid $Sc(OTf)_3$ to $Mn^{IV}(O)$(N4Py) resulted in the Lewis acid-bound adduct.[66] Support for this formulation was obtained by X-ray absorption spectroscopy (XAS) and analysis of the extended fine structure region (EXAFS). XAS showed that the high-valent state of the

$Mn^{IV}(O)(N4Py)$ was maintained after Sc^{3+} binding, and EXAFS fitting analysis showed an intense peak at 3.5 Å, consistent with a metal-metal scatterer and assigned to the Mn–Sc distance. These data indicated that the Sc^{3+} was likely binding at the terminal oxo ligand. Reactivity studies in the presence and absence of Lewis acid revealed different effects on the rate constants for OAT and HAT. The Sc^{3+}-bound $Mn^{IV}(O)(N4Py)$ exhibited enhanced rates of OAT with thioanisoles but slower rates of HAT with weak C–H bonds (e.g. 1,4-CHD) compared to the starting $Mn^{IV}(O)(N4Py)$ complex. This anomaly in reactivity could be explained using the redox potentials of the two complexes. The Sc^{3+} -bound $Mn^{IV}(O)(N4Py)$ complex had a higher redox potential than the starting complex, and this induced a change in mechanism from concerted O-atom transfer to a step-wise electron-transfer/oxygen-atom-transfer mechanism. However, the substrate CHD has a much higher redox potential than either the starting $Mn^{IV}(O)(N4Py)$ or the Lewis acid complex, and therefore the HAT reaction was slowed in the presence of Sc^{3+} due to increased sterics around the metal-oxo unit.[66]

The influence of a protic Lewis acid on two non-heme high-valent Mn-oxo complexes was also studied. Addition of triflic acid (HOTf) resulted in the oxo-bound HOTf adducts $[LMn^{IV}(O)]^{2+}$–$(HOTf)_2$ (L = N4Py, Bn-TPEN) (Bn-TPEN = *N*-benzyl-*N,N′,N′*-tris-(2-pyridylmethyl)ethane-1,2-diamine).[67] As in the case of the $(N4Py)Mn^{IV}(O–Sc^{3+})$ complexes,[66,68] the $[LMn^{IV}(O)]^{2+}$–$(HOTf)_2$ complexes exhibited one-electron reduction potentials that were shifted significantly positive relative to the starting $[LMn^{IV}(O)]^{2+}$ complexes, and showed enhanced rates of ET with one-electron reductants and OAT to *para*-substituted thioanisoles. The HAT reactivity with CHD was decelerated for the $[LMn^{IV}(O)]^{2+}$–$(HOTf)_2$ complexes compared to the starting

$[LMn^{IV}(O)]^{2+}$ complexes, which is also in line with the HAT reactivity found for the scandium bound complexes. A summary of this reactivity is shown Scheme 1.12. However, when a toluene derivative was used as H-atom donor substrate for oxidation by $(N4Py)Mn^{IV}(O–(HOTf)_2)$ at room temperature, a stepwise ET/PT mechanism was observed.[69] This result was attributed to the fact that the oxidation and reduction potentials of the toluene derivative and protonated Mn-oxo complex are close, which favors an ET-controlled pathway. Another change in mechanism to a concerted HAT pathway was observed when this same reaction was studied at lower temperature, at the boundary where the driving force for ET becomes more endergonic than HAT.

Scheme 1.12. Summary of the comparative reactivity of non-heme $Mn^{IV}(O)$ complexes and Lewis acid-bound complexes.

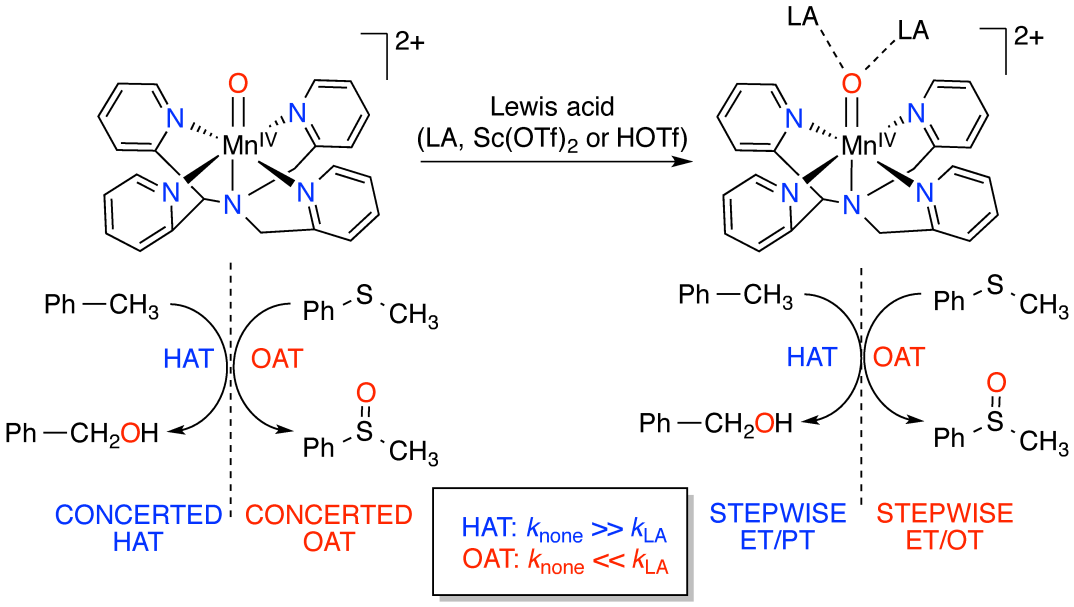

In contrast to the manganese case, Lewis and Brönsted acids have been found to accelerate both H-atom abstraction and OAT in non-heme iron-oxo complexes. The addition of HOTf to $Fe^{IV}(O)(N4Py)$ resulted in greatly enhanced rates of C–H cleavage in toluene derivatives.[70] When the KIE was measured for the deuterated substrates, it was

found to decrease with increasing HOTf concentration. A switch in mechanism from HAT to PCET was invoked, with exergonic electron-transfer from the toluene derivative providing the driving force for overall H• abstraction. Support for this mechanism came from comparing the reduction potential of the Fe^{IV}(O)(N4Py)-HOTf adduct to the oxidation potentials of the toluene derivative susbtrates. Similar to the non-heme manganese-oxo case, in the presence of either Sc^{3+} or H^{+}, the rate of the reaction of Fe^{IV}(O)(N4Py) with thioanisole derivatives was accelerated.[70] This acceleration was due to a switch in mechanism from direct oxygen atom transfer to an electron-transfer/oxygen-transfer, which was driven thermodynamically by the downhill electron-transfer reaction. In these non-heme iron-oxo complexes, Lewis/Brönsted acids were proposed to bind at the terminal oxo unit in these complexes. In contrast, addition of acid to an Fe^{IV}(O) complex bound by the tripodal tetradentate ligand $[H_3beua]^{3-}$ (H_3beua = tris[(*N*′-*tert*-butylureaylato)-*N*-ethyl)]aminato^{3-}) resulted in protonation of the chelating ligand rather than the terminal oxo ligand.[71]

Lewis acids have also been used for "trapping" of meta-stable high-valent intermediates. In 2014, Ray, Nam, and coworkers reported evidence for a high-valent cobalt-oxo species, which was stabilized in the presence of the redox-inactive metal ions Sc^{3+}, Ce^{3+}, Y^{3+}, and Zn^{2+}.[72] Oxidation of a Co^{III}(TAML) complex by PhIO in the presence of these strong Lewis acids resulted in a metastable species, assigned as a Co^{IV}–O–Lewis acid complex, in which the Lewis acid is bound to the oxo ligand, based on characterization provided by CSI-MS, EPR, and XAS (Scheme 1.13). The Co(O) complex could not be generated with weaker Lewis acids such as Mg^{2+}, Ca^{2+}, or Sr^{2+}, indicating the importance of Lewis acid strength in generating the high-valent species.

The Co(O)–Lewis acid species was capable of oxidizing xanthene via an HAT reaction. Support for C–H bond cleavage as the rate-determining step comes from a KIE experiment with detuerated xanthene, and an observed linear correlation between the C–H bond strengths of other C–H substrates and their rates of reaction. OAT to sulfides was also observed, and a Hammett plot with *para*-substituted thioanisoles revealed a large negative slope of −2.8, consistent with a highly electrophilic Co(O) species. DFT calculations found that the ground state of the Co(O)-Lewis acid species had a $Co^{IV}(O^{2-})$ electronic structure. In contrast, the authors found that the ground state of the Co(O) *without* the Lewis acid was best described as a Co^{III}-oxyl ($Co^{III}(O\bullet)$) species, with a large percentage of unpaired electron spin localized on oxygen. However, there was no experimental evidence presented for this species.

Scheme 1.13. Synthesis of a high-valent Co–O species in the presence of Lewis acids

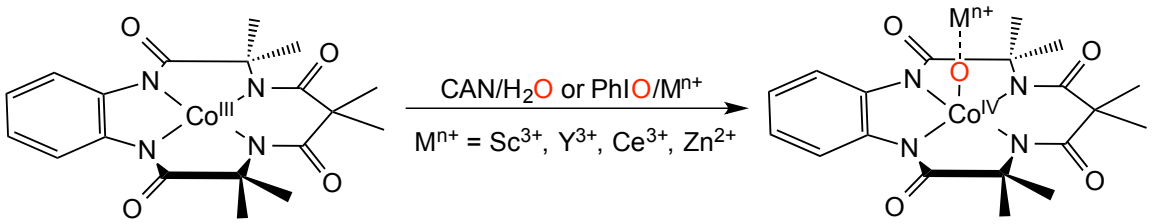

Another example of this Lewis acid "trapping" method was employed to generate a meta-stable copper-nitrene intermediate. When scandium triflate and a copper(I) source, $[Cu(L1)]^+$ (L1 = 3,3′-iminobis(*N*,*N*-dimethylpropylamine)), are mixed with the nitrene donor PhINTs ([*N*-(*p*-toluenesolfonyl)imino](2-*tert*-butylsulfonyl)phenyliodinane), a copper-nitrene species, formulated as $Cu^{II}(N\bullet Ts)$, could be observed as an intermediate prior to H• abstraction to give a $Cu^{II}(NHTs)$ amido complex.[73] When PhINTs and the Cu(I) source were mixed in the absence of Lewis acid, no intermediate was observed, indicating that the Lewis acid is key to stabilizing the high-valent intermediate. As with

the case of Co(O)(TAML), the valence tautomer of Cu^{II}(N•Ts), in which the Cu is oxidized by one electron and the nitrene species is reduced by one electron to give a Cu^{III}(NTs), was proposed as one possible intermediate of oxidation catalysis in the absence of the Lewis acid. However, this valence tautomer was not observed.

Lewis acids have been found to aid in dioxygen activation by low-valent Mn and Fe complexes. Borovik and coworkers showed that the rate of O_2 activation by a $[Mn^{II}(MST)]^-$ (MST = *N,N′,N″*-[2,2′,2″-nitrilotris(ethane-2,1-diyl)]tris(2,4,6-trimethylbenzenesulfonamido)$^{3-}$) complex was accelerated in the presence of a mixture of $Ca(OTf)_2$ and 15-crown-5 ether.[74] While no O_2-bound intermediates could be identified, the product of this reaction was the heterodinuclear hydroxide-bridged managanese-calcium complex, $[Mn^{III}(OH–Ca^{2+})(MST)]^+$, with the hydroxide originating from dioxygen. The authors proposed that the role of the Lewis acid was to alleviate negative charge build-up from the putative Mn-superoxo species formed from electron transfer to the metal following O_2 binding (Scheme 1.14). When the complex was changed from Mn to Fe, an increase in the O_2 activation rates was observed. As with the Mn case, adding Lewis acids to the $[Fe^{II}(MST)]^-/O_2$ reaction resulted in a rate enhancement in O_2 activation, and the rates depended on the identity of the Lewis acid.[75] Furthermore, the rate of O_2 activation for the two Lewis acids Sr^{2+} and Ca^{2+} was identical, despite their different Lewis acidities. In nature, the only ion that can replace the Ca^{2+} ion in the enzymatic photosynthetic reaction is Sr^{2+} ion, implying that Lewis acidity is not the only requirement for water oxidation function. The isolated product of the $[Fe^{II}(MST)]^-/O_2$/Lewis acid reaction was the heterodinuclear hydroxide-bridged $[Fe^{III}(OH–Ca^{2+})(MST)]^+$ complex. When O_2 was replaced with another O-atom donor oxidant, 4-

methylmorpholine-*N*-oxide (NMO), the reactivity of the $[Fe^{II}(MST)]^-$ complex could be directed towards inter- or intra-molecular reactivity by the presence or absence of Lewis acids.[76] When Lewis acids were absent, $[Fe^{II}(MST)]^-$ reacted with NMO to hydroxylate a methyl group on one arm of the ligand to give an alkoxide-coordinated Fe^{III} product. In the presence of Lewis acids, however, the major product was an $[Fe^{III}(OH–Ca^{2+})(MST)]$ complex, in which the H-atom source is external to the complex. In this case, an $Fe^{IV}(O)$ species is proposed to be the active oxidant, although it is not observed.

Scheme 1.14. Proposed involvement of Ca^{2+} ion in the mechanism for oxygen activation by a non-heme Mn^{II} complex.

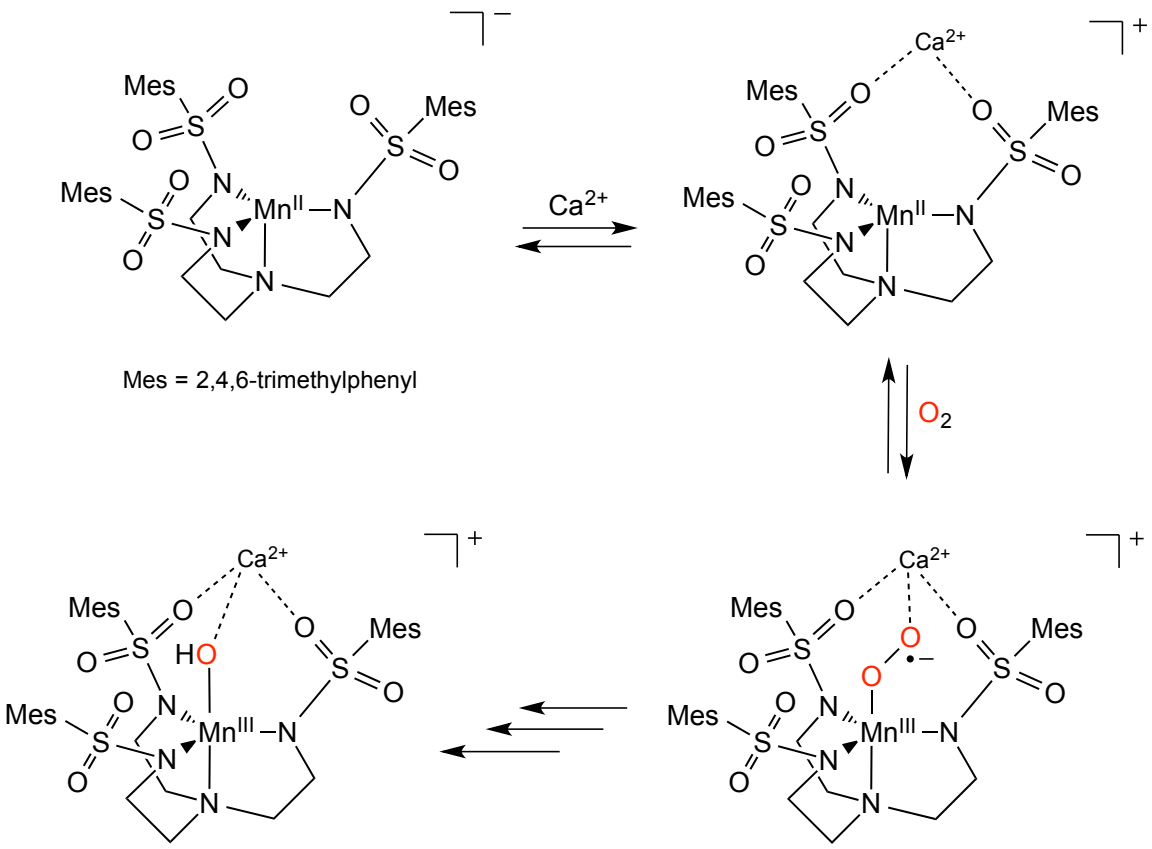

Lewis acids have found use in transition metal-mediated catalysis. An early example comes from Lau and coworkers, in which the catalytic rate of oxidations of inert C–H substrates by potassium permanganate ($KMnO_4$) could be accelerated in the

presence of the nonmetallic Lewis acid, trifluoroborane (BF_3).[77] It was proposed that the borane center bound to the oxo units of MnO_4^- enhanced the electrophilicity of the metal-oxo, which caused an increase in the rate. More recently, Yin and coworkers showed that the rates of catalytic sulfoxidation reactions by non-heme Mn(II) bridged cyclam complexes could be enhanced in the presence of Lewis acids of varying strength.[78]

As demonstrated in this section, Lewis acids have allowed for the control of reactivity in various chemical transformations performed by inorganic complexes. Aside from the two cases where the involvement of valence tautomerism was proposed (although not observed), controllable valence tautomerism did not come into play in the non-heme systems discussed here.

1.5. Manganese-Oxo Corrolazine

1.5.1. Synthesis of Manganese-Oxo Corrolazine

The high-valent manganese-oxo corrolazine can be made from addition of iodosylbenzene (PhIO) to the $Mn^{III}(TBP_8Cz)$ complex, followed by flash column chromatography to give the pure material (Scheme 1.15).[34] The $Mn^{V}(O)(TBP_8Cz)$ could also be generated photochemically by visible light irradiation of $Mn^{III}(TBP_8Cz)$ in the presence of dioxygen and an appropriate H-atom donor.[79,80] The $Mn^{V}(O)(TBP_8Cz)$ complex was stable as a solid and was characterized by a variety of spectroscopic methods, and, very recently, by X-ray crystallography to give the structure shown in Figure 1.1.[36] The structure revealed a short Mn–O distance of 1.5455(18) Å, indicative of a triple bond, and that the Mn ion was five-coordinate, in contrast with the six-coordinate structure proposed for Mn(O) porphyrin complexes.[14,15]

Scheme 1.15. Synthesis of $Mn^{V}(O)(TBP_8Cz)$

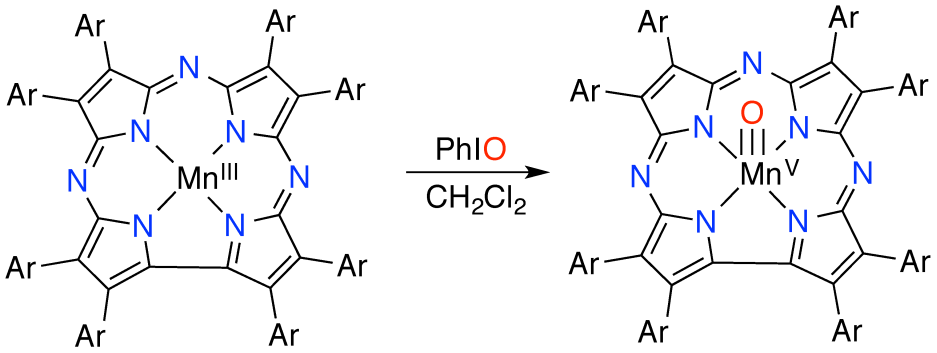

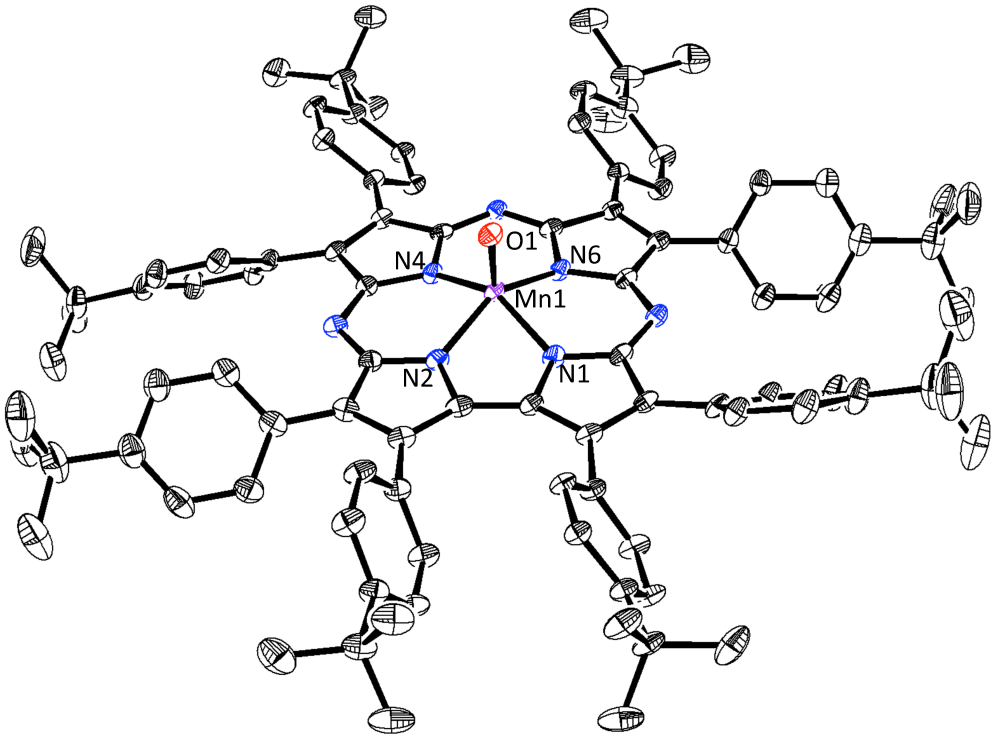

Figure 1.1. Crystal structure of the high-valent manganese-oxo corrolazine complex, $Mn^{V}(O)(TBP_8Cz)$, displacement ellipsoids set at 50 % probability level. Figure from reference 36.

1.5.2. Reactivity of $Mn^{V}(O)(TBP_8Cz)$

Despite the stability of $Mn^{V}(O)(TBP_8Cz)$, this complex was capable of oxidizing organic substrates. In the initial report of the $Mn^{V}(O)(TBP_8Cz)$ complex, it was found to oxidize PPh_3. Much more recently, the kinetics of this oxygen atom transfer reaction

were studied. By varying the steric and electronic properties of triarylphosphine substrates, mechanistic information about the OAT reactivity of this complex was obtained.[56] A large steric effect on the OAT reactivity for $Mn^{V}(O)(TBP_8Cz)$ was obtained when *ortho*-, *meta*-, and *para*- substituted tri(tolyl)phosphines were used. A 3700-fold rate decrease was observed upon going from *para*- to *ortho*- tri(tolyl)phosphine, indicating a concerted OAT mechanism in which the phosphine substrate must attack the oxo unit while avoiding steric clash with the corrolazine ligand. A significant electronic effect of changing the substituent on *para*-substituted triarylphosphines was determined in a Hammett study. A slope value of $\rho = -0.92$ was obtained, consistent with an electrophilic mechanism.

The H-atom abstraction reactivity of $Mn^{V}(O)(TBP_8Cz)$ was studied with O–H and C–H substrates.[81] The rates of reaction for 4-X-2,6-di-*tert*-butylphenols with $Mn^{V}(O)(TBP_8Cz)$ were measured and plotted against the bond dissociation energies (BDEs) for the O–H bonds and against the Hammett σ^{+} parameters. Both of these yielded linear correlations with negative slopes, which indicated a concerted hydrogen atom transfer from the phenol O–H bond as the rate-limiting step of the reaction. This conclusion was supported by a large kinetic isotope effect ($k_H/k_D = 6$) for the deuterated phenol substrate. The $Mn^{V}(O)(TBP_8Cz)$ was also capable of oxidizing the substrates 9,10-dihydroanthracene and 1,4 cyclohexadiene, which contain very weak C–H bonds. However, the reactions were very slow, with second order rate constants on the order of $\sim 10^{-4}$ M^{-1} s^{-1}. The $Mn^{V}(O)(TBP_8Cz)$ complex was therefore demonstrated to be capable of H-atom transfer from weak C–H and O–H bonds, making this complex an ideal starting point for studying how the reactivity changes when post-synthetic modifications

are made to the first (axial ligands, ring oxidation) or second coordination sphere (Lewis acids).

1.5.3. Lewis Acid Activation of $Mn^{V}(O)(TBP_8Cz)$

A few years ago, our group found that when $Zn(OTf)_2$, a redox-inactive Lewis acid, was added to the low-spin $Mn^{V}(O)(TBP_8Cz)$, a high-spin valence tautomer was stabilized.[54] This high-spin tautomer was characterized by ^{1}H-NMR, UV-vis, and EPR, and was assigned as $Mn^{IV}(O–Zn(OTf)_2)(TBP_8Cz^{\bullet+})$, in which one electron was transferred from the corrolazine ligand to the metal center (Scheme 1.16). The formation of this complex was reversible by addition of a strong zinc(II) chelator, 1,10-phenanthroline.

Scheme 1.16. Synthesis of the $Mn^{IV}(O–Zn(OTf)_2)(TBP_8Cz^{\bullet+})$ valence tautomer.

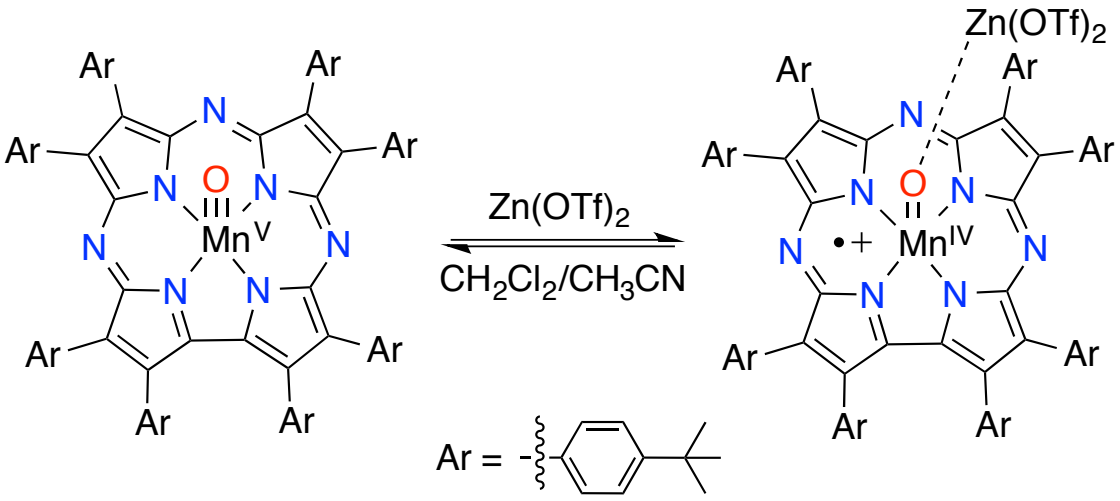

The $Mn^{IV}(O–Zn(OTf)_2)(TBP_8Cz^{\bullet+})$ complex exhibited distinct electron transfer reactivity compared with the starting $Mn^{V}(O)(TBP_8Cz)$ complex. In earlier work,[82] it was found that $Mn^{V}(O)(TBP_8Cz)$ was capable of being reduced by decamethylferrocene ($E_{1/2}$ = −0.56 V vs Fc^{+}/Fc^{0}), a strong one-electron reductant, to give the two-electron reduced $Mn^{III}(TBP_8Cz)$ complex, but it was unreactive with ferrocene ($E_{1/2}$ = 0.00 V vs Fc^{+}/Fc^{0}).

In contrast, the $Mn^{IV}(O–Zn(OTf)_2)(TBP_8Cz^{\bullet+})$ complex was able to oxidize ferrocene indicating that the redox potential for the Zn^{2+}-complex was increased by at least 0.5 V. Despite the boost in redox potential, the $Mn^{IV}(O–Zn(OTf)_2)(TBP_8Cz^{\bullet+})$ complex showed only moderate rate enhancements (3x) in H-atom abstraction with phenol substrates than the starting $Mn^{V}(O)(TBP_8Cz)$. Furthermore, the redox stoichiometry for oxidation reactions (both ET and HAT) was also different in the presence of Zn^{2+} (Scheme 1.17). In the absence of $Zn(OTf)_2$, two-electron chemistry is observed to give a $Mn^{III}(TBP_8Cz)$ product. However, the $Mn^{IV}(O–Zn(OTf)_2)(TBP_8Cz^{\bullet+})$ complex reacts with H• or e^- to give a $Mn^{IV}(X)(TBP_8Cz)$ product, suggesting that the Lewis acid stabilizes the higher valent Mn^{IV} oxidation state.

Scheme 1.17. Comparison of reaction stoichiometries for $Mn^{V}(O)(TBP_8Cz)$ versus $Mn^{IV}(O–Zn(OTf)_2)(TBP_8Cz^{\bullet+})$ with 2,4-di-*tert*-butylphenol.

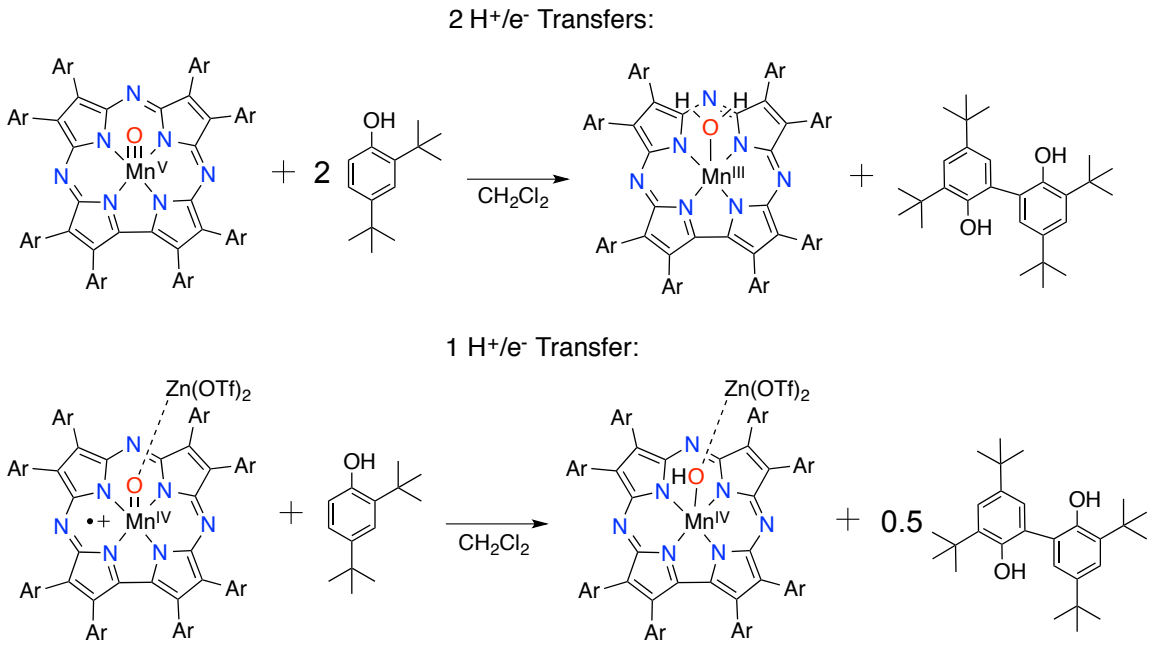

When $Zn(OTf)_2$ was replaced with the strong nonmetallic Lewis acid tris(pentafluorophenyl)borane ($B(C_6F_5)_3$), an increase in HAT reactivity was observed. Large rate enhancements (up to 100-fold) for oxidation of phenol substrates by Mn^{IV}(O–

$B(C_6F_5)_3)(TBP_8Cz^{\bullet+})$ were obtained.[55] This result showed that the identity of the Lewis acid was important in determining HAT reactivity for these complexes. The synthesis, characterization, and HAT reactivity of the $Mn^{IV}(O–B(C_6F_5)_3)(TBP_8Cz^{\bullet+})$ complex is discussed in Chapter 3.

Mn K-edge X-ray absorption spectroscopy was performed in order to obtain structural information on the $Mn^{IV}(O–LA)(TBP_8Cz^{\bullet+})$ (LA = $Zn(OTf)_2$ and $B(C_6F_5)_3$) complexes.[83] The edge position of the spectrum confirmed the +4 oxidation state of the Mn ion, and fitting the EXAFS region showed an elongated Mn–O bond, consistent with Lewis acid binding to the terminal oxo ligand. These data are discussed in Chapter 4 of this thesis.

A comparative study of the OAT reactivity between $Mn^{V}(O)(TBP_8Cz)$ and the Lewis acid complexes $Mn^{IV}(O–LA)(TBP_8Cz^{\bullet+})$ (LA = $Zn(OTf)_2$, $B(C_6F_5)_3$, and H^+) was accomplished by addition of substituted triarylphosphine substrates.[56] A dramatic rate deceleration was observed for the Lewis acid adducts compared to the starting $Mn^{V}(O)(TBP_8Cz)$. For example, the reaction between $Mn^{IV}(O–Zn(OTf)_2)(TBP_8Cz^{\bullet+})$ and PPh_3 was slowed by over 14,000-fold compared to the parent $Mn^{V}(O)$ complex. Within the Lewis acid adduct reactivity, a dependence of the rate of triarylphosphine oxidation on Lewis acid strength was observed, with H^+ as the fastest Lewis acid, which also was the strongest Lewis acid tested. However, the parent $Mn^{V}(O)(TBP_8Cz)$ complex remained the most potent oxidant for the triarylphosphine substrates. These results led to the conclusion that the Lewis acid adducts, $Mn^{IV}(O–LA)(TBP_8Cz^{\bullet+})$, were less electrophilic than $Mn^{V}(O)(TBP_8Cz)$ and this was due to changing the oxidation state at the metal center from the Mn^{V} to the Mn^{IV} oxidation level.

The H-atom abstraction reactivity of a series of Mn^{IV}(O–LA)($TBP_8Cz^{\bullet+}$) (LA = $Zn(OTf)_2$, $B(C_6F_5)_3$, $HBAr^F$, and TFA) complexes was examined with C–H substrates. The rates of C–H cleavage were accelerated when LA = $Zn(OTf)_2$, $B(C_6F_5)_3$ or $HBAr^F$, but when LA = TFA a slight rate deceleration was observed, and the magnitude of the rate enhancements were correlated to the strength of the Lewis acid, which underlined the importance of the *identity* of the Lewis acid. For the Lewis acids $B(C_6F_5)_3$ and $HBAr^F$ large nonclassical KIEs were measured (k_H/k_D = 25-27), indicating rate limiting C–H cleavage in the rate determining step. Support for an HAT mechanism was obtained from a linear correlation between the rates of oxidation for a series of C–H substrates and their BDE(C–H) values. The HAT reactivity of Mn^{IV}(O–LA)($TBP_8Cz^{\bullet+}$) complexes with C–H substrates was found to be highly dependent on the strength of the Lewis acid. This story is discussed in detail in Chapter 4 of this thesis.

1.6. Chromium-Oxo Corrolazine

The high-valent chromium-oxo corrolazine was synthesized by oxidative aerobic metallation of the metal-free corrolazine ligand with the low-valent chromium source, $Cr(CO)_6$ (Scheme 1.18).[36] The resulting Cr^V(O)(TBP_8Cz) complex was purified by flash silica gel chromatography, and was characterized by UV-vis, ^{1}H-NMR, and EPR spectroscopies, as well as X-ray crystallography. The crystal structure is shown in Figure 1.2. The Cr^V(O)(TBP_8Cz) was isomorphous with the Mn^V(O)(TBP_8Cz) complex, with almost identical structural parameters (Table 1.1). A benchmark for the reduced Cr-corrolazine product was also synthesized. The reaction between Cr^V(O)(TBP_8Cz) and triphenylphosphine resulted in a Cr^{III}(TBP_8Cz) complex, which was characterized by UV-vis, EPR, and XRD (structure shown in Figure 1.3).

Scheme 1.18. The synthesis of $Cr^{V}(O)(TBP_8Cz)$.

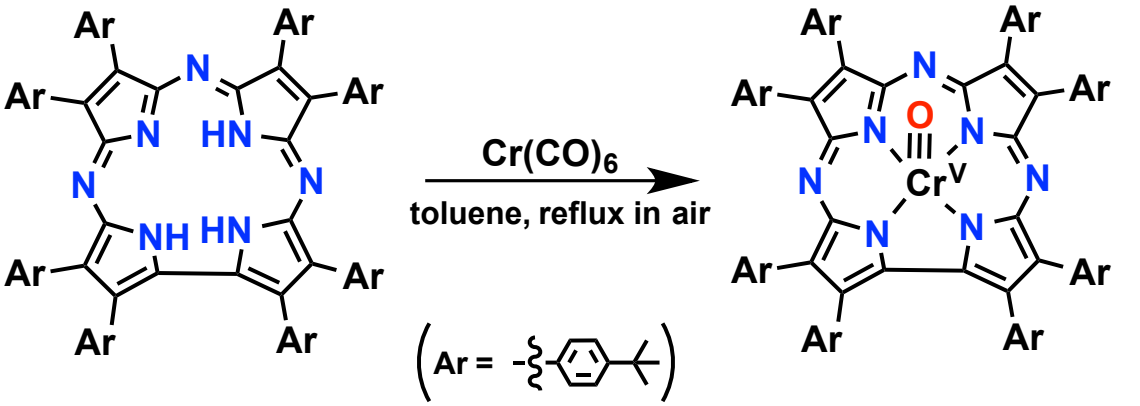

free base corrolazine

93% yield (based on CzH_3)

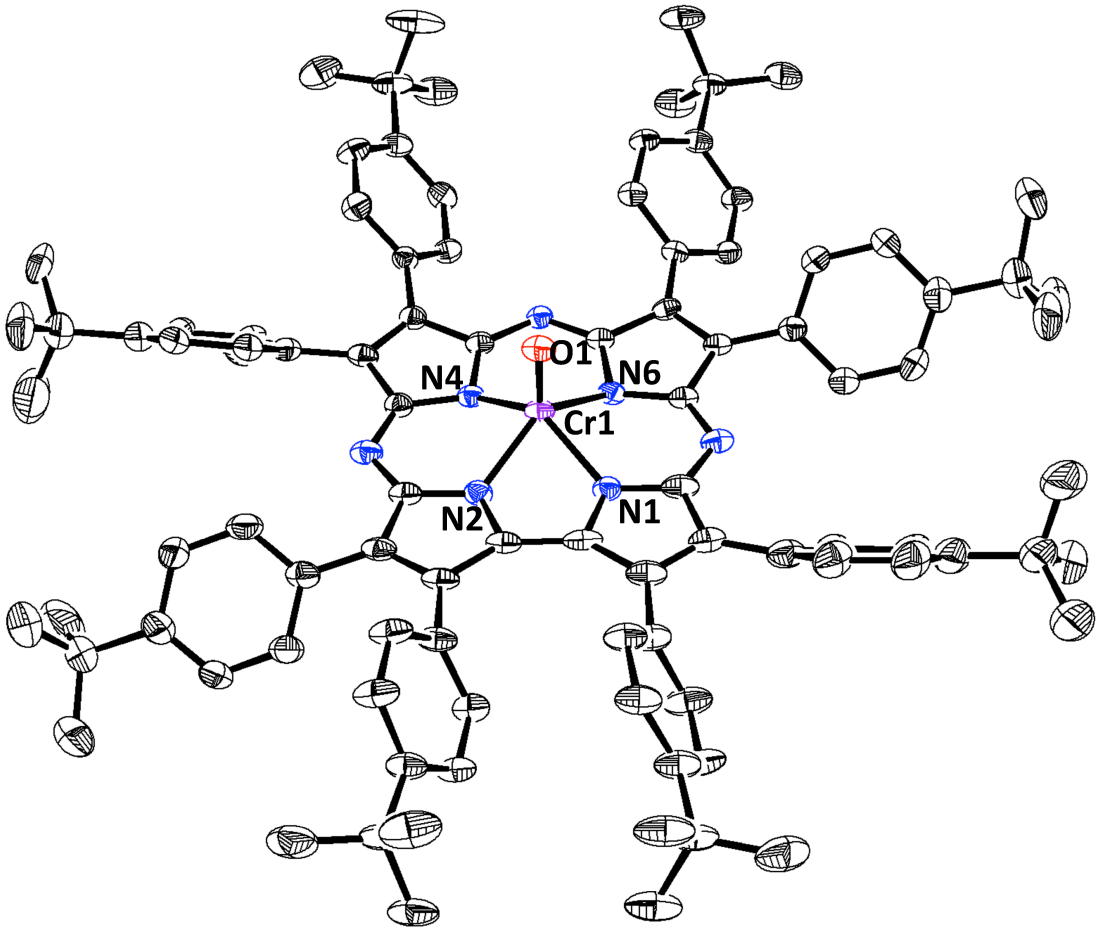

Figure 1.2. Crystal structure of the high-valent chromium-oxo corrolazine complex, $Cr^{V}(O)(TBP_8Cz)$, displacement ellipsoids set at 50 % probability level. Figure from reference 36.

Table 1.1. Comparison of atomic distances from X-ray diffraction for the first coordination sphere of $Cr^{V}(O)(TBP_8Cz)$ and $Mn^{V}(O)(TBP_8Cz)$.

M-X	M = Cr (Å)	M = Mn (Å)
M-O1	1.553(2)	1.5455(18)
M-N1	1.913(2)	1.8808(19)
M-N2	1.901(2)	1.873(2)
M-N4	1.900(2)	1.8855(18)
M-N6	1.916(2)	1.8974(19)
M-N_4 plane	0.613	0.588

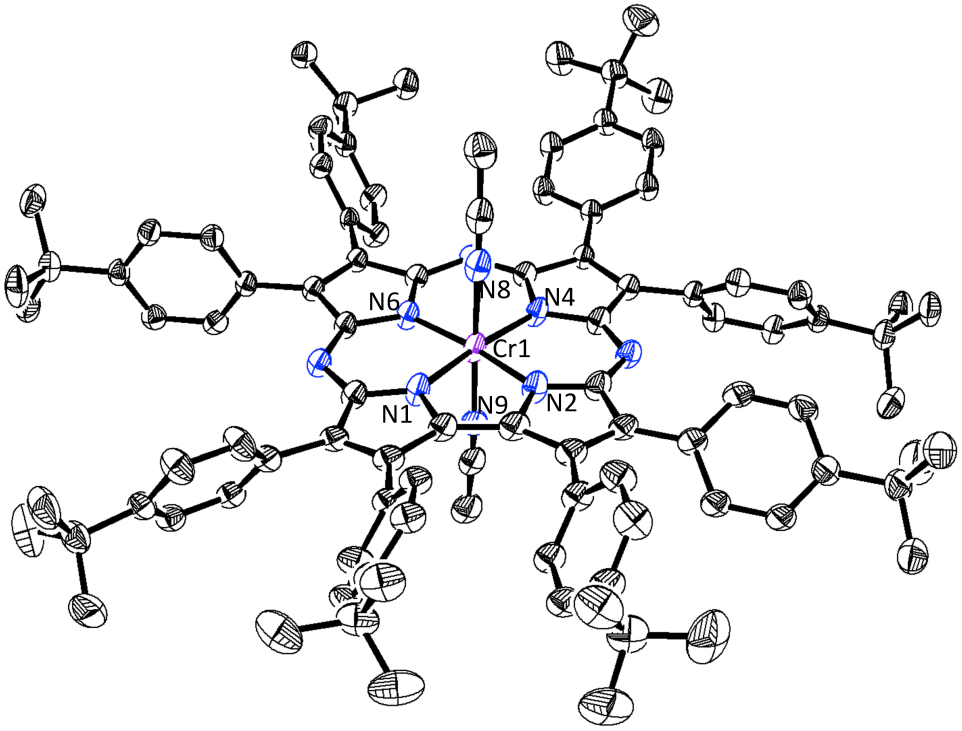

Figure 1.3. Displacement ellipsoid plot (50% probability) of $Cr^{III}(TBP_8Cz)(CH_3CN)_2$, obtained from reference 36.

The identical ligand environments for these two metal-oxo ($Mn^{V}(O)$ and $Cr^{V}(O)$) complexes provided a unique opportunity to study their comparative reactivities in H-atom abstraction reactions, which we discuss in Chapter 2 of this thesis. It was found that the $Mn^{V}(O)$ complex was capable of oxidizing H-atom donors with O–H or C–H bond strengths up to at least 80 kcal/mol, whereas the $Cr^{V}(O)$ complex could only oxidize the substrate TEMPOH which has a weak O–H bond of 67 kcal/mol. It was proposed that the putative one-electron-reduced $[Mn^{IV}(O)]^{-}$ was much more basic than the corresponding $[Cr^{IV}(O)]^{-}$ species, and that this difference in basicity controlled the difference in thermodynamic driving force for the two metal-oxo complexes.

1.7. References

(1) Poulos, T. L. Heme Enzyme Structure and Function. *Chem. Rev.* **2014**, *114*, 3919-3962.
(2) Groves, J. T.; Han, Y. In *Cytochrome P450: Structure, Mechanism and Biochemistry*; 2nd ed.; Ortiz de Montellano, P. R., Ed.; Plenum Press: New York, 1995.
(3) Rittle, J.; Green, M. T. Cytochrome P450 Compound I: Capture, Characterization, and C-H Bond Activation Kinetics. *Science* **2010**, *330*, 933-937.
(4) Yosca, T. H.; Rittle, J.; Krest, C. M.; Onderko, E. L.; Silakov, A.; Calixto, J. C.; Behan, R. K.; Green, M. T. Iron(IV)hydroxide pKa and the Role of Thiolate Ligation in C–H Bond Activation by Cytochrome P450. *Science* **2013**, *342*, 825-829.
(5) Green, M. T.; Dawson, J. H.; Gray, H. B. Oxoiron(IV) in Chloroperoxidase Compound II Is Basic: Implications for P450 Chemistry. *Science* **2004**, *304*, 1653-1656.
(6) Yosca, T. H.; Behan, R. K.; Krest, C. M.; Onderko, E. L.; Langston, M. C.; Green, M. T. Setting an Upper Limit on the Myoglobin Iron(IV)Hydroxide pKa: Insight into Axial Ligand Tuning in Heme Protein Catalysis. *J. Am. Chem. Soc.* **2014**, *136*, 9124-9131.
(7) Wang, X.; Ullrich, R.; Hofrichter, M.; Groves, J. T. Heme-thiolate ferryl of aromatic peroxygenase is basic and reactive. *Proc. Natl. Acad. Sci.* **2015**, *112*, 3686-3691.
(8) Yano, J.; Yachandra, V. Mn4Ca Cluster in Photosynthesis: Where and How Water is Oxidized to Dioxygen. *Chem. Rev.* **2014**, *114*, 4175-4205.
(9) Umena, Y.; Kawakami, K.; Shen, J.-R.; Kamiya, N. Crystal structure of oxygen-evolving photosystem II at a resolution of 1.9 Å. *Nature* **2011**, *473*, 55-60.
(10) Siegbahn, P. E. M. Structures and Energetics for O2 Formation in Photosystem II. *Acc. Chem. Res.* **2009**, *42*, 1871-1880.
(11) Siegbahn, P. E. M.; Crabtree, R. H. Manganese Oxyl Radical Intermediates and O-O Bond Formation in Photosynthetic Oxygen Evolution and a Proposed Role for the Calcium Cofactor in Photosystem II. *J. Am. Chem. Soc.* **1999**, *121*, 117-127.
(12) Groves, J. T.; Nemo, T. E.; Myers, R. S. Hydroxylation and epoxidation catalyzed by iron-porphine complexes. Oxygen transfer from iodosylbenzene. *J. Am. Chem. Soc.* **1979**, *101*, 1032-1033.
(13) Groves, J. T.; Haushalter, R. C.; Nakamura, M.; Nemo, T. E.; Evans, B. J. High-valent iron-porphyrin complexes related to peroxidase and cytochrome P-450. *J. Am. Chem. Soc.* **1981**, *103*, 2884-2886.
(14) Groves, J. T.; Lee, J.; Marla, S. S. Detection and Characterization of an Oxomanganese(V) Porphyrin Complex by Rapid-Mixing Stopped-Flow Spectrophotometry. *J. Am. Chem. Soc.* **1997**, *119*, 6269-6273.
(15) Arunkumar, C.; Lee, Y.-M.; Lee, J. Y.; Fukuzumi, S.; Nam, W. Hydrogen-Atom Abstraction Reactions by Manganese(V)– and Manganese(IV)–Oxo Porphyrin Complexes in Aqueous Solution. *Chem. - Eur. J.* **2009**, *15*, 11482-11489.
(16) Lee, J. Y.; Lee, Y.-M.; Kotani, H.; Nam, W.; Fukuzumi, S. High-valent manganese(v)-oxo porphyrin complexes in hydride transfer reactions. *Chemical Communications* **2009**, 704-706.
(17) Groves, J. T.; Kruper, W. J. Preparation and characterization of an oxoporphinatochromium(V) complex. *J. Am. Chem. Soc.* **1979**, *101*, 7613-7615.
(18) Groves, J. T.; Haushalter, R. C. E.s.r. evidence for chromium (V) porphyrinates. *J. Chem. Soc., Chem. Commun.* **1981**, 1165-1166.

(19) Budge, J. R.; Gatehouse, B. M. K.; Nesbit, M. C.; West, B. O. The autoxidation of a chromium (II) porphyrin: synthesis and structural characterisation by X-ray crystallography of [small alpha][small beta][gamma][small delta]-tetraphenyl-porphinato-oxochromium(IV). *J. Chem. Soc., Chem. Commun.* **1981**, 370-371.
(20) Groves, J. T.; Kruper, W. J.; Haushalter, R. C.; Butler, W. M. Synthesis, characterization, and molecular structure of oxo(porphyrinato)chromium(IV) complexes. *Inorg. Chem.* **1982**, *21*, 1363-1368.
(21) Johnson, A.; Kay, I. 306. Corroles. Part I. Synthesis. *Journal of the Chemical Society (Resumed)* **1965**, 1620-1629.
(22) Gross, Z.; Galili, N.; Saltsman, I. The First Direct Synthesis of Corroles from Pyrrole. *Angew. Chem., Int. Ed.* **1999**, *38*, 1427-1429.
(23) Gross, Z.; Galili, N.; Simkhovich, L.; Saltsman, I.; Botoshansky, M.; Bl√ § ser, D.; Boese, R.; Goldberg, I. Solvent-Free Condensation of Pyrrole and Pentafluorobenzaldehyde:‚Äâ A Novel Synthetic Pathway to Corrole and Oligopyrromethenes. *Organic Letters* **1999**, *1*, 599-602.
(24) Paolesse, R.; Mini, S.; Sagone, F.; Boschi, T.; Jaquinod, L.; J. Nurco, D.; M. Smith, K. 5,10,15-Triphenylcorrole: a product from a modified Rothemund reaction. *Chemical Communications* **1999**, 1307-1308.
(25) Koszarna, B.; Gryko, D. T. Efficient Synthesis of meso-Substituted Corroles in a H2O‚àíMeOH Mixture. *J. Org. Chem.* **2006**, *71*, 3707-3717.
(26) Orłowski, R.; Gryko, D.; Gryko, D. T. Synthesis of Corroles and Their Heteroanalogs. *Chem. Rev.* **2016**, Article ASAP.
(27) Gross, Z.; Golubkov, G.; Simkhovich, L. Epoxidation Catalysis by a Manganese Corrole and Isolation of an Oxomanganese(V) Corrole. *Angew. Chem., Int. Ed.* **2000**, *39*, 4045-4047.
(28) Meier-Callahan, A. E.; Gray, H. B.; Gross, Z. Stabilization of High-Valent Metals by Corroles: Oxo[tris(pentafluorophenyl)corrolato]chromium(V). *Inorg. Chem.* **2000**, *39*, 3605-3607.
(29) Zhang, W.; Lai, W.; Cao, R. Energy-Related Small Molecule Activation Reactions: Oxygen Reduction and Hydrogen and Oxygen Evolution Reactions Catalyzed by Porphyrin- and Corrole-Based Systems. *Chem. Rev.* **2016**, Article ASAP.
(30) Teo, R. D.; Hwang, J. Y.; Termini, J.; Gross, Z.; Gray, H. B. Fighting Cancer with Corroles. *Chem. Rev.* **2016**, Article ASAP.
(31) Paolesse, R.; Nardis, S.; Monti, D.; Stefanelli, M.; Di Natale, C. Porphyrinoids for Chemical Sensor Applications. *Chem. Rev.* **2016**, Article ASAP.
(32) Ramdhanie, B.; Stern, C. L.; Goldberg, D. P. Synthesis of the First Corrolazine: A New Member of the Porphyrinoid Family. *J. Am. Chem. Soc.* **2001**, *123*, 9447-9448.
(33) Joslin, E. E.; Zaragoza, J. P. T.; Baglia, R. A.; Siegler, M. A.; Goldberg, D. P. Complete Synthesis of Octaaryl Corrolazines and the Influence of Para-Substituents on Mn(V)-Oxo Reactivity. *Inorg. Chem.* **2016**, submitted for publication.
(34) Lansky, D. E.; Mandimutsira, B.; Ramdhanie, B.; Clausén, M.; Penner-Hahn, J.; Zvyagin, S. A.; Telser, J.; Krzystek, J.; Zhan, R.; Ou, Z.; Kadish, K. M.; Zakharov, L.; Rheingold, A. L.; Goldberg, D. P. Synthesis, Characterization, and Physicochemical Properties of Manganese(III) and Manganese(V)-Oxo Corrolazines. *Inorg. Chem.* **2005**, *44*, 4485-4498.

(35) Kerber, W. D.; Ramdhanie, B.; Goldberg, D. P. H2O2 Oxidations Catalyzed by an Iron(III) Corrolazine: Avoiding High-Valent Iron–Oxido Species? *Angew. Chem., Int. Ed.* **2007**, *46*, 3718-3721.
(36) Baglia, R. A.; Prokop-Prigge, K. A.; Neu, H. M.; Siegler, M. A.; Goldberg, D. P. Mn(V)(O) versus Cr(V)(O) Porphyrinoid Complexes: Structural Characterization and Implications for Basicity Controlling H-Atom Abstraction. *J. Am. Chem. Soc.* **2015**, *137*, 10874-10877.
(37) Zaragoza, J. P. T.; Siegler, M. A.; Goldberg, D. P. Rhenium(v)-oxo corrolazines: isolating redox-active ligand reactivity. *Chemical Communications* **2016**, *52*, 167-170.
(38) Evangelio, E.; Ruiz-Molina, D. Valence Tautomerism: New Challenges for Electroactive Ligands. *Eur. J. Inorg. Chem.* **2005**, *2005*, 2957-2971.
(39) Luca, O. R.; Crabtree, R. H. Redox-active ligands in catalysis. *Chem. Soc. Rev.* **2013**, *42*, 1440-1459.
(40) Chirik, P. J. Preface: Forum on Redox-Active Ligands. *Inorg. Chem.* **2011**, *50*, 9737-9740.
(41) Praneeth, V. K. K.; Ringenberg, M. R.; Ward, T. R. Redox-Active Ligands in Catalysis. *Angew. Chem., Int. Ed.* **2012**, *51*, 10228-10234.
(42) Groves, J. T.; Quinn, R.; McMurry, T. J.; Nakamura, M.; Lang, G.; Boso, B. Preparation and Characterization of a Dialkoxyiron(IV) Porphyrin. *J. Am. Chem. Soc.* **1985**, *107*, 354-360.
(43) Hickman, D. L.; Nanthakumar, A.; Goff, H. M. Identification of high-valent fluoroiron porphyrin intermediates associated with the electrocatalytic functionalization of hydrocarbons. *J. Am. Chem. Soc.* **1988**, *110*, 6384-6390.
(44) Phillippi, M. A.; Shimomura, E. T.; Goff, H. M. Investigation of axial anionic ligand and porphyrin substituent effects on the oxidation of iron(III) porphyrins: porphyrin-centered vs. metal-centered oxidation. *Inorg. Chem.* **1981**, *20*, 1322-1325.
(45) Buisson, G.; Deronzier, A.; Duee, E.; Gans, P.; Marchon, J. C.; Regnard, J. R. Iron(III)-porphyrin .pi.-cation radical complexes. Molecular structures and magnetic properties. *J. Am. Chem. Soc.* **1982**, *104*, 6793-6796.
(46) Kelly, S. L.; Kadish, K. M. Counterion and solvent effects on the electrode reactions of manganese porphyrins. *Inorg. Chem.* **1982**, *21*, 3631-3639.
(47) Camenzind, M. J.; Hollander, F. J.; Hill, C. L. Syntheses, ground electronic state, and crystal and molecular structure of the monomeric manganese(VI) porphyrin complex dimethoxy(5,10,15,20-tetraphenylporphinato)manganese(IV). *Inorg. Chem.* **1982**, *21*, 4301-4308.
(48) Kaustov, L.; Tal, M. E.; Shames, A. I.; Gross, Z. Spin Transition in a Manganese(III) Porphyrin Cation Radical, Its Transformation to a Dichloromanganese(IV) Porphyrin, and Chlorination of Hydrocarbons by the Latter. *Inorg. Chem.* **1997**, *36*, 3503-3511.
(49) Liu, W.; Huang, X.; Cheng, M.-J.; Nielsen, R. J.; Goddard, W. A.; Groves, J. T. Oxidative Aliphatic C-H Fluorination with Fluoride Ion Catalyzed by a Manganese Porphyrin. *Science* **2012**, *337*, 1322-1325.
(50) Simkhovich, L.; Goldberg, I.; Gross, Z. Iron(III) and Iron(IV) Corroles:,Äâ Synthesis, Spectroscopy, Structures, and No Indications for Corrole Radicals. *Inorg. Chem.* **2002**, *41*, 5433-5439.

(51) Walker, F. A.; Licoccia, S.; Paolesse, R. Iron corrolates: Unambiguous chloroiron(III) (corrolate)2,àí œÄ-cation radicals. *J. Inorg. Biochem.* **2006**, *100*, 810-837.
(52) Ye, S.; Tuttle, T.; Bill, E.; Simkhovich, L.; Gross, Z.; Thiel, W.; Neese, F. The Electronic Structure of Iron Corroles: A Combined Experimental and Quantum Chemical Study. *Chem. - Eur. J.* **2008**, *14*, 10839-10851.
(53) Pan, Z.; Harischandra, D. N.; Newcomb, M. Formation of stable and metastable porphyrin- and corrole-iron(IV) complexes and isomerizations to iron(III) macrocycle radical cations. *J. Inorg. Biochem.* **2009**, *103*, 174-181.
(54) Leeladee, P.; Baglia, R. A.; Prokop, K. A.; Latifi, R.; de Visser, S. P.; Goldberg, D. P. Valence Tautomerism in a High-Valent Manganese-Oxo Porphyrinoid Complex Induced by a Lewis Acid. *J. Am. Chem. Soc.* **2012**, *134*, 10397-10400.
(55) Baglia, R. A.; Dürr, M.; Ivanović-Burmazović, I.; Goldberg, D. P. Activation of a High-Valent Manganese-Oxo Complex by a Nonmetallic Lewis Acid. *Inorg. Chem.* **2014**, *53*, 5893-5895.
(56) Zaragoza, J. P. T.; Baglia, R. A.; Siegler, M. A.; Goldberg, D. P. Strong Inhibition of O-Atom Transfer Reactivity for MnIV(O)(π-Radical-Cation)(Lewis Acid) versus MnV(O) Porphyrinoid Complexes. *J. Am. Chem. Soc.* **2015**, *137*, 6531-6540.
(57) Cong, Z.; Kurahashi, T.; Fujii, H. Formation of Iron(III) meso-Chloro-isoporphyrin as a Reactive Chlorinating Agent from Oxoiron(IV) Porphyrin π-Cation Radical. *J. Am. Chem. Soc.* **2012**, *134*, 4469-4472.
(58) Tsurumaki, H.; Watanabe, Y.; Morishima, I. Preparation, characterization, and reactions of novel iron(III) porphyrin dication complexes. *J. Am. Chem. Soc.* **1993**, *115*, 11784-11788.
(59) Umena, Y.; Kawakami, K.; Shen, J.-R.; Kamiya, N. Crystal structure of oxygen-evolving photosystem II at a resolution of 1.9[thinsp]A. *Nature* **2011**, *473*, 55-60.
(60) Suga, M.; Akita, F.; Hirata, K.; Ueno, G.; Murakami, H.; Nakajima, Y.; Shimizu, T.; Yamashita, K.; Yamamoto, M.; Ago, H.; Shen, J.-R. Native structure of photosystem II at 1.95 A resolution viewed by femtosecond X-ray pulses. *Nature* **2015**, *517*, 99-103.
(61) Kanady, J. S.; Tsui, E. Y.; Day, M. W.; Agapie, T. A Synthetic Model of the Mn3Ca Subsite of the Oxygen-Evolving Complex in Photosystem II. *Science* **2011**, *333*, 733-736.
(62) Miller, C. G.; Gordon-Wylie, S. W.; Horwitz, C. P.; Strazisar, S. A.; Peraino, D. K.; Clark, G. R.; Weintraub, S. T.; Collins, T. J. A method for driving O-atom transfer: secondary ion binding to a tetraamide macrocyclic ligand. *J. Am. Chem. Soc.* **1998**, *120*, 11540-11541.
(63) Hong, S.; Lee, Y.-M.; Sankaralingam, M.; Vardhaman, A. K.; Park, Y. J.; Cho, K.-B.; Ogura, T.; Sarangi, R.; Fukuzumi, S.; Nam, W. A Manganese(V)-Oxo Complex: Synthesis by Dioxygen Activation and Enhancement of Its Oxidizing Power by Binding Scandium Ion. *J. Am. Chem. Soc.* **2016**.
(64) Klinker, E. J.; Kaizer, J.; Brennessel, W. W.; Woodrum, N. L.; Cramer, C. J.; Que, L. Structures of Nonheme Oxoiron(IV) Complexes from X-ray Crystallography, NMR Spectroscopy, and DFT Calculations. *Angew. Chem., Int. Ed.* **2005**, *44*, 3690-3694.
(65) Leto, D. F.; Ingram, R.; Day, V. W.; Jackson, T. A. Spectroscopic properties and reactivity of a mononuclear oxomanganese(iv) complex. *Chemical Communications* **2013**, *49*, 5378-5380.

(66) Chen, J.; Lee, Y.-M.; Davis, K. M.; Wu, X.; Seo, M. S.; Cho, K.-B.; Yoon, H.; Park, Y. J.; Fukuzumi, S.; Pushkar, Y. N.; Nam, W. A Mononuclear Non-Heme Manganese(IV)-Oxo Complex Binding Redox-Inactive Metal Ions. *J. Am. Chem. Soc.* **2013**, *135*, 6388-6391.
(67) Chen, J.; Yoon, H.; Lee, Y.-M.; Seo, M. S.; Sarangi, R.; Fukuzumi, S.; Nam, W. Tuning the reactivity of mononuclear nonheme manganese(iv)-oxo complexes by triflic acid. *Chem. Sci.* **2015**, *6*, 3624-3632.
(68) Yoon, H.; Lee, Y.-M.; Wu, X.; Cho, K.-B.; Sarangi, R.; Nam, W.; Fukuzumi, S. Enhanced Electron-Transfer Reactivity of Nonheme Manganese(IV)–Oxo Complexes by Binding Scandium Ions. *J. Am. Chem. Soc.* **2013**, *135*, 9186-9194.
(69) Jung, J.; Kim, S.; Lee, Y.-M.; Nam, W.; Fukuzumi, S. Switchover of the Mechanism between Electron Transfer and Hydrogen-Atom Transfer for a Protonated Manganese(IV)–Oxo Complex by Changing Only the Reaction Temperature. *Angew. Chem., Int. Ed.* **2016**, *55*, 7450-7454.
(70) Park, J.; Morimoto, Y.; Lee, Y.-M.; Nam, W.; Fukuzumi, S. Unified View of Oxidative C-H Bond Cleavage and Sulfoxidation by a Nonheme Iron(IV)-Oxo Complex via Lewis Acid-Promoted Electron Transfer. *Inorg. Chem.* **2014**, *53*, 3618-3628.
(71) Hill, E. A.; Weitz, A. C.; Onderko, E.; Romero-Rivera, A.; Guo, Y.; Swart, M.; Bominaar, E. L.; Green, M. T.; Hendrich, M. P.; Lacy, D. C.; Borovik, A. S. Reactivity of an FeIV-Oxo Complex with Protons and Oxidants. *J. Am. Chem. Soc.* **2016**, *138*, 13143-13146.
(72) Hong, S.; Pfaff, F. F.; Kwon, E.; Wang, Y.; Seo, M.-S.; Bill, E.; Ray, K.; Nam, W. Spectroscopic Capture and Reactivity of a Low-Spin Cobalt(IV)-Oxo Complex Stabilized by Binding Redox-Inactive Metal Ions. *Angew. Chem., Int. Ed.* **2014**, *53*, 10403-10407.
(73) Kundu, S.; Miceli, E.; Farquhar, E.; Pfaff, F. F.; Kuhlmann, U.; Hildebrandt, P.; Braun, B.; Greco, C.; Ray, K. Lewis Acid Trapping of an Elusive Copper,ÄìTosylnitrene Intermediate Using Scandium Triflate. *J. Am. Chem. Soc.* **2012**, *134*, 14710-14713.
(74) Park, Y. J.; Ziller, J. W.; Borovik, A. S. The Effects of Redox-Inactive Metal Ions on the Activation of Dioxygen: Isolation and Characterization of a Heterobimetallic Complex Containing a MnIII–(μ-OH)–CaII Core. *J. Am. Chem. Soc.* **2011**, *133*, 9258-9261.
(75) Park, Y. J.; Cook, S. A.; Sickerman, N. S.; Sano, Y.; Ziller, J. W.; Borovik, A. S. Heterobimetallic complexes with MIII-([small mu]-OH)-MII cores (MIII = Fe, Mn, Ga; MII = Ca, Sr, and Ba): structural, kinetic, and redox properties. *Chem. Sci.* **2013**, *4*, 717-726.
(76) Cook, S. A.; Ziller, J. W.; Borovik, A. S. Iron(II) Complexes Supported by Sulfonamido Tripodal Ligands: Endogenous versus Exogenous Substrate Oxidation. *Inorg. Chem.* **2014**, *53*, 11029-11035.
(77) Lam, W. W. Y.; Yiu, S.-M.; Lee, J. M. N.; Yau, S. K. Y.; Kwong, H.-K.; Lau, T.-C.; Liu, D.; Lin, Z. BF3-Activated Oxidation of Alkanes by MnO4. *J. Am. Chem. Soc.* **2006**, *128*, 2851-2858.
(78) Chen, Z.; Yin, G. The reactivity of the active metal oxo and hydroxo intermediates and their implications in oxidations. *Chem. Soc. Rev.* **2015**, *44*, 1083-1100.
(79) Prokop, K. A.; Goldberg, D. P. Generation of an Isolable, Monomeric Manganese(V)–Oxo Complex from O2 and Visible Light. *J. Am. Chem. Soc.* **2012**, *134*, 8014-8017.

(80) Jung, J.; Ohkubo, K.; Prokop-Prigge, K. A.; Neu, H. M.; Goldberg, D. P.; Fukuzumi, S. Photochemical Oxidation of a Manganese(III) Complex with Oxygen and Toluene Derivatives to Form a Manganese(V)-Oxo Complex. *Inorg. Chem.* **2013**, *52*, 13594-13604.
(81) Lansky, D. E.; Goldberg, D. P. Hydrogen Atom Abstraction by a High-Valent Manganese(V)-Oxo Corrolazine. *Inorg. Chem.* **2006**, *45*, 5119-5125.
(82) Fukuzumi, S.; Kotani, H.; Prokop, K. A.; Goldberg, D. P. Electron- and Hydride-Transfer Reactivity of an Isolable Manganese(V)-Oxo Complex. *J. Am. Chem. Soc.* **2011**, *133*, 1859-1869.
(83) Baglia, R. A.; Krest, C. M.; Yang, T.; Leeladee, P.; Goldberg, D. P. High-Valent Manganese–Oxo Valence Tautomers and the Influence of Lewis/Br√ ∂ nsted Acids on C–H Bond Cleavage. *Inorg. Chem.* **2016**, *55*, 10800-10809.

2. Chapter 2. Mn(V)(O) versus Cr(V)(O) Porphyrinoid Complexes: Structural Characterization and Implications for Basicity Controlling H-Atom Abstraction

This work was co-written with the following authors and was published under the following title and citation:

Baglia, R. A.; Prokop-Prigge, K. A.; Neu, H. M.; Siegler, M. A.; Goldberg, D. P. "Mn(V)(O) versus Cr(V)(O) Porphyrinoid Complexes: Structural Characterization and Implications for Basicity Controlling H-Atom Abstraction" *J. Am. Chem. Soc.*, **2015**, *137*, 10874-10877.

2.1. Introduction

The ability of high-valent metal-oxo complexes to abstract hydrogen atoms from organic compounds is of critical importance to the functioning of metal-based oxidation catalysts. Included among these catalysts are enzymatic systems that utilize both heme and nonheme metal active sites.[1,2] How the metal ion, the coordinating ligands, and surrounding protein matrix in the case of biological catalysts, control the reactivity of metal-oxo intermediates in H-atom abstraction is a question of fundamental importance. In heme enzymes, the Cytochrome P450s are among the most powerful H-atom abstractors, utilizing Compound I ((Fe^{IV}(O)(porph$^{\bullet+}$)(cys)) for strong C-H cleavage.[1] The large driving force presented for H-atom abstraction by P450 can be related to the bond dissociation free energy (BDFE) of the O-H bond of Compound II (Fe^{IV}(OH)(porph)(cys)), formed after H-atom transfer (HAT). The O-H BDFE can be further dissected into electron (E°) and proton (pK_a) affinities (or basicity), and evidence

indicates that it is the elevated basicity of the Fe^{IV}=O unit in Cpd-II (pK_a ~ 12) that provides an advantage in driving force for HAT.[1c,e]

Attempts to synthesize biomimetic high-valent metal-oxo species and examine their propensity for HAT has led to parallel insights regarding the thermodynamic control of these reactions.[3,4] These studies have helped support the analysis of the biological systems, and supplied information for the design of synthetic oxidation catalysts. However, much remains to be learned regarding how the metal ion and ligand(s) of M(O)(L_n) complexes tune M(O-H) BDFEs, redox potentials, pK_as, and ultimately HAT reactivity.

In this report we compare the H-atom abstraction abilities of Mn^V(O) and Cr^V(O) porphyrinoid complexes. Both of these complexes are characterized by single crystal X-ray diffraction (XRD). To our knowledge, the manganese complex is the first example of a structurally characterized Mn^V(O) complex in a heme-type environment. The Cr and Mn complexes are isomorphous, providing a unique opportunity to determine the inherent HAT reactivity of Mn^V(O) versus Cr^V(O) moieties. Although Cr^V(O) complexes, including porphyrins, are known, little information is available regarding their H-atom abstraction abilities.5 In this report we show that Cr^V(O) is a better 1-e^- oxidant than Mn^V(O), but is a much *weaker* H-atom abstractor.

2.2. Experimental Methods

2.2.1. General methods and materials

Compounds TBP_8CzH_3 and Mn^V(O)(TBP_8Cz) (**2**) were synthesized according to published procedures.[6,7] The commercially available reagents triphenylphosphine (PPh_3), chromium hexacarbonyl, and tetrabutylammonium hexafluorophosphate were obtained

from Sigma-Aldrich at the best available purity and used as received. The H-atom donor 2,2,6,6-tetramethylpiperidine hydroxylamine (TEMPOH) and its deuterated analogue TEMPOD were synthesized according to published procedures.[8] Deuterated chloroform ($CDCl_3$, 0.03% v/v TMS) for NMR was purchased from Cambridge Isotopes, Inc. Toluene was purified via a Pure-Solv solvent purification system from Innovative Technologies, Inc, and all other solvents were purchased and used as received.

2.2.2. Analytical methods

UV-vis spectroscopy was performed on a Hewlett-Packard 8452 diode-array spectrophotometer equipped with HPChemstation software. ^{1}H-NMR spectra were recorded on a Bruker Avance 400 NMR instrument at 400 MHz. Electron paramagnetic resonance (EPR) spectra were recorded with a Bruker EMX spectrometer equipped with a Bruker ER 041 X G microwave bridge and a continuous-flow liquid helium cryostat (ESR900) coupled to an Oxford Instruments TC503 temperature controller. Cyclic voltammetry measurements were undertaken in methylene chloride using a BAS 100B electrochemical analyzer with a glassy carbon working electrode and a platinum wire auxiliary electrode. Potentials were recorded versus an $Ag/AgNO_3$ electrode. Scans were run at 25 mV/s under Ar atmosphere using $[Bu_4N][PF_6]$ (0.1 M) as the supporting electrolyte.

2.2.3. Single Crystal X-ray Crystallography

All reflection intensities were measured at 110(2) K using a SuperNova diffractometer (equipped with Atlas detector) with Cu *K*α radiation (λ = 1.54178 Å) under the program CrysAlisPro (Versions 1.171.36.32 or 1.171.37.31, Agilent Technologies, 2013-2014). The same program was used to refine the cell dimensions and

for data reduction. The structure was solved with the program SHELXS-2013 (Sheldrick, 2013) and was refined on F^2 with SHELXL-2013 (Sheldrick, 2013). Analytical numeric absorption correction based on a multifaceted crystal model was applied using CrysAlisPro. The temperature of the data collection was controlled using the system Cryojet (manufactured by Oxford Instruments). The H atoms were placed at calculated positions using the instructions AFIX 43 or AFIX 137 with isotropic displacement parameters having values 1.2 or 1.5 times *U*eq of the attached C atoms.

2.2.4. Structure of $Mn^{V}(O)(TBP_8Cz)$

One of the eight tert-butylphenyl (TBP) groups is found to be disordered over two orientations. The occupancy factor of the major component of the disorder refines to 0.910(4). The $Mn^{V}{\equiv}O$ fragment is also slightly disordered, with the oxo ligand coordinated on either side of the plane of the corrolazine ligand. The occupancy factor of the major component of the disorder refines to 0.8671(7). The crystal lattice contains some amount of ordered and disordered lattice MeCN solvent molecules. The occupancy factors of the ordered lattice MeCN solvent molecules were refined using free variables, and there are *ca.* 1.94 ordered MeCN molecules per Mn complex. Some electron density in the asymmetric unit – i.e., some amount of very disordered solvent MeCN molecules with partial occupancy – has been taken out in the final refinement using the SQUEEZE procedure (SQUEEZE details are provided in the CIF file, Spek, 2003).

$Mn^{V}(O)(TBP_8Cz)$: Fw = 1506.43, dark thin brown-purple lath, 0.62 × 0.06 × 0.02 mm^3, triclinic, *P*-1 (no. 2), a = 13.2613(4), b = 16.7068(5), c = 22.4780(8) Å, α = 75.669(3), β = 75.927(3), γ = 78.815(3)°, V = 4632.6(3) $Å^3$, Z = 2, D_x = 1.080 g cm^{-3}, μ = 1.533 mm^{-1}, abs. corr. range: 0.674–0.972. 55653 Reflections were measured up to a resolution of

(sin $\theta/\lambda)_{max}$ = 0.62 Å^{-1}. 18021 Reflections were unique (R_{int} = 0.0611), of which 12850 were observed [$I > 2\sigma(I)$]. 1120 Parameters were refined using 357 restraints. $R1/wR2$ [$I > 2\sigma(I)$]: 0.0580/0.1339. $R1/wR2$ [all refl.]: 0.0878/ 0.1490. S = 1.009. Residual electron density found between −0.51 and 0.41 e Å^{-3}.

2.2.5. Structure of $Cr^{V}(O)(TBP_8Cz)$

Two of the eight tert-butylphenyl (TBP) groups are found to be disordered over two orientations. The occupancy factors of the two major components of the disorder refine to 0.54(2) and 0.760(5). The $Cr^{V}{\equiv}O$ fragment is also slightly disordered, with the oxo ligand coordinated on either side of the plane of the corrolazine ligand. The occupancy factor of the major component of the disorder refines to 0.9175(8). The crystal lattice contains some amount of ordered and disordered lattice MeCN solvent molecules. The occupancy factors of the ordered lattice MeCN solvent molecules were refined using free variables, and there are *ca.* 1.94 ordered MeCN molecules per Cr complex. Some electron density in the asymmetric unit – *i.e.*, some amount of very disordered solvent MeCN molecules with partial occupancy – has been taken out in the final refinement using the SQUEEZE procedure (SQUEEZE details are provided in the CIF file, Spek, 2003). The crystal that was mounted on the diffractometer was not single, but rather two crystals stuck together with random orientations (the crystal was not twinned). The diffraction patterns of components 1 and 2 are related by a rotation *ca.* 2.80° around the vector 0.7123**a*** + 0.6150**b*** + 0.3382**c***. Data integration of both components was performed using CrysAlisPro (Version 1.171.37.31 Agilent Technologies, 2014), and a HKLF 5 file was made. In order to perform the SQUEEZE

procedure , the detwinning option was set in SHELXL-2013 via a LIST 8 style FCF. The BASF scale factor refines to 0.2615(14).

$Cr^{V}(O)(TBP_8Cz)$: Fw = 1503.50, brown plate, 0.20 × 0.10 × 0.03 mm^3, triclinic, *P*-1 (no. 2), a = 13.2521(4), b = 16.7844(5), c = 22.5120(8) Å, α = 75.947(3), β = 75.899(3), γ = 78.856(3)°, V = 4663.0(3) $Å^3$, Z = 2, D_x = 1.071 g cm^{-3}, μ = 1.381 mm^{-1}, abs. corr. range: 0.803–0.967. 49216 Reflections were measured up to a resolution of $(\sin \theta/\lambda)_{max}$ = 0.60 $Å^{-1}$. 21055 Reflections were unique (R_{int} = 0.0413), of which 11606 were observed [$I > 2\sigma(I)$]. 1206 Parameters were refined using 675 restraints. $R1/wR2$ [$I > 2\sigma(I)$]: 0.0491/0.1091. $R1/wR2$ [all refl.]: 0.0860/0.1174. S = 0.787. Residual electron density found between −0.42 and 0.40 e $Å^{-3}$.

2.2.6. Structure of $Cr^{III}(TBP_8Cz)(CH_3CN)_2$

The crystal lattice was found to contain a small impurity of $Cr^{V}(O)(TBP_8Cz)$ (starting material), and the occupancy factor of the minor impurity refines to 0.053(2). The crystal lattice also contains some amount of uncoordinated acetonitrile solvent molecules. The asymmetric unit contains one ordered (occupancy factor: 0.799(7)) and one disordered (the occupancy factors of the two components of the disorder refine to 0.588(8) and 0.341(8)) MeCN lattice molecules.

$Cr^{III}(TBP_8Cz)(CH_3CN)_2$: Fw = 1557.35, dark brown irregular block, 0.37 × 0.14 × 0.10 mm^3, triclinic, *P*-1 (no. 2), a = 12.2628(3), b = 18.0788(4), c = 20.8997(5) Å, α = 75.7972(18), β = 81.3662(19), γ = 75.8437(19)°, V = 4335.30(18) $Å^3$, Z = 2, D_x = 1.193 g cm^{-3}, μ = 1.500 mm^{-1}, T_{min}–T_{max}: 0.710–0.895. 56707 Reflections were measured up to a resolution of $(\sin \theta/\lambda)_{max}$ = 0.62 $Å^{-1}$. 17015 Reflections were unique (R_{int} = 0.0267), of which 14721 were observed [$I > 2\sigma(I)$]. 1117 Parameters were refined using 118

restraints. $R1/wR2$ [$I > 2\sigma(I)$]: 0.0637/0.1812. $R1/wR2$ [all refl.]: 0.0717/0.1908. S = 1.022. Residual electron density found between -0.50 and 0.90 e $Å^{-3}$.

2.2.7. Synthesis of $Cr^{V}(O)(TBP_8Cz)$ (3)

An amount of $Cr(CO)_6$ (0.14 mmol, 30 mg) was added to the metal-free corrolazine, TBP_8CzH_3 (44 mg, 0.032 mmol), in refluxing toluene under air. After 2 h, the toluene was removed under vacuum. The crude material was then purified by flash column chromatography on silica gel using CH_2Cl_2/hexanes (60:40) as eluent. The purified material was collected and dried under vacuum. Purity checked by UV-vis (Figure 2.2) and TLC. Crystals were obtained by slow vapor diffusion of acetonitrile into a toluene solution of **3** over the course of two weeks. Yield, (19 mg, 42%). R_f = 0.77 (CH_2Cl_2:Hex, 60:40 on silica gel). UV-vis (CH_2Cl_2): λ_{max} (nm) ($\varepsilon \times 10^{-4}$ M^{-1} cm^{-1}) 448 (7.08) (soret), 653 (2.71) (Q band). *Anal. Calcd* for $C_{96}H_{104}N_7CrO$: C, 80.98; H, 7.36; N, 6.89. Found: C, 81.01; H, 7.62; N, 6.47.

2.2.8. Synthesis of $Cr^{III}(TBP_8Cz)(CH_3CN)_2$ (4)

To an amount of **3** (0.9 mmol) in toluene was added PPh_3 (1 equiv), followed by vapor diffusion of acetonitrile into the reaction mixture. After two weeks, X-ray quality crystals of **4** were obtained. UV-vis: 465 nm (soret), 711 nm (Q band).

2.2.9. Evans method measurement

An amount of **3** (0.84 mM) in $CDCl_3$ containing 0.03 % TMS was placed in an NMR tube with a coaxial inner tube containing blank solvent ($CDCl_3$ with 0.03 % v/v TMS). ^{1}H NMR spectra were recorded at 298 K, and the chemical shift of the TMS peak in the presence of the paramagnetic **3** was compared to that of the TMS peak in the inner

tube containing only the TMS standard (Figure 2.5). The effective spin-only magnetic moment was calculated by a simplified Evans method analysis[9] according to Eq. 1:

$$\mu_{eff} = 0.0618\sqrt{\frac{\Delta\nu \mathrm{T}}{2\mathrm{fM}}} \qquad (1)$$

where f is the oscillator frequency (MHz) of the superconducting spectrometer, T is the temperature (K), M is the molar concentration of the paramagnetic metal complex, and $\Delta\nu$ is the difference in frequency (Hz) between the two reference (TMS) signals.

2.2.10. EPR Spectroscopy of $Cr^{III}(TBP_8Cz)$

To an amount of **3** (1.3 mmol) dissolved in toluene was added a toluene solution of PPh_3 (1.3 mmol, 1 equiv) in a drybox and allowed to react for 16 h. A subtle color change from a lustrous green to a deep dull forest green was observed. This solution was loaded into an EPR tube, and an EPR spectrum (9.44 GHz, 294 K) was obtained. The same sample was annealed at 77 K and an EPR spectrum was recorded at 12 K (Figure 2.8).

2.2.11. Kinetics of the Reaction of 3 with TEMPOH(D)

To an amount of **3** (2.4×10^{-8} mol) dissolved in CH_2Cl_2 (2 mL) was added TEMPOH(D) (25 – 100 equiv) and the reaction was followed by UV-vis. The spectrum for **3** (448, 653 nm) isosbestically converted to a new spectrum for $Cr^{III}(TBP_8Cz)$ (λ_{max} = 465, 711 nm). Plots of the decay in absorbance due to **3** at 653 nm versus time appeared to be pseudo-first order up to 5 half-lives, and were well-fit by the first-order expression shown in Eq 2:

$$\mathrm{Abs_t} = \mathrm{Abs_f} + (\mathrm{Abs_0}\text{-}\mathrm{Abs_f})e^{-k_{obs}t} \qquad (2)$$

where Abs_t = absorbance at time t, Abs_f = final absorbance, Abs_0 = initial absorbance, and k_{obs} is the pseudo-first-order rate constant (Figure 2.9b). A plot of k_{obs} versus concentration of TEMPOH was found to be linear, and the slope of the best-fit line gave k_2, the second-order rate constant (Figure 2.12).

2.2.12. Quantitation of TEMPO• by X-band EPR Spectroscopy

An amount of **3** dissolved in toluene (1 mM) was mixed with TEMPOH (5 equivalents) under an Ar atmostphere. The reaction mixture was loaded into an EPR tube, and an EPR spectrum (294 K) (Figure 2.11, blue) was obtained. The 3-line signal centered at g = 2.00 is assigned to the TEMPO radical product and gives an 82% yield according to the stoichiometry given in Scheme 1. Quantification of the TEMPO• product was determined by double integration against a calibration curve of an external TEMPO radical standard. The 9-line signal centered at g = 1.987 is attributed to unreacted $Cr^V(O)$ complex (5% of starting **3** by quantitation). The starting TEMPOH substrate contained a small TEMPO• impurity (~7% by quantitation, Figure 2.11, red spectrum).

2.3. Results and Discussion

2.3.1. Characterization of $Mn^V(O)(TBP_8Cz)$ by X-ray Diffraction

The synthesis of $Mn^V(O)(TBP_8Cz)$ (TBP_8Cz = octakis(*p-tert*-butylphenyl)corrolazinato^{3-}) was carried out in a manner similar to that previously reported.[4a] Addition of freshly prepared PhIO (10 equiv) to $Mn^{III}(TBP_8Cz)$ (**1**) in CH_2Cl_2 gives the oxidized $Mn^V(O)(TBP_8Cz)$ (**2**), which can be purified by silica gel chromatography. Dissolution of **2** in toluene to give a dark green solution followed by slow vapor diffusion of CH_3CN leads to the growth of dark green needles after a few days. These crystals were suitable for X-ray structure determination, and the structure of

2 is shown in Figure 2.1. Previous attempts at growing crystals of **2** in other solvent combinations were plagued by decomposition of the complex. However, we observed that **2** was stable in toluene/CH_3CN for at least two weeks, and favored slow crystal growth. This crystallization method was also highly reproducible. As depicted in Figure 2.1, the Mn^V ion is 5-coordinate, with Mn–$N_{pyrrole}$ distances between 1.873(2) – 1.8974(19) Å, and a short Mn–O distance of 1.5455(18) Å consistent with an Mn≡O triple bond. These distances are in agreement with those determined previously by EXAFS (d(Mn–O) = 1.56 Å, d(Mn–$N_{pyrrole}$) = 1.88 Å).[4a] Structurally characterized non-heme complexes have Mn–O bond distances of 1.548(4) Å – 1.558(4) Å, which are comparable with that of **2**.[10] The manganese ion in **2** is significantly displaced by ca. 0.59 Å from the plane of the four pyrrole N atoms toward the terminal oxo ligand. For the isoelectronic Mn^V(NMes)(TBP_8Cz), the terminal mesitylimido Mn–N distance is slightly longer at 1.595(4) – 1.611(4) Å, while the Mn ion is less displaced out of the $N_{pyrrole}$ plane (Mn – N_4(plane) = 0.55 Å).[4c] The structure unequivocally shows that the Mn^V(O) complex is 5-coordinate, as opposed to the proposed structures for related Mn^V(O) porphyrins.[11]

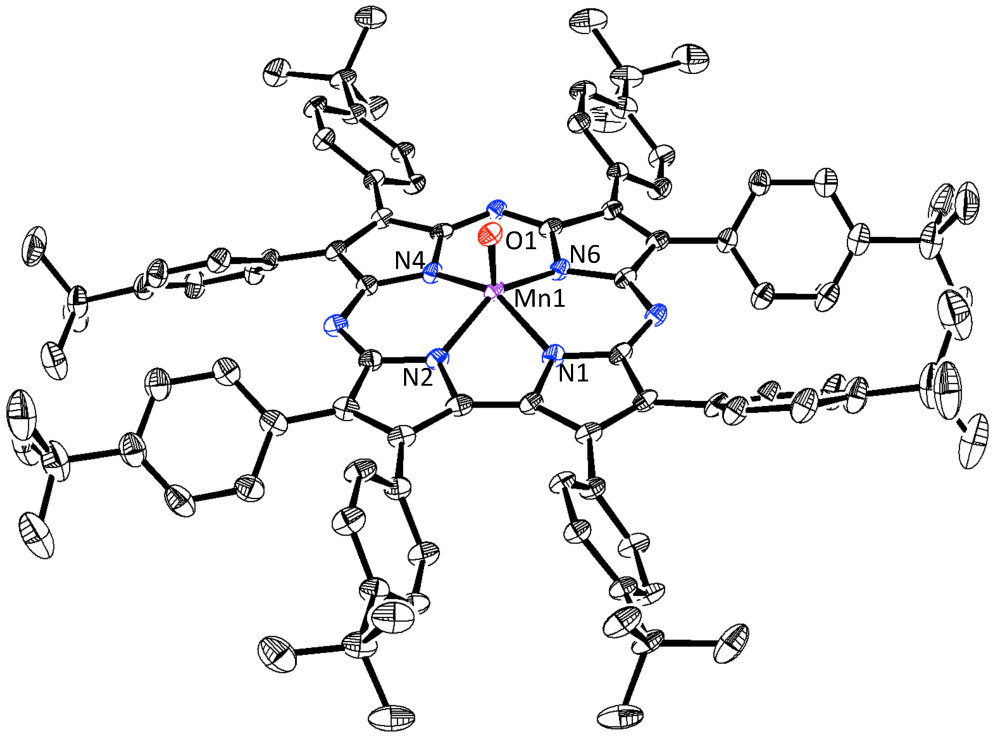

Figure 2.1. Displacement ellipsoid plot (50% probability level) of $Mn^{V}(O)(TBP_8Cz)$ (2) at 110(2) K. H-atoms and disorder are omitted for clarity.

2.3.2. Synthesis and Characterization of $Cr^{V}(O)(TBP_8Cz)$

The analogous $Cr^{V}(O)(TBP_8Cz)$ (**3**) was synthesized by aerobic, oxidative metallation of the metal-free corrolazine, TBP_8CzH_3, with $Cr(CO)_6$ in refluxing toluene.[5d] No significant color change from the deep green of the metal-free starting material (l_{max} = 456, 679 nm) was noted, but monitoring the reaction by UV-vis revealed distinct shifts in both the Soret and Q-band regions (**3**: l_{max} = 448, 653 nm) (Figure 2.2). Complex **3** was purified by flash chromatography (eluent: 60:40, CH_2Cl_2:hexanes), and recrystallized from vapor diffusion of acetonitrile into a toluene solution of **3** over 1 week. X-ray structure determination was carried out and its structure, which is isomorphous with the $Mn^{V}(O)$ complex, is shown in Figure 2.3. The Cr^{V} ion is 5-coordinate as seen for Mn,

and Cr–O = 1.553(2) Å. This distance is similar to that seen for Cr^{V}(O) corroles (~1.57 Å).[5d,12] The out of plane displacement of the chromium in **3** (Cr–N_4(plane) = 0.61 Å) is slightly larger than that seen for the corrole analogs (0.56-0.58), probably arising from the smaller cavity size of corrolazine (trans $N_{pyrrole}$–$N_{pyrrole}$: 3.61 Å) versus corrole (trans $N_{pyrrole}$–$N_{pyrrole}$: 3.67-3.69 Å). The metal-oxo distance for **3** is identical to that of **2**, but the M–$N_{pyrrole}$ distances are slightly longer for **3** versus **2** (see Table 2.1)**.** The out-of-plane distance for **3** is also slightly larger than **2**. These observations are consistent with the larger ionic radius of the Cr^{V} versus Mn^{V} ion.[13]

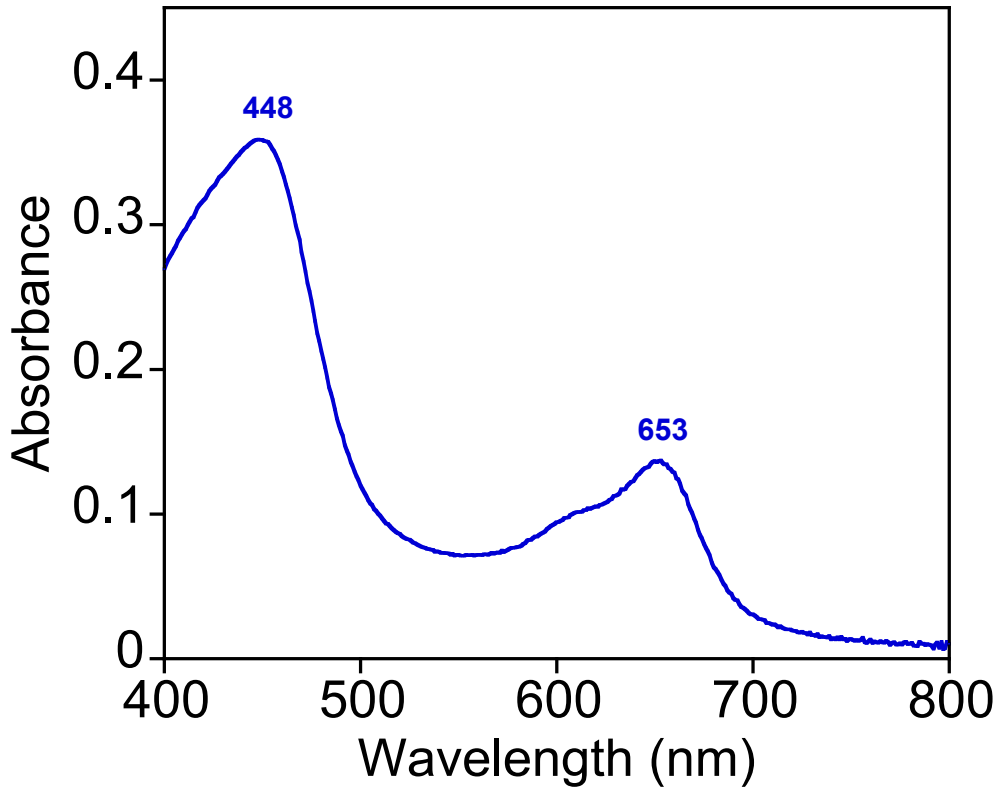

Figure 2.2. UV-visible spectrum of complex 3 (5 µM) in CH_2Cl_2.

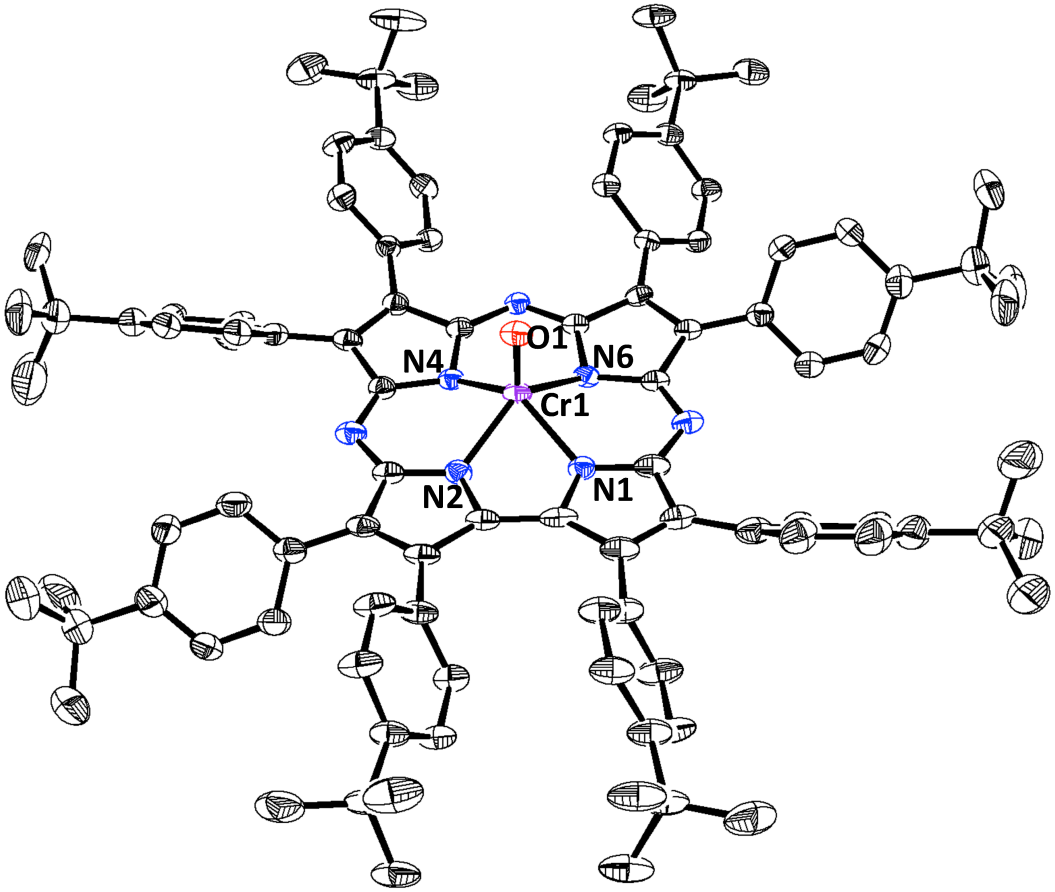

Figure 2.3. Displacement ellipsoid plot (50% probability level) of $Cr^{V}(O)(TBP_8Cz)$ (3) at 110(2) K. H-atoms and disorder are omitted for clarity.

Table 2.1. Comparison of atomic distances from X-ray diffraction for the first coordination sphere of $Cr^{V}(O)(TBP_8Cz)$ (3) and $Mn^{V}(O)(TBP_8Cz)$ (2).

M-X	M = Cr (Å)	M = Mn (Å)
M-O1	1.553(2)	1.5455(18)
M-N1	1.913(2)	1.8808(19)
M-N2	1.901(2)	1.873(2)
M-N4	1.900(2)	1.8855(18)
M-N6	1.916(2)	1.8974(19)
M-N_4 plane	0.613	0.588

The EPR spectrum (9.44 GHz, 294 K) of **3** is shown in Figure 2.4. A 9 line signal centered at g = 1.987 is observed, consistent with a Cr^{V} (d^1, S = ½) ion with hyperfine coupling to four equivalent pyrrole nitrogen atoms (^{14}N, I = 1). The satellite signals at high and low fields are due to hyperfine splitting from ^{53}Cr (9.5% abundant, I = 3/2). Evans method NMR measurement gave a magnetic moment of μ_{eff} = 1.36 μ_B, which is close to the predicted spin-only value of 1.73 μ_B for an S = ½ ion. These data confirm the +5 oxidation state of the Cr ion, and rule out the involvement of other potential ground state electronic configurations, such as $Cr^{IV}(O)(TBP_8Cz^{\bullet+})$.[4g,h]

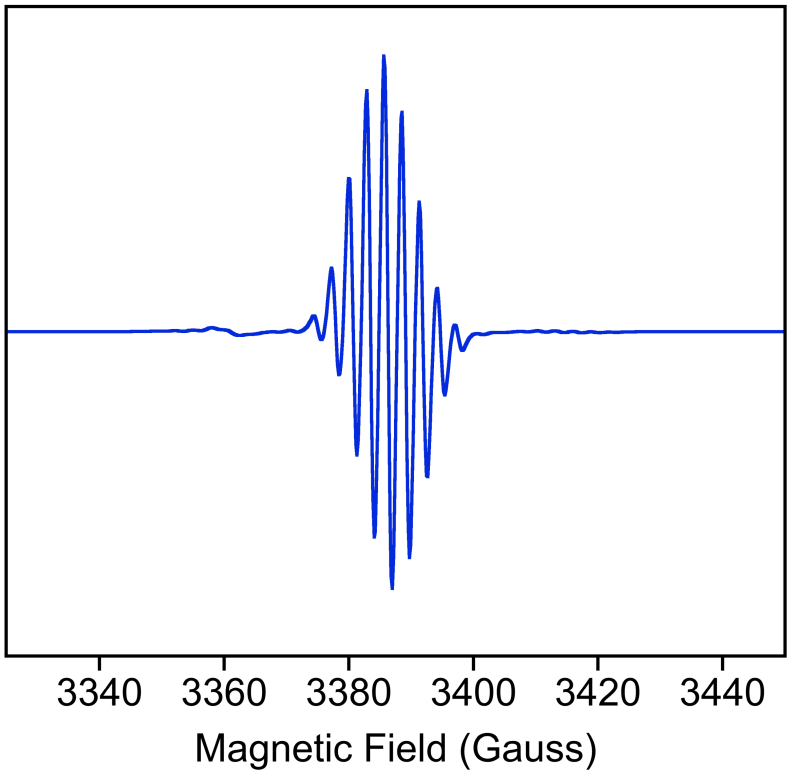

Figure 2.4. The EPR spectrum (9.44 GHz) of 3 (2.0 mM in CH_2Cl_2) was obtained at 294 K under non-saturating microwave power conditions. Hyperfine coupling to four equivalent nitrogen atoms gives a 9-line signal centered at g = 1.987 with a hyperfine coupling constant of $A_{iso}(^{14}N)$ = 2.9 G. Satellite signals at 3360 and 3414 G are attributed to coupling to the ^{53}Cr nucleus. Experimental conditions: Microwave frequency = 9.4400 GHz; Microwave power = 0.06 mW; Modulation amplitude = 1 G, Receiver gain = 5×10^3.

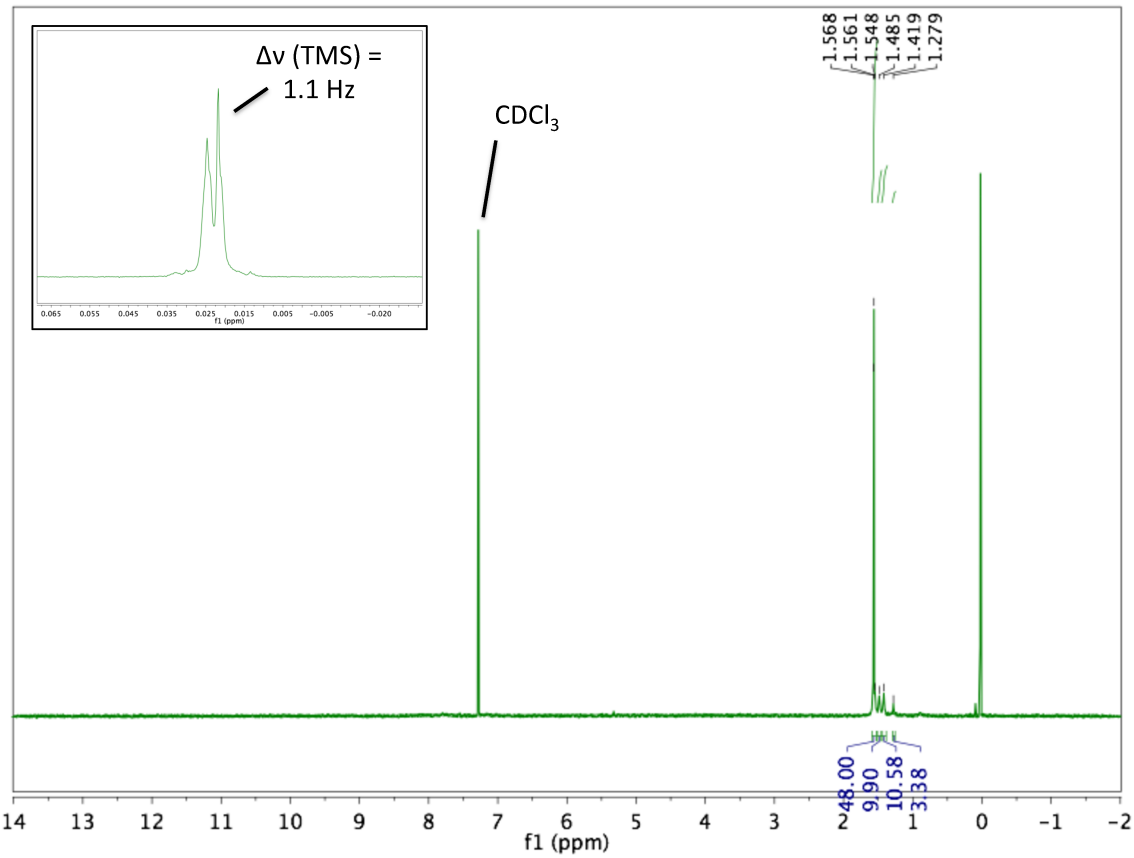

Figure 2.5. Evans method 1H-NMR spectrum of 3 (0.84 mM) in $CDCl_3$ (0.03 % TMS v/v).

2.3.3. Synthesis and Characterization of $Cr^{III}(TBP_8Cz)(CH_3CN)_2$

Prior to examining the reactivity of the $Cr^{V}(O)$ complex **3**, we synthesized the reduced chromium(III) analog to obtain a spectroscopic benchmark for this species. Addition of triphenylphosphine, an oxygen atom acceptor, to **3** in toluene, followed by slow vapor diffusion of CH_3CN over the course of 2 weeks led to X-ray quality crystals of $Cr^{III}(TBP_8Cz)(CH_3CN)_2$ (**4**). The crystal structure of **4** is shown in Figure 2.6. Complex **4** is 6-coordinate, with the Cr^{III} ion bound by 2 axial CH_3CN molecules. Unlike in **3**, the Cr ion is displaced from the N_4(plane) by only 0.013 Å to accommodate the sixth ligand. The UV-vis spectrum of **4** in CH_2Cl_2 gives Soret and Q-bands at 465 and

709 nm, respectively, which are easily distinguished from those observed for the $Cr^{V}(O)$ complex (Figure 2.7). The low-temperature EPR spectrum of **4** (9.44 GHz, 12 K) is consistent with the S =3/2 ground state expected for the Cr^{III} (d^3) ion (Figure 2.8).[12a]

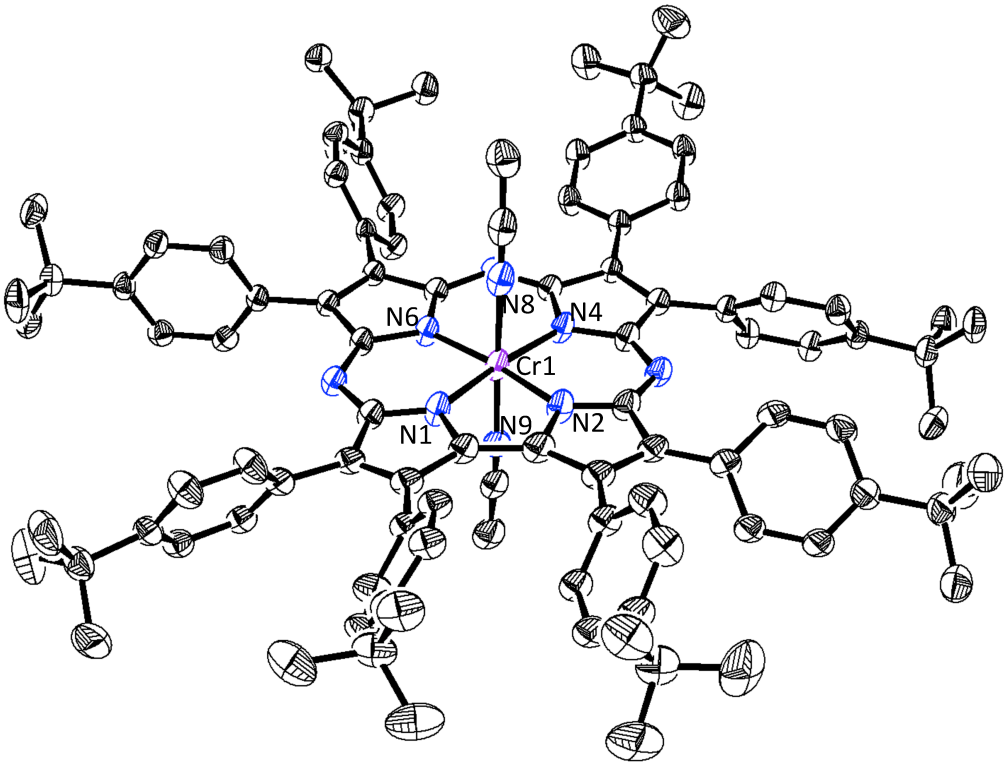

Figure 2.6. Displacement ellipsoid plot (50% probability) of $Cr^{III}(TBP_8Cz)(CH_3CN)_2$ (4) at 110(2) K. H-atoms and disorder are omitted for clarity.

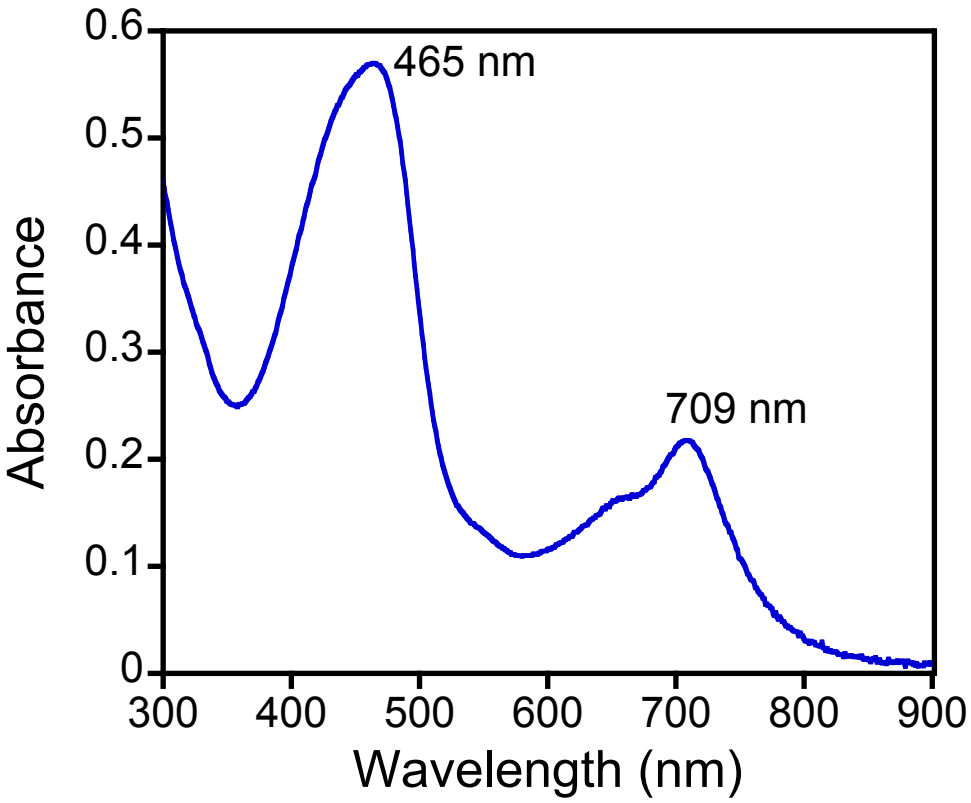

Figure 2.7. UV-visible spectrum of crystals of 4 redissolved in CH_2Cl_2.

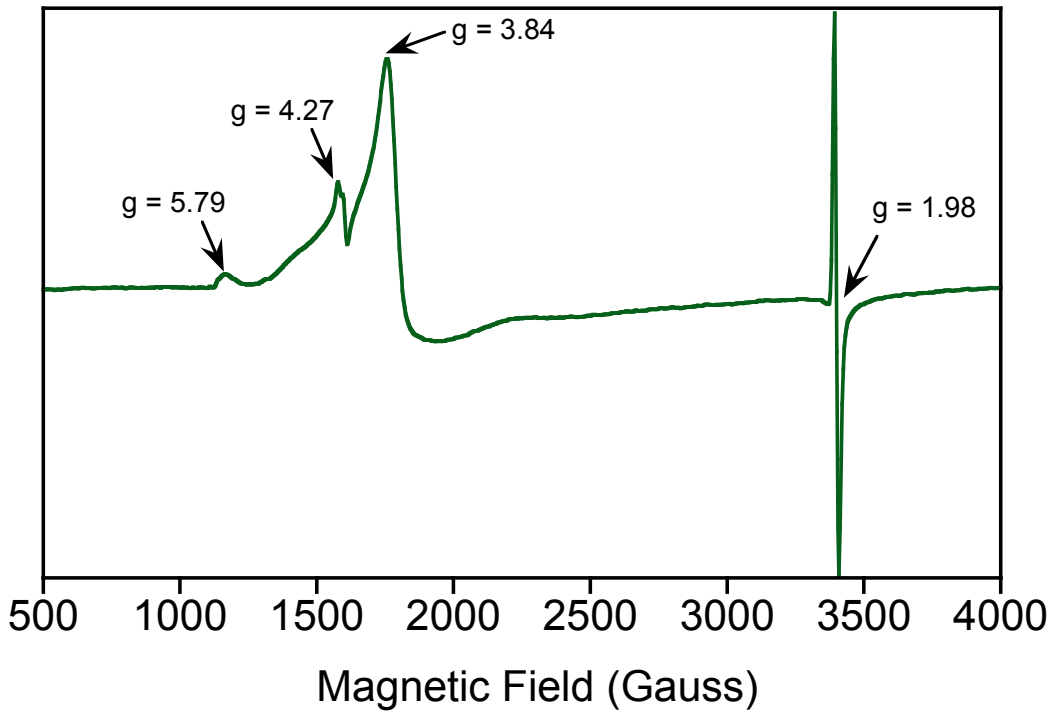

Figure 2.8. Low temperature (12 K) X-band EPR spectrum of $Cr^{III}(TBP_8Cz)$, synthesized by addition of PPh_3 (1 equiv) in toluene to 3 (2.6 mM). The sharp signal at g~2 is likely due to a small amount of unreacted $Cr^{V}(O)(TBP_8Cz)$, which has an S = ½ ground state (d^1 ion). Experimental conditions: Microwave frequency = 9.43 GHz; Microwave power = 0.2 mW; Modulation amplitude = 10 G, Receiver gain = 5 × 10^3.

2.3.4. Comparative Reactivity of $Mn^{V}(O)(TBP_8Cz)$ and $Cr^{V}(O)(TBP_8Cz)$ in H-atom Abstraction Reactions

The $Mn^{V}(O)$ and $Cr^{V}(O)$ complexes are ideal candidates for examining the relative reactivity of high-valent, biomimetic metal-oxo complexes bound in identical ligand environments. Previously, we showed that **2** reacts with a range of H-atom donors, including both substituted phenols (O–H bonds) and hydrocarbon (C–H) substrates, which exhibited bond dissociation energies (BDEs) from 66 - 80 kcal/mol.[4b,d] We

examined complex **3** for its potential reactivity toward substrates with similar bond strengths. A rapid reaction between **3** and excess TEMPOH in CH_2Cl_2 was observed by UV-vis spectroscopy, resulting in the isosbestic conversion of **3** (448, 653 nm) to a Cr^{III} product with a spectrum similar to **4** in the presence of excess TEMPOH (Figure 2.9a, Figure 2.10). The corresponding yield of TEMPO• was 82% (EPR quantitation) or 1.62 equiv relative to **3** (Figure 2.11). These data indicate the stoichiometry for this reaction follows that shown in Scheme 2.1, in which two equiv of TEMPOH react with **3** to give one equiv of reduced Cr^{III} product and two equiv of TEMPO• product. No Cr^{IV} intermediates were observed. This reaction exhibited pseudo-first-order behavior over 5 half-lives, and a plot of k_{obs} (s^{-1}) values correlated linearly with [TEMPOH] to give a second-order rate constant of $k_2 = 16 \pm 1\ M^{-1}\ s^{-1}$ (Figure 2.9b). A kinetic isotope effect of $k_H/k_D = 5.2 \pm 0.6$ was measured for TEMPOH/D (Figure 2.12). These observations are consistent with a concerted H-atom transfer (HAT) mechanism for the reaction of **2** with TEMPOH.

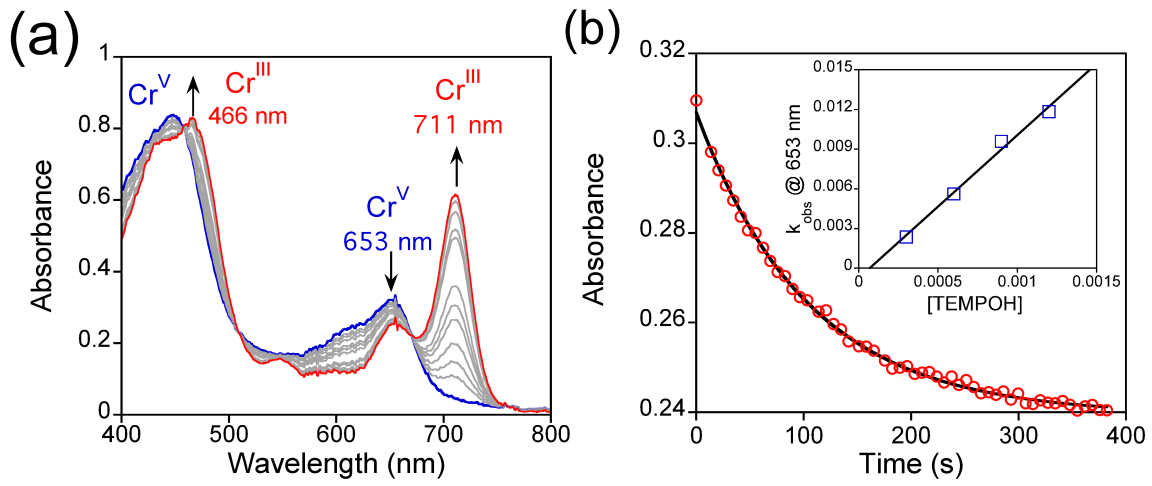

Figure 2.9. (a) UV-vis spectral changes (0 – 3 min) for the reaction of 3 (12 μM) with TEMPOH (150 equiv) at 25 °C. (b) Change in absorbance at 653 nm versus time

corresponding to the decay of 3 (red circles) and best fit (black line). Inset: second-order rate plot.

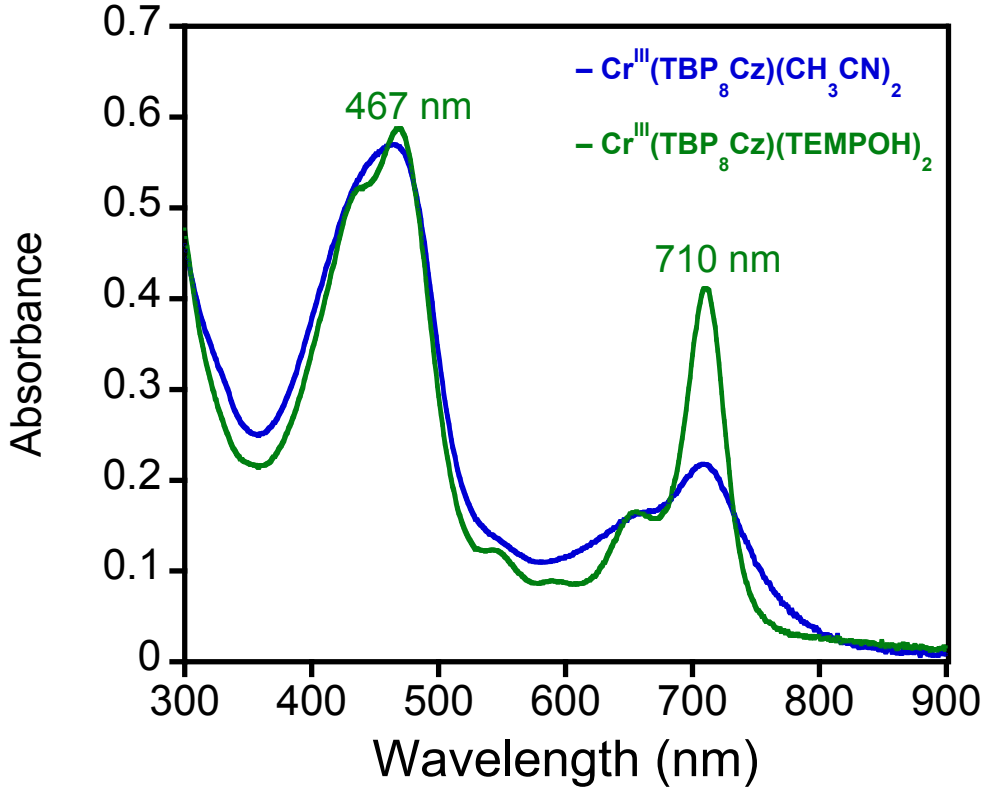

Figure 2.10. UV-visible spectra of crystals of 4 dissolved in CH_2Cl_2 (blue line) and after addition of excess TEMPOH to 4 (green line), which matches the final spectrum obtained from the reaction of 3 with TEMPOH.

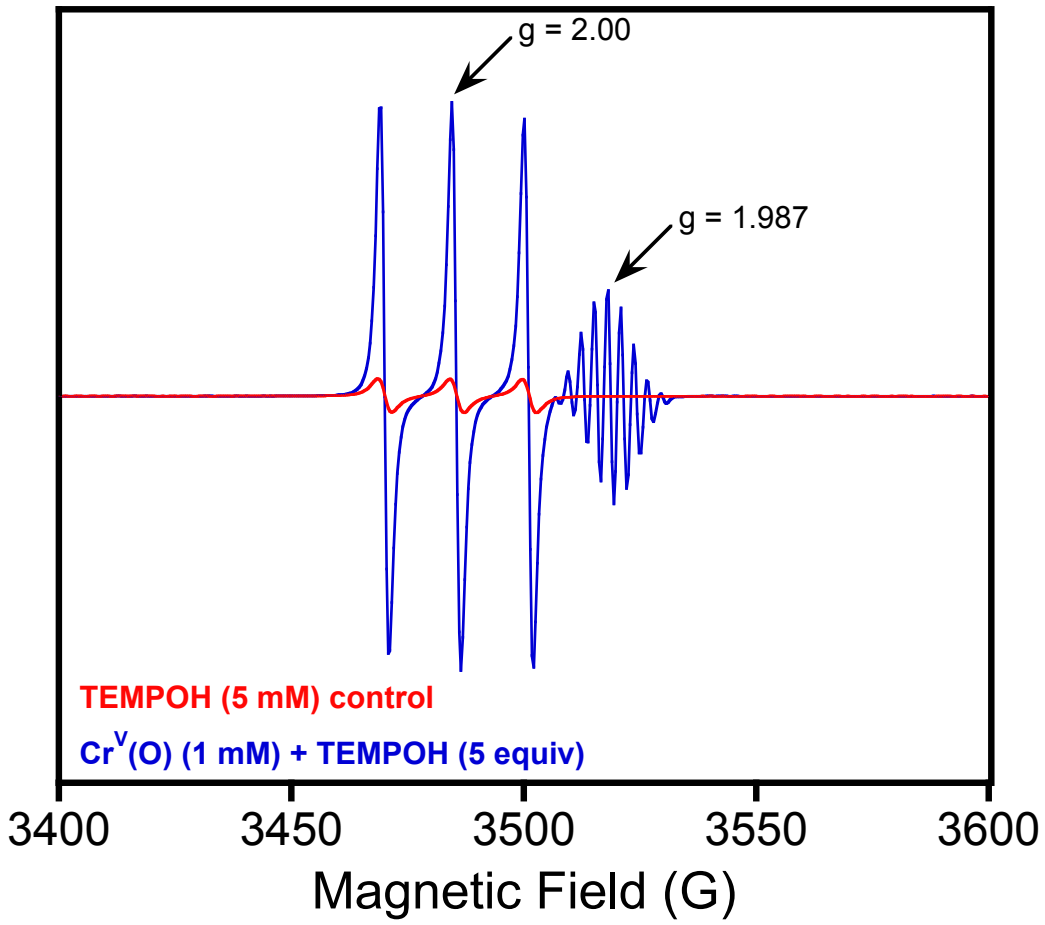

Figure 2.11. Room temperature EPR spectrum (9.77 GHz) for the reaction of 3 with TEMPOH (blue spectrum) in toluene to give an 82% yield of TEMPO• (3-line signal at g=2.00). The red spectrum is the starting TEMPOH substrate, with a TEMPO• impurity (~7 % by quantitation). Experimental conditions: Microwave power = 0.2 mW; Modulation amplitude = 1 G, Receiver gain = 5×10^3.

Scheme 2.1.

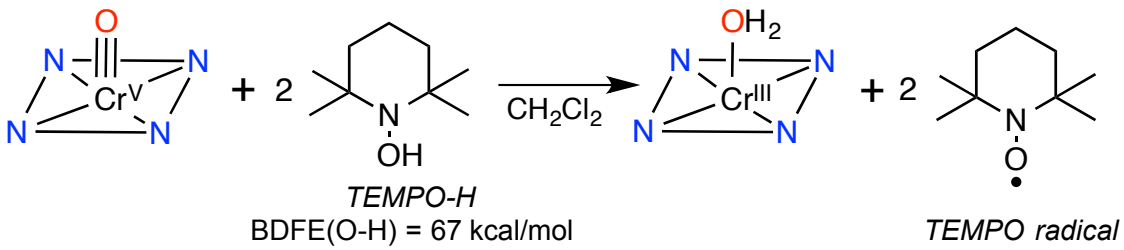

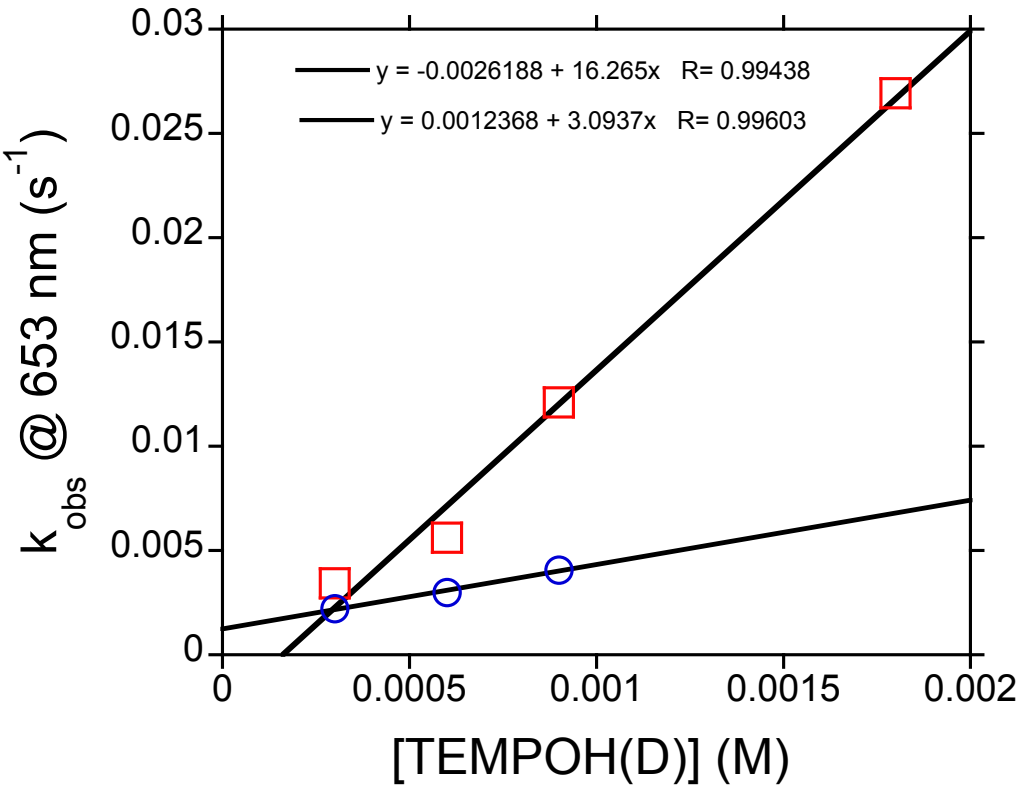

Figure 2.12. Second-order plots for the reaction of 3 with either TEMPOH (red squares) or TEMPOD (blue circles). The ratio of the second-order rate constants from the slopes of the best fit lines gives a KIE (k_H/k_D) of 5.2 ± 0.6.

As seen in Table 2.2, complex **3** was only capable of oxidizing TEMPOH, with a weak O–H bond of 67 kcal/mol. It was unreactive toward other H-atom donors, even under higher temperatures and prolonged reaction times. For example, a mixture of **3** and

excess xanthene (BDFE = 73.3 kcal/mol) in toluene at 70 °C for 40 h gives back only starting material. In contrast, the $Mn^{V}(O)$ complex **2** reacts with substrates that have BDFEs up to 80 kcal/mol.

Table 2.2. Reaction of 2 ($Mn^{V}(O)$) or 3 ($Cr^{V}(O)$) with H-atom donors (C-H and O-H) with a range of BDFEs

Substrate	$Mn^{V}(O)$	$Cr^{V}(O)$	BDFE[3a]
2.4. HMB[a]	no	no	83
2.5. 2,4,6-TTBP[b]	yes	no	80
2.6. DHA[c]	yes	no	77
xanthene	yes	no	73
TEMPOH	yes	yes	67

[a]HMB = hexamethylbenzene. [b]2,4,6-TTBP = 2,4,6-tri-*tert*-butylphenol. [c]DHA = 9,10-dihydroanthracene.

A thermodynamic analysis of H-atom abstraction for **2** and **3** can provide insight into the differences in reactivity seen for these two complexes. H-atom abstraction by the metal-oxo complexes can be described as shown in Scheme 2.2, where HAT follows either the concerted (diagonal) or step-wise electron-transfer (ET, horizontal) and proton-transfer (PT, vertical) steps shown in the square scheme. The thermodynamic parameters (E^0, pK_a) associated with the ET and PT steps combined with the free energy of formation of the hydrogen atom (C_G), can be used to calculate the bond dissociation free energy (BDFE) for M(O-H) (Eq 1).[14a] The difference in BDFE (ΔBDFE) for $Mn^{IV}(OH)$

versus $Cr^{IV}(OH)$ is expressed in Eq 2 and relies only on the differences in E^0 and pK_a, eliminating the requirement for an accurate measure of C_G. Assuming the reaction is under thermodynamic control, the BDFE of the M(O-H) bond must be similar to or greater than the X–H bond being cleaved in the substrate. The correlation of HAT reactivity with BDFE has been observed for metal-oxo complexes.[3] The results in Table 2.2 indicate that the BDFE for $Mn^{IV}(OH)$ should be between 80 – 83 kcal/mol, whereas for $Cr^{IV}(OH)$ the BDFE is 67 – 73 kcal/mol. These data imply a ΔBDFE of at least 8 kcal/mol for these two complexes.[15]

$$\text{BDFE (kcal/mol)} = 1.37\ \text{p}K_a + 23.06\ E^o + C_G \qquad (1)$$

$$\Delta\text{BDFE} = 1.37\Delta\text{p}K_a + 23.06\Delta E^o \qquad (2)$$

Scheme 2.2.

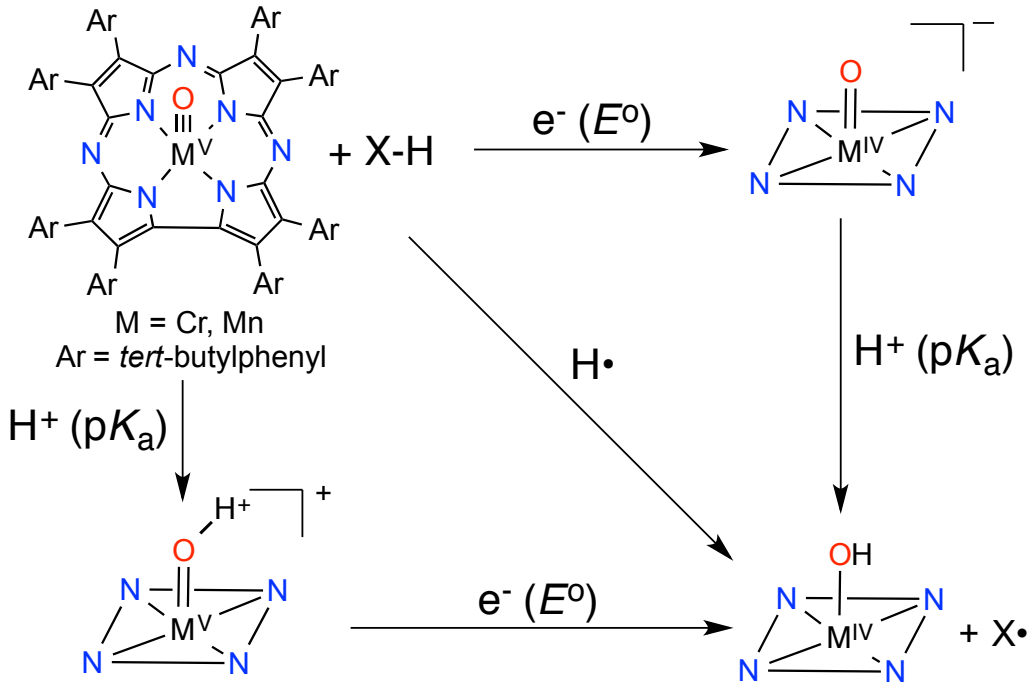

The $Mn^V(O)$ and $Cr^V(O)$ complexes were also capable of reacting with separated electron-transfer/proton-transfer reagents through a proton-coupled electron-transfer

(PCET) mechanism. It has been shown that an effective 'BDFE' for separate reductant/acid pairs can be calculated from their individual E^0 and pK_a values.[14b,c] Complex **2** reacts with the reductant dimethylferrocene (Me_2Fc) ($E_{1/2}$ = -0.24 V versus Fc^+/Fc in CH_3CN) in the presence of the H^+ donor acetic acid (pK_a = 23.5), to give $Mn^{III}(TBP_8Cz)(OH_2)$ in CH_2Cl_2 as shown by UV-vis (Figure 2.13). However, no reaction occurs with either Me_2Fc or CH_3CO_2H alone, supporting a PCET process.[4e] The BDFE for the Me_2Fc/CH_3CO_2H pair is 81.6 kcal/mol in CH_3CN (C_G = 54.9 kcal/mol). However, replacement of the Me_2Fc reductant with unsubstituted Fc ($E_{1/2}$ = 0.00 V) leads to no reaction (Figure 2.14). An effective BDFE = 87.1 kcal/mol is calculated for Fc/CH_3CO_2H. Similar experiments with the $Cr^V(O)$ complex showed efficient PCET from Me_2Fc and trifluoroacetic acid (TFA) (pK_a = 12.6) to give $Cr^{III}(TBP_8Cz)$, but no reaction was observed for Fc/TFA. These reductant/acid pairs have effective BDFEs of 66.5 and 75.5 kcal/mol, respectively. The results obtained for the separated PCET reagents provide good support for the BDFE range predicted for both **2** and **3** from the reactivity pattern with the H-atom donors in Table 2.2.

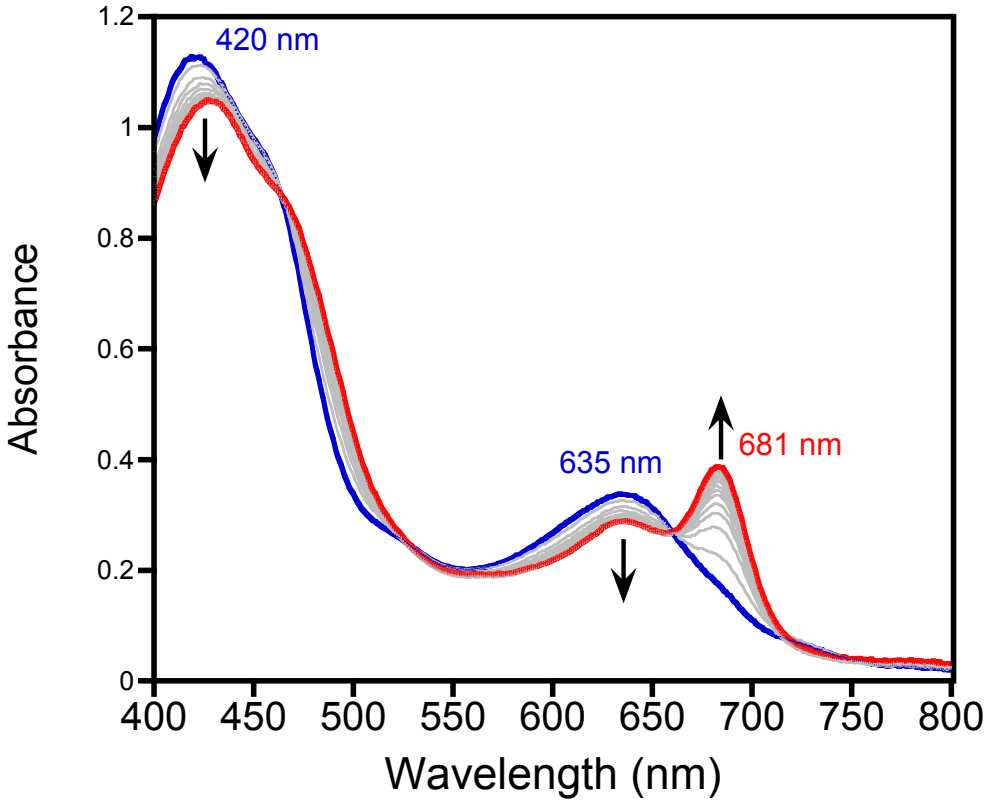

Figure 2.13. Time resolved UV-vis spectra for the reaction of 2 (0 – 3 h) with Me_2Fc ($E_{1/2}$ = -0.24 V versus Fc^+/Fc) and acetic acid (pK_a = 23.51). Effective BDFE for the reductant/acid pair is 81.6 kcal/mol.

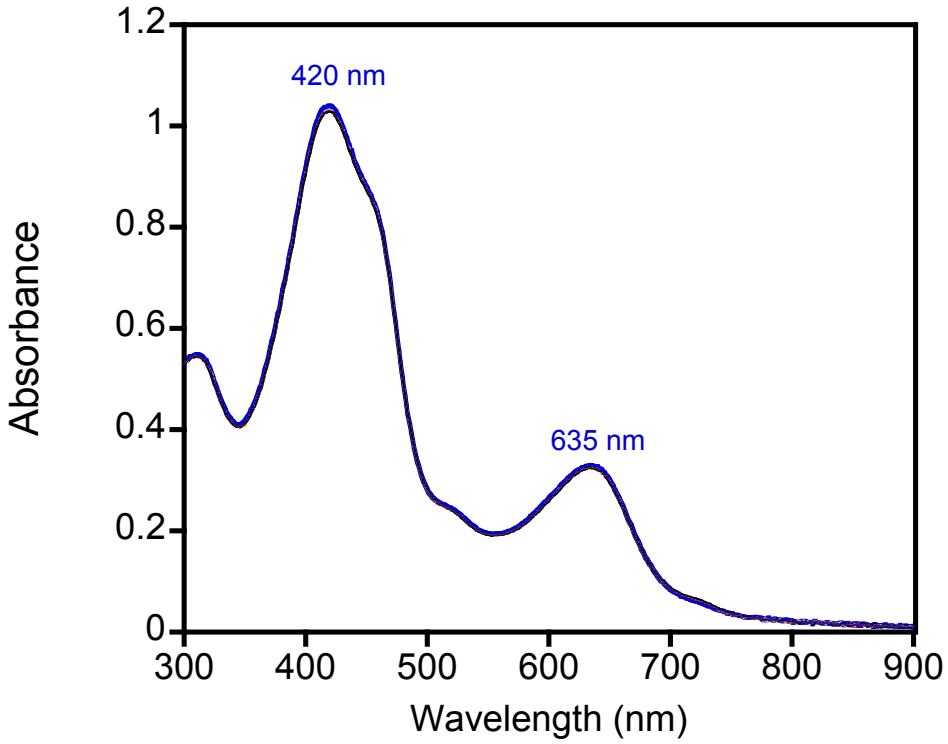

Figure 2.14. UV-vis spectrum for the mixture of 2 (0 – 3 h) with Fc ($E_{1/2}$ = 0.0 V versus Fc^+/Fc) and acetic acid (pK_a = 23.5), showing no change in the spectrum for 2. Effective BDFE for the reductant/acid pair is 87.1 kcal/mol.

Insight into the origin of the large difference in BDFE and related reactivity for **2** and **3**, comes from cyclic voltammetry (Figure 2.15). The quasi-reversible wave at $E_{1/2}$ = -0.43 V is assigned to the Cr^V/Cr^{IV} redox potential based on previous assignments for metallocorrolazines, including **2**.[4a] Interestingly, the Cr^V/Cr^{IV} potential is ~100 mV more positive than that seen for Mn^V/Mn^{IV} ($E_{1/2}$(**2**) = -0.55 V) (Figure 2.16). According to eq 1, the larger redox potential for **3** should provide a 2.3 kcal/mol (23.06 × (0.1 V)) *increase* in BDFE compared to **2**. However, the BDFE for Cr^{IV}(OH) appears to be *weaker* than the BDFE for Mn^{IV}(OH) by at least 8 kcal/mol based on the observed HAT and PCET reactivity. Assuming a ΔBDFE of 8 kcal/mol, and including the measured ΔE^o = -0.1 V,

we find that ΔpK_a must be ~8 according to eq 2. This result indicates that a reduced $[Mn^{IV}(O)^{-}]$ species is at least 8 orders of magnitude *more basic* than the corresponding $[Cr^{IV}(O)^{-}]$, and this basicity dominates the difference in driving force for H-atom abstraction. We previously have suggested that the basicity of $[Mn^{IV}(O)^{-}]$ was a potential key factor in HAT,[4b] and more recent studies have supported this conclusion.[16] However, this study provides a rare direct comparison of two high-valent metal-oxo species in identical ligand environments, and demonstrates that a dramatic difference in reactivity can be assigned to the different basicities of the metal-oxo units.

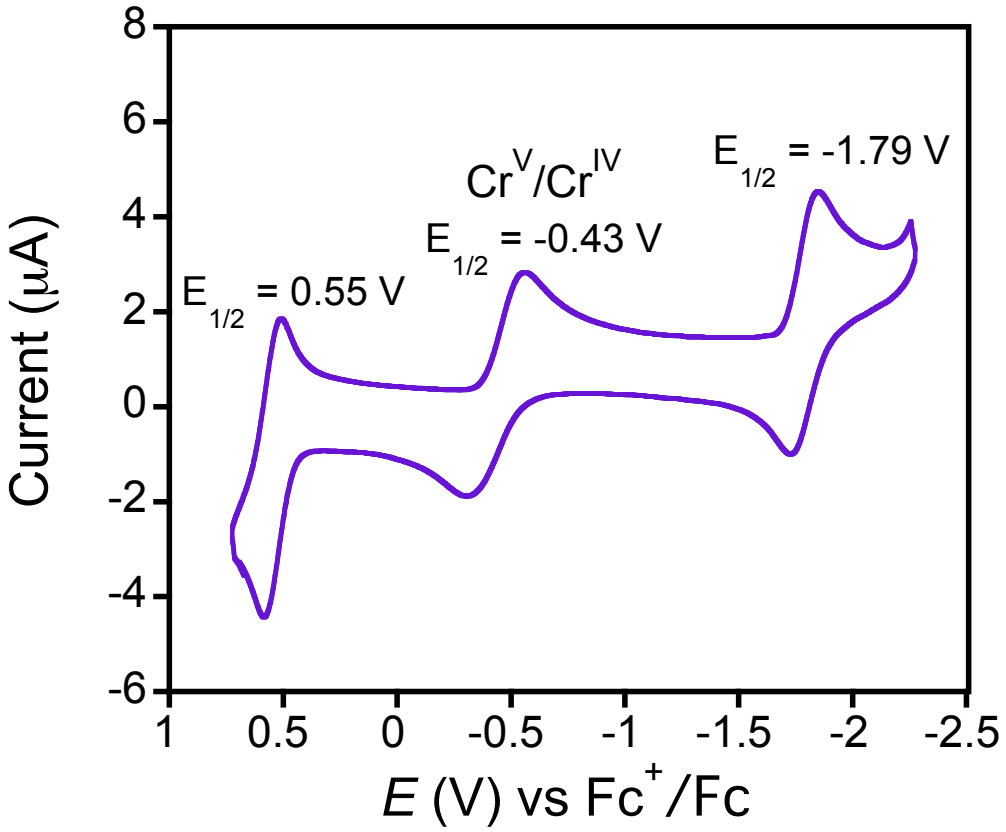

Figure 2.15. CV of 3 in CH_2Cl_2 with 0.1 M $TBAPF_6$ as supporting electrolyte, scan rate 25 mV/s.

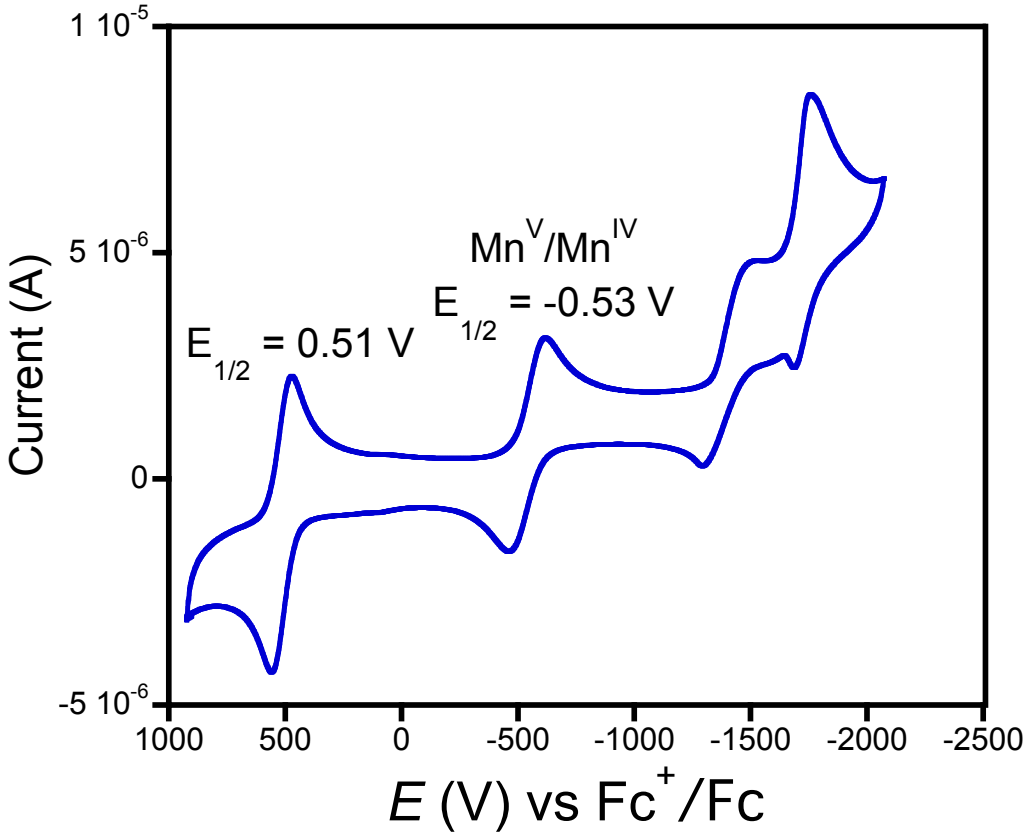

Figure 2.16. Cyclic voltammogram of a 0.33 mM solution of 2 in CH_2Cl_2 with 0.1 M $TBAPF_6$ as supporting electrolyte, scan rate 25 mV/s.

2.7. Conclusions

In summary, we report a new $Cr^{V}(O)$ porphyrinoid complex, and the first X-ray structure of an $Mn^{V}(O)$ porphyrinoid complex. A comparison of HAT/PCET reactivity for these two adjacent first-row metal-oxo complexes (Mn, Cr) in identical ligand environments implies that $Mn^{V}(O)$ must have a much larger driving force (~8 kcal/mol) for H• abstraction than the corresponding $Cr^{V}(O)$, despite the latter complex having a 100 mV larger $E_{1/2}$ value. The larger driving force can be attributed to the basicity of the one-electron reduced [$Mn^{IV}(O)^{-}$], which we estimate to be ~8 orders of magnitude more basic

than [$Cr^{IV}(O)^{-}$]. This work supports the hypothesis that the basicity of high-valent metal-oxo species in heme enzymes is a critical factor in tuning reactivity.

2.8. References

(1) (a) Denisov, I. G.; Makris, T. M.; Sligar, S. G.; Schlichting, I. *Chem. Rev.* **2005**, *105*, 2253. (b) Rittle, J.; Green, M. T. *Science* **2010**, *330*, 933. (c) Yosca, T. H.; Rittle, J.; Krest, C. M.; Onderko, E. L.; Silakov, A.; Calixto, J. C.; Behan, R. K.; Green, M. T. *Science* **2013**, *342*, 825. (d) Poulos, T. L. *Chem. Rev.* **2014**, *114*, 3919. (e) Yosca, T. H.; Behan, R. K.; Krest, C. M.; Onderko, E. L.; Langston, M. C.; Green, M. T. *J. Am. Chem. Soc.* **2014**, *136*, 9124.

(2) (a) Krebs, C.; Galonić Fujimori, D.; Walsh, C. T.; Bollinger, J. M. *Acc. Chem. Res.* **2007**, *40*, 484. (b) Bruijnincx, P. C.; van Koten, G.; Gebbink, R. J. K. *Chem. Soc. Rev.* **2008**, *37*, 2716.

(3) (a) Warren, J. J.; Tronic, T. A.; Mayer, J. M. *Chem. Rev.* **2010**, *110*, 6961. (b) Borovik, A. S. *Chem. Soc. Rev.* **2011**, *40*, 1870. (c) Bigi, J. P.; Harman, W. H.; Lassalle-Kaiser, B.; Robles, D. M.; Stich, T. A.; Yano, J.; Britt, R. D.; Chang, C. J. *J. Am. Chem. Soc.* **2012**, *134*, 1536. (d) Usharani, D.; Lacy, D. C.; Borovik, A. S.; Shaik, S. *J. Am. Chem. Soc.* **2013**, *135*, 17090. (e) Nam, W.; Lee, Y.-M.; Fukuzumi, S. *Acc. Chem. Res.* **2014**, *47*, 1146. (f) Chen, Z.; Yin, G. *Chem. Soc. Rev.* **2015**, *44*, 1083. (g) Puri, M.; Que, L. *Acc. Chem. Res.* **2015**, *Article ASAP,* DOI: 10.1021/acs.accounts.5b00244.

(4) (a) Lansky, D. E.; Mandimutsira, B.; Ramdhanie, B.; Clausén, M.; Penner-Hahn, J.; Zvyagin, S. A.; Telser, J.; Krzystek, J.; Zhan, R.; Ou, Z.; Kadish, K. M.; Zakharov, L.; Rheingold, A. L.; Goldberg, D. P. *Inorg. Chem.* **2005**, *44*, 4485. (b) Lansky, D. E.; Goldberg, D. P. *Inorg. Chem.* **2006**, *45*, 5119. (c) Lansky, D. E.; Kosack, J. R.; Narducci Sarjeant, A. A.; Goldberg, D. P. *Inorg. Chem.* **2006**, *45*, 8477. (d) Prokop, K. A.; de Visser, S. P.; Goldberg, D. P. *Angew. Chem., Int. Ed.* **2010**, *49*, 5091. (e) Fukuzumi, S.; Kotani, H.; Prokop, K. A.; Goldberg, D. P. *J. Am. Chem. Soc.* **2011**, *133*, 1859. (f) Cho, K.; Leeladee, P.; McGown, A. J.; DeBeer, S.; Goldberg, D. P. *J. Am. Chem. Soc.* **2012**, *134*, 7392. (g) Leeladee, P.; Baglia, R. A.; Prokop, K. A.; Latifi, R.; de Visser, S. P.;

Goldberg, D. P. *J. Am. Chem. Soc.* **2012**, *134*, 10397. (h) Baglia, R. A.; Dürr, M.; Ivanović-Burmazović, I.; Goldberg, D. P. *Inorg. Chem.* **2014**, *53*, 5893.

(5) (a) Groves, J. T.; Haushalter, R. C. *J. Chem. Soc., Chem. Commun.* **1981**, 1165. (b) Garrison, J. M.; Bruice, T. C. *J. Am. Chem. Soc.* **1989**, *111*, 191. (c) Collins, T. J.; Slebodnick, C.; Uffelman, E. S. *Inorg. Chem.* **1990**, *29*, 3433. (d) Meier-Callahan, A. E.; Gray, H. B.; Gross, Z. *Inorg. Chem.* **2000**, *39*, 3605. (e) Bakac, A.; Guzei, I. A. *Inorg. Chem.* **2000**, *39*, 736. (f) Hess, J. S.; Leelasubcharoen, S.; Rheingold, A. L.; Doren, D. J.; Theopold, K. H. *J. Am. Chem. Soc.* **2002**, *124*, 2454. (g) O'Reilly, M.; Falkowski, J. M.; Ramachandran, V.; Pati, M.; Abboud, K. A.; Dalal, N. S.; Gray, T. G.; Veige, A. S. *Inorg. Chem.* **2009**, *48*, 10901. (h) Cho, J.; Woo, J.; Eun Han, J.; Kubo, M.; Ogura, T.; Nam, W. *Chem. Sci.* **2011**, *2*, 2057. (i) Kotani, H.; Kaida, S.; Ishizuka, T.; Sakaguchi, M.; Ogura, T.; Shiota, Y.; Yoshizawa, K.; Kojima, T. *Chem. Sci.* **2015**, *6*, 945.

(6) Mandimutsira, B. S.; Ramdhanie, B.; Todd, R. C.; Wang, H.; Zareba, A. A.; Czernuszewicz, R. S.; Goldberg, D. P. A Stable Manganese(V)-Oxo Corrolazine Complex. *J. Am. Chem. Soc.* **2002**, *124*, 15170-15171.

(7) Lansky, D. E.; Mandimutsira, B.; Ramdhanie, B.; Clausén, M.; Penner-Hahn, J.; Zvyagin, S. A.; Telser, J.; Krzystek, J.; Zhan, R.; Ou, Z.; Kadish, K. M.; Zakharov, L.; Rheingold, A. L.; Goldberg, D. P. Synthesis, Characterization, and Physicochemical Properties of Manganese(III) and Manganese(V)-Oxo Corrolazines. *Inorg. Chem.* **2005**, *44*, 4485-4498.

(8) Marque, S.; Fischer, H.; Baier, E.; Studer, A. Factors Influencing the C,àíO Bond Homolysis of Alkoxyamines:,Äâ Effects of H,àíBonding and Polar Substituents. *J. Org. Chem.* **2001**, *66*, 1146-1156.

(9) Evans, D. F.; Jakubovic, D. A. Water-soluble hexadentate Schiff-base ligands as sequestrating agents for iron(III) and gallium(III). *J. Chem. Soc., Dalton Trans.* **1988**, 2927-2933.

(10) (a) Collins, T. J.; Gordon-Wylie, S. W. *J. Am. Chem. Soc.* **1989**, *111*, 4511. (b) MacDonnell, F. M.; Fackler, N. L. P.; Stern, C.; O'Halloran, T. V. *J. Am. Chem. Soc.* **1994**, *116*, 7431.

(11) (a) Groves, J. T.; Lee, J.; Marla, S. S. *J. Am. Chem. Soc.* **1997**, *119*, 6269. (b) Arunkumar, C.; Lee, Y.-M.; Lee, J. Y.; Fukuzumi, S.; Nam, W. *Chem. - Eur. J.* **2009**, *15*, 11482.

(12) (a) Meier-Callahan, A. E.; Di Bilio, A. J.; Simkhovich, L.; Mahammed, A.; Goldberg, I.; Gray, H. B.; Gross, Z. *Inorg. Chem.* **2001**, *40*, 6788. (b) Egorova, O. A.; Tsay, O. G.; Khatua, S.; Huh, J. O.; Churchill, D. G. *Inorg. Chem.* **2009**, *48*, 4634. (c) Egorova, O. A.; Tsay, O. G.; Khatua, S.; Meka, B.; Maiti, N.; Kim, M.-K.; Kwon, S. J.; Huh, J. O.; Bucella, D.; Kang, S.-O.; Kwak, J.; Churchill, D. G. *Inorg. Chem.* **2010**, *49*, 502.

(13) Shannon, R. D. Revised effective ionic radii and systematic studies of interatomic distances in halides and chalcogenides. *Acta Crystallogr., Sect. A*. **1976**, *32*, 751-767.

(14) (a) Bordwell, F. G.; Cheng, J. P.; Harrelson, J. A. *J. Am. Chem. Soc.* **1988**, *110*, 1229. (b) Waidmann, C. R.; Miller, A. J. M.; Ng, C.-W. A.; Scheuermann, M. L.; Porter, T. R.; Tronic, T. A.; Mayer, J. M. *Energy Environ. Sci.* **2012**, *5*, 7771. (c) Tarantino, K. T.; Liu, P.; Knowles, R. R. *J. Am. Chem. Soc.* **2013**, *135*, 10022.

(15) This ΔBDFE assumes that the BDFE of $Cr^{IV}(OH)$ is below that of the xanthene, ie 72 kcal/mol or less, whereas the BDFE of $Mn^{IV}(OH)$ is assumed to be ≥ 80 kcal/mol.

(16) Green, M. T. *Curr. Opin. Chem. Biol.* **2009**, *13*, 84., and references therein.

3. Chapter 3. Activation of a High-Valent Manganese-Oxo Complex by A Non-Metallic Lewis Acid

This work was co-written with the following authors and was published under the following title and citation:

Baglia, R. A.; Dürr, M.; Ivanović-Burmazović, I.; Goldberg, D. P. "Activation of a High-Valent Manganese–Oxo Complex by a Nonmetallic Lewis Acid" *Inorg. Chem*., **2014**, *53*, 5893-5895.

3.1. Introduction

High-valent metal-oxo species are invoked as key players in both biological and synthetic oxidations. Examples include an $Fe^{IV}(O)$ porphyrin π-radical-cation, the key intermediate in Cytochrome P450,[1-5] and postulated $Mn^{IV}/Mn^{V}(O)$ intermediates in photosynthetic water oxidation.[6-9] In heme systems such as P450, there are two possible valence tautomers, $Fe^{V}(O)(p)$ or $Fe^{IV}(O)(p^{+\bullet})$, and the redox-active nature of the porphyrin ligand plays a critical role in stabilizing the latter. The synthesis of analogous transition metal complexes with redox-active ligands that enhance reactivity has been targeted for multi-electron catalysis.[10-14] The design of complexes that can undergo controlled valence tautomerism is also important for molecular device applications.[15,16]

Previously we introduced a new method for controlling valence tautomerism in a $Mn^{V}(O)$ porphyrinoid complex.[17] The addition of the Lewis acidic Zn^{II} ion was shown to convert $Mn^{V}(O)(TBP_8Cz)$ into the valence tautomer $Mn^{IV}(O)(TBP_8Cz^{+\bullet})$. The influence of Lewis acids on the reactivity of biologically relevant high-valent metal-oxo species is of intense current interest,[18-24] especially because of the Ca^{2+} ion involved in Mn-mediated water oxidation.[6-9] Herein, we show for the first time that a non-metal ion

Lewis acid, $B(C_6F_5)_3$, can induce valence tautomerism in a high-valent metal-oxo complex. We find that the addition of $B(C_6F_5)_3$ also causes dramatically enhanced hydrogen-atom abstraction reactivity toward phenol substrates.

3.2. Experimental Methods

3.2.1. General methods and materials

The starting material $(TBP_8Cz)Mn^V(O)$ was synthesized according to published procedures.[25] The commercially available reagents $B(C_6F_5)_3$, $[(Me_2N)_3S]^+[Si(CH_3)_3(F)_2]^-$ (tris(dimethylamino)sulfonium difluorotrimethylsilicate, (TASF)), and dichloromethane (CHROMASOLV®) were obtained from Sigma-Aldrich at the best available purity and used as received. The compound 2,4-di-*tert*-butylphenol was purchased from Sigma-Aldrich and recrystallized from petroleum ether. The compound 2,4,6-tri-*tert*-butylphenol was purchased from Sigma-Aldrich and recrystallized from acetonitrile. Deuterated 2,4,6-tri-*tert*-butylphenol (2,4,6-TTBP-OD) was synthesized according to a published procedure.[26] Deuterated chloroform ($CDCl_3$, 0.05% v/v TMS) for NMR was purchased from Cambridge Isotopes.

3.2.2. Analytical methods

UV-vis spectroscopy was performed on a Hewlett-Packard 8452 diode-array spectrophotometer equipped with HPChemstation software. Gas chromatography was performed on an Agilent 6850 gas chromatograph fitted with a DB-5 5% phenylmethyl siloxane capillary column and equipped with a flame-ionization detector (FID). GC-FID response factors for 2,4-di-tert-butylphenol and 3,3',5,5'-tetra-tert-butyl-(1,1'-biphenyl)-2,2'-diol (bis(phenol) dimer) were prepared versus dodecane as the internal standard. ^{1}H-NMR spectra were recorded on a Bruker Avance 400 NMR instrument at 400 MHz.

Electron paramagnetic resonance (EPR) spectra were recorded with a Bruker EMX spectrometer equipped with a Bruker ER 041 X G microwave bridge and a continuous-flow liquid helium cryostat (ESR900) coupled to an Oxford Instruments TC503 temperature controller. Spectra were obtained at 11 K under nonsaturating microwave power conditions (ν = 9.449 GHz, microwave power = 20.01 mW, modulation amplitude = 10 G, microwave frequency = 100 kHz, receiver gain = 5.02×10^3). EPR spectra were simulated by using the Bruker SimFonia Software version 1.26, 1997. Cryospray ionization mass spectrometry (CSIMS) measurements were recorded on a UHR-ToF Bruker Daltonik (Bremen, Germany) maXis, an ESI-ToF MS capable of resolution of at least 40.000 FWHM, which was coupled to a Bruker cryospray unit. Detection was in positive-ion mode and the source voltage was held at 4 kV. The flow rates were 250 μL h^{-1}. The drying gas (N_2) was held at -45 °C and the spray gas was held at -50 °C. In source collision induced decomposition (ISCID) was achieved by increasing the DC potential between funnel 1 and funnel 2 in the double stage ion funnel transfer zone which leads to decomposition of dimeric ion moieties formed during the ionization process. The ISCID energy was held at 100 eV. The machine was calibrated prior to every experiment via direct infusion of the Agilent ESI-ToF low concentration tuning mixture, which provided an *m/z* range of singly charged peaks up to 2700 Da in both ion modes.

3.2.3. UV-vis spectral titrations for $Mn^V(O)(TBP_8Cz) + B(C_6F_5)_3$

To a solution of $Mn^V(O)(TBP_8Cz)$ (5 μM) in CH_2Cl_2 (6 mL) was added 0.1 - 3.0 equiv of $B(C_6F_5)_3$ in 0.1 equiv increments from a stock solution in CH_2Cl_2. A color change of green to brown occurred, and a UV-vis spectrum was taken after each addition

of Lewis acid, showing isosbestic conversion of green $Mn^{V}(O)(TBP_8Cz)$ (419, 634 nm) to brown $Mn^{IV}(O)(TBP_8Cz^{+\bullet})$:$B(C_6F_5)_3$ (419, 789 nm). The reaction mixture was allowed to equilibrate fully until no further spectral change was observed prior to the next addition of Lewis acid. A plot of the change in absorbance at 789 nm versus $[B(C_6F_5)_3]$ resulted in the binding curve shown in Figure 3.2. This curve could be well fit by a 1:1 binding model , eq 1 – 4:

$$Mn^{V}(O)(TBP_8Cz)+B(C_6F_5)_3 \rightleftharpoons Mn^{IV}(O)(TBP_8Cz^{+\bullet})\text{-}B(C_6F_5)_3 \quad (1)$$

$$K_a = \frac{[Mn^{IV}(O)(TBP_8Cz^{+\bullet})\text{-}B(C_6F_5)_3]}{[Mn^{V}(O)(TBP_8Cz)][B(C_6F_5)_3]} \quad (2)$$

$$\frac{(A-A_0)}{(\varepsilon_{Mn(O)B}-\varepsilon_{Mn(O)})} = [Mn^{IV}(O)(TBP_8Cz^{+\bullet})\text{-}B(C_6F_5)_3] \quad (3)$$

$$\left[Mn^{IV}(O)(TBP_8Cz^{+\bullet})\text{-}B(C_6F_5)_3\right] =$$

$$\frac{1}{2}\left[\left\{[B(C_6F_5)_3] + [Mn^{V}(O)]_i + \left(\frac{1}{K_a}\right)\right\} - \sqrt{\left([B(C_6F_5)_3] + [Mn^{V}(O)]_i + \left(\frac{1}{K_a}\right)\right)^2 - 4[B(C_6F_5)_3][Mn^{V}(O)]_i}\right] \quad (4)$$

The best fit of the plot in Figure S1 gives K_a = 2.03 (±0.5) x 10^7 M^{-1}.

3.2.4. Reaction of $Mn^{IV}(O)(TBP_8Cz^{+\bullet})$:$B(C_6F_5)_3$ with TASF

An amount of $Mn^{V}(O)(TBP_8Cz)$ (15 μM) was combined with $B(C_6F_5)_3$ (1 equiv, 10 μL of a 4.56 mM stock solution) in CH_2Cl_2 (3 mL), and the reaction was followed by UV-vis, showing rapid (~20 s) isosbestic conversion of $Mn^{V}(O)(TBP_8Cz)$ to $Mn^{IV}(O)(TBP_8Cz^{+\bullet})$:$B(C_6F_5)_3$ (419, 789 nm). A stock solution of TASF (20.0 mM) in $CH_2Cl_2$was prepared. An amount of TASF (10 μL, 20 equiv) was then added to the

reaction mixture, resulting in a rapid change as seen by UV-vis, to give a final spectrum with peaks at 421, 634 nm corresponding to the regeneration of $Mn^{V}(O)(TBP_8Cz)$ (~87%, based on $\varepsilon = 1.99 \times 10^4\ M^{-1}\ cm^{-1}$ at 634 nm). There was also a relatively sharp peak observed at 677 nm, corresponding to $[Mn^{III}(TBP_8Cz)F]^-$ (Figure 3.6).

3.2.5. Hydrogen-atom-transfer (HAT) with the phenol substrate 2,4-DTPB (Product analysis)

An amount of $Mn^{V}(O)(TBP_8Cz)$ (7.0×10^{-7} mol) was combined with $B(C_6F_5)_3$ (1 equiv) in CH_2Cl_2 (50 mL), and the reaction mixture was monitored by UV-vis until complete formation of $Mn^{IV}(O)(TBP_8Cz^{+\bullet}):B(C_6F_5)_3$ was observed. The phenol substrate 2,4-DTBP was then added in CH_2Cl_2 (250 μL of a 14.6 mM stock solution, 3.5×10^{-6} mol), and the spectrum for $Mn^{IV}(O)(TBP_8Cz^{+\bullet}):B(C_6F_5)_3$ (420, 789 nm) converted to the spectrum for $Mn^{IV}(OH)(TBP_8Cz)$ (λ = 443, 727 nm). The reaction mixture was concentrated under vacuum to ca. 500 μL, and dodecane was added as an internal standard. The solution was then immediately injected onto the GC-FID for product analysis. The coupled product 3,3',5,5'-tetra-tert-butyl-(1,1'-biphenyl)-2,2'-diol was identified by comparison of retention time with an authentic sample, and quantitation was performed by integration of the peak and comparison with a calibration curve constructed with the internal standard. A yield of 77% (average of three runs) for the bis(phenol) product was obtained. Unreacted 2,4-DTBP was also identified and quantified by GC-FID, giving 2.3×10^{-6} mol phenol left (3.3 equiv).

3.2.6. EPR spectroscopy for $Mn^{IV}(O)(TBP_8Cz^{+\bullet}):B(C_6F_5)_3$ + 2,4-DTBP

A concentrated solution of $Mn^{V}(O)(TBP_8Cz)$ (1.0 mM) was combined with $B(C_6F_5)_3$ (1 equiv) in CH_2Cl_2 (400 μL), and monitoring by UV-vis confirmed the

formation of $Mn^{IV}(O)(TBP_8Cz^{+\bullet})$:$B(C_6F_5)_3$. Excess 2,4-DTBP (10 mg, 120 equiv) was added, and a change in the UV-vis spectrum was observed, resulting in a new spectrum for $Mn^{IV}(OH)(TBP_8Cz)$. The solution was then loaded into an EPR tube and slowly annealed at 77 K. EPR spectra were obtained at 12 K under non-saturating microwave power conditions (ν = 9.48 GHz, microwave power = 20.01 mW, modulation amplitude = 10 G, modulation frequency = 100 kHz). The resulting spectrum shows major features near g = 4 and g = 2 with hyperfine splitting from the ^{55}Mn nucleus (I = 5/2). The spectrum was satisfactorily simulated with a fictitious spin of S' = ½, and g = [4.61, 4.20, 1.92]; $A_{iso}(^{55}Mn)$ = [82, 86, 50] G. The 6-line signal observed at g = 2 is dominated by a relatively small amount of a Mn(II) impurity, which has been independently characterized from the decomposition of $Mn^{III}(TBP_8Cz)$ with HOTf and has a characteristic hyperfine coupling constant of $A_{iso}(^{55}Mn)$ = 120 G .

3.2.7. Kinetics of HAT with phenol substrates

A typical kinetic experiment was carried out by the following procedure. An amount of $Mn^{V}(O)(TBP_8Cz)$ (15 μM) was combined with $B(C_6F_5)_3$ (1 equiv, 25 μL of a 1.1 mM stock solution) in CH_2Cl_2 (2 mL), and the reaction was followed by UV-vis. After complete formation of $Mn^{IV}(O)(TBP_8Cz^{+\bullet})$ was observed, a substituted phenol substrate (50 – 200 equiv) was added from a stock solution in CH_2Cl_2. The spectrum for $Mn^{IV}(O)(TBP_8Cz^{+\bullet})$ (420, 789 nm) decayed, and a new spectrum appeared for $Mn^{IV}(OH)(TBP_8Cz)$ (λ = 443, 727 nm). Plots of the growth in absorbance at 727 nm versus time appeared to be first-order up to 5 half-lives, and were well fit by the first-order expression shown in eq 5:

$$\boldsymbol{Abs_t = Abs_f + (Abs_0 - Abs_f)e^{-k_{obs}t}} \quad (5)$$

where Abs_t = absorbance at time t, Abs_f = final absorbance, Abs_0 = initial absorbance, and k_{obs} is the pseudo-first-order rate constant. A plot of k_{obs} versus concentration of phenol was found to be linear, and the slope of the best-fit line gave k_2, the second-order rate constant (Figure 3.9 and Figure 3.10).

3.2.8. Evans method measurement

To an amount of $Mn^{V}(O)(TBP_8Cz)$ (1 μmol) in $CDCl_3$ containing 0.05% TMS was added $B(C_6F_5)_3$ (1 equiv) as a stock solution in $CDCl_3$, to give a final concentration of 2.00 mM of Mn complex. A color change from green to brown was observed. The solution was placed in a NMR tube with a coaxial inner tube containing blank solvent ($CDCl_3$ with 0.05% v/v TMS). ^1H NMR spectra were recorded at 297.5 K, and the chemical shift of the TMS peak in the presence of the paramagnetic $Mn^{IV}(O)(TBP_8Cz^{+\bullet}):B(C_6F_5)_3$ complex was compared to that of the TMS peak in the inner tube containing only the TMS standard (Figure 3.4). The effective spin-only magnetic moment was calculated by a simplified Evans method analysis[27] according to Eq. 6:

$$\mu_{eff} = 0.0618\sqrt{\frac{\Delta\nu \mathrm{T}}{2\mathrm{fM}}} \tag{6}$$

where f is the oscillator frequency (MHz) of the superconducting spectrometer, T is the temperature (K), M is the molar concentration of the paramagnetic metal complex, and $\Delta\nu$ is the difference in frequency (Hz) between the two reference (TMS) signals. In a control experiment, an Evans method measurement was performed on the $(TBP_8Cz)Mn^{V}(O)$ complex in the absence of $B(C_6F_5)_3$, and showed no shift in the standard TMS peak (Figure 3.3).

3.2.9. Cryospray Ionization Mass Spectrometry (CSIMS)

All samples were prepared in a glovebox under Argon atmosphere by dissolving the given samples in dry CH_2Cl_2 and transferring them into a tandem cuvette for UV-vis experiments. One side was filled with $Mn^V(O)(TBP_8Cz)$ (1 mL of a 35.5 μM solution), and the other side was filled with $B(C_6F_5)_3$ (25 μL of an 1.4 mM stock solution) and complemented to 1 mL with dry CH_2Cl_2. UV-vis spectra were recorded before and after mixing. The reaction took place in about 15 seconds. MS measurements also were performed out of the solutions of the cuvette. Better results were obtained by preparing the solutions in the glovebox and directly transferring into Hamilton gastight syringes for injection into the MS.

3.3. Results and Discussion

3.3.1. Synthesis and Characterization of $Mn^{IV}(O)(TBP_8Cz^{+\bullet}):B(C_6F_5)_3$

The reaction of $Mn^V(O)(TBP_8Cz)$ with one equivalent of $B(C_6F_5)_3$ in CH_2Cl_2 at room temperature (Scheme 3.1) was monitored by UV-visible spectroscopy. An immediate color change from the green solution for $Mn^V(O)(TBP_8Cz)$ to a red-brown solution was observed together with the disappearance of the spectrum for $Mn^V(O)(TBP_8Cz)$ (λ_{max} = 420, 634 nm) and the appearance of new peaks at λ_{max} = 420, 789 nm (Figure 3.1). The broadening and decrease in intensity of the Soret band at 420 nm together with the formation of a relatively weak band in the near-IR region at 789 nm is characteristic of the formation of a porphyrinoid π-radical-cation.[17]

Scheme 3.1. Formation of $Mn^{IV}(O)(TBP_8Cz^{+\bullet})$

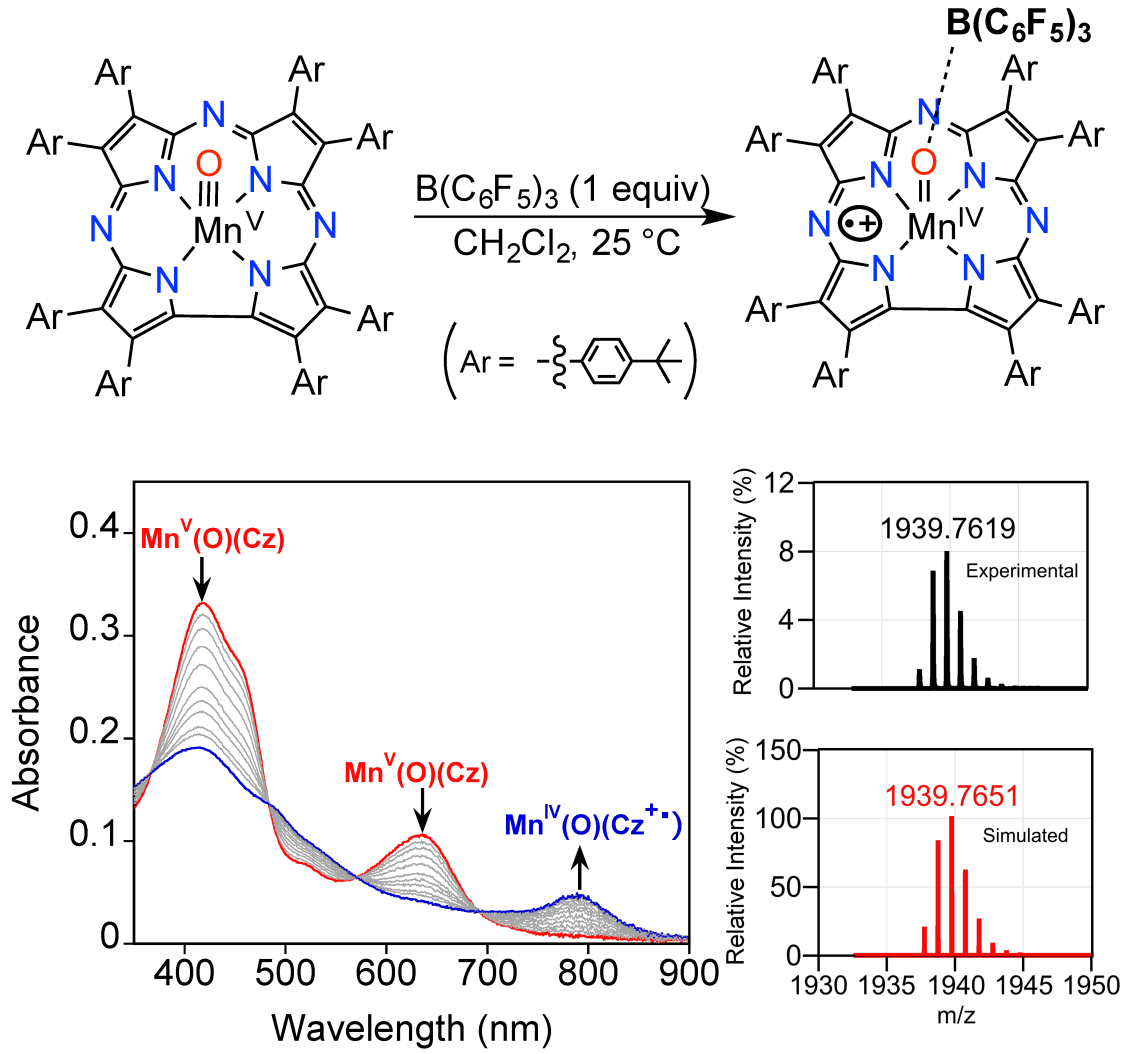

Figure 3.1. a) Spectral titration of $Mn^{V}(O)(TBP_8Cz)$ (5 μM) + $B(C_6F_5)_3$ (0.1 – 1.0 equiv) in CH_2Cl_2. b) CSIMS(+) of $[Mn(O)(TBP_8Cz):B(C_6F_5)_3+H]^+$ at -50 °C.

The new spectrum also matches that observed previously upon addition of the Lewis acid $Zn^{II}(OTf)_2$ to the $Mn^{V}(O)$ complex, which was shown to convert the low-spin (ls) ($S = 0$) Mn^{V} complex into a high-spin (hs) triplet ($S = 1$) (or possibly quintet $S = 2$) state with an electronic configuration best described as a Mn^{IV} corrolazine π-radical-cation.[17] UV-vis spectral titrations were performed with $B(C_6F_5)_3$, and tight isosbestic behavior was seen throughout the titration (Figure 3.1a). A plot of absorbance at 789 nm versus $[B(C_6F_5)_3]$ (Figure 3.2) reaches a plateau at ~1 equiv of $B(C_6F_5)_3$, and no further spectral changes are seen with the addition of more $B(C_6F_5)_3$. Assuming that the

triarylborane reversibly binds to the $Mn^{V}(O)$ complex under equilibrium conditions, a good fit of the data can be obtained with a model for a one-to-one binding isotherm. This fit gives an association constant (K_a) of 2.03 (±0.5) x 10^7 M^{-1}, close to that measured for Zn^{2+} ($K_a(Zn^{2+})$ = 4.03 x 10^6 M^{-1}).[17]

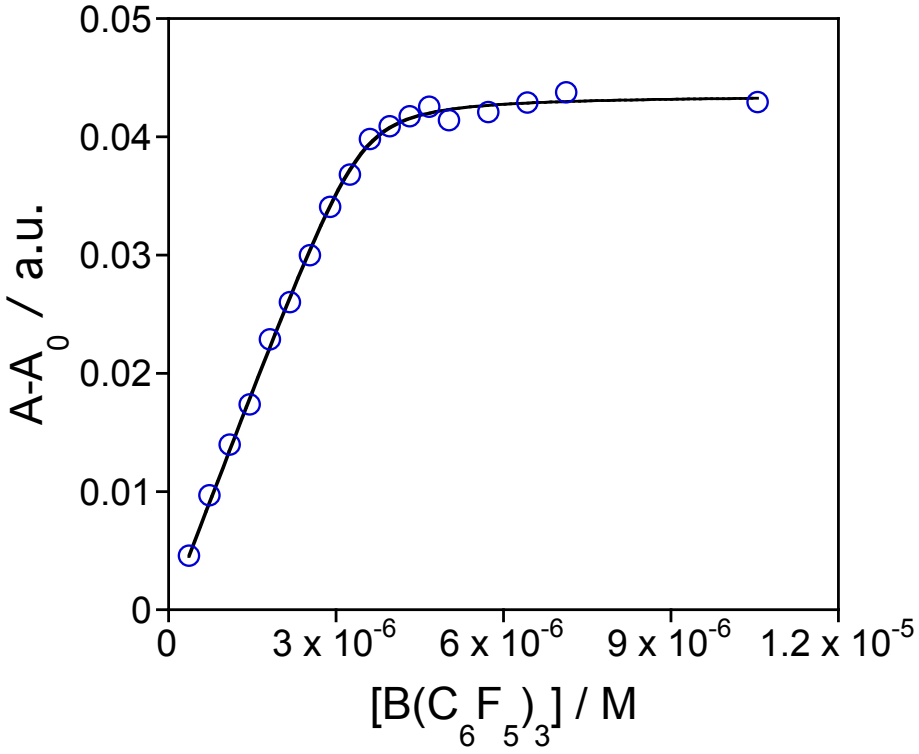

Figure 3.2. Binding isotherm at 789 nm resulting from the reaction of $Mn^{V}(O)(TBP_8Cz)$ (5 µM in 6 mL dichloromethane) and $B(C_6F_5)_3$ (1 equiv).

The ^{1}H-NMR spectrum of $Mn^{V}(O)(TBP_8Cz)$ + $B(C_6F_5)_3$ (1:1 molar ratio) in $CDCl_3$ reveals paramagnetically shifted and broadened peaks, as opposed to the sharp, diamagnetic spectrum seen for ls-$Mn^{V}(O)(TBP_8Cz)$. The paramagnetic NMR spectrum is consistent with the formation of a $Mn^{IV}(O)(TBP_8Cz^{+\bullet})$ complex, in which a high spin (S = 3/2) Mn^{IV} ion is either ferromagnetically (S = 2) or antiferromagnetically coupled (S = 1) to the corrolazine π- radical cation (S = ½). An Evans method measurement in $CDCl_3$ gives μ_{eff} = 4.19 μ_B, which falls in between the predicted spin-only values of 2.83 and

4.90 μ_B for the triplet and quintet spin states, respectively. The X-band EPR spectrum of $Mn^{IV}(O)(TBP_8Cz^{+\bullet})$ in CH_2Cl_2 at 12 K showed only relatively weak EPR-active impurities, consistent with the main product having integer spin (S = 1 or 2). The UV-vis, NMR and EPR data all support the conclusion that the non-metallic Lewis acid $B(C_6F_5)_3$ stabilizes the open-shell valence tautomer $Mn^{IV}(O)(TBP_8Cz^{+\bullet})$.

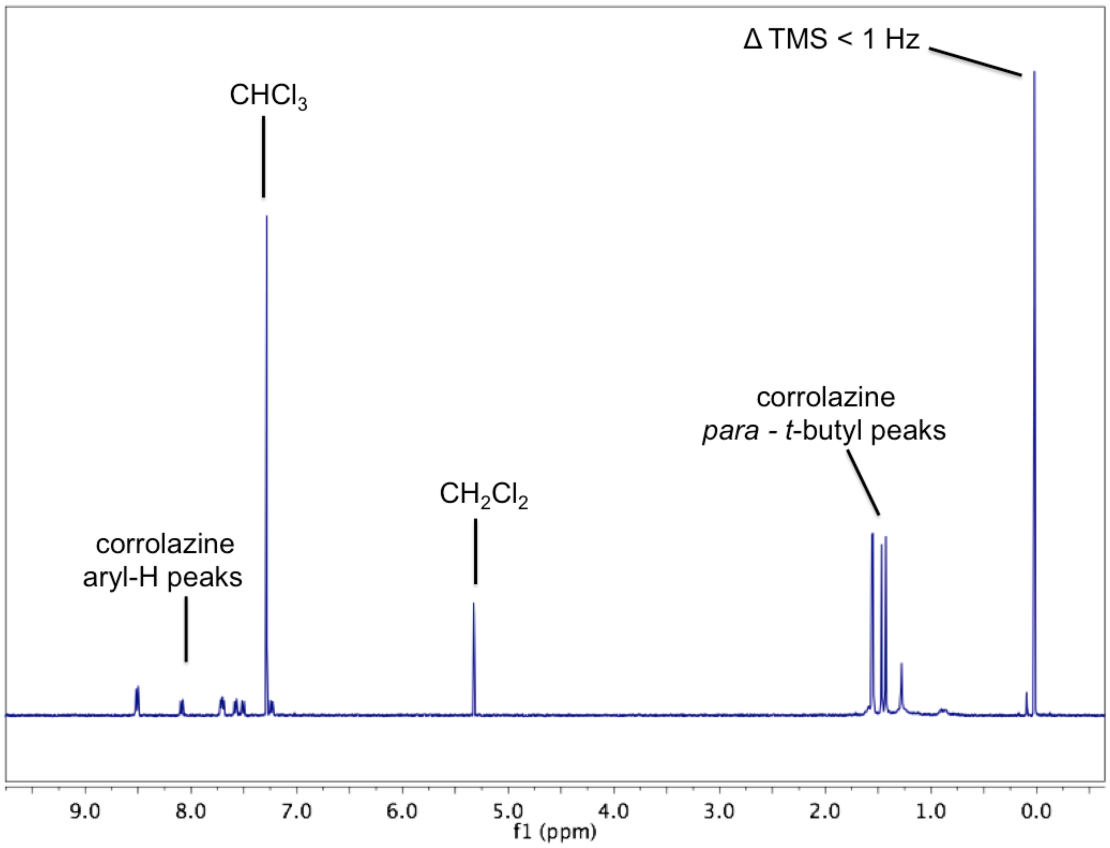

Figure 3.3. Evans method ^{1}H-NMR spectrum of $Mn^V(O)(TBP_8Cz)$ (2.00 mM) in $CDCl_3$ (0.05% TMS).

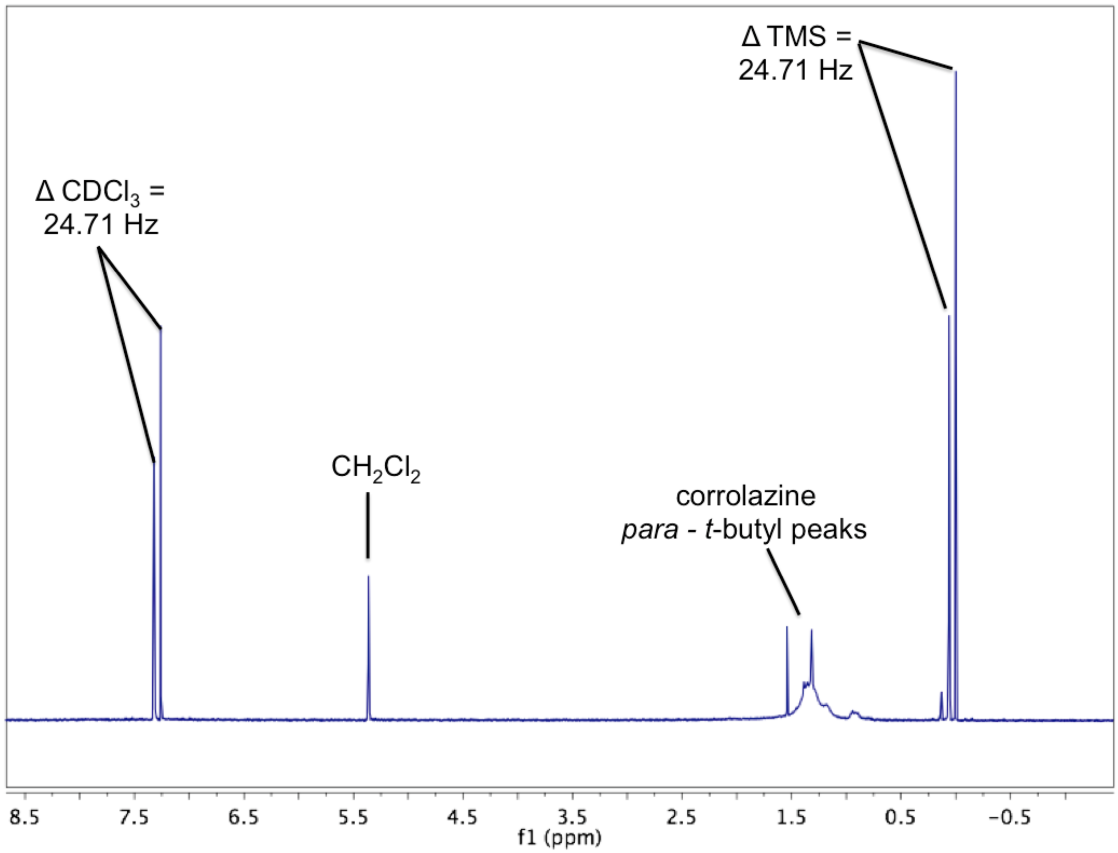

Figure 3.4. Evans method ^{1}H-NMR spectrum of $Mn^{IV}(O)(TBP_8Cz^{+\bullet})$:$B(C_6F_5)_3$ (2.00 mM) in $CDCl_3$ (0.05% TMS).

Attempts to isolate the 1:1 complex $Mn^{IV}(O)(TBP_8Cz^{+\bullet})$:$B(C_6F_5)_3$ in the solid state led to significant reduction, giving an $Mn^{III}(TBP_8Cz)$ product. However, it was possible to characterize the $B(C_6F_5)_3$ complex in solution by cryospray ionization mass spectrometry (CSIMS). The reaction of $Mn^{V}(O)(TBP_8Cz)$ + $B(C_6F_5)_3$ (1 equiv) in CH_2Cl_2 at 20 °C was monitored by UV-vis to ensure good conversion to $Mn^{IV}(O)(TBP_8Cz^{+\bullet})$, and then analyzed directly by CSIMS (Figure 3.1b). A cluster centered at *m/z* 1939.7619 is observed, and the high-resolution, isotopic distribution pattern matches well for the complex of formula $[Mn(O)(TBP_8Cz)–B(C_6F_5)_3+H]^{+}$. The cluster observed at 1426.7712 corresponds to $[Mn(O)(TBP_8Cz)]^{+}$, which likely results from fragmentation of the

$B(C_6F_5)_3$ complex (Figure 3.5). These data provide strong evidence for the formation of a 1:1 complex between the Mn(O) corrolazine and the Lewis acidic triarylborane.

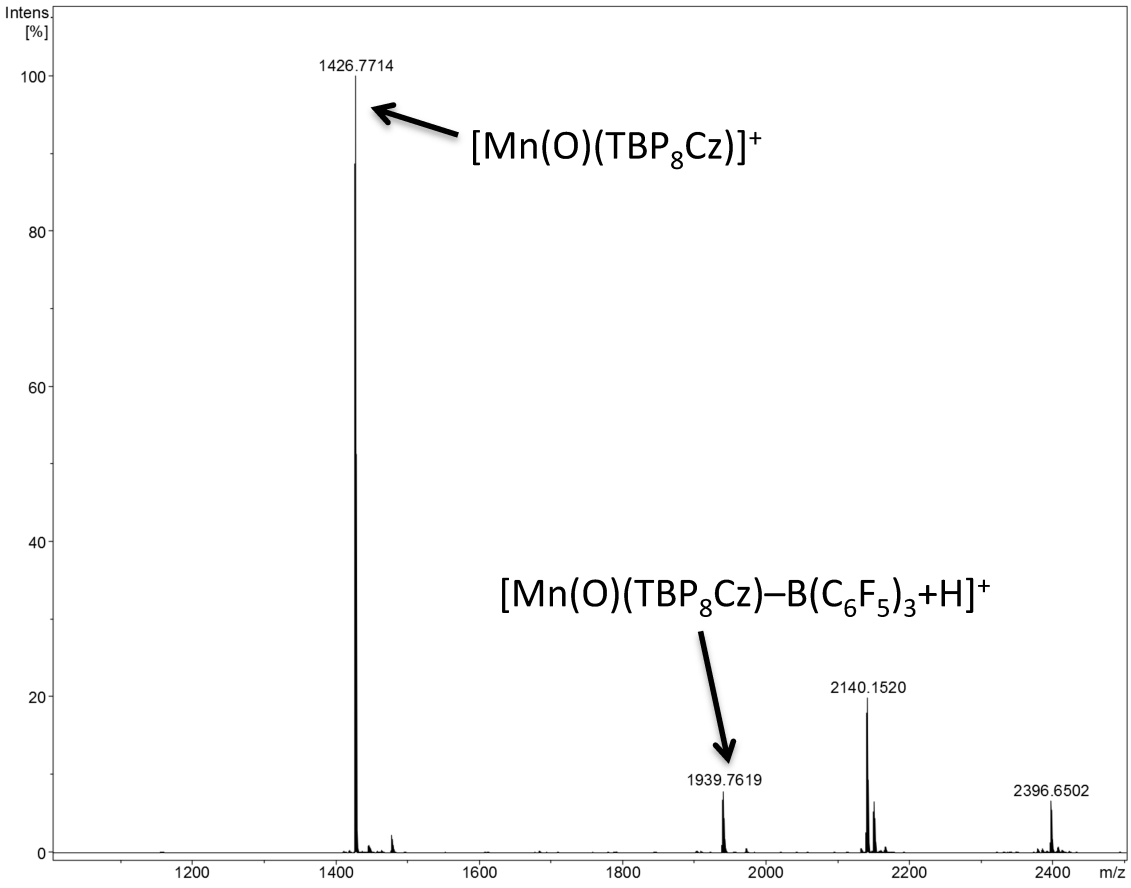

Figure 3.5. CSI-MS (positive mode, -50 °C) data from the reaction of $Mn^{V}(O)(TBP_8Cz)$ (35.5 µM in CH_2Cl_2) with $B(C_6F_5)_3$ (1 equiv).

Athough we have yet to obtain direct structural information for the Zn^{II}- or borane-derived complexes, the $B(C_6F_5)_3$ is anticipated to bind to the oxo ligand of $Mn^{IV}(O)(TBP_8Cz^{+\bullet})$. Precedent for this conclusion can be see in the X-ray structure of an isoelectronic $Re^{V}(O)$-$B(C_6F_5)_3$ complex, in which the boron atom is bound directly to the terminal oxo ligand.[28] In addition, it was proposed that Sc^{3+} coordinates directly to the oxo group of non-heme $Mn^{IV}(O)$ complexes based on X-ray absorption spectroscopy and other supporting data.[19,20]

3.3.2. Reversibility of $Mn^{IV}(O)(TBP_8Cz^{+\bullet}):B(C_6F_5)_3$ Formation

The reversibility of the formation of $Mn^{IV}(O)(TBP_8Cz^{+\bullet})$ was examined with the addition of fluoride anion. Triarylboranes are known to readily form fluoroborate products ($[FB(Ar)_3]^-$) upon addition of F^-.[29] The reagent $[((CH_3)_2N)_3S]^+[F_2Si(CH_3)_3]^-$ (TASF) was employed as a soluble, anhydrous fluoride source. Addition of TASF to a freshly prepared solution of $Mn^{IV}(O)(TBP_8Cz^{+\bullet}):B(C_6F_5)_3$ led to rapid recovery of the starting ls-$Mn^V(O)$ complex as seen by UV-vis (λ_{max} = 634 nm, Figure 3.6), together with a small amount of the reduced Mn^{III} complex $[Mn^{III}(TBP_8Cz)(F)]^-$.[30] The addition of excess chloride anion (Bu_4NCl), in contrast, produced no observable change by UV-vis (Figure 3.7). The difference in reactivity of F^- versus Cl^- parallels their independent reactivity toward triarylboranes, in which Cl^- binds only weakly to $B(Ar)_3$.[31]

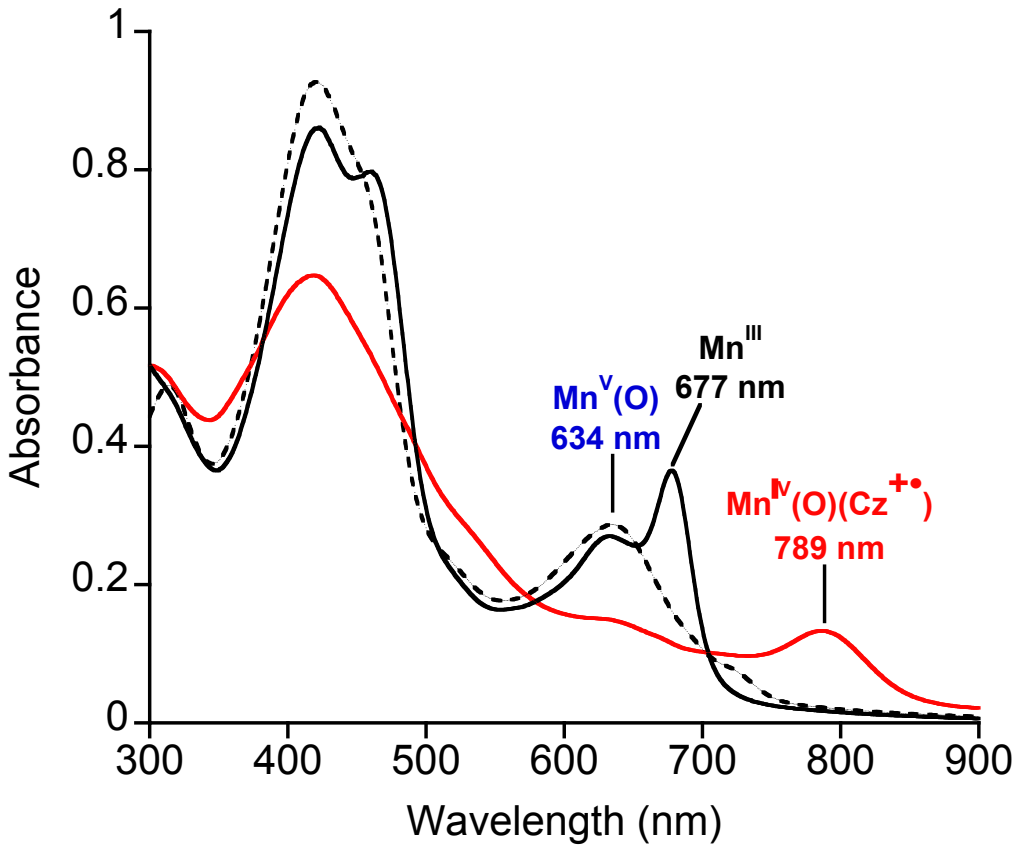

Figure 3.6. UV-vis spectral data for $Mn^{V}(O)(TBP_8Cz)$ (dotted line), $Mn^{IV}(O)(TBP_8Cz^{+\bullet})$: $B(C_6F_5)_3$ (red line), and after addition of TASF (20 equiv) (black solid line).

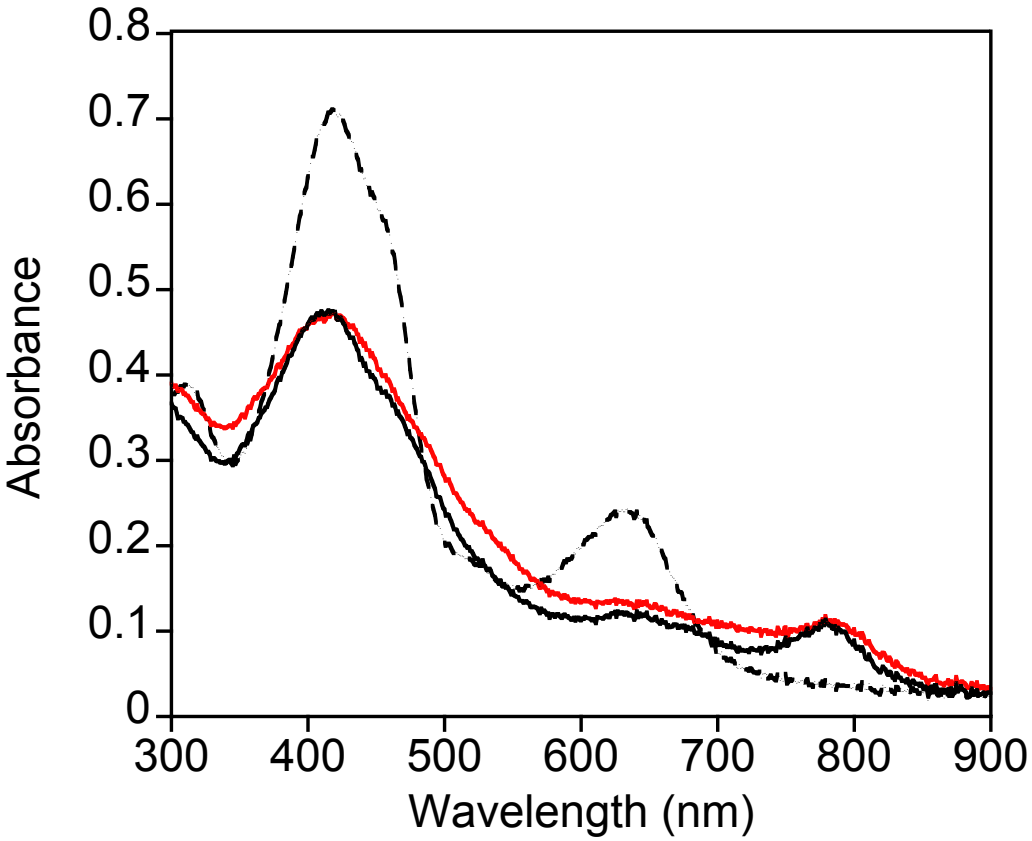

Figure 3.7. UV-vis spectral data for $Mn^{V}(O)(TBP_8Cz)$ (dotted line), $Mn^{IV}(O)(TBP_8Cz^{+\bullet})$: $B(C_6F_5)_3$ (red line), and after addition of tetrabutylammonium chloride (260 equiv) (black solid line).

3.3.3. Reactivity of $Mn^{IV}(O)(TBP_8Cz^{+\bullet}):B(C_6F_5)_3$ in H-atom Abstraction Reactions

The reactivity of $Mn^{IV}(O)(TBP_8Cz^{+\bullet}):B(C_6F_5)_3$ in hydrogen atom transfer (HAT) reactions was examined with phenol substrates. The reaction with 2,4-di-tert-butylphenol (2,4-DTBP) was monitored by UV-vis (Figure 3.8). Isosbestic conversion to a final spectrum with λ_{max} = 443, 727 nm was observed, and is similar to that seen for $[Mn^{IV}(TBP_8Cz)]^{+}$.[32] EPR spectroscopy gives a well resolved spectrum with $g \sim 4$, 2 and hyperfine splitting consistent with ^{55}Mn (I = 5/2) (Figure 3.8b). The spectrum was satisfactorily simulated with a fictitious spin of S' = ½, and g = [4.61, 4.20, 1.92]; $A_{iso}(^{55}Mn)$ = [82, 86, 50] G. These parameters are within the range of previously reported hs-Mn^{IV} (S = 3/2) corrolazines and other hs-Mn^{IV} porphyrinoid complexes.[32] These data indicate that the reaction with 2,4-DTBP results in one-electron reduction of $Mn^{IV}(O)(TBP_8Cz^{+\bullet})$, consistent with H-atom abstraction from the O-H bond.

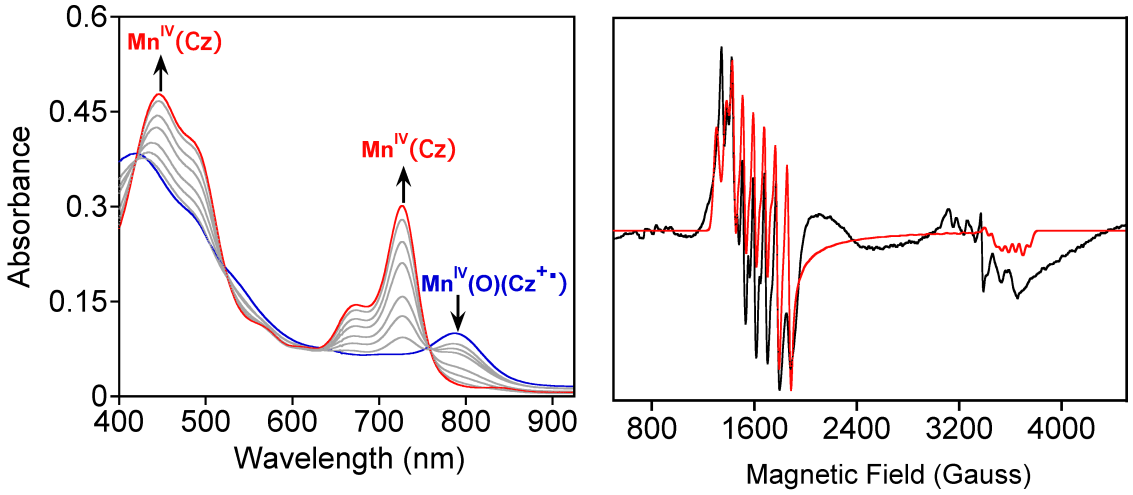

Figure 3.8. (a) UV-vis spectral changes (0 – 60 s) for $Mn^{IV}(O)(TBP_8Cz^{+\bullet}):B(C_6F_5)_3$ + 2,4-DTBP (300 equiv) at 25 °C. (b) EPR spectrum (12 K) after reaction with 2,4-DTBP. Exptl (black line), simulation (red line).

Scheme 3.2

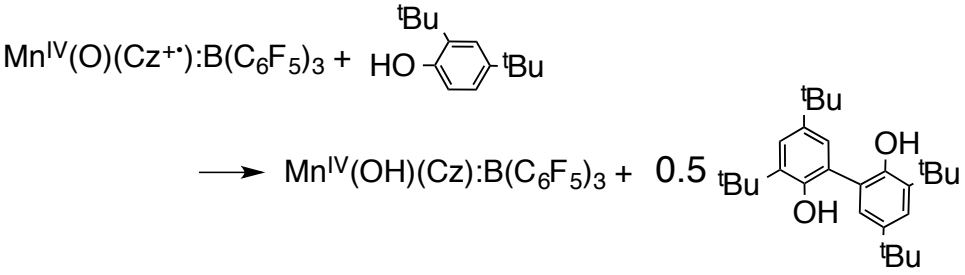

The product of the oxidation of 2,4-DTBP was identified by GC-FID as the expected bis-phenol dimer (Scheme 3.2). A maximal yield of 0.5 equiv of dimer per Mn complex is predicted if the Mn complex serves as a one-electron oxidant, and a yield of 0.39 equiv based on Mn was obtained. This result further supports the $Mn^{IV}(O)(TBP_8Cz^{+\bullet})$ complex functioning as a one-electron oxidant, in stark contrast to the reactivity seen for the ls-$Mn^{V}(O)$ complex, which acts as a two-electron oxidant toward phenol and C-H substrates.[30,32,33]

Kinetics for phenol substrates were measured to gain insight into the reactivity of $Mn^{IV}(O)(TBP_8Cz^{+\bullet}):B(C_6F_5)_3$. Reactions with excess 2,4-DTBP were monitored by UV-vis and found to be first-order over 5 half-lives (Figure 3.9). A plot of [2,4-DTBP] versus k_{obs} was linear, consistent with the rate law rate = k_2[Mn(O)][ArOH]. These methods yielded second-order rate constants, k_2, for both $B(C_6F_5)_3$ and Zn^{II}, as well as the more sterically hindered 2,4,6-tri-*tert*-butylphenol (2,4,6-TTBP), and are compared in Table 3.1. The generation of $Mn^{IV}(O)(TBP_8Cz^{+\bullet})$ by either Zn^{II} or $B(C_6F_5)_3$ leads to a *significant increase* (up to 100-fold) in reactivity as compared to the starting ls-$Mn^{V}(O)$ complex for both phenol substrates. The identity of the Lewis acid further influences the reaction rates, with the triarylborane being more reactive in both cases. In addition, the much slower rate constants for the more sterically hindered 2,4,6-TTBP indicate a

mechanism involving HAT. Support for this mechanism was obtained by measuring a kinetic isotope effect of 3.2 ± 0.3 for 2,4,6-TTBP-OD (Figure 3.11).[34] It was reported that addition of Sc^{3+} to a non-heme $Mn^{IV}(O)$ complex caused a *decrease* in HAT rates, attributed to steric hindrance from the Sc^{3+} ion.[19] Our results appear to contrast these findings, with Lewis acids strongly *increasing* the HAT reactivity of an $Mn^{IV}(O)(Cz^{+\bullet})$ complex. However, this comparison is complicated by the fact that the inherent HAT reactivity of the valence tautomer with the electronic structure $Mn^{IV}(O)(Cz^{+\bullet})$ is not known. The influence of the electronic structure on the reactivity of high-valent metal-oxo complexes remains an area of intense debate.[35-37]

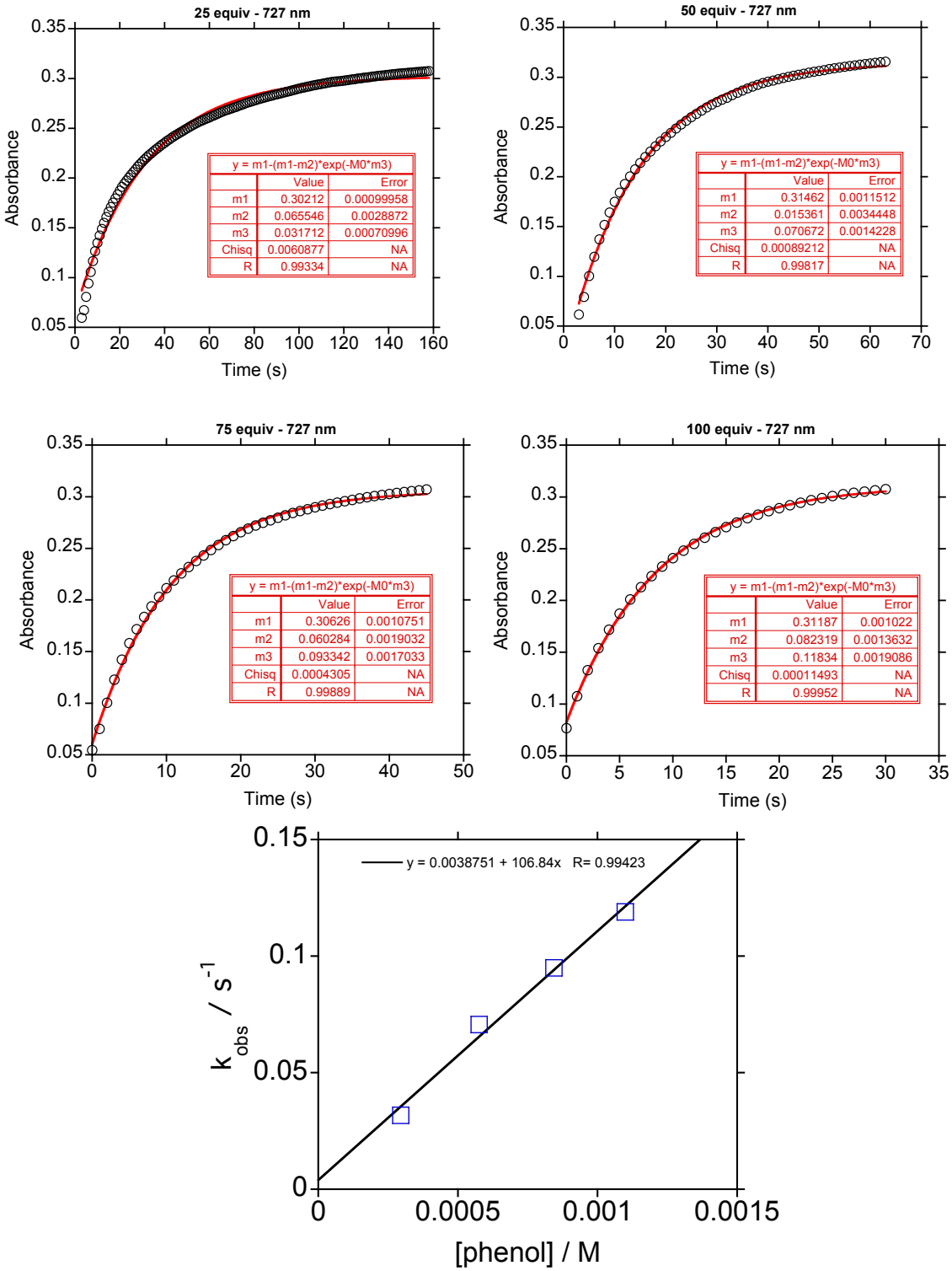

Figure 3.9. Kinetic plots of absorbance at 727 nm versus time for the reaction between $Mn^{IV}(O)(TBP_8Cz^{+\bullet})$:$B(C_6F_5)_3$ and 2,4-DTBP (25 – 100 equiv), and corresponding second order plot of k_{obs} versus [2,4-DTBP], where the slope of the best fit line gives $k_2 = 107 \pm 8\ M^{-1}\ s^{-1}$.

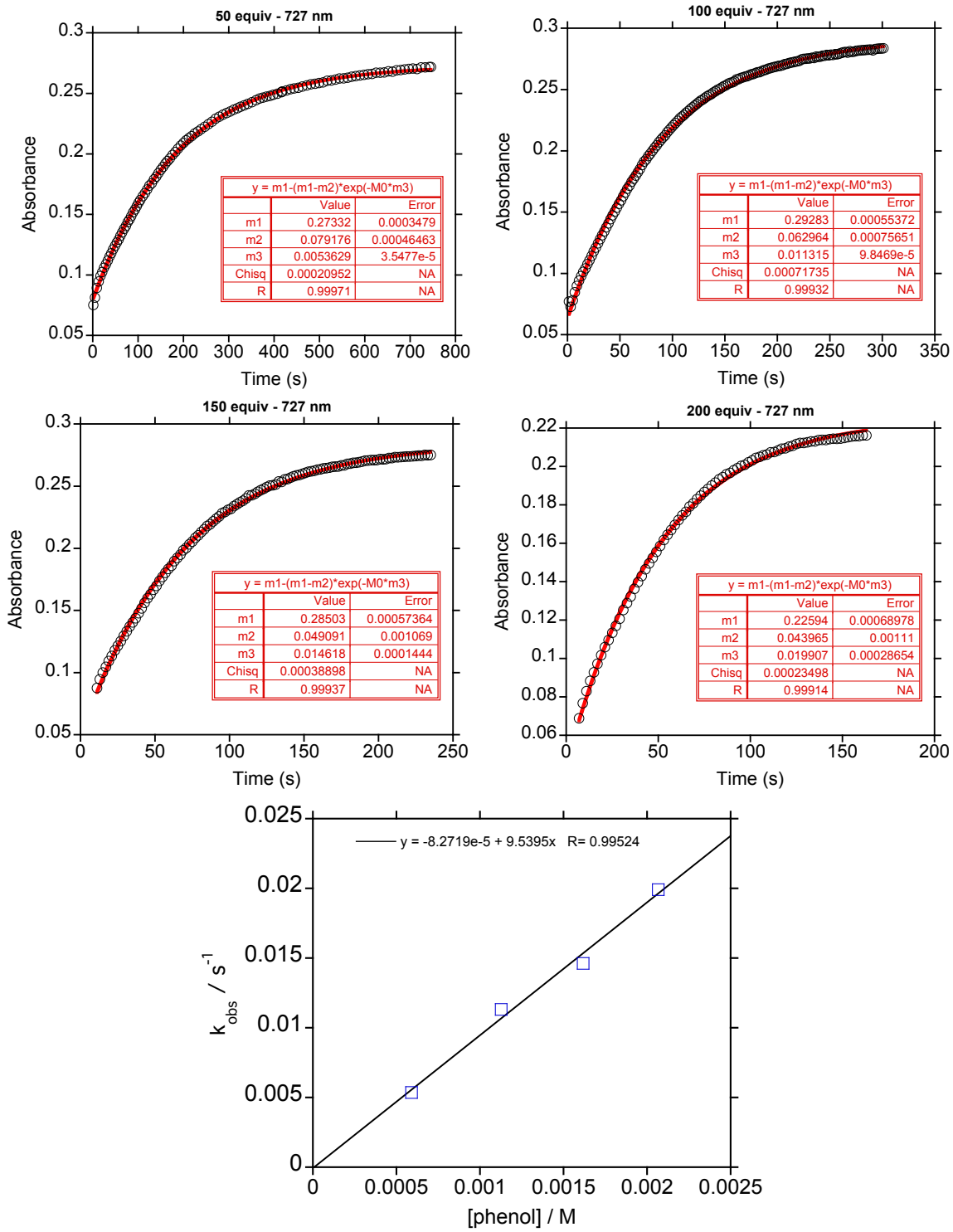

Figure 3.10. Kinetic plots of absorbance at 727 nm versus time for the reaction between $Mn^{IV}(O)(TBP_8Cz^{+\bullet}):B(C_6F_5)_3$ and 2,4,6-TTBP (50 – 200 equiv), and corresponding second order plot of k_{obs} versus [2,4,6-TTBP], where the slope of the best fit line gives $k_2 = 9.5 \pm 0.7\ M^{-1}\ s^{-1}$.

Table 3.1. Rate Constants for HAT from Phenol Substrates

Substrate	Lewis Acid	k_2 (M^{-1} s^{-1})	$k_{Acid}/k_{Mn(O)}$
2,4-DTPB	Zn^{2+}	17 ± 1	5.9
	$B(C_6F_5)_3$	107 ± 8	37
	none	2.9 ± 0.1	-
2,4,6-TTBP	Zn^{2+}	0.157 ± 0.008	2.1
	$B(C_6F_5)_3$	9.5 ± 0.7	130
	none	0.074 ± 0.007	-

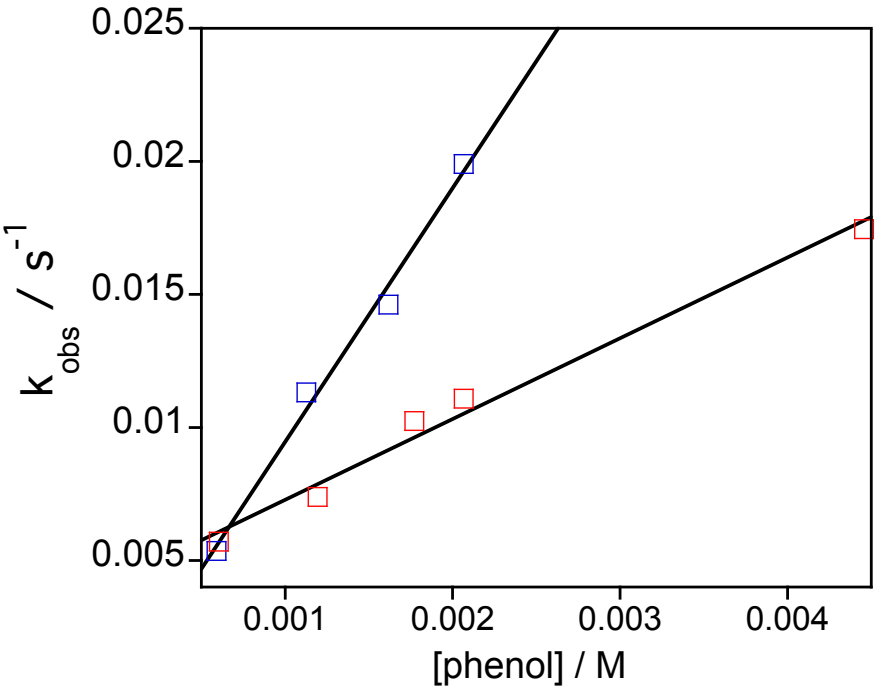

Figure 3.11. Second order plots of $Mn^{IV}(O)(TBP_8Cz^{+\bullet})$:$B(C_6F_5)_3$ with 2,4,6-TTBP (blue) and 2,4,6-TTBP-OD (red). Ratio of the second-order rate constants obtained from the slopes of the best fit lines gives a KIE (k_H/k_D) of 3.2 ± 0.3.

3.4. Conclusions

In summary, we have demonstrated for the first time that a *non-metal ion Lewis acid* can induce reversible valence tautomerism in a metalloporphyrinoid compound. We have also shown that the HAT reactivity of an $Mn^{IV}(O)(porphyrinoid^{+\bullet})$ complex in the presence of Lewis acids is strongly enhanced compared to its closed-shell $Mn^{V}(O)$

valence tautomer. This work provides new insight regarding how to control valence tautomerism in porphyrinoid compounds, as well as on how Lewis acids influence the reactivity of high-valent metal-oxo species.

3.5. References

(1) Denisov, I. G.; Makris, T. M.; Sligar, S. G.; Schlichting, I. Structure and chemistry of cytochrome P450. *Chem. Rev.* **2005**, *105*, 2253-2278.

(2) Rittle, J.; Green, M. T. Cytochrome P450 Compound I: Capture, Characterization, and C-H Bond Activation Kinetics. *Science* **2010**, *330*, 933-937.

(3) Yosca, T. H.; Rittle, J.; Krest, C. M.; Onderko, E. L.; Silakov, A.; Calixto, J. C.; Behan, R. K.; Green, M. T. Iron(IV)hydroxide pKa and the Role of Thiolate Ligation in C‚ÄìH Bond Activation by Cytochrome P450. *Science* **2013**, *342*, 825-829.

(4) Poulos, T. L. Heme Enzyme Structure and Function. *Chem. Rev.* **2014**, *114*, 3919-3962.

(5) Yosca, T. H.; Behan, R. K.; Krest, C. M.; Onderko, E. L.; Langston, M. C.; Green, M. T. Setting an Upper Limit on the Myoglobin Iron(IV)Hydroxide pKa: Insight into Axial Ligand Tuning in Heme Protein Catalysis. *J. Am. Chem. Soc.* **2014**, *136*, 9124-9131.

(6) McEvoy, J. P.; Brudvig, G. W. Water-splitting chemistry of photosystem II. *Chem. Rev.* **2006**, *106*, 4455-4483.

(7) Siegbahn, P. E. M. Structures and Energetics for O2 Formation in Photosystem II. *Acc. Chem. Res.* **2009**, *42*, 1871-1880.

(8) Britt, R. D. In *Oxygenic Photosynthesis: The Light Reactions*; Ort, D., Yocum, C., Heichel, I., Eds.; Springer Netherlands: 1996; Vol. 4, p 137-164.

(9) Umena, Y.; Kawakami, K.; Shen, J.-R.; Kamiya, N. Crystal structure of oxygen-evolving photosystem II at a resolution of 1.9 Å. *Nature* **2011**, *473*, 55-60.

(10) Chirik, P. J. Preface: Forum on Redox-Active Ligands. *Inorg. Chem.* **2011**, *50*, 9737-9740.

(11) Praneeth, V. K. K.; Ringenberg, M. R.; Ward, T. R. Redox-Active Ligands in Catalysis. *Angew. Chem., Int. Ed.* **2012**, *51*, 10228-10234.

(12) Luca, O. R.; Crabtree, R. H. Redox-active ligands in catalysis. *Chem. Soc. Rev.* **2013**, *42*, 1440-1459.

(13) Lyons, C. T.; Stack, T. D. P. Recent advances in phenoxyl radical complexes of salen-type ligands as mixed-valent galactose oxidase models. *Coord. Chem. Rev.* **2013**, *257*, 528-540.

(14) Kurahashi, T.; Kikuchi, A.; Tosha, T.; Shiro, Y.; Kitagawa, T.; Fujii, H. Transient Intermediates from Mn(salen) with Sterically Hindered Mesityl Groups: Interconversion between MnIV-Phenolate and MnIII-Phenoxyl Radicals as an Origin for Unique Reactivity. *Inorg. Chem.* **2008**, *47*, 1674-1686.

(15) Weiss, R.; Bulach, V.; Gold, A.; Terner, J.; Trautwein, A. X. Valence-tautomerism in high-valent iron and manganese porphyrins. *J. Biol. Inorg. Chem.* **2001**, *6*, 831-845.

(16) Evangelio, E.; Ruiz-Molina, D. Valence Tautomerism: New Challenges for Electroactive Ligands. *Eur. J. Inorg. Chem.* **2005**, *2005*, 2957-2971.

(17) Leeladee, P.; Baglia, R. A.; Prokop, K. A.; Latifi, R.; de Visser, S. P.; Goldberg, D. P. Valence Tautomerism in a High-Valent Manganese-Oxo Porphyrinoid Complex Induced by a Lewis Acid. *J. Am. Chem. Soc.* **2012**, *134*, 10397-10400.

(18) Tsui, E. Y.; Tran, R.; Yano, J.; Agapie, T. Redox-inactive metals modulate the reduction potential in heterometallic manganese-oxido clusters. *Nat Chem* **2013**, *5*, 293-299.

(19) Chen, J.; Lee, Y.-M.; Davis, K. M.; Wu, X.; Seo, M. S.; Cho, K.-B.; Yoon, H.; Park, Y. J.; Fukuzumi, S.; Pushkar, Y. N.; Nam, W. A Mononuclear Non-Heme Manganese(IV)-Oxo Complex Binding Redox-Inactive Metal Ions. *J. Am. Chem. Soc.* **2013**, *135*, 6388-6391.

(20) Yoon, H.; Lee, Y.-M.; Wu, X.; Cho, K.-B.; Sarangi, R.; Nam, W.; Fukuzumi, S. Enhanced Electron-Transfer Reactivity of Nonheme Manganese(IV)-Oxo Complexes by Binding Scandium Ions. *J. Am. Chem. Soc.* **2013**, *135*, 9186-9194.

(21) Park, Y. J.; Ziller, J. W.; Borovik, A. S. The Effects of Redox-Inactive Metal Ions on the Activation of Dioxygen: Isolation and Characterization of a Heterobimetallic Complex Containing a MnIII,Äì(Œº-OH),ÄìCaII Core. *J. Am. Chem. Soc.* **2011**, *133*, 9258-9261.

(22) Lam, W. W. Y.; Yiu, S.-M.; Lee, J. M. N.; Yau, S. K. Y.; Kwong, H.-K.; Lau, T.-C.; Liu, D.; Lin, Z. BF3-Activated Oxidation of Alkanes by MnO4. *J. Am. Chem. Soc.* **2006**, *128*, 2851-2858.

(23) Dong, L.; Wang, Y.; Lv, Y.; Chen, Z.; Mei, F.; Xiong, H.; Yin, G. Lewis-Acid-Promoted Stoichiometric and Catalytic Oxidations by Manganese Complexes Having Cross-Bridged Cyclam Ligand: A Comprehensive Study. *Inorg. Chem.* **2013**, *52*, 5418-5427.

(24) Mukherjee, S.; Stull, J. A.; Yano, J.; Stamatatos, T. C.; Pringouri, K.; Stich, T. A.; Abboud, K. A.; Britt, R. D.; Yachandra, V. K.; Christou, G. Synthetic model of the asymmetric [Mn3CaO4] cubane core of the oxygen-evolving complex of photosystem II. *Proc. Natl. Acad. Sci.* **2012**.

(25) Lansky, D. E.; Mandimutsira, B.; Ramdhanie, B.; Clausén, M.; Penner-Hahn, J.; Zvyagin, S. A.; Telser, J.; Krzystek, J.; Zhan, R.; Ou, Z.; Kadish, K. M.; Zakharov, L.; Rheingold, A. L.; Goldberg, D. P. Synthesis, Characterization, and Physicochemical Properties of Manganese(III) and Manganese(V),àíOxo Corrolazines. *Inorg. Chem.* **2005**, *44*, 4485-4498.

(26) Zdilla, M. J.; Dexheimer, J. L.; Abu-Omar, M. M. Hydrogen Atom Transfer Reactions of Imido Manganese(V) Corrole:,Äâ One Reaction with Two Mechanistic Pathways. *J. Am. Chem. Soc.* **2007**, *129*, 11505-11511.

(27) Evans, D. F.; Jakubovic, D. A. Water-soluble hexadentate Schiff-base ligands as sequestrating agents for iron(III) and gallium(III). *J. Chem. Soc., Dalton Trans.* **1988**, 2927-2933.

(28) Smeltz, J. L.; Lilly, C. P.; Boyle, P. D.; Ison, E. A. The Electronic Nature of Terminal Oxo Ligands in Transition-Metal Complexes: Ambiphilic Reactivity of Oxorhenium Species. *J. Am. Chem. Soc.* **2013**, *135*, 9433-9441.

(29) Wade, C. R.; Broomsgrove, A. E. J.; Aldridge, S.; Gabbai, F. P. Fluoride Ion Complexation and Sensing Using Organoboron Compounds. *Chem. Rev.* **2010**, *110*, 3958-3984.

(30) Prokop, K. A.; de Visser, S. P.; Goldberg, D. P. Unprecedented Rate Enhancements of Hydrogen-Atom Transfer to a Manganese(V)–Oxo Corrolazine Complex. *Angew. Chem., Int. Ed.* **2010**, *49*, 5091-5095.

(31) Zhao, H.; Reibenspies, J. H.; Gabbai, F. P. Lewis acidic behavior of B(C6Cl5)3. *Dalton Trans.* **2013**, *42*, 608-610.

(32) Fukuzumi, S.; Kotani, H.; Prokop, K. A.; Goldberg, D. P. Electron- and Hydride-Transfer Reactivity of an Isolable Manganese(V)-Oxo Complex. *J. Am. Chem. Soc.* **2011**, *133*, 1859-1869.

(33) Lansky, D. E.; Goldberg, D. P. Hydrogen Atom Abstraction by a High-Valent Manganese(V)-Oxo Corrolazine. *Inorg. Chem.* **2006**, *45*, 5119-5125.

(34) An ET/PT or PT/ET mechanism cannot be definitively ruled out.

(35) Saouma, C. T.; Mayer, J. M. Do spin state and spin density affect hydrogen atom transfer reactivity? *Chem. Sci.* **2014**, *5*, 21-31.

(36) Sahu, S.; Widger, L. R.; Quesne, M. G.; de Visser, S. P.; Matsumura, H.; Moënne-Loccoz, P.; Siegler, M. A.; Goldberg, D. P. Secondary Coordination Sphere Influence on the Reactivity of Nonheme Iron(II) Complexes: An Experimental and DFT Approach. *J. Am. Chem. Soc.* **2013**, *135*, 10590-10593.

(37) Usharani, D.; Janardanan, D.; Li, C.; Shaik, S. A Theory for Bioinorganic Chemical Reactivity of Oxometal Complexes and Analogous Oxidants: The Exchange and Orbital-Selection Rules. *Acc. Chem. Res.* **2012**, *46*, 471-482.

4. Chapter 4. High-Valent Manganese-Oxo Valence Tautomers and the Influence of Lewis/Brönsted Acids on C–H Bond Cleavage

This work was co-written with the following authors and was published under the following title and citation:

Baglia, R. A.; Crest, C. M.; Yang, T.; Leeladee, P.; Goldberg, D. P. "High-Valent Manganese-Oxo Valence Tautomers and the Influence of Lewis/Brönsted Acids on C–H Bond Cleavage" *Inorg. Chem.*, **2016**, Accepted.

4.1. Introduction

A broad range of heme enzymes rely on high-valent iron-oxo porphyrin intermediates to carry out substrate oxidation.[1-3] The general structure of these species can be divided into $Fe^{IV}(O)(Por^{\bullet+})(X)$ (Compound I (Cpd-I), $Por^{\bullet+}$ = porphyrin π-radical-cation, X = axial ligand), and $Fe^{IV}(O)(por)$ (Compound II (Cpd-II)). Cpd-I can be a potent oxidant, and is capable of cleaving C–H bonds with bond strengths up to ~95 kcal/mol in Cytochrome P450. Cpd-II is usually considered to be a weaker oxidant than Cpd-I, in part because Cpd-I is at the formally higher oxidation level of Fe^{V}. The redox-active nature of the porphyrin ligand allows access to such formally high oxidation states because of the porphyrin's ability to delocalize some of the positive charge on the aromatic π-system. The delocalization can be viewed in the extreme case as an intramolecular electron transfer from the porphyrin ligand to the oxidized metal center, resulting in a 'valence tautomer' with a one-electron-reduced metal center and a π-based radical on the ring. There was significant debate regarding which valence tautomer best described Cpd-I in Cyt-P450 until recently, when definitive spectroscopic evidence

showed that this species corresponded to the $Fe^{IV}(O)(\pi$-radical-cation) tautomer.[1] However, the requirements for stabilizing one valence tautomer over the other in high-valent metalloporphyrins, and their relative reactivities, remains poorly understood.

In synthetic porphyrin systems, valence tautomerism has been induced by chemical or nonchemical (temperature, irradiation) changes.[4-6] However, there are few examples of metal-oxo complexes in which both valence tautomers have been characterized. Our group showed previously that treatment of $Mn^{V}(O)(TBP_8Cz)$ (TBP_8Cz = octakis(*p-tert*-butylphenyl)corrolazinato^{3-}) with metallic and nonmetallic Lewis and Brönsted acids (LA = $Zn(OTf)_2$, $B(C_6F_5)_3$, H^+) (OTf^- = trifluoromethylsulfonate) led to stabilization of the valence tautomer $Mn^{IV}(O–LA)(TBP_8Cz^{\bullet+})$, with an Mn^{IV} ion coupled to a corrolazine π-cation radical and the Lewis/Bronsted acid bound to the terminal oxo ligand.[7-10] The $Mn^{IV}(O–LA)(TBP_8Cz^{\bullet+})$ complexes exhibited significantly enhanced reactivity toward O–H bond cleavage with phenol derivatives in comparison to the closed-shell $Mn^{V}(O)(TBP_8Cz)$. In contrast, dramatically decreased rates of oxygen-atom-transfer (OAT) to triarylphosphines were observed for $Mn^{IV}(O–LA)(TBP_8Cz^{\bullet+})$ as compared to the $Mn^{V}(O)$ tautomer. Acid-dependent valence tautomerism was observed when trifluoroacetic acid (TFA) was added to $Fe^{IV}(O)(TPFP^{\bullet+})(L)$ (TPFP = 5,10,15,20-tetrakis-(pentafluorophenyl)porphyrinato$^{2–}$), resulting in the formation of the isoporphyrin complex $Fe^{III}(TPFP^{++})(L)_2$.[11] Addition of chloride ion to the isoporphyrin complex allowed for chlorination of aromatic compounds and olefins. More recently, reversible valence tautomerism was implicated for oxo-ferryl porphyrins by stopped-flow UV-visible spectroscopy, where $Fe^{IV}(O)(por)$ was present at high pH but could be converted to $Fe^{III}(OH_2)(por^{\bullet+})$ at low pH.[12]

In Mn(salen) systems, addition of one equivalent of hydroxide to $Mn^{III}(OH_2)(salen^{\bullet+})$ resulted in the formation of the valence tautomer $Mn^{IV}(OH)(salen)$. Further deprotonation of this complex gave the $Mn^{IV}(O)(salen)$ complex, which was the most reactive complex in this series in both HAT and OAT reactions.[13] In 2015, Abu-Omar showed that addition of TFA to $Mn^{V}(O)(tpfc)$ (tpfc = 5,10,15-tris(pentafluorophenyl)corrolato^{3-}) resulted in formation of the valence tautomer $Mn^{IV}(OH)(tpfc^{\bullet+})$.[14]

Lewis and Brönsted acids are known to exert a critical influence on the reactivity of metal-oxo and related species. In biological systems, these acids can play important roles in tuning redox potentials and redox reactivity. One example is the non-redox active Ca^{2+} ion bound to the Mn cluster of the oxygen-evolving complex (OEC) in Photosystem II.[15-17] Possible intermediates during water oxidation by the OEC are high-valent $Mn^{IV}(O)/Mn^{V}(O)$ species, and the role of the Ca^{2+} ion in this process remains poorly understood. Addition of redox inactive metal ions to manganese-oxo cluster complexes allowed for modulation of the reduction potentials of these compounds.[16] The addition of Lewis/Bronsted acids (e.g. Sc^{3+}, HOTf) has been found to enhance electron transfer (ET), OAT, and PCET (PCET = proton-coupled electron transfer) rates of non-heme $Fe^{IV}(O)$ complexes.[18] Addition of triflic acid and $Sc(OTf)_3$ to non-heme $Mn^{IV}(O)$ complexes was found to accelerate ET and OAT rates, but inhibit rates of H-atom abstraction.[19,20] Non-redox active metal ions have also been found to accelerate the rates and improve efficiencies of Mn-mediated catalytic oxidation reactions.[21,22] The rates of O_2 activation in non-heme Mn and Fe complexes were also enhanced in the presence of Lewis acids.[23] In these nonheme systems, however, valence tautomerism did not come into play.

In this work, a series of $Mn^{IV}(O–LA)(TBP_8Cz^{\bullet+})$ complexes (LA = $Zn(OTf)_2$, $B(C_6F_5)_3$, $HBAr^F$, CF_3CO_2H) are generated and their reactivity toward C–H bond cleavage is assessed. The $Mn^{IV}(O–LA)(TBP_8Cz^{\bullet+})$ complexes (LA = $Zn(OTf)_2$, $B(C_6F_5)_3$) were characterized by Mn K-edge X-ray absorption spectroscopy (XAS), providing the first structural information for these complexes and yielding key information on both the oxidation state of the Mn and the perturbation of the Mn–O bond length. The reactivity of the $Mn^{IV}(O–LA)(TBP_8Cz^{\bullet+})$ complexes with a series of C–H substrates of varying C–H bond strengths (BDE(C–H)) were studied. Rate enhancements of C–H cleavage were observed for the Lewis acid complexes compared to the closed-shell $Mn^{V}(O)$ valence tautomer, with the exception of TFA. The magnitude of the rate enhancement depended strongly on the identity of the Lewis acid.

4.2. Experimental Methods

4.2.1. General methods and materials

The compound $Mn^{V}(O)(TBP_8Cz)$ was synthesized according to a published procedure.[24] All other reagents were commercially available and were purchased at the highest level of purity and used as received unless otherwise specified here. The oxonium acid $HBAr^F$ ($[H(OEt_2)_2]^+[B(C_6F_5)_4]^-$) was synthesized according to a published procedure.[25] The substrate 9,10-dihydro-10-methylacridine ($AcrH_2$) was synthesized according to a published procedure.[26] The substrates xanthene (Xn) and 9,10-dihydroanthracene (DHA) were purchased from Sigma-Aldrich and recrystallized at least three times from ethanol. The substrate 1,4-cyclohexadiene (CHD) was purchased from Sigma-Aldrich and purified by running through an alumina pipette column immediately before use. The deuterated substrate xanthene-d_2 was synthesized according to a

published procedure.[27] Deuterated solvents ($CDCl_3$ and CD_2Cl_2) for NMR were purchased from Cambridge Isotopes, Inc.

4.2.2. Analytical methods

UV-vis spectroscopy was performed on a Hewlett-Packard 8453 diode-array spectrophotometer equipped with HPChemstation software. A UV filter was used to block light < 400 nm to protect the reaction mixtures from photoreduction. $^{31}P[^{1}H]$-NMR (161.9 MHz) spectra were recorded on a Bruker Avance 400 MHz NMR spectrometer at room temperature. Electron paramagnetic resonance (EPR) spectra were recorded with a Bruker EMX spectrometer equipped with a Bruker ER 041 X G microwave bridge and a continuous-flow liquid helium cryostat (ESR900) coupled to an Oxford Instruments TC503 temperature controller. The spectra were obtained at 12 K under non-saturating microwave power conditions (microwave frequency = 9.43 GHz, microwave power = 20.1 mW, modulation amplitude = 10 G, modulation frequency = 100 kHz). Gas chromatography was performed on an Agilent 6850 gas chromatograph fitted with a DB-5 5% phenylmethyl siloxane capillary column and equipped with a flame-ionization detector (FID). The GC-FID response factor for anthracene was prepared versus eicosane as the internal standard. Stopped-flow experiments were carried out by using HiTech SHU-61SX2 (TgK scientific Ltd.) with a xenon light source and Kinetic Studio software. All calculations were performed using the Orca 3.0.3 program packages.[28] For computational convenience, all the *tert*-butylphenyl groups on the TBP_8Cz ligand were replaced with H (H_8Cz). Unless specified, the resolution of identity (RI) approximation and the chain-of-sphere approximation (COSX), with the corresponding auxiliary basis sets, were applied to the Coulomb integrals on the DFT portion and exchange integrals on

the Hartee-Fock (HF) portion, respectively, for hybrid functionals. The RI approximation was applied when pure functionals were used. LA = Lewis acids, which are $Zn(OTf)_2$ (with η^1,η^2-$(OTf)_2$) and $B(C_6F_5)_3$.

4.2.3. X-ray Absorption Spectroscopy (XAS)

XAS data were recorded at the Stanford Synchrotron Radiation Laboratory (SSRL) on beamline 7-3, under ring conditions of 3 GeV and 495-500 mA. A Si(220), ϕ=90, double crystal monochromator was used for energy selection, and a Rh-coated mirror (set to an energy cutoff of 9.5 keV) was used for harmonic rejection. Energy calibration was performed by assigning the first inflection point of the Mn foil spectrum to 6539.0 eV. All samples were maintained at ~10 K during data collection using an Oxford Instruments CF1208 continuous-flow liquid helium cryostat. Data were measured in fluorescence mode (using a Canberra Ge element array detector). Samples were monitored for photoreduction throughout the course of data collection. Only the scans which showed no evidence of photoreduction were used in the final data average.

The data were calibrated and averaged using EXAFSPAK. Pre-edge subtraction and splining were conducted using EXAFSPAK. A three-region cubic spline was used to model the smooth background above the edge. Normalization of the data was achieved by subtracting the spline and normalizing the postedge region to 1. The resultant EXAFS was k^3-weighted to enhance the impact of high-k data.

Theoretical EXAFS signals $c(k)$ were calculated using FEFF (version 7.0) and fit to the data using EXAFSPAK. The nonstructural parameter E_0 was also allowed to vary but was restricted to a common value for every component in a given fit. The structural parameters that were varied during the refinements were the bond distance (R) and the

Debye-Waller factor, which is a measure of thermal vibration, and to the static disorder of the absorbers and scatterers. Coordination numbers were systematically varied in the course of the analysis, but they were not allowed to vary within a given fit.

4.2.4. Formation of Mn^{IV}(O–LA)($TBP_8Cz^{\bullet+}$) for XAS

In a typical reaction, $Mn^{V}(O)(TBP_8Cz)$ (2 mM) was mixed with 1 equiv of Lewis acid ($Zn(OTf)_2$ or $B(C_6F_5)_3$) in benzonitrile. The reaction was monitored by UV-vis to ensure complete formation of Mn^{IV}(O–LA)($TBP_8Cz^{\bullet+}$) and transferred to a kapton XAS sample cell and carefully frozen in liquid nitrogen.

4.2.5. Analysis of the reaction between Mn^{IV}(O–LA)($TBP_8Cz^{\bullet+}$) and C–H substrates by EPR Spectroscopy

To an amount of $Mn^{V}(O)(TBP_8Cz)$ (1 mM) was added Lewis acid (1 equiv) ($Zn(OTf)_2$, $B(C_6F_5)_3$, or $HBAr^F$) and a color change from green to brown was observed, indicating formation of Mn^{IV}(O–LA)($TBP_8Cz^{\bullet+}$). Excess C–H substrate (100 equiv of either xanthene, DHA, or $AcrH_2$) was added and the reaction was monitored by UV-vis until complete formation of the reduced Mn product was observed. This reaction mixture was then transferred to an EPR tube, and frozen and stored at 77 K until EPR spectra could be recorded. The spectra were obtained at 12 K under non-saturating microwave power conditions (microwave frequency = 9.43 GHz, microwave power = 20.1 mW, modulation amplitude = 10 G, modulation frequency = 100 kHz).

4.2.6. Product Analysis by GC-FID

To an amount of $Mn^{V}(O)(TBP_8Cz)$ (1.9 mM) in CH_2Cl_2 was added $B(C_6F_5)_3$ (1 equiv) and a color change from green to brown was observed indicating the formation of Mn^{IV}(O–LA)($TBP_8Cz^{\bullet+}$). Excess DHA (100 equiv) in CH_2Cl_2 was added and the reaction

was monitored by UV-vis until complete formation of $Mn^{IV}(OH)(TBP_8Cz)$ was observed. Eicosane was added as an internal standard and the mixture was injected onto the GC-FID for product analysis. The anthracene product was identified by comparison of retention time with an authentic sample, and quantitation was performed by integration of the peak and comparison with a calibration curve constructed with the internal standard. A yield of 65% (average of three runs) for the anthracene product was obtained.

4.2.7. Kinetics of reaction between $Mn^{IV}(O–LA)(TBP_8Cz^{\bullet+})$ and C–H substrates

In a typical reaction, to an amount of $Mn^{V}(O)(TBP_8Cz)$ (64 μM) was added Lewis acid (1 equiv) (LA = TFA, $Zn(OTf)_2$, $B(C_6F_5)_3$, $HBAr^F$) in CH_2Cl_2 and the reaction was monitored by UV-vis until full formation of $Mn^{IV}(O–LA)(TBP_8Cz^{\bullet+})$ was observed. Excess C–H substrate (Xn, DHA, or CHD) was added and the spectrum for $Mn^{IV}(O–B(C_6F_5)_3)(TBP_8Cz^{\bullet+})$ (λ_{max} = 420, 789 nm) was converted isosbestically to $Mn^{IV}(X)(TBP_8Cz)$ (λ_{max} = 446, 722-727 nm). The pseudo first-order rate constants, k_{obs}, for these reactions were obtained by nonlinear least-squares fitting of the plots of absorbances at 789 nm and 727 nm (Abs_t) versus time (t) according to the equation: $Abs_t = Abs_f + (Abs_0 – Abs_f) \exp(-k_{obs}t)$, where Abs_0 and Abs_f are initial and final absorbance, respectively. The second order rate constant was obtained from the slope of the best-fit line from a plot of k_{obs} versus substrate concentration and normalized per reactive C–H bond (k_2'). The reaction of $Mn^{IV}(O–B(C_6F_5)_3)(TBP_8Cz^{\bullet+})$ with the C–H substrate $AcrH_2$ was too fast to be analyzed by conventional UV-vis kinetics, and was instead monitored by stopped-flow UV-vis spectroscopy. When $AcrH_2$ was added to $Mn^{IV}(O–B(C_6F_5)_3)(TBP_8Cz^{\bullet+})$, the spectrum changed to that of $Mn^{III}(OH_2)(TBP_8CzH^+)$ (λ_{max} = 446, 727). The rate constants were extracted as described earlier.

4.2.8. Lewis Acidity Measurements by the Gutmann-Beckett Method

A 3:1 mixture of Lewis acid ($HBAr^F$, TFA) and triethylphosphine oxide was prepared in CD_2Cl_2, and analyzed by $^{31}P[^1H]$ NMR spectroscopy. Spectra were collected and calibrated against an H_3PO_4 external standard. The following equation was used to calculate the acceptor number (A.N.): A.N. = $2.21(\delta_{sample} - 41.0)$, where δ_{sample} is the chemical shift for the $OPEt_3$ – Lewis acid adduct.[29,30]

4.2.9. Geometry optimization and spin-state ordering by DFT

Initial geometries for geometry optimization were obtained from the reported crystal structure for $Mn^V(O)(TBP_8Cz)$[31]. Geometry optimization was performed using the unrestricted hybrid-GGA B3LYP[32] with dispersion correction (D3) from Grimme, et al. in 2010.[33] The effective core potential basis set LANLDZ[34-38] was used for metal atoms and 6-31G(d)[39,40] was used for the remaining atoms. Frequency calculations were performed on the optimized geometries and no imaginary frequencies were observed. The Lewis acid complexes were examined in various spin states as follows: singlet ^{1}[Mn(O–LA)(H_8Cz)], triplet (ls-Mn^{IV}) ^{3}[Mn(O–LA)(H_8Cz)] (ls = low-spin), triplet (hs-Mn^{IV}) ^{3}[Mn(O–LA)(H_8Cz)] (hs = high-spin), and quintet ^{5}[Mn(O–LA)(H_8Cz)]. The triplet (ls-Mn^{IV}) ^{3}[Mn(O–LA)(H_8Cz)] has one unpaired spin on the Mn and one unpaired spin on the corrolazine with a $d_\pi^1 a''^1$ configuration. The other triplet state (hs-Mn^{IV}) ^{3}[Mn(O–LA)(H_8Cz)] has three unpaired spins on the Mn and an unpaired spin on the corrolazine ligand which is anti-ferromagnetically coupled.

Single-point energy calculations on the optimized geometries were performed using range-separated hybrid meta-GGA wB97X with dispersion correction[33] (wB97X-D3) with def2-TZVPP on the metal atom and def2-SVP on the rest of the atoms. The zeroth-order regular approximation (ZORA) with a model potential[41] was applied along

with segmented all-electron relativistically recontracted (SARC) version of the basis sets.[42,43] The RI approximation was applied to the Coulomb integral on the DFT portion and the exchange integrals on the HF portion were solved exactly. Numerical grid was increased to "grid 4" in Orca notation, which equals to Lebedev 302 points. Solvent was modeled by the conductor-like screening model (COSMO) with ε = 9.08 and refractive index = 1.424 for CH_2Cl_2.

4.2.10. Functional/basis set benchmarking for the geometry of Mn(O–B(C_6F_5)$_3$)(H_8Cz) by DFT

The initial geometry of Mn(O–B(C_6F_5)$_3$)(H_8Cz) for geometry optimizations was obtained from the reported crystal structure of Mn^V(O)(TBP_8Cz)[31] and the placement of a B(C_6F_5)$_3$ unit on the oxo ligand. Geometry optimizations were performed using the following combinations of functionals and basis sets: 1) BP86[44,45] and def2-TZVPP on Mn with def2-SVPD on the rest of the atoms. ZORA with a model potential[41] was applied and the basis sets were recontracted (SARCs)[42,43] to be consistent with the ZORA. 2) B3PW91[45] with SDD[46] on Mn and 6-31G(d,p)[39,40] on the rest of the atoms. 3) B3LYP[32] with def2-TZVPP on Mn and def2-SVPD on the rest of the atoms. ZORA with a model potential[41] and SARCs[42,43] were applied. 4) B3LYP[32] with TZVPP on all atoms. ZORA with a model potential[41] and SARCs[42,43] were applied. 5) B3LYP[32] with LANLDZ[34-38] on Mn and 6-31G[39] on the rest of the atoms. 6) PBE0[47] with def2-TZVPP on Mn and def2-SVPD on the rest of the atoms. ZORA with a model potential[41] and SARCs[42,43] were applied.

4.2.11. Relaxed surface scans for triplet (ls-Mn^{IV}) ^{3}[Mn(O–LA)(H_8Cz)] and quintet (hs-Mn^{IV}) ^{5}[Mn(O–LA)(H_8Cz)] by DFT

A similar procedure was used as for geometry optimization. Relaxed surface scans were performed with Mn–O distances varied from 1.61 – 1.71 Å with a fixed increment of 0.01 Å. Frequency calculations on the constrained geometries were not performed because the molecules were not fully relaxed. Single-point energies were calculated based on the constrained geometries using LANLDZ[34-38] on the metal atom and 6-31G(d)[39,40] on the rest of the atoms. For comparison, all the single point energies at different Mn–O distances were compared to that of the optimized ^{5}[Mn(O–LA)(H_8Cz)].

4.3. Results and Discussion

4.3.1. Synthesis and structural characterization of the Mn^{IV}(O-LA)($TBP_8Cz^{\bullet+}$) complexes by X-ray Absorption Spectroscopy

Previously, we found that the addition of Lewis/Brönsted acids (Zn^{II}, $B(C_6F_5)_3$, $HBAr^F$, HBF_4) to closed-shell Mn^V(O)(TBP_8Cz) resulted in stabilization of the open-shell valence tautomer Mn^{IV}(O–LA)($TBP_8Cz^{\bullet+}$) in solution. Characterization of the latter species was carried out by UV-vis, NMR, and EPR spectroscopies, and in the case of $B(C_6F_5)_3$ by ESI-MS, which confirmed the 1:1 nature of the Lewis acid adduct. The spectroscopic data showed that the open-shell Mn^{IV}(O–LA)($TBP_8Cz^{\bullet+}$) complexes were paramagnetic, with an Mn^{IV} ion ferro- or antiferromagnetically coupled to a π-cation-radical on the Cz ring. Valence tautomerization was reversible, with the closed-shell Mn^V(O) complex being reformed upon addition of the appropriate reagent to sequester the Lewis/Brönsted acid (Scheme 4.1).

Scheme 4.1. Reversible Binding of Lewis/Bronsted Acids to Give Mn^{IV}(O-LA)($TBP_8Cz^{\bullet+}$) Complexes

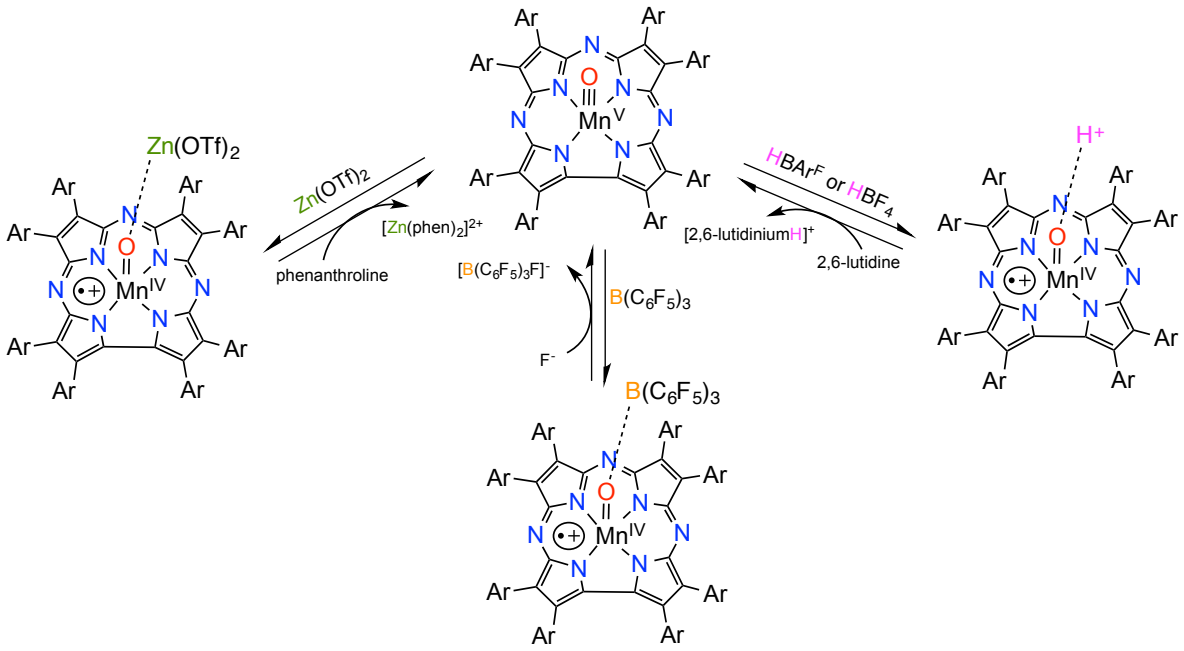

Although the Mn^{IV}(O–LA)($TBP_8Cz^{\bullet+}$) complexes are stable at 23 °C in dilute solution, attempts to isolate these complexes as solids results in autoreduction to Mn^{III}. Therefore we sought to obtain structural information on Mn^{IV}(O–LA)($TBP_8Cz^{\bullet+}$) in solution by X-ray Absorption Spectroscopy (XAS). XAS is incompatible with halogenated solvents because of large background fluorescence from the solvent, and we needed to find an alternative to the previously employed mixed solvent system CH_2Cl_2/CH_3CN. The Mn^{IV}(O–LA)($TBP_8Cz^{\bullet+}$)complexes were formed in benzonitrile by addition of Lewis acid to Mn^{V}(O)(TBP_8Cz), and the UV-vis spectral changes matched those seen in CH_2Cl_2/CH_3CN. The Mn K-edge X-ray absorption spectra for Mn^{V}(O)(TBP_8Cz) and Mn^{IV}(O–LA)($TBP_8Cz^{\bullet+}$) (LA = Zn^{II}, $B(C_6F_5)_3$) are shown in Figure 4.1. The XAS data for Mn^{V}(O)(TBP_8Cz) was reported previously,[24,48] but was re-measured here for comparison. The energy of the rising Mn K-edge is dependent on both

oxidation state and structure. The positions of the rising edge for the Lewis acid adducts are shifted to lower energy relative to $Mn^{V}(O)(TBP_8Cz)$. This shift is consistent with a lowering of the oxidation state on the metal, and the edge energies match well with other Mn^{IV} complexes.[13,49,50] The intensity of the pre-edge peaks for $Mn^{IV}(O–LA)(TBP_8Cz^{\bullet+})$ at ~6541.3 eV are significantly lower than the peak seen for $Mn^{V}(O)(TBP_8Cz)$ at 6541.6 eV. The pre-edge peak arises from a 1s-to-3d transition, and a decrease in intensity for this transition is consistent with a lengthening of the Mn–O bond, as can be expected from the binding of a Lewis acid to the terminal oxo ligand. Fitting of the EXAFS data (Figure 4.1) for the $Mn^{IV}(O–LA)(TBP_8Cz^{\bullet+})$ complexes gives 4 N/O scatterers at an average distance of 1.89 Å from the Mn, in good agreement with Mn–N bond distances for the pyrrole N atoms characterized by single crystal X-ray diffraction for Mn^{III} and $Mn^{V}(O)$ corrolazines.[24,31] Best fits of the data also required a fifth N/O scatterer at an average of 1.61 Å from the Mn center, which can be assigned to the terminal oxo group (Table 4.1). The Mn–O distance is elongated by 0.05 Å compared to the starting $Mn^{V}(O)$ which we reported as 1.56 Å in our previous EXAFS measurements[24] and 0.06 Å elongation compared to the distance determined by X-ray crystallography.[31] This change in bond distance is consistent with that seen for several other high-valent M-oxo-Lewis acid (M = Mn, Re, W) complexes, which show M–O bond elongations upon binding of LA in the range D(M–O) = 0.05 – 0.07 Å.[51-54] For best results, fits included an Mn–C scatterer at an average distance of 2.90 Å and a multiple scattering shell of Mn–N–C and Mn–C–N at 3.12 Å. Fits of the EXAFS data for $Mn^{IV}(O–Zn^{II})(TBP_8Cz^{\bullet+})$ were not significantly improved by inclusion of backscattering from the Zn ion. However, it is known that the observation of metal-metal scattering in related dimetallic porphyrin

systems such as Fe–L–Cu porphyrins (L = O^{2-}, OH^-), is highly dependent on the Fe–L–Cu angle.[55,56] An angle of ~180° leads to the observation of a strong metal-metal scatterer, while an angle of less than ~150° leads to no obvious metal-metal scatterer seen in the EXAFS spectrum. Density functional theory (DFT) calculations (vide infra) on $Mn^{IV}(O–Zn^{II})(TBP_8Cz^{\bullet+})$ suggest an Mn–O–Zn angle of <150°, consistent with the absence of metal-metal scattering in the EXAFS for this complex.

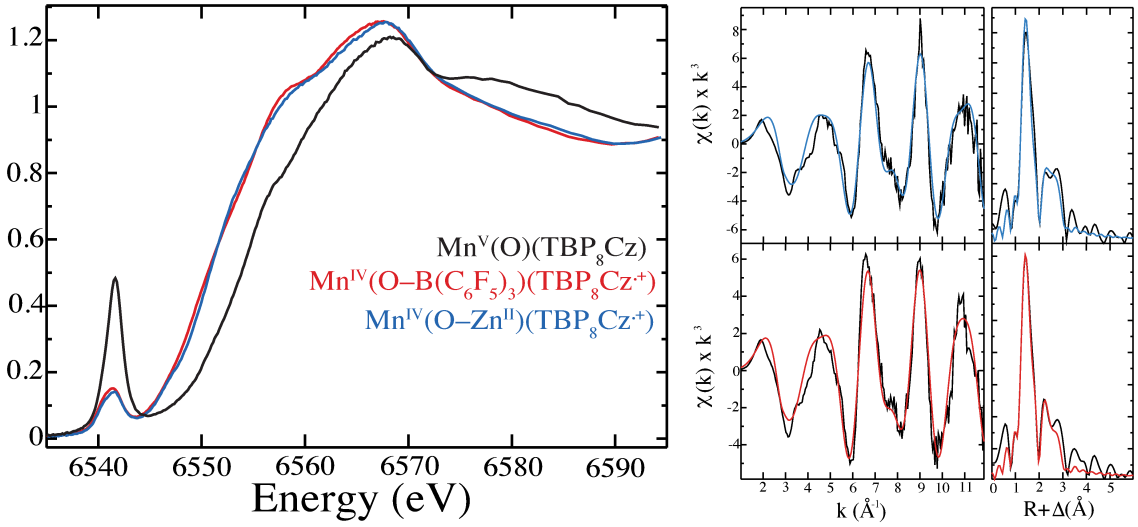

Figure 4.1. Left, Mn K-edge X-ray absorption spectra for $Mn^{V}(O)(TBP_8Cz)$ (black), $Mn^{IV}(O–LA)(TBP_8Cz^{\bullet+})$ (LA = $Zn(OTf)_2$ (blue), $B(C_6F_5)_3$ (red)) in benzonitrile. Right, EXAFS data of $Mn^{IV}(O–LA)(TBP_8Cz^{\bullet+})$ (LA = $Zn(OTf)_2$ (blue), $B(C_6F_5)_3$ (red)), data in black, best fits in color specified. Fit parameters of the best fits can be found in Table 4.1.

Table 4.1. EXAFS Best Fit Results for Mn^{IV}(O–LA)($TBP_8Cz^{\bullet+}$)

	LA = Zn^{2+}		LA = $B(C_6F_5)_3$	
	R (Å)	σ ($Å^2$)	R (Å)	σ ($Å^2$)
1 Mn–O	1.61	0.0174	1.61	0.0167
4 Mn–N	1.89	0.00195	1.89	0.00223
16 Mn–N–C	3.12	0.00455	3.13	0.00981
8 Mn–C	2.90	0.00384	2.89	0.00551
ΔE_0	-5.28		-6.84	
error	0.312		0.295	

In earlier work we employed DFT calculations to analyze the geometry of Mn^{IV}(O–Zn^{II})($TBP_8Cz^{\bullet+}$).[7] The optimized geometry of this complex exhibited an elongated Mn–O bond distance of 1.74 Å and a Zn–O distance of 1.89 Å. The Mn–O bond length is ~0.1 Å longer than the Mn–O distance found experimentally by EXAFS, and therefore further calculations were performed in this work. Geometry optimizations were carried out using different functional and basis set combinations, and the geometries were not sensitive to the choice of functional/basis set (Appendix X). Singlet, triplet, and quintet spin states for Mn^{IV}(O–LA)($TBP_8Cz^{\bullet+}$) (LA = Zn^{II} and $B(C_6F_5)_3$) were all assessed. A calculated Mn–O distance of 1.65 – 1.66 Å is found for the respective triplet states, corresponding to one unpaired spin on the Mn^{IV} ion and one unpaired spin on the Cz ring ($d_\pi^1 a''^1$ configuration). This distance is reasonably close to the experimentally determined value from EXAFS. The calculated Mn–O distances for the other triplet and quintet states examined were not as good a match with the experimental value. The

calculations also suggest that the quintet state ($d_{xy}^1 d_{xz}^1 d_{yz}^1 a''^1$) is the ground state, being ~1-5 kcal/mol in energy below the former triplet state, depending on the functional and basis set. However, DFT is known to have significant difficulty in determining the energy ordering of multiple spin states in transition metal complexes, especially in Mn.[57-60] The singlet states were found to be the highest in energy, but did show Mn–O distances close to the XAS value. However, the singlet states are not consistent with the experimentally determined paramagnetic π-cation-radical complexes, and can be ruled out. Interestingly, surface scans along the Mn–O distance for the triplet states reveal surfaces that are energetically flat (Appendix C). The Mn–O distances were varied over 0.1 Å, but the relative energies changed by only ~1 kcal/mol. The surface scans suggest that the Mn–O bond is relatively loose compared to the $Mn^{V}(O)$ starting material. Based on these results, we tentatively assign $Mn^{IV}(O–LA)(TBP_8Cz^{\bullet+})$ to the triplet state with a $d_\pi^1 a''^1$ configuration.[61,62]

4.3.2. Reactivity with C–H bonds

The reactivity of $Mn^{IV}(O–LA)(TBP_8Cz^{\bullet+})$ complexes with the C–H substrate xanthene (Xn) (Chart 4.1) was examined for the series of Lewis acids shown in Table 2. The $Mn^{IV}(O–LA)(TBP_8Cz^{\bullet+})$ complexes with LA = $Zn(OTf)_2$, $B(C_6F_5)_3$, and $HBAr^F$ were characterized previously.[7,8,10] A recent report from Abu-Omar showed that TFA reacts with an $Mn^{V}(O)$ corrole, $Mn^{V}(O)$(tpfc), to stabilize the analogous $Mn^{IV}(OH)(tpfc^{\bullet+})$ valence tautomer, and the HAT reactivity of this species was examined with phenol O–H substrates.[14] We included TFA in the current study to provide a direct comparison with the corrole system. The characteristic spectral changes for the valence tautomer $Mn^{IV}(O–TFA)(TBP_8Cz^{\bullet+})$ were observed following the addition of TFA to $Mn^{V}(O)(TBP_8Cz)$

(Figure 4.2). Addition of Xn to the Mn^{IV}(O–LA)($TBP_8Cz^{\bullet+}$) complexes was carried out in CH_2Cl_2 at 23 °C, and the reaction was monitored by UV-vis. Representative data for the reaction of Mn^{IV}(O–$B(C_6F_5)_3$)($TBP_8Cz^{\bullet+}$) with Xn is shown in Figure 4.3a. The features for the Mn complex (419, 789 nm) undergo isosbestic conversion to a new species (443, 727 nm) over 30 min. The final spectrum is indicative of [Mn^{IV}(TBP_8Cz)(OH)].[7,8,26] Similar spectral changes were seen for the other LA complexes. The final reaction mixtures were examined by EPR spectroscopy (X-band, 12 K), and revealed intense spectra typical of a high-spin Mn^{IV} (S = 3/2) ion, and quite similar to the spectra seen for other Mn^{IV} corrolazines (Figure 4.4 and Figure 4.5).[8,26] Taken together, the UV-vis and EPR data indicate that the reaction of the open shell valence tautomer with the C–H bond substrate Xn yields a one electron-reduced Mn^{IV} corrolazine, and implicates a single hydrogen-atom transfer event.

Chart 4.1

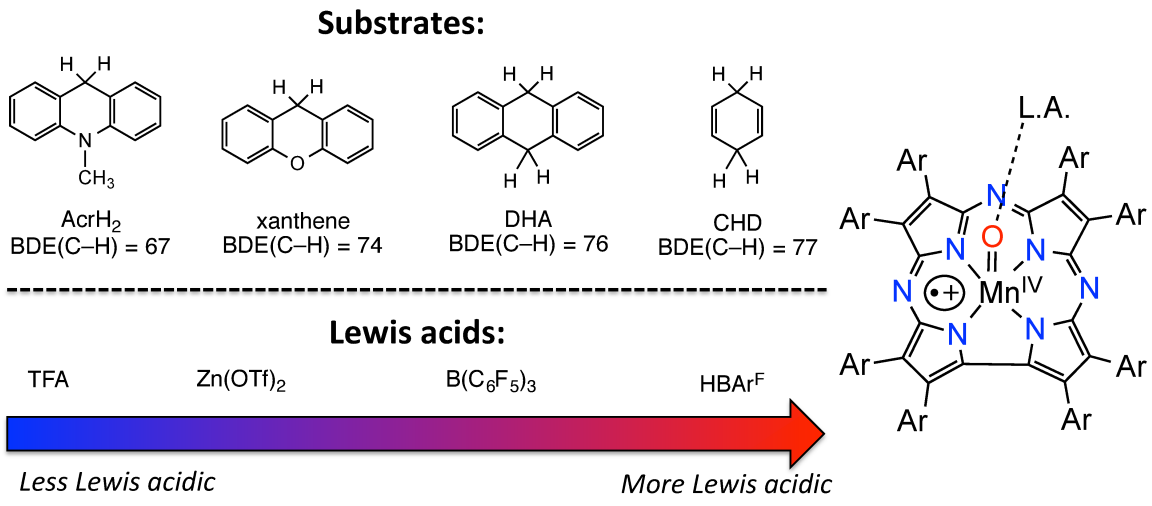

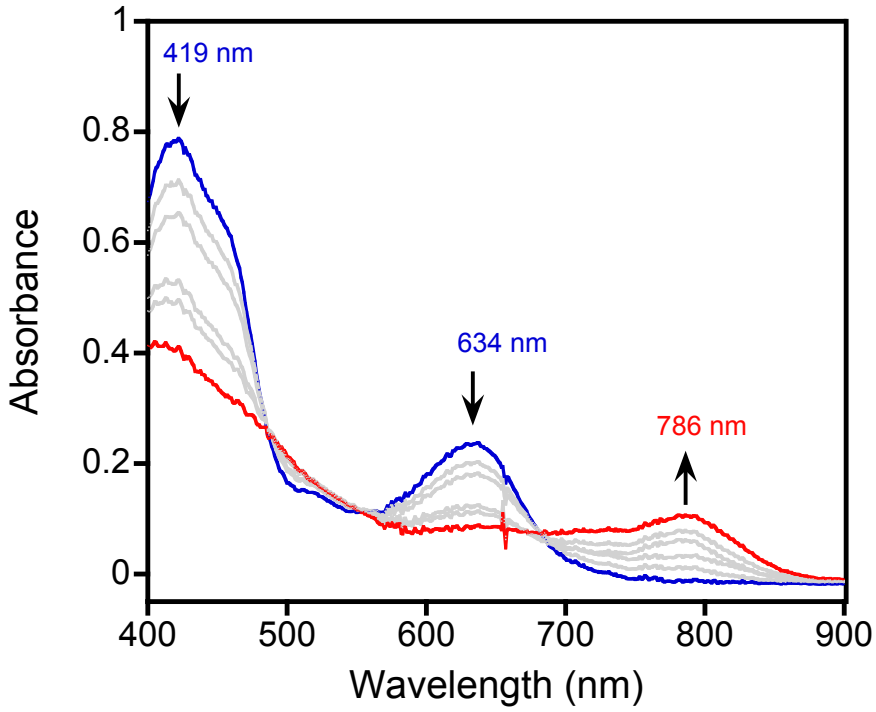

Figure 4.2. Reaction of $Mn^{V}(O)(TBP_8Cz)$ (15.6 µM) with TFA (1 equiv) in CH_2Cl_2

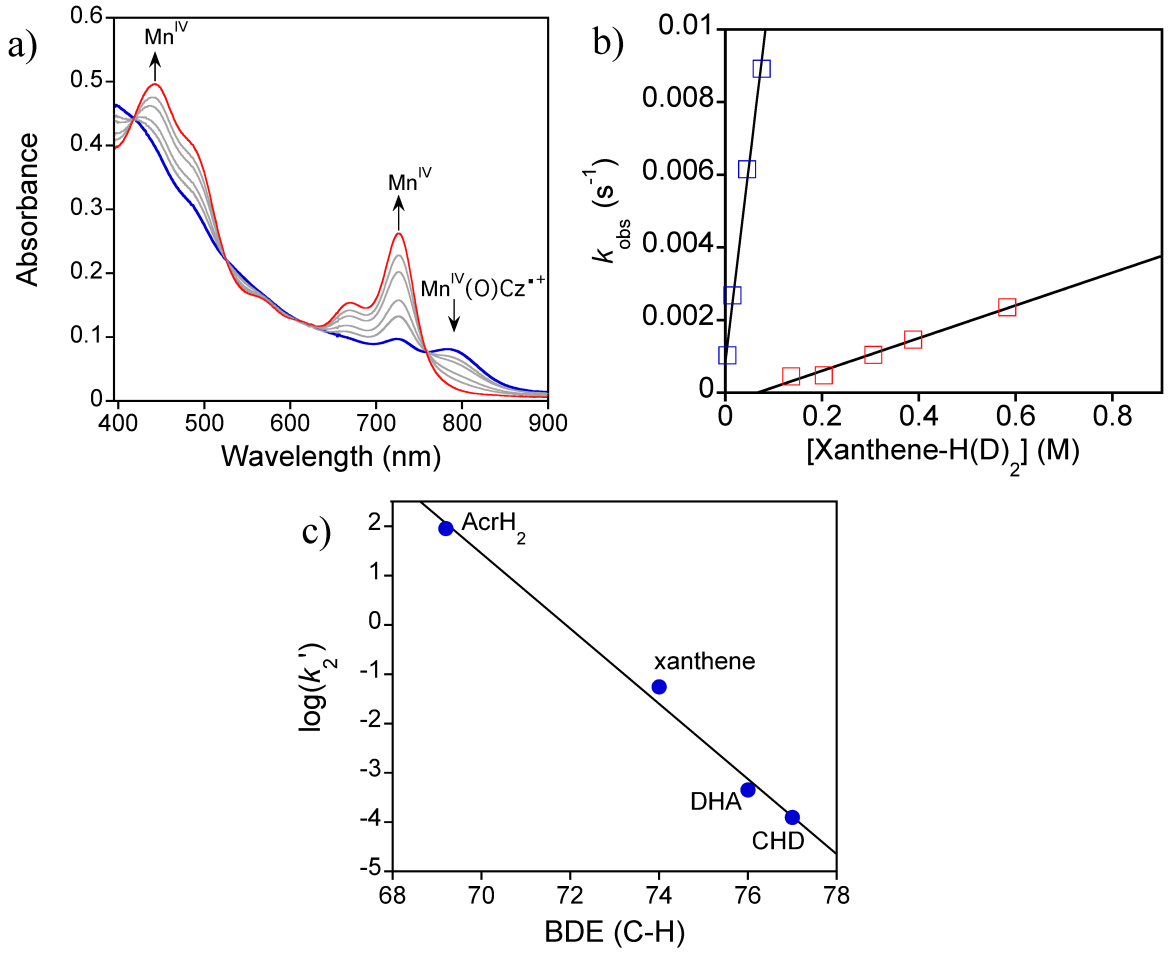

Figure 4.3. a) Time-resolved UV-vis spectra (0 – 30 min) for the reaction of Mn^{IV}(O–$B(C_6F_5)_3$)($TBP_8Cz^{\bullet+}$) (14 µM) with excess xanthene in CH_2Cl_2 at 23 °C. b) Second-order plots for xanthene (blue squares) and xanthene-d_2 (red squares) with Mn^{IV}(O–$B(C_6F_5)_3$)($TBP_8Cz^{\bullet+}$). KIE = k_H/k_D = 25 ± 2. c) Dependence of the log k values for Mn^{IV}(O–$B(C_6F_5)_3$)($TBP_8Cz^{\bullet+}$) on the BDE values of the scissile C–H bond. Slope($B(C_6F_5)_3$) = - 0.76 ± 0.05.

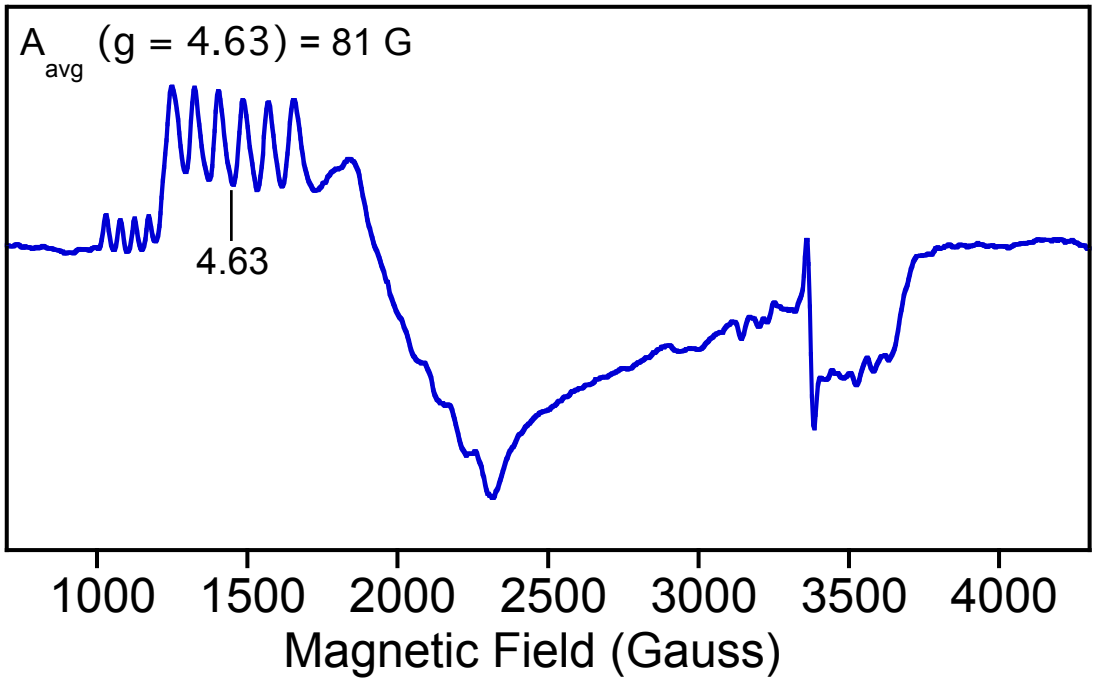

Figure 4.4. X-band EPR spectrum at 12 K for the reaction of Mn^{IV}(O–$B(C_6F_5)_3$)($TBP_8Cz^{\bullet+}$) (1.0 mM) with xanthene (100 equiv) (blue line) in CH_2Cl_2.

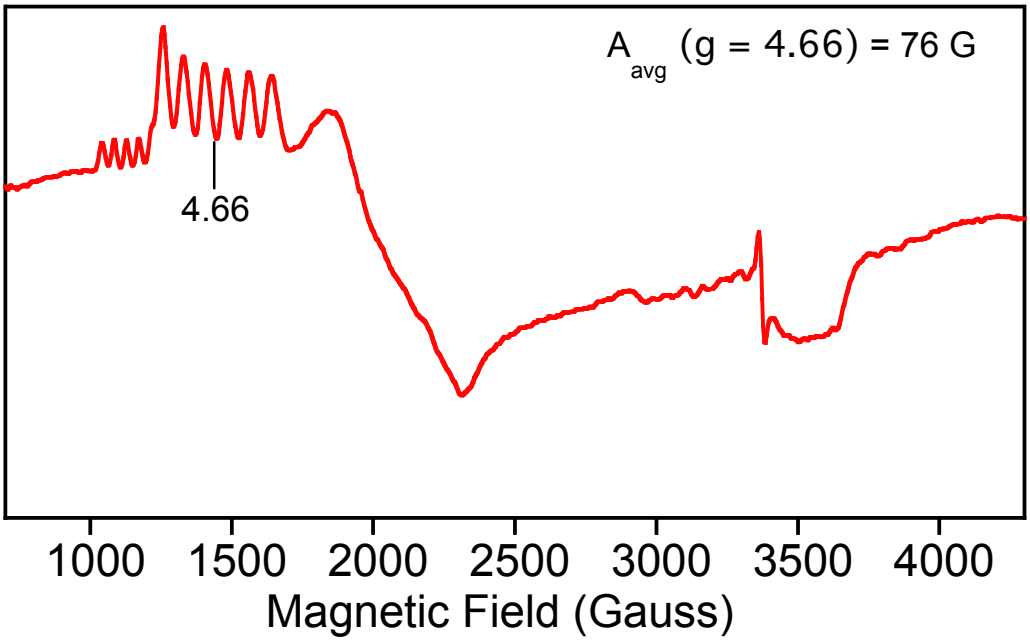

Figure 4.5. X-band EPR spectrum at 12 K for the reaction of Mn^{IV}(O–$HBAr^F$)($TBP_8Cz^{\bullet+}$) (1.0 mM) with xanthene (100 equiv) (blue line) in CH_2Cl_2.

The rates of reaction of Mn^{IV}(O–LA)($TBP_8Cz^{\bullet+}$) with Xn were obtained from plots of absorbance versus time, which were well-fit with a single exponential expression and gave the pseudo-first-order rate constants (k_{obs}). Measurement of k_{obs} versus [Xn] led to linear plots as shown in Figure 4.3b, whose slope, when normalized per reactive C–H bond n, (n = 2 for Xn), gave the second-order rate constants (k_2') shown in Table 4.2. These rate constants were compared to the reaction of the closed-shell Mn^{V}(O) valence tautomer in the absence of Lewis acids (Table 4.2, column 3). As can be seen from the k_{LA}/k_{none} values, there is a significant increase in the rate of C–H cleavage for LA = Zn^{II}, $B(C_6F_5)_3$, $HBAr^F$. Rate enhancements were seen previously for Mn^{IV}(O–LA)($TBP_8Cz^{\bullet+}$) (LA = Zn^{II}, $B(C_6F_5)_3$) in similar HAT reactions with substituted phenol O–H substrates, with the more Lewis acidic triarylborane giving the more reactive species. We have

quantified the Lewis acidity of the LAs in Table 4.2 with the Gutmann-Beckett method, in which the ^{31}P NMR chemical shifts of Et_3PO are measured in the presence of the different Lewis acids.[29,30] This method leads to the acceptor numbers (A.N.) shown in Table 4.2, with the higher A.N. values indicating greater Lewis acidity. As seen in Table 4.2, the second-order rate constants follow an overall correlation with the A.N. values, although the triarylborane gives a slightly larger k_2' value for the Xn substrate than $HBAr^F$. Interestingly, the only Lewis acid that did not accelerate the C–H cleavage rate was TFA. In the work by Abu-Omar, addition of TFA also slightly decreased the H-atom abstraction rate for the corrole complex, although no other Lewis acids were tested in this study.[14] Our results strongly suggest that the identity of the Lewis acid is critical in determining the HAT reactivity of Mn^{IV}(O–LA)(π-cation-radical) complexes (vide infra).

Table 4.2. Second-order rate constants (k_2') (normalized per reactive C–H bond) for the reaction of Mn^{IV}(O–LA)($TBP_8Cz^{\bullet+}$) with H-atom donor substrates. Units (k_2') = M^{-1} s^{-1}.

Lewis acid (A.N.[a])	xanthene	k_{LA}/k_{non}	DHA[b]	CHD[c]
		e (Xn)		
none (n/a)[63,64]	$1.8 \pm 0.2 \times 10^{-3}$	-	$1.8 \pm 0.5 \times 10^{-5}$	$3.3 \pm 0.1 \times 10^{-5}$
TFA (40)	$9 \pm 1 \times 10^{-4}$	0.5	-	-
$Zn(OTf)_2$ (68)	$8.1 \pm 0.4 \times 10^{-3}$	4	-	-
$HBAr^F$ (102)	$1.9 \pm 0.2 \times 10^{-2}$	10	$6.7 \pm 0.1 \times 10^{-4}$	$2.0 \pm 0.1 \times 10^{-4}$
$B(C_6F_5)_3$ (82)	$5.5 \pm 0.3 \times 10^{-2}$	28	$4.3 \pm 0.2 \times 10^{-4}$	$1.3 \pm 0.8 \times 10^{-4}$

[a]A.N. = acceptor number. [b]DHA = 9,10-dihydroanthracene. [c]CHD = 1,4-cyclohexadiene.

Examination of two of the Mn^{IV}(O–LA)($TBP_8Cz^{\bullet+}$) species with Xn-d_2 revealed large KIEs (k_H/k_D = 25 for $B(C_6F_5)_3$ (Figure 4.3b), k_H/k_D = 27 for $HBAr^F$), both well above the classical limit. A KIE for this substrate with Mn^{V}(O)(TBP_8Cz) could not be obtained because of very slow reaction rates and the limited solubility of Xn at high concentrations. Previously a classical KIE = 3.2 was observed for O–H versus O–D cleavage with Mn^{IV}(O–LA)($TBP_8Cz^{\bullet+}$) and 2,4,6-tri-*tert*-butylphenol (2,4,6-TTBP).[8] The KIE values indicate that HAT is the rate-limiting step for both O–H and C–H substrates. The KIEs for C–H cleavage are also much larger than that observed for the axially ligated $[Mn^{V}(O)(TBP_8Cz)(X)]^{-}$ (X = anionic donor), (KIE(C–H) = 11), or for O–H cleavage by the 5-coordinate Mn^{V}(O)(TBP_8Cz) (KIE(O–H) = 6).[63,65] The corrole complex (Mn^{IV}(OH)($tpfc^{\bullet+}$) exhibited a particularly small KIE = 1.3 for HAT with 2,4-di-tert-butylphenol.[14] The large non-classical KIEs for Mn^{IV}(O–LA)($TBP_8Cz^{\bullet+}$) with C–H substrate suggests that significant tunneling may be occurring through the HAT barrier. Further work is needed to determine the origin of the wide range in KIEs observed for the different corrolazine and corrole complexes.

The stoichiometry for the oxidation of C–H bond substrates by Mn^{IV}(O–LA)($TBP_8Cz^{\bullet+}$) was further examined by product analysis for the reaction with 9,10-dihydroanthracene (DHA) as substrate. DHA reacts with Mn^{IV}(O–LA)($TBP_8Cz^{\bullet+}$) in CH_2Cl_2 to give the one-electron-reduced Mn^{IV} product, as seen by UV-vis. Analysis of a bulk reaction for Mn^{IV}(O–$B(C_6F_5)_3$)($TBP_8Cz^{\bullet+}$) plus DHA gave a 65% yield of the expected dehydrogenated anthracene product by GC-FID, following the stoichiometry in Scheme 4.2. Based on this stoichiometry, a mechanism is proposed where the first H-atom abstraction gives DHA radical (DHA•), which is then rapidly dehydrogenated by

another Mn^{IV}(O–LA)($TBP_8Cz^{\bullet+}$) via a second H-atom abstraction. The stoichiometry contrasts that found for the closed-shell Mn^{V}(O)(TBP_8Cz), which functions as a two-electron oxidant and abstracts both H-atoms from a single DHA, producing one anthracene molecule per Mn^{V}(O) complex.[63,65] The former stoichiometry also fundamentally differs from the analogous corrole Mn^{IV}(OH)($tpfc^{\bullet+}$), which acts as a two-electron oxidant with phenol substrates to give two equivalents of phenoxyl radical and one equivalent of Mn^{III} corrole.[14]

Scheme 4.2. Comparison of Reaction Stoichiometries for Mn^{V}(O)(TBP_8Cz) versus Mn^{IV}(O–LA)($TBP_8Cz^{\bullet+}$)

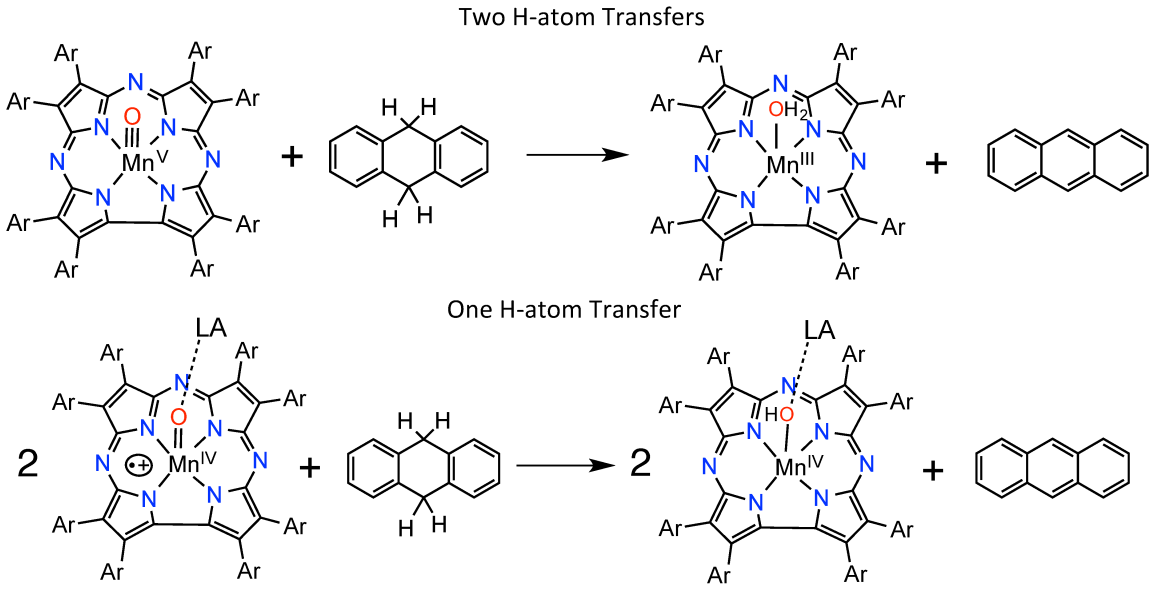

The most reactive species with Xn is Mn^{IV}(O–$B(C_6F_5)_3$)($TBP_8Cz^{\bullet+}$), and therefore we examined reaction kinetics of this species with the additional C–H substrates $AcrH_2$, DHA, and CHD (Figure 4.3c) to gain further insight into the nature of the HAT reactions and their dependence on substrate C–H bond strength.[66] Similar reaction conditions were used as compared to Xn, and good pseudo-first-order kinetics were observed by UV-vis, showing conversion of Mn^{IV}(O–$B(C_6F_5)_3$)($TBP_8Cz^{\bullet+}$) into the one-electron-reduced Mn^{IV}

product for all substrates except the $AcrH_2$, which gives an Mn^{III} product. However, $AcrH_2$ is well-known to act as a hydride donor by initial H• abstraction followed by fast electron transfer.[26] Normalized second-order rate constants (k_2') for each substrate were obtained from plots of k_{obs} versus substrate concentration, and a plot of log(k_2') versus C–H bond strength is shown in Figure 4.3c. The linear relationship seen provides good support for the proposed mechanism involving a concerted HAT step as the rate-determining step.[66,67] Second-order kinetics for DHA and CHD were also obtained for $HBAr^F$, and also gave a linear correlation between log(k_2') and BDE(C–H) (Figure 4.6). Similar correlations with the BDE(C–H) of C–H substrates have been observed for both $Mn^V(O)(Cz)$ and $Fe^{IV}(O)(Cz^{\bullet+})$ species, implicating concerted HAT mechanisms.[65,68]

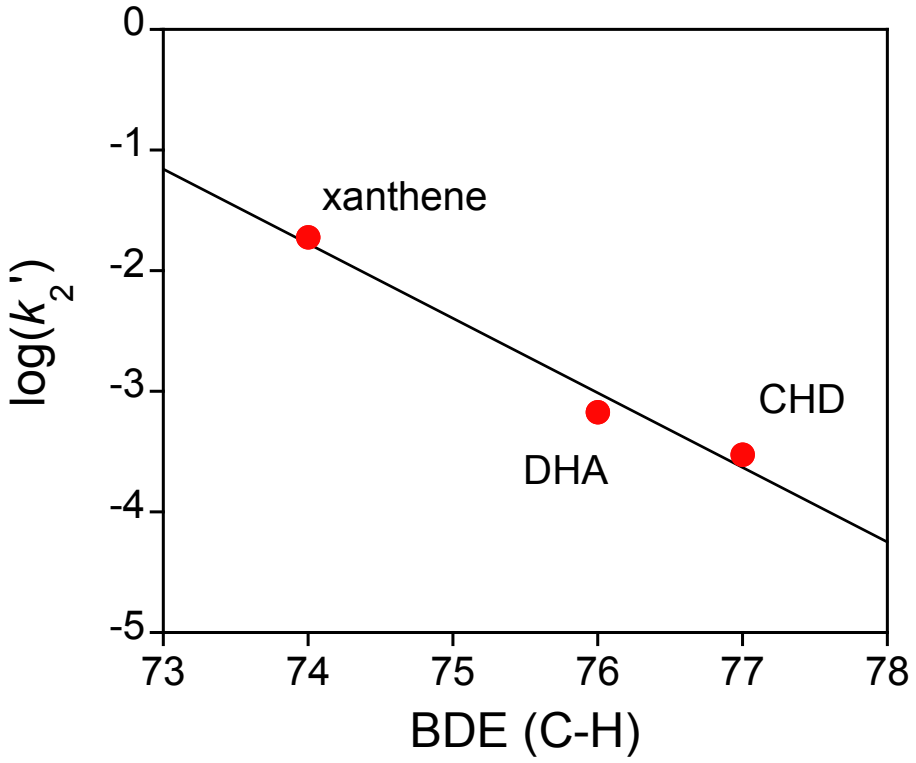

Figure 4.6. Dependence of the log *k* values for $Mn^{IV}(O–HBAr^F)(TBP_8Cz^{\bullet+})$ on the BDE values of the scissile C–H bond. Slope($HBAr^F$) = -0.61 ± 0.09.

As reported by Abu-Omar, the corrole species $Mn^{IV}(OH)(tpfc^{\bullet+})$, generated by addition of TFA to $Mn^{V}(O)(tpfc)$, is a close analog of $Mn^{IV}(O–LA)(TBP_8Cz^{\bullet+})$. It was concluded that the reactivity of the $Mn^{IV}(OH)(tpfc^{\bullet+})$ valence tautomer was strikingly different from the corrolazine analog, because of the stoichiometry of phenol oxidation and the lack of any rate enhancement in HAT compared to the $Mn^{V}(O)$ precursor. However, at the time of this study there was no information available on the corrolazine system with TFA as the Lewis acid. We have now examined the influence of TFA for the corrolazine case, and have found a remarkable similarity with the corrole results. The TFA adduct actually exhibits a slight deceleration in the rate of HAT for C–H bonds, as opposed to the other Lewis acids, all of which lead to rate enhancements. We speculate that there is little electronic effect on the HAT rate because TFA is such a weak Lewis acid, and the slight rate deceleration compared to the starting $Mn^{V}(O)$ may be due to a small steric inhibition from TFA. There does remain a significant difference in the stoichiometry of HAT between the corrolazine and corrole complexes in the presence of TFA, with the Cz complex functioning as a one-electron oxidant while the corrole complex functions as a two-electron oxidant. This difference suggests that the Mn^{IV} product following HAT is more stable in the Cz case.

The influence of Lewis acids on nonheme $M^{IV}(O)(N4Py)$ (M = Mn, Fe) has been investigated by Fukuzumi and Nam, and both rate accelerations and decelerations have been reported for C–H cleavage reactions.[18-20,69,70] Rate enhancements are observed if the driving force of electron-transfer between the metal-oxo/Lewis acid adduct and the C–H substrate is reasonably favorable, as in the case of toluene derivatives as substrates.[18,70] For these substrates, the mechanism of C–H cleavage is described as proton-coupled

electron-transfer (PCET), where rate-limiting ET controls the kinetics and no KIE (i.e. KIE ~ 1) for C–H/C–D is observed. In contrast, rate decelerations are observed when the redox potential of the substrate makes ET highly endergonic, such as for CHD.[19,20] An HAT mechanism is proposed for these substrates, and the lower reactivity is assigned to steric inhibition caused by the Lewis acid group.

For our corrolazine system, the data clearly point to an HAT mechanism, and steric inhibition is not a significant factor. The dominant influence over the reactivity is the strength of the Lewis acid, with stronger Lewis acids leading to much higher reaction rates for HAT by Mn^{IV}(O–LA)($TBP_8Cz^{\bullet+}$) as compared to Mn^{V}(O)(TBP_8Cz). Furthermore, the high spin nature of the open-shell Mn^{IV}(O–LA)($TBP_8Cz^{\bullet+}$) does not appear to be the source of the enhanced reactivity, because the TFA derivatives for both corrolazine and corrole show a decrease in HAT reaction rates. The reactivity of these heme-like metal-oxo Lewis acid adducts appear to be controlled by the strength of the Lewis acid.

4.4. Conclusions

We have characterized the valence tautomer Mn^{IV}(O–LA)($TBP_8Cz^{\bullet+}$) by XAS, which confirmed the metal oxidation state is Mn^{IV} and showed that the Mn–O bond is elongated as compared to the Mn^{V}(O) complex. The Mn^{IV}(O–LA)($TBP_8Cz^{\bullet+}$) complexes are able to cleave the C–H bonds in activated C–H substrates, and the reaction rates are dependent on C–H bond strength. These results together with large KIEs indicate C–H cleavage goes by an HAT mechanism. The strength of the Lewis acid in these complexes can change the rates of HAT by almost 30-fold. The change in electronic configuration for Mn^{IV}(O–LA)($TBP_8Cz^{\bullet+}$) versus Mn^{V}(O)(TBP_8Cz) does not necessarily lead to

enhanced reactivity of C–H cleavage, but rather the HAT reactivity appears to be dominated by the identity of the Lewis acid. These results suggest that careful tuning of high-valent metal-oxo reactivity in a heme protein environment could be controlled by appropriately timed proton delivery or H-bonding to the metal-oxo unit.

4.5. References

(1) Rittle, J.; Green, M. T. Cytochrome P450 Compound I: Capture, Characterization, and C-H Bond Activation Kinetics. *Science* **2010**, *330*, 933-937.

(2) Denisov, I. G.; Makris, T. M.; Sligar, S. G.; Schlichting, I. Structure and chemistry of cytochrome P450. *Chem. Rev.* **2005**, *105*, 2253-2278.

(3) Poulos, T. L. Heme Enzyme Structure and Function. *Chem. Rev.* **2014**, *114*, 3919-3962.

(4) Weiss, R.; Bulach, V.; Gold, A.; Terner, J.; Trautwein, A. X. Valence-tautomerism in high-valent iron and manganese porphyrins. *J. Biol. Inorg. Chem.* **2001**, *6*, 831-845.

(5) Evangelio, E.; Ruiz-Molina, D. Valence Tautomerism: New Challenges for Electroactive Ligands. *Eur. J. Inorg. Chem.* **2005**, *2005*, 2957-2971.

(6) Chirik, P. J. Preface: Forum on Redox-Active Ligands. *Inorg. Chem.* **2011**, *50*, 9737-9740.

(7) Leeladee, P.; Baglia, R. A.; Prokop, K. A.; Latifi, R.; de Visser, S. P.; Goldberg, D. P. Valence Tautomerism in a High-Valent Manganese-Oxo Porphyrinoid Complex Induced by a Lewis Acid. *J. Am. Chem. Soc.* **2012**, *134*, 10397-10400.

(8) Baglia, R. A.; Dürr, M.; Ivanović-Burmazović, I.; Goldberg, D. P. Activation of a High-Valent Manganese-Oxo Complex by a Nonmetallic Lewis Acid. *Inorg. Chem.* **2014**, *53*, 5893-5895.

(9) Zaragoza, J. P. T.; Baglia, R. A.; Siegler, M. A.; Goldberg, D. P. Strong Inhibition of O-Atom Transfer Reactivity for MnIV(O)(π-Radical-Cation)(Lewis Acid) versus MnV(O) Porphyrinoid Complexes. *J. Am. Chem. Soc.* **2015**, *137*, 6531-6540.

(10) Neu, H. M.; Jung, J.; Baglia, R. A.; Siegler, M. A.; Ohkubo, K.; Fukuzumi, S.; Goldberg, D. P. Light-Driven, Proton-Controlled, Catalytic Aerobic C-H Oxidation Mediated by a Mn(III) Porphyrinoid Complex. *J. Am. Chem. Soc.* **2015**, *137*, 4614-4617.

(11) Cong, Z.; Kurahashi, T.; Fujii, H. Formation of Iron(III) meso-Chloro-isoporphyrin as a Reactive Chlorinating Agent from Oxoiron(IV) Porphyrin π-Cation Radical. *J. Am. Chem. Soc.* **2012**, *134*, 4469-4472.

(12) Boaz, N. C.; Bell, S. R.; Groves, J. T. Ferryl Protonation in Oxoiron(IV) Porphyrins and Its Role in Oxygen Transfer. *J. Am. Chem. Soc.* **2015**, *137*, 2875-2885.

(13) Kurahashi, T.; Kikuchi, A.; Tosha, T.; Shiro, Y.; Kitagawa, T.; Fujii, H. Transient Intermediates from Mn(salen) with Sterically Hindered Mesityl Groups: Interconversion between MnIV-Phenolate and MnIII-Phenoxyl Radicals as an Origin for Unique Reactivity. *Inorg. Chem.* **2008**, *47*, 1674-1686.

(14) Bougher, C. J.; Liu, S.; Hicks, S. D.; Abu-Omar, M. M. Valence Tautomerization of High-Valent Manganese(V)-Oxo Corrole Induced by Protonation of the Oxo Ligand. *J. Am. Chem. Soc.* **2015**, *137*, 14481-14487.

(15) Umena, Y.; Kawakami, K.; Shen, J.-R.; Kamiya, N. Crystal structure of oxygen-evolving photosystem II at a resolution of 1.9 Å. *Nature* **2011**, *473*, 55-60.

(16) Tsui, E. Y.; Tran, R.; Yano, J.; Agapie, T. Redox-inactive metals modulate the reduction potential in heterometallic manganese-oxido clusters. *Nat Chem* **2013**, *5*, 293-299.

(17) Suga, M.; Akita, F.; Hirata, K.; Ueno, G.; Murakami, H.; Nakajima, Y.; Shimizu, T.; Yamashita, K.; Yamamoto, M.; Ago, H.; Shen, J.-R. Native structure of photosystem II at 1.95 A resolution viewed by femtosecond X-ray pulses. *Nature* **2015**, *517*, 99-103.

(18) Park, J.; Morimoto, Y.; Lee, Y.-M.; Nam, W.; Fukuzumi, S. Unified View of Oxidative C-H Bond Cleavage and Sulfoxidation by a Nonheme Iron(IV)-Oxo Complex via Lewis Acid-Promoted Electron Transfer. *Inorg. Chem.* **2014**, *53*, 3618-3628.

(19) Chen, J.; Lee, Y.-M.; Davis, K. M.; Wu, X.; Seo, M. S.; Cho, K.-B.; Yoon, H.; Park, Y. J.; Fukuzumi, S.; Pushkar, Y. N.; Nam, W. A Mononuclear Non-Heme Manganese(IV)-Oxo Complex Binding Redox-Inactive Metal Ions. *J. Am. Chem. Soc.* **2013**, *135*, 6388-6391.

(20) Chen, J.; Yoon, H.; Lee, Y.-M.; Seo, M. S.; Sarangi, R.; Fukuzumi, S.; Nam, W. Tuning the reactivity of mononuclear nonheme manganese(iv)-oxo complexes by triflic acid. *Chem. Sci.* **2015**, *6*, 3624-3632.

(21) Dong, L.; Wang, Y.; Lv, Y.; Chen, Z.; Mei, F.; Xiong, H.; Yin, G. Lewis-Acid-Promoted Stoichiometric and Catalytic Oxidations by Manganese Complexes Having Cross-Bridged Cyclam Ligand: A Comprehensive Study. *Inorg. Chem.* **2013**, *52*, 5418-5427.

(22) Lam, W. W. Y.; Yiu, S.-M.; Lee, J. M. N.; Yau, S. K. Y.; Kwong, H.-K.; Lau, T.-C.; Liu, D.; Lin, Z. BF3-Activated Oxidation of Alkanes by MnO4. *J. Am. Chem. Soc.* **2006**, *128*, 2851-2858.

(23) Cook, S. A.; Borovik, A. S. Molecular Designs for Controlling the Local Environments around Metal Ions. *Acc. Chem. Res.* **2015**, *48*, 2407-2414.

(24) Lansky, D. E.; Mandimutsira, B.; Ramdhanie, B.; Clausén, M.; Penner-Hahn, J.; Zvyagin, S. A.; Telser, J.; Krzystek, J.; Zhan, R.; Ou, Z.; Kadish, K. M.; Zakharov, L.; Rheingold, A. L.; Goldberg, D. P. Synthesis, Characterization, and Physicochemical Properties of Manganese(III) and Manganese(V)-Oxo Corrolazines. *Inorg. Chem.* **2005**, *44*, 4485-4498.

(25) Jutzi, P.; Müller, C.; Stammler, A.; Stammler, H.-G. Synthesis, Crystal Structure, and Application of the Oxonium Acid [H(OEt2)2]+[B(C6F5)4]. *Organometallics* **2000**, *19*, 1442-1444.

(26) Fukuzumi, S.; Kotani, H.; Prokop, K. A.; Goldberg, D. P. Electron- and Hydride-Transfer Reactivity of an Isolable Manganese(V)-Oxo Complex. *J. Am. Chem. Soc.* **2011**, *133*, 1859-1869.

(27) Goldsmith, C. R.; Jonas, R. T.; Stack, T. D. P. C-H Bond Activation by a Ferric Methoxide Complex: Modeling the Rate-Determining Step in the Mechanism of Lipoxygenase. *J. Am. Chem. Soc.* **2002**, *124*, 83-96.

(28) Neese, F. The ORCA program system. *Wiley Interdiscip. Rev.: Comput. Mol. Sci.* **2012**, *2*, 73-78.

(29) Mayer, U.; Gutmann, V.; Gerger, W. The acceptor number - A quantitative empirical parameter for the electrophilic properties of solvents. *Monatsh. Chem.* **1975**, *106*, 1235-1257.

(30) Beckett, M. A.; Strickland, G. C.; Holland, J. R.; Sukumar Varma, K. A convenient n.m.r. method for the measurement of Lewis acidity at boron centres: correlation of

reaction rates of Lewis acid initiated epoxide polymerizations with Lewis acidity. *Polymer* **1996**, *37*, 4629-4631.

(31) Baglia, R. A.; Prokop-Prigge, K. A.; Neu, H. M.; Siegler, M. A.; Goldberg, D. P. Mn(V)(O) versus Cr(V)(O) Porphyrinoid Complexes: Structural Characterization and Implications for Basicity Controlling H-Atom Abstraction. *J. Am. Chem. Soc.* **2015**, *137*, 10874-10877.

(32) Lee, C.; Yang, W.; Parr, R. G. Development of the Colle-Salvetti correlation-energy formula into a functional of the electron density. *Phys. Rev. B* **1988**, *37*, 785-789.

(33) Grimme, S.; Antony, J.; Ehrlich, S.; Krieg, H. A consistent and accurate ab initio parametrization of density functional dispersion correction (DFT-D) for the 94 elements H-Pu. *J. Chem. Phys.* **2010**, *132*, 154104.

(34) Hay, P. J.; Wadt, W. R. Ab initio effective core potentials for molecular calculations. Potentials for K to Au including the outermost core orbitals. *J. Chem. Phys.* **1985**, *82*, 299-310.

(35) Hay, P. J.; Wadt, W. R. Ab initio effective core potentials for molecular calculations. Potentials for the transition metal atoms Sc to Hg. *J. Chem. Phys.* **1985**, *82*, 270-283.

(36) Feller, D. The role of databases in support of computational chemistry calculations. *J. Comput. Chem.* **1996**, *17*, 1571-1586.

(37) Wadt, W. R.; Hay, P. J. Ab initio effective core potentials for molecular calculations. Potentials for main group elements Na to Bi. *J. Chem. Phys.* **1985**, *82*, 284-298.

(38) Schuchardt, K. L.; Didier, B. T.; Elsethagen, T.; Sun, L.; Gurumoorthi, V.; Chase, J.; Li, J.; Windus, T. L. Basis Set Exchange: A Community Database for Computational Sciences. *J. Chem. Inf. Model.* **2007**, *47*, 1045-1052.

(39) Hehre, W. J.; Ditchfield, R.; Pople, J. A. Self-Consistent Molecular Orbital Methods. XII. Further Extensions of Gaussian-Type Basis Sets for Use in Molecular Orbital Studies of Organic Molecules. *J. Chem. Phys.* **1972**, *56*, 2257-2261.

(40) Hariharan, P. C.; Pople, J. A. The influence of polarization functions on molecular orbital hydrogenation energies. *Theor. Chim. Acta* **1973**, *28*, 213-222.

(41) van Wüllen, C. Molecular density functional calculations in the regular relativistic approximation: Method, application to coinage metal diatomics, hydrides, fluorides and

chlorides, and comparison with first-order relativistic calculations. *J. Chem. Phys.* **1998**, *109*, 392-399.

(42) Pantazis, D. A.; Chen, X.-Y.; Landis, C. R.; Neese, F. All-Electron Scalar Relativistic Basis Sets for Third-Row Transition Metal Atoms. *J. Chem. Theory Comput.* **2008**, *4*, 908-919.

(43) The Ahlrichs (2df,2pd) polarization functions were obtained from the TurboMole basis set library under ftp.chemie.uni-karlsruhe.de/pub/basen.

(44) Perdew, J. P. Density-functional approximation for the correlation energy of the inhomogeneous electron gas. *Phys. Rev. B* **1986**, *33*, 8822-8824.

(45) Becke, A. D. Density-functional exchange-energy approximation with correct asymptotic behavior. *Phys. Rev. A* **1988**, *38*, 3098-3100.

(46) Dolg, M.; Wedig, U.; Stoll, H.; Preuss, H. Energy-adjusted abinitio pseudopotentials for the first row transition elements. *J. Chem. Phys.* **1987**, *86*, 866-872.

(47) Perdew, J. P.; Burke, K.; Ernzerhof, M. Generalized Gradient Approximation Made Simple. *Phys. Rev. Lett.* **1996**, *77*, 3865-3868.

(48) Neu, H. M.; Quesne, M. G.; Yang, T.; Prokop-Prigge, K. A.; Lancaster, K. M.; Donohoe, J.; DeBeer, S.; de Visser, S. P.; Goldberg, D. P. Dramatic Influence of an Anionic Donor on the Oxygen-Atom Transfer Reactivity of a MnV–Oxo Complex. *Chem. - Eur. J.* **2014**, *20*, 14584-14588.

(49) Charnock, J. M.; Garner, C. D.; Trautwein, A. X.; Bill, E.; Winkler, H.; Ayougou, K.; Mandon, D.; Weiss, R. Characterization of an Oxo(porphyrinato)manganese(IV) Complex by X-ray Absorption Spectroscopy. *Angew. Chem., Int. Ed. Engl.* **1995**, *34*, 343-346.

(50) Leto, D. F.; Ingram, R.; Day, V. W.; Jackson, T. A. Spectroscopic properties and reactivity of a mononuclear oxomanganese(iv) complex. *Chemical Communications* **2013**, *49*, 5378-5380.

(51) Smeltz, J. L.; Lilly, C. P.; Boyle, P. D.; Ison, E. A. The Electronic Nature of Terminal Oxo Ligands in Transition-Metal Complexes: Ambiphilic Reactivity of Oxorhenium Species. *J. Am. Chem. Soc.* **2013**, *135*, 9433-9441.

(52) Yoon, H.; Lee, Y.-M.; Wu, X.; Cho, K.-B.; Sarangi, R.; Nam, W.; Fukuzumi, S. Enhanced Electron-Transfer Reactivity of Nonheme Manganese(IV)-Oxo Complexes by Binding Scandium Ions. *J. Am. Chem. Soc.* **2013**, *135*, 9186-9194.

(53) Peryshkov, D. V.; Schrock, R. R.; Takase, M. K.; Müller, P.; Hoveyda, A. H. Z-Selective Olefin Metathesis Reactions Promoted by Tungsten Oxo Alkylidene Complexes. *J. Am. Chem. Soc.* **2011**, *133*, 20754-20757.

(54) Barrado, G.; Doerrer, L.; L. H. Green, M.; A. Leech, M. Adducts of the Lewis acid [B(C6F5)3] with transition metal oxo compounds. *J. Chem. Soc., Dalton Trans.* **1999**, 1061-1066.

(55) Scott, M. J.; Zhang, H. H.; Lee, S. C.; Hedman, B.; Hodgson, K. O.; Holm, R. H. Oxygen-Bridged Iron-Copper Assemblies Pertinent to Heme-Copper Oxidases: Synthesis and Structure of an [FeIII-(OH)-CuII] Bridge and Exafs Multiple-Scattering Effects of Linear Oxo and Nonlinear Hydroxo Bridges. *J. Am. Chem. Soc.* **1995**, *117*, 568-569.

(56) Fox, S.; Nanthakumar, A.; Wikström, M.; Karlin, K. D.; Blackburn, N. J. XAS Structural Comparisons of Reversibly Interconvertible Oxo- and Hydroxo-Bridged Heme-Copper Oxidase Model Compounds. *J. Am. Chem. Soc.* **1996**, *118*, 24-34.

(57) De Angelis, F.; Jin, N.; Car, R.; Groves, J. T. Electronic Structure and Reactivity of Isomeric Oxo-Mn(V) Porphyrins: Effects of Spin-State Crossing and pKa Modulation. *Inorg. Chem.* **2006**, *45*, 4268-4276.

(58) de Visser, S. P.; Ogliaro, F.; Gross, Z.; Shaik, S. What Is the Difference between the Manganese Porphyrin and Corrole Analogues of Cytochrome P450's Compound I? *Chem. - Eur. J.* **2001**, *7*, 4954-4960.

(59) Siegbahn, P. E. M.; Crabtree, R. H. Manganese Oxyl Radical Intermediates and O-O Bond Formation in Photosynthetic Oxygen Evolution and a Proposed Role for the Calcium Cofactor in Photosystem II. *J. Am. Chem. Soc.* **1999**, *121*, 117-127.

(60) Ghosh, A.; Taylor, P. R. High-level ab initio calculations on the energetics of low-lying spin states of biologically relevant transition metal complexes: a first progress report. *Curr. Opin. Chem. Biol.* **2003**, *7*, 113-124.

(61) Kropp, H.; King, A. E.; Khusniyarov, M. M.; Heinemann, F. W.; Lancaster, K. M.; DeBeer, S.; Bill, E.; Meyer, K. Manganese Nitride Complexes in Oxidation States III, IV, and V: Synthesis and Electronic Structure. *J. Am. Chem. Soc.* **2012**, *134*, 15538-15544.

(62) Ding, M.; Cutsail, G.; Aravena, D.; Amoza, M.; Rouzieres, M.; Dechambenoit, P.; Lozovyy, Y.; Pink, M.; Ruiz, E.; Clerac, R.; Smith, J. M. A Low Spin Manganese(IV) Nitride Single Molecule Magnet. *Chem. Sci.* **2016**.

(63) Lansky, D. E.; Goldberg, D. P. Hydrogen Atom Abstraction by a High-Valent Manganese(V)-Oxo Corrolazine. *Inorg. Chem.* **2006**, *45*, 5119-5125.

(64) Joslin, E. E.; Zaragoza, J. P. T.; Baglia, R. A.; Siegler, M. A.; Goldberg, D. P. The Influence of Peripheral Substituent Modification on PV, MnIII, and MnV(O) Corrolazines: X-ray Crystallography, Electrochemical and Spectroscopic Properties, and HAT and OAT Reactivities. *Inorg. Chem.* **2016**, Article ASAP.

(65) Prokop, K. A.; de Visser, S. P.; Goldberg, D. P. Unprecedented Rate Enhancements of Hydrogen-Atom Transfer to a Manganese(V)–Oxo Corrolazine Complex. *Angew. Chem., Int. Ed.* **2010**, *49*, 5091-5095.

(66) Warren, J. J.; Tronic, T. A.; Mayer, J. M. Thermochemistry of proton-coupled electron transfer reagents and its implications. *Chem. Rev.* **2010**, *110*, 6961-7001.

(67) Mayer, J. M. Understanding Hydrogen Atom Transfer: From Bond Strengths to Marcus Theory. *Acc. Chem. Res.* **2011**, *44*, 36-46.

(68) Cho, K.; Leeladee, P.; McGown, A. J.; DeBeer, S.; Goldberg, D. P. A High-Valent Iron-Oxo Corrolazine Activates C-H Bonds via Hydrogen-Atom Transfer. *J. Am. Chem. Soc.* **2012**, *134*, 7392-7399.

(69) Jung, J.; Kim, S.; Lee, Y.-M.; Nam, W.; Fukuzumi, S. Switchover of the Mechanism between Electron Transfer and Hydrogen-Atom Transfer for a Protonated Manganese(IV)–Oxo Complex by Changing Only the Reaction Temperature. *Angew. Chem., Int. Ed.* **2016**, n/a-n/a.

(70) Park, J.; Lee, Y.-M.; Nam, W.; Fukuzumi, S. Brönsted Acid-Promoted C-H Bond Cleavage via Electron Transfer from Toluene Derivatives to a Protonated Nonheme Iron(IV)-Oxo Complex with No Kinetic Isotope Effect. *J. Am. Chem. Soc.* **2013**, *135*, 5052-5061.

4.6. Appendix A. Lewis Acidity Measurement by the Gutmann-Beckett Method

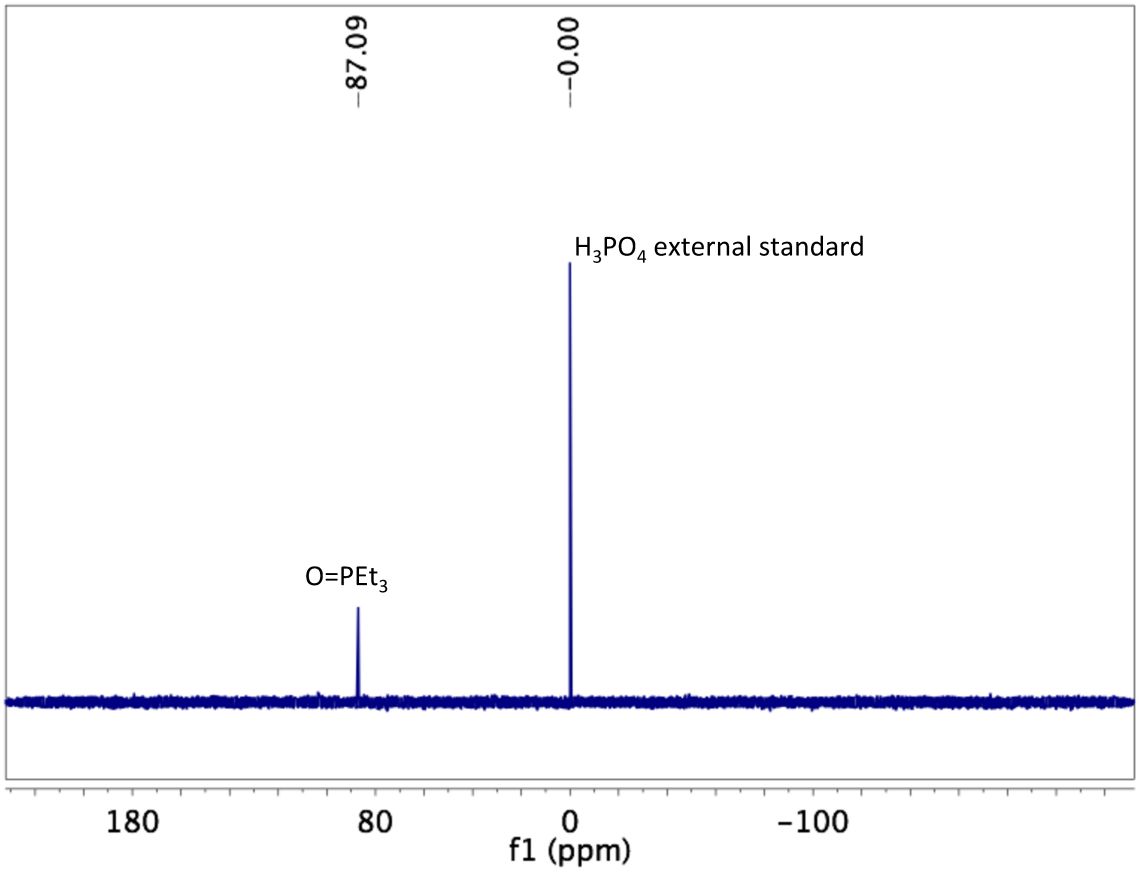

Figure 4.7. ^{31}P-NMR spectrum of a mixture of triethylphosphine oxide and HBAr^{F} (3:1 molar ratio) in CD_2Cl_2 referenced to an 85% H_3PO_4 solution as an external standard.

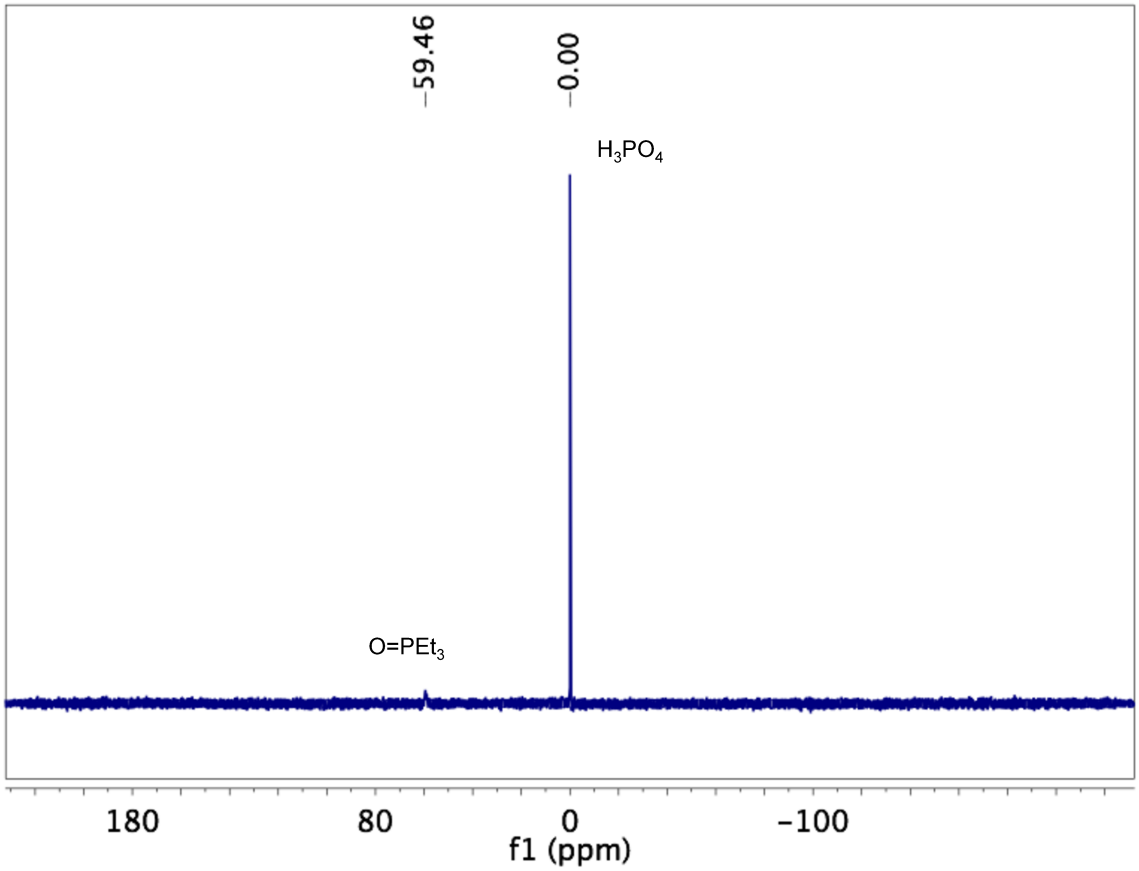

Figure 4.8. ^{31}P-NMR spectrum of a mixture of triethylphosphine oxide and trifluoroacetic acid (1:3 molar ratio) in CD_2Cl_2 referenced to an 85% H_3PO_4 solution as an external standard.

4.7. Appendix B. UV-vis Kinetics Studies

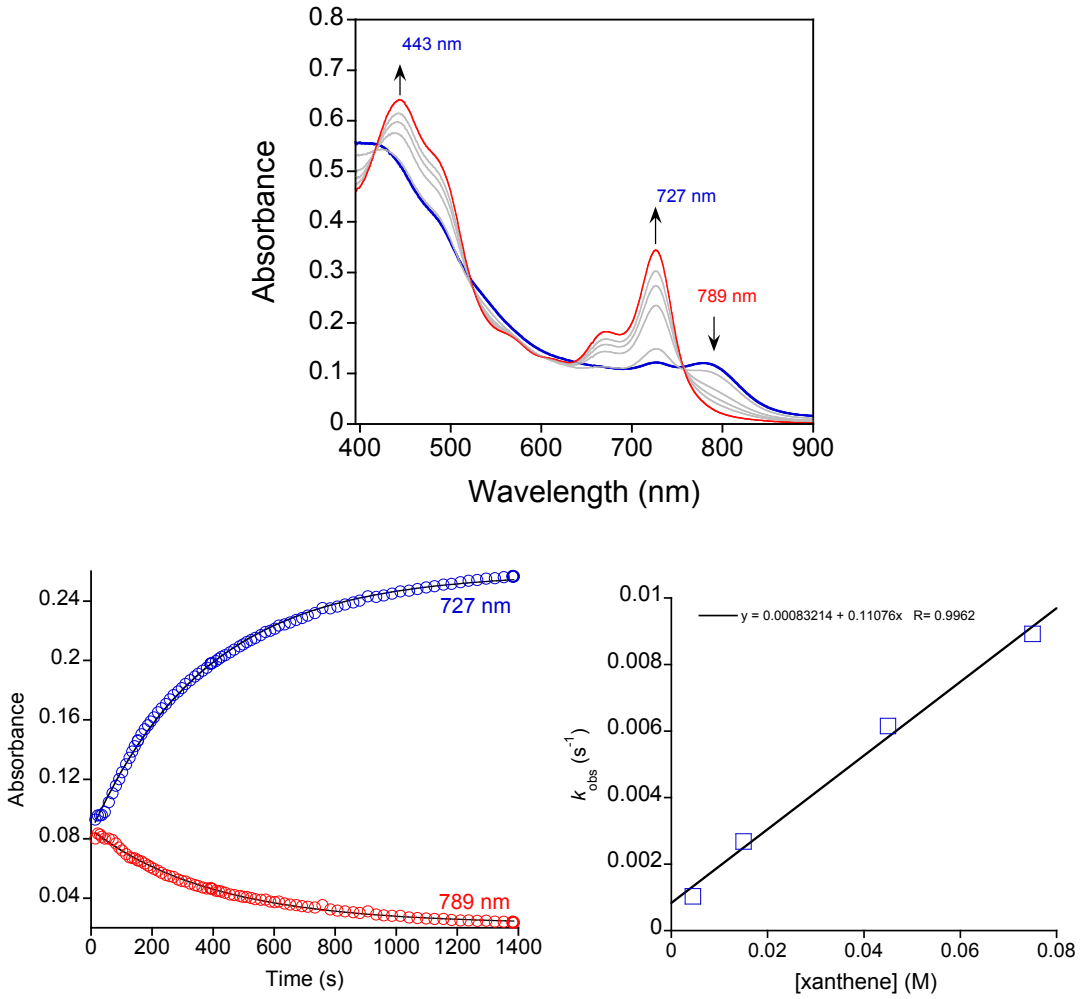

Figure 4.9. Top: Time-resolved UV-vis spectra for the reaction of Mn^{IV}(O–$B(C_6F_5)_3$)($TBP_8Cz^{\bullet+}$) (14 μM in CH_2Cl_2) with xanthene (0.014 M) in a cuvette with a 1 cm pathlength. Bottom left: Absorbance versus time plots for the growth of Mn^{IV} product (727 nm) and decay of Mn^{IV}(O– $B(C_6F_5)_3$)($TBP_8Cz^{\bullet+}$) (789 nm) together with the best fit lines to the appropriate single-exponential expression. Bottom right: Plot of k_{obs} versus [xanthene] yielding the second order rate constant 5.5 ± 0.3 × 10^{-2} M^{-1} s^{-1} (k_2') from the slope of the best-fit line and normalized per reactive C–H bond.

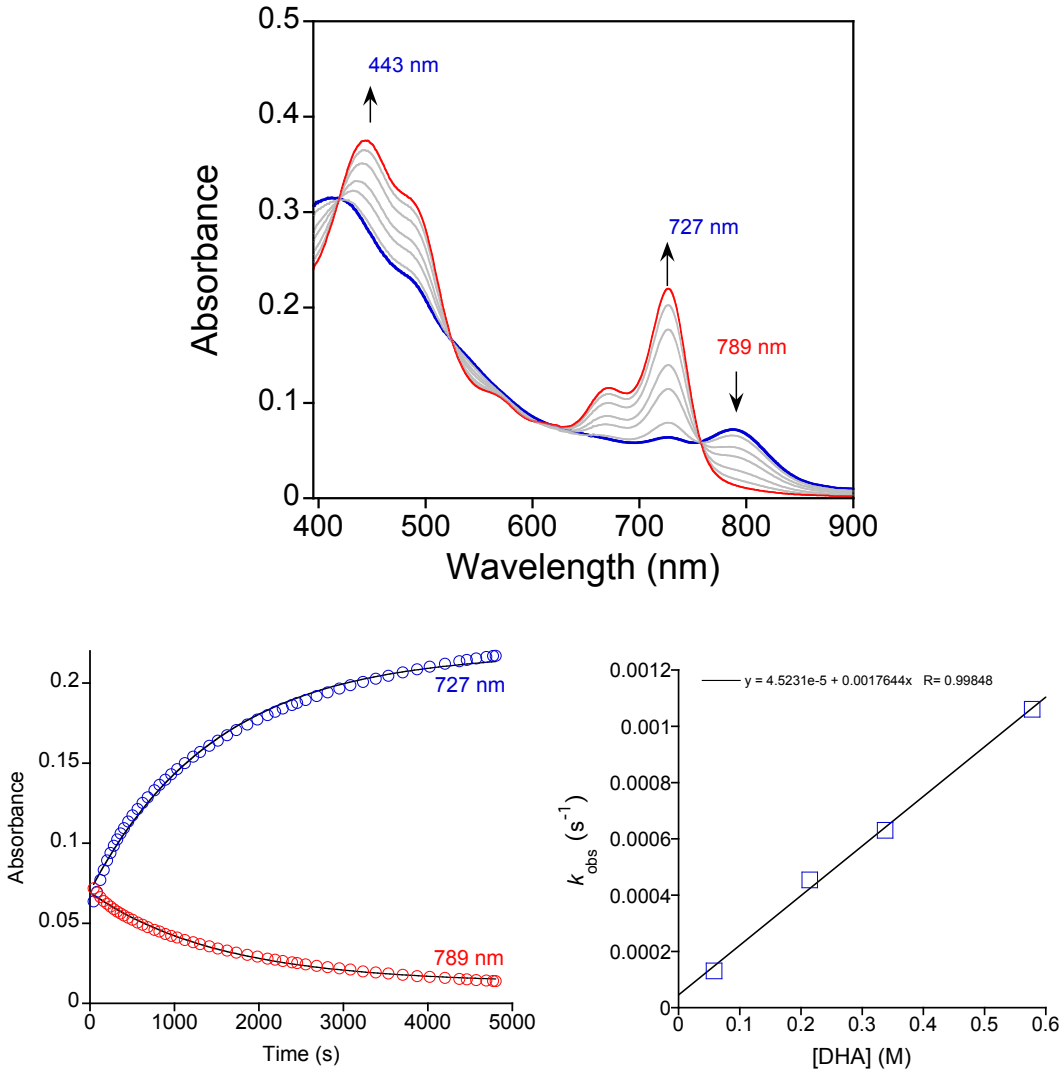

Figure 4.10. Top: Time-resolved UV-vis spectra for the reaction of Mn^{IV}(O–$B(C_6F_5)_3$)($TBP_8Cz^{\bullet+}$) (55 µM in CH_2Cl_2) with DHA (0.33 M) in a cuvette with a 2 mm pathlength. Bottom left: Absorbance versus time plots for the growth of Mn^{IV} product (727 nm) and decay of Mn^{IV}(O– $B(C_6F_5)_3$)($TBP_8Cz^{\bullet+}$) (789 nm) together with the best fit lines to the appropriate single-exponential expression. Bottom right: Plot of k_{obs} versus [DHA] yielding the second order rate constant 4.3 ± 0.2 × 10^{-4} M^{-1} s^{-1} (k_2') from the slope of the best-fit line and normalized per reactive C–H bond.

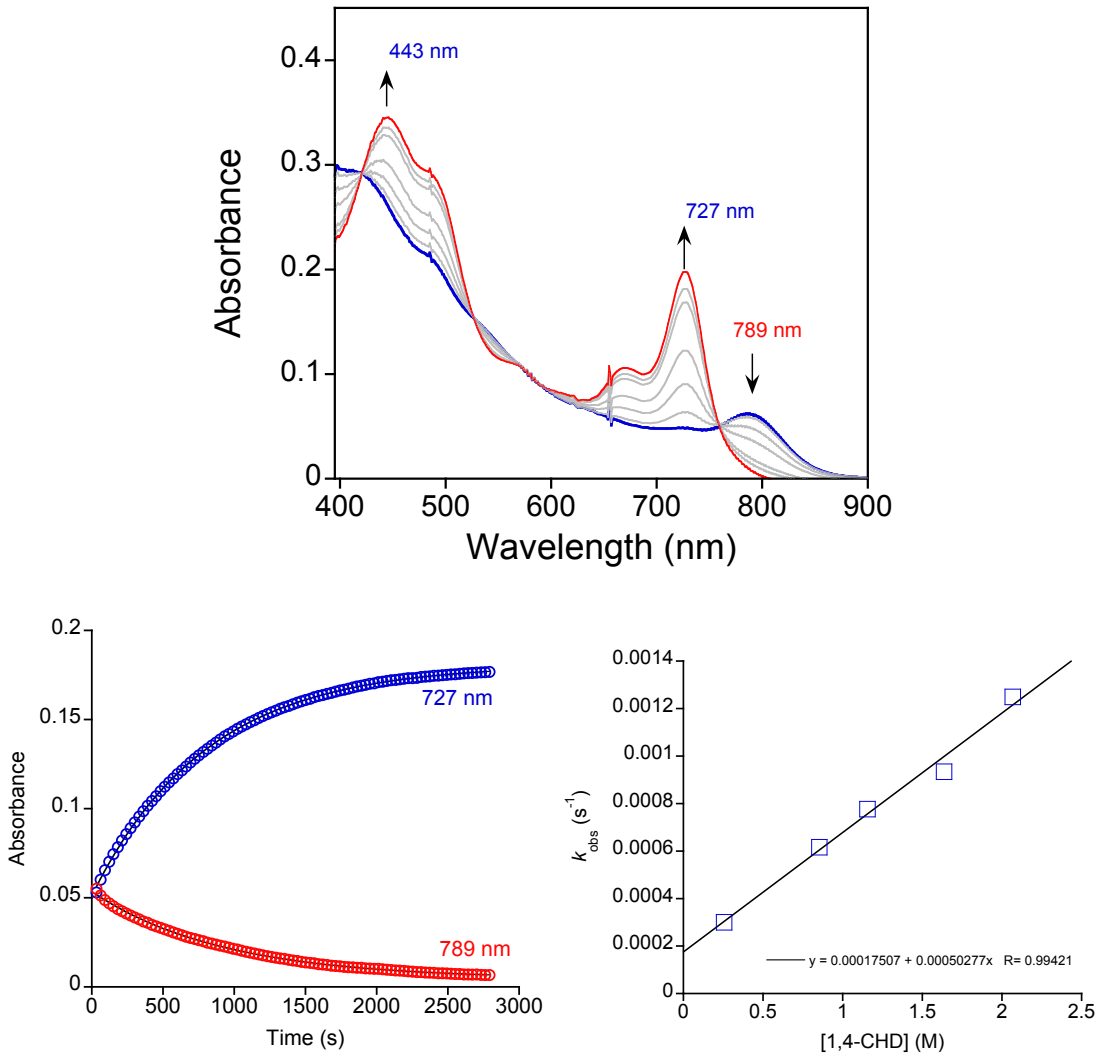

Figure 4.11. Top: Time-resolved UV-vis spectra for the reaction of Mn^{IV}(O–$B(C_6F_5)_3$)($TBP_8Cz^{\bullet+}$) (56 µM in CH_2Cl_2) with 1,4-CHD (0.85 M) in a cuvette with a 2 mm pathlength. Bottom left: Absorbance versus time plots for the growth of Mn^{IV} product (727 nm) and decay of Mn^{IV}(O– $B(C_6F_5)_3$)($TBP_8Cz^{\bullet+}$) (789 nm) together with the best fit lines to the appropriate single-exponential expression. Bottom right: Plot of k_{obs} versus [1,4-CHD] yielding the second order rate constant 1.3 ± 0.8 × 10^{-4} M^{-1} s^{-1} (k_2') from the slope of the best-fit line and normalized per reactive C–H bond.

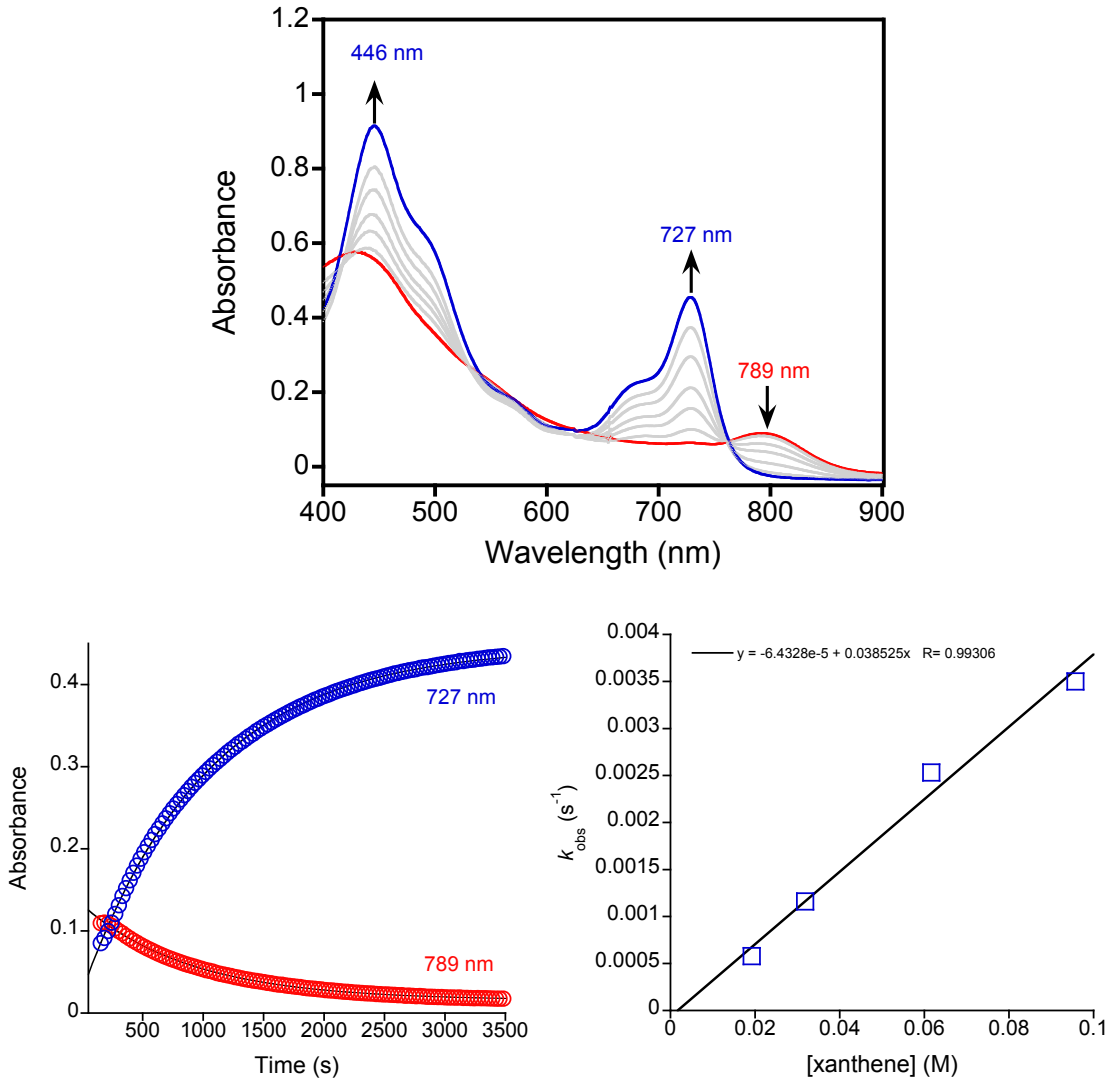

Figure 4.12. Top: Time-resolved UV-vis spectra for the reaction of Mn^{IV}(O–$HBAr^F$)($TBP_8Cz^{\bullet+}$) (17 μM in CH_2Cl_2) with xanthene (0.032 M) in a cuvette with a 1 cm pathlength. Bottom left: Absorbance versus time plots for the growth of Mn^{IV} product (727 nm) and decay of Mn^{IV}(O– $HBAr^F$)($TBP_8Cz^{\bullet+}$) (789 nm) together with the best fit lines to the appropriate single-exponential expression. Bottom right: Plot of k_{obs} versus [xanthene] yielding the second order rate constant 1.9 ± 0.2 × 10^{-2} M^{-1} s^{-1} (k_2') from the slope of the best-fit line and normalized per reactive C–H bond.

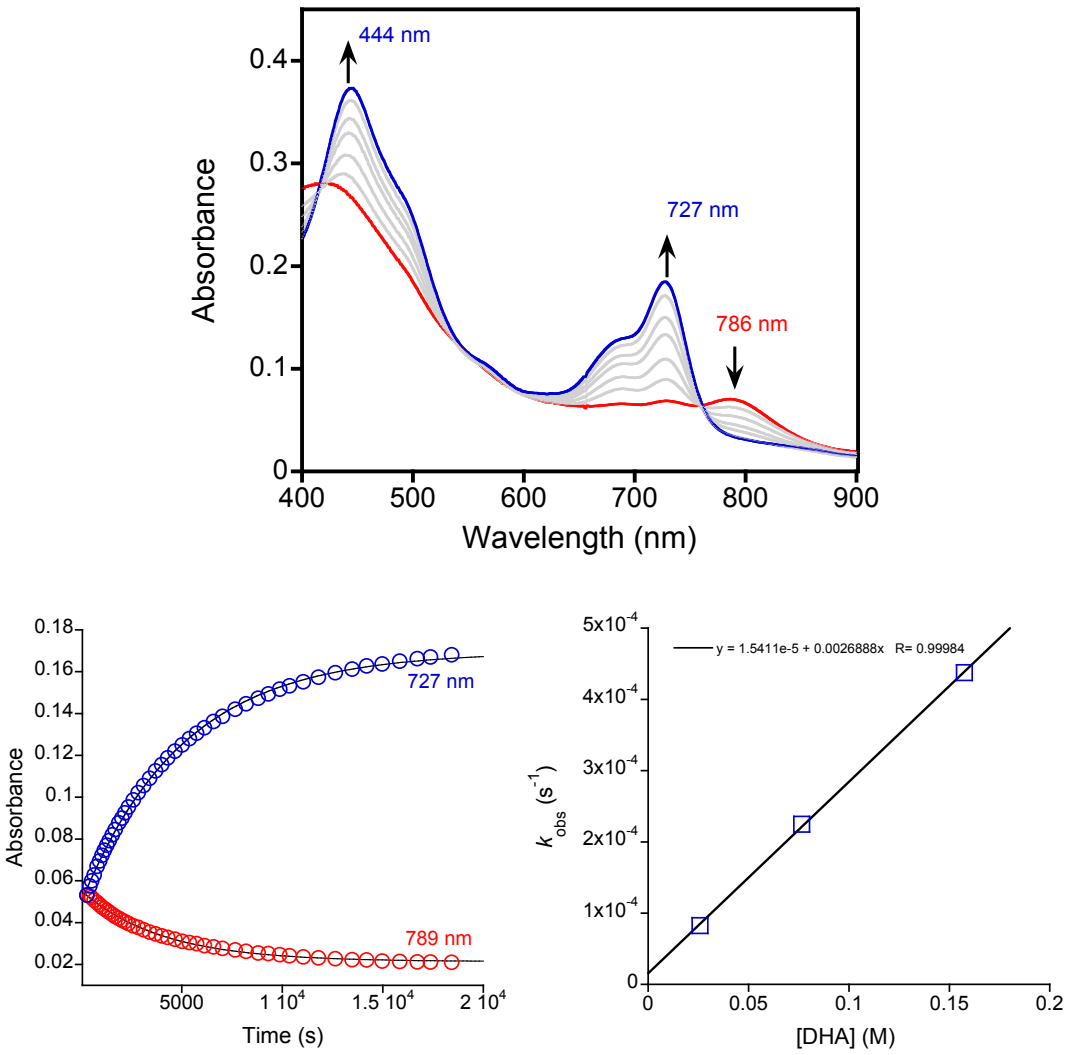

Figure 4.13. Top: Time-resolved UV-vis spectra for the reaction of Mn^{IV}(O–HBAr^F)(TBP$_8$Cz$^{\bullet+}$) (56 µM in CH_2Cl_2) with DHA (0.077 M) in a cuvette with a 2 mm pathlength. Bottom left: Absorbance versus time plots for the growth of Mn^{IV} product (727 nm) and decay of Mn^{IV}(O– HBAr^F)(TBP$_8$Cz$^{\bullet+}$) (789 nm) together with the best fit lines to the appropriate single-exponential expression. Bottom right: Plot of k_{obs} versus [DHA] yielding the second order rate constant 6.7 ± 0.1 × 10^{-4} M^{-1} s^{-1} (k_2') from the slope of the best-fit line and normalized per reactive C–H bond.

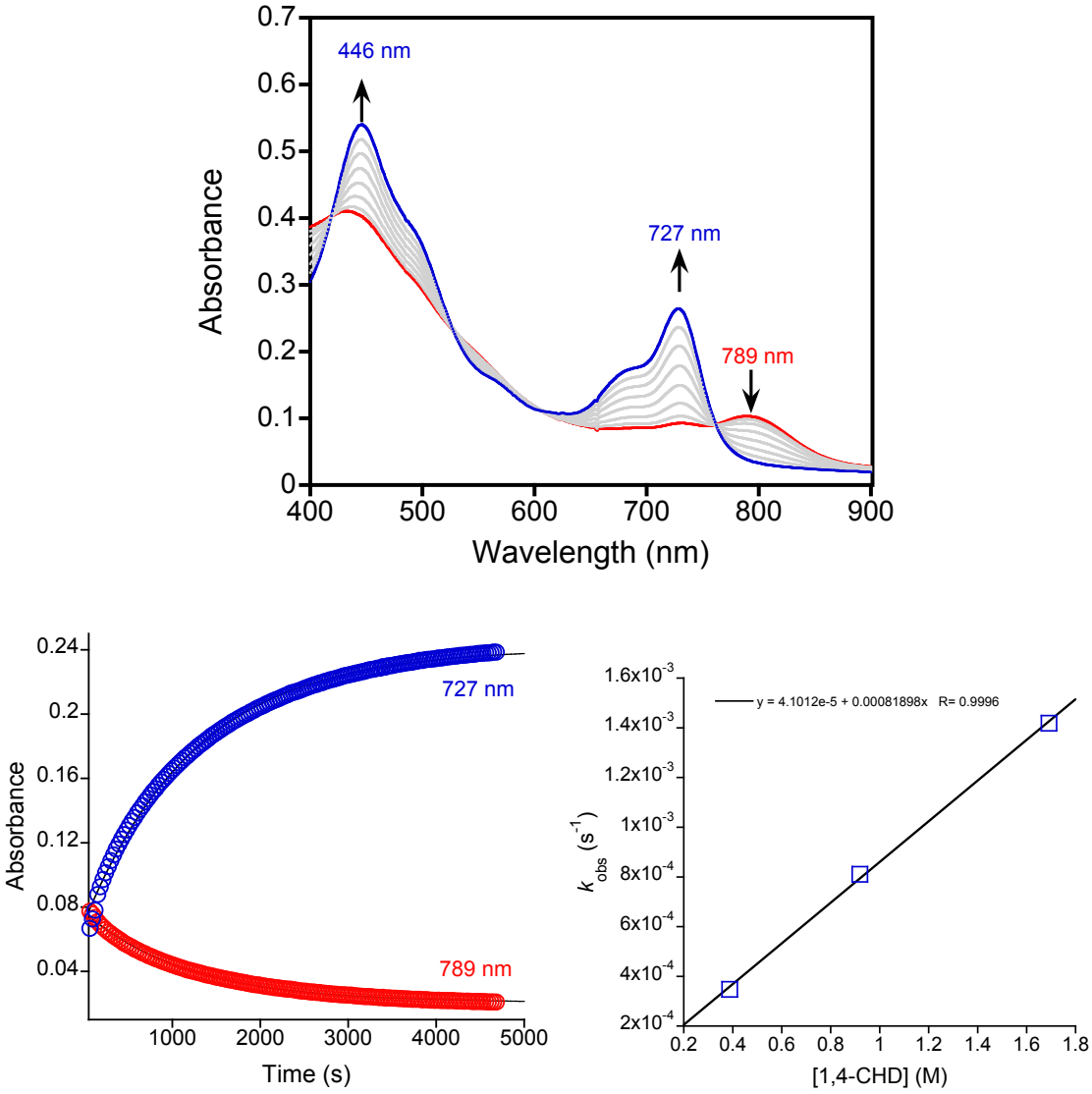

Figure 4.14. Top: Time-resolved UV-vis spectra for the reaction of Mn^{IV}(O–HBAr^F)(TBP$_8$Cz$^{\bullet+}$) (56 µM in CH_2Cl_2) with 1,4-CHD (0.92 M) in a cuvette with a 2 mm pathlength. Bottom left: Absorbance versus time plots for the growth of Mn^{IV} product (727 nm) and decay of Mn^{IV}(O– HBAr^F)(TBP$_8$Cz$^{\bullet+}$) (789 nm) together with the best fit lines to the appropriate single-exponential expression. Bottom right: Plot of k_{obs} versus [1,4-CHD] yielding the second order rate constant 2.0 ± 0.1 × 10^{-4} M^{-1} s^{-1} (k_2') from the slope of the best-fit line and normalized per reactive C–H bond.

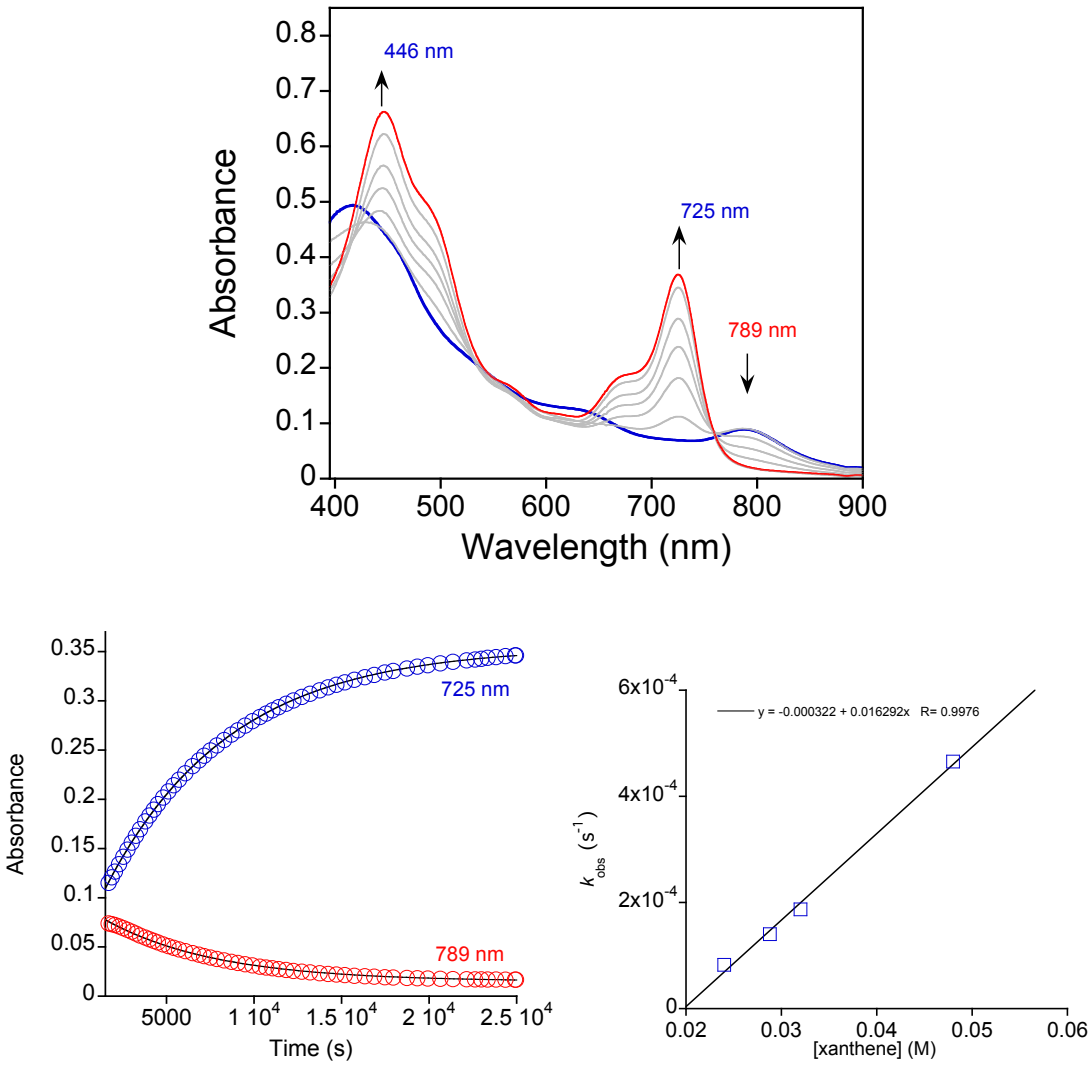

Figure 4.15. Top: Time-resolved UV-vis spectra for the reaction of Mn^{IV}(O–Zn^{II})($TBP_8Cz^{\bullet+}$) (12 μM in CH_2Cl_2) with xanthene (0.024 M) in a cuvette with a 1 cm pathlength. Bottom left: Absorbance versus time plots for the growth of Mn^{IV} product (725 nm) and decay of Mn^{IV}(O– Zn^{II})($TBP_8Cz^{\bullet+}$) (789 nm) together with the best fit lines to the appropriate single-exponential expression. Bottom right: Plot of k_{obs} versus [xanthene] yielding the second order rate constant 8.1 ± 0.4 × 10^{-3} M^{-1} s^{-1} (k_2') from the slope of the best-fit line and normalized per reactive C–H bond.

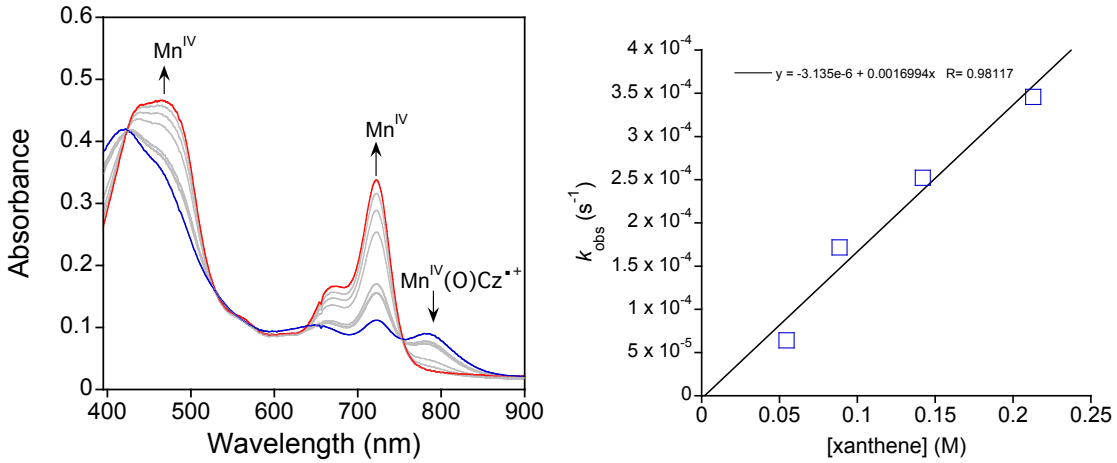

Figure 4.16. Left: Reaction of Mn^{IV}(O–TFA)($TBP_8Cz^{\bullet+}$) (56 µM in CH_2Cl_2) with excess xanthene (0.142 M) in a cuvette with a 2 mm pathlength. Right: Plot of k_{obs} versus [xanthene] yielding the second order rate constant 9 ± 1 × 10^{-4} M^{-1} s^{-1} (k_2') from the slope of the best-fit line and normalized per reactive C–H bond.

4.8. Appendix C. DFT Studies

Table 4.3. Select bond distances (Å) and angles (deg) for the optimized geometry of ^{5}[Mn(O–B(C_6F_5)$_3$)(H_8Cz)] with different functional-basis set combinations.

Methods	Basis set	rMnO	rOB	$rMnN_d$[a]	$rMnN_p$[b]	ΔMn	aMnOB
BP86	def2-TZVPP/def2-SVPD/ZORA	1.74	1.51	1.91	1.93	0.48	136
B3PW91	SDD/6-31G(d,p)	1.70	1.50	1.89	1.90	0.48	146
B3LYP	def2TZVPP/def2-SVPD/ZOR	1.72	1.51	1.91	1.93	0.49	139
B3LYP	TZVPP/ZPRA	1.71	1.49	1.89	1.90	0.48	141
B3LYP	LANLDZ/6-31G	1.72	1.54	1.91	1.91	0.50	162
PBE0	def2-TZVPP/def2-SVPD/ZORA	1.71	1.50	1.90	1.92	0.50	138

[a] $rMnN_d$ = Mn–N pyrrole distances for the two pyrrole nitrogens furthest from the Cα-Cα bond. [b] $rMnN_p$ = Mn–N pyrrole distances for the two pyrrole nitrogens adjacent to the Cα-Cα bond.

Table 4.4. Select bond distances (Å) and angles (deg) for the optimized geometry of singlet, triplet (ls-Mn^{IV}), triplet (hs-Mn^{IV}) and quintet [Mn(O–LA)(H_8Cz)] at RIJCOSX-B3LYP/LANLDZ/6-31G where LA = $B(C_6F_5)_3$, $Zn(OTf)_2$.

LA	*S*	rMnO	rOB	$rMnN_d$	$rMnN_p$	ΔMn	aMnO[LA]
$B(C_6F_5)_3$	0	1.61	1.66	1.90	1.87	0.59	173
$B(C_6F_5)_3$	1 (ls-Mn^{IV})	1.66	1.56	1.91	1.90	0.57	166
$B(C_6F_5)_3$	1 (hs-Mn^{IV})	1.71	1.54	1.90	1.91	0.50	163
$B(C_6F_5)_3$	2	1.72	1.54	1.91	1.91	0.50	162
$Zn(OTf)_2$	0	1.65	1.98	1.90	1.90	0.54	138
$Zn(OTf)_2$	1 (ls-Mn^{IV})	1.65	1.98	1.91	1.89	0.53	147
$Zn(OTf)_2$	1 (hs-Mn^{IV})	1.71	1.95	1.90	1.89	0.44	137
$Zn(OTf)_2$	2	1.71	1.94	1.90	1.89	0.46	148

[a] $rMnN_d$ = Mn–N pyrrole distances for the two pyrrole nitrogens furthest from the Cα-Cα bond. [b] $rMnN_p$ = Mn–N pyrrole distances for the two pyrrole nitrogens adjacent to the Cα-Cα bond.

Table 4.5. Mulliken group spin densities of singlet, triplet (ls-Mn^{IV}), triplet (hs-Mn^{IV}) and quintet [Mn(O–LA)(H_8Cz)] at RIJCOSX-B3LYP/LANLDZ/6-31G where LA = $B(C_6F_5)_3$, $Zn(OTf)_2$

LA	*S*	ρ(Mn)	ρ(H_8Cz)	ρ(O)	ρ(LA)
$B(C_6F_5)_3$	0	0.00	0.00	0.00	0.00
$B(C_6F_5)_3$	1 (ls-Mn^{IV})	0.87	0.97	0.16	0.01
$B(C_6F_5)_3$	1 (hs-Mn^{IV})	2.58	-0.99	0.40	0.01
$B(C_6F_5)_3$	2	2.60	0.97	0.41	0.02
$Zn(OTf)_2$	0	0.00	0.00	0.00	0.00
$Zn(OTf)_2$	1 (ls-Mn^{IV})	0.83	1.00	0.15	0.01
$Zn(OTf)_2$	1 (hs-Mn^{IV})	2.69	-0.95	0.26	0.01
$Zn(OTf)_2$	2	2.75	1.03	0.20	0.01

Table 4.6. Absolute energies (in Eh) of singlet, triplet (ls-Mn^{IV}), triplet (hs-Mn^{IV}) and quintet [Mn(O–LA)(H_8Cz)] at RIJCOSX-B3LYP/LANLDZ/6-31G where LA = $B(C_6F_5)_3$, $Zn(OTf)_2$

LA	*S*	E	ZPVE+Thermo	Entropy
$B(C_6F_5)_3$	0	-3382.81	0.42	0.11
$B(C_6F_5)_3$	1 (ls-Mn^{IV})	-3382.82	0.42	0.11
$B(C_6F_5)_3$	1 (hs-Mn^{IV})	-3382.83	0.42	0.12
$B(C_6F_5)_3$	2	-3382.83	0.42	0.12
$Zn(OTf)_2$	0	-3163.27	0.31	0.10
$Zn(OTf)_2$	1 (ls-Mn^{IV})	-3163.27	0.31	0.10
$Zn(OTf)_2$	1 (hs-Mn^{IV})	-3163.28	0.31	0.10
$Zn(OTf)_2$	2	-3163.28	0.31	0.10

Table 4.7. Relative energies (in kcal·mol^{-1}) of singlet, triplet (ls-Mn^{IV}), triplet (hs-Mn^{IV}) and quintet [Mn(O–LA)(H_8Cz)] at RIJCOSX-B3LYP/LANLDZ/6-31G where LA = $B(C_6F_5)_3$, $Zn(OTf)_2$

LA	*S*	ΔE	ΔH	ΔG
$B(C_6F_5)_3$	0	8.14	8.83	11.74
$B(C_6F_5)_3$	1 (ls-Mn^{IV})	4.41	5.03	5.58
$B(C_6F_5)_3$	1 (hs-Mn^{IV})	0.01	0.07	0.23
$B(C_6F_5)_3$	2	0.00	0.00	0.00
$Zn(OTf)_2$	0	6.17	6.93	8.65
$Zn(OTf)_2$	1 (ls-Mn^{IV})	4.91	4.92	6.42
$Zn(OTf)_2$	1 (hs-Mn^{IV})	-0.80	0.12	-0.16
$Zn(OTf)_2$	2	0.00	0.00	0.00

Table 4.8. Absolute energies (in Eh) of singlet, triplet (ls-Mn^{IV}), triplet (hs-Mn^{IV}) and quintet [Mn(O–LA)(H_8Cz)] at RIJONX-wB97X-D3/def2-TZVPP/def2-SVP/ZORA//RIJCOSX-B3LYP/LANLDZ/6-31G where LA = $B(C_6F_5)_3$, $Zn(OTf)_2$

LA	*S*	E	ZPVE+Thermo	Entropy	Solv
$B(C_6F_5)_3$	0	-4441.90	0.42	0.11	-0.02
$B(C_6F_5)_3$	1 (ls-Mn^{IV})	-4441.92	0.42	0.11	-0.02
$B(C_6F_5)_3$	1 (hs-Mn^{IV})	-4441.92	0.42	0.12	-0.03
$B(C_6F_5)_3$	2	-4441.92	0.42	0.12	-0.03
$Zn(OTf)_2$	0	-5965.96	0.31	0.10	-0.03
$Zn(OTf)_2$	1 (ls-Mn^{IV})	-5966.00	0.31	0.10	-0.03
$Zn(OTf)_2$	1 (hs-Mn^{IV})	-5966.01	0.31	0.10	-0.04
$Zn(OTf)_2$	2	-5966.02	0.31	0.10	-0.04

Table 4.9. Relative energies (in kcal·mol^{-1}) of singlet, triplet (ls-Mn^{IV}), triplet (hs-Mn^{IV}) and quintet [Mn(O–LA)(H_8Cz)] at RIJONX-wB97X-D3/def2-TZVPP/def2-SVP/ZORA//RIJCOSX-B3LYP/LANLDZ/6-31G where LA = $B(C_6F_5)_3$, $Zn(OTf)_2$

LA	*S*	ΔE	ΔH	ΔG	ΔG_{solv}
$B(C_6F_5)_3$	0	13.56	14.24	17.16	21.92
$B(C_6F_5)_3$	1 (ls-Mn^{IV})	2.65	3.28	3.83	5.49
$B(C_6F_5)_3$	1 (hs-Mn^{IV})	0.54	0.61	0.77	0.71
$B(C_6F_5)_3$	2	0.00	0.00	0.00	0.00
$Zn(OTf)_2$	0	33.87	34.63	36.35	39.31
$Zn(OTf)_2$	1 (ls-Mn^{IV})	7.36	7.36	8.86	12.50
$Zn(OTf)_2$	1 (hs-Mn^{IV})	4.72	5.64	5.36	6.94
$Zn(OTf)_2$	2	0.00	0.00	0.00	0.00

Table 4.10. Absolute energies (E, in Eh) and relative energy (ΔE, in kcal·mol^{-1}), with respect to the quintet state, and Mulliken group spin densities of the triplet (ls-Mn^{IV}) ^{3}[Mn(O–Zn(OTf)$_2$)(H_8Cz)] at RIJCOSX-B3LYP/LANLDZ/6-31G

rMnO	E	ΔE[a]	ρ(Mn)	ρ(H_8Cz)	ρ(O)	ρ(LA)
1.61	-3163.28	1.17	0.84	1.00	0.14	0.02
1.62	-3163.28	0.75	0.85	1.00	0.14	0.01
1.63	-3163.28	0.62	0.85	1.00	0.14	0.01
1.64	-3163.28	0.58	0.85	1.00	0.14	0.01
1.65	-3163.28	0.62	0.85	1.00	0.14	0.01
1.66	-3163.28	0.74	0.86	1.00	0.14	0.01
1.67	-3163.28	0.93	0.86	0.99	0.13	0.01
1.68	-3163.28	1.36	0.85	1.00	0.14	0.01
1.69	-3163.28	1.69	0.86	1.00	0.14	0.01
1.70	-3163.27	2.10	0.86	1.00	0.13	0.01
1.71	-3163.27	2.57	0.86	1.00	0.13	0.01

a ^{5}[(H_8Cz)Mn(O)-Zn(OTf)$_2$] was optimized at RIJCOSX-B3LYP/LANLDZ/6-31G.

Table 4.11. Absolute energies (E, in Eh) and relative energy (ΔE, in kcal·mol^{-1}), with respect to the quintet state, and Mulliken group spin densities of the triplet (ls-Mn^{IV}) ^{3}[Mn(O–B(C$_6$F$_5$)$_3$)(H$_8$Cz)] at RIJCOSX-B3LYP/LANLDZ/6-31G

rMnO	E	ΔE[a]	ρ(Mn)	ρ(H$_8$Cz)	ρ(O)	ρ(LA)
1.61	-3382.82	4.69	0.88	0.98	0.13	0.01
1.62	-3382.82	4.69	0.90	0.98	0.12	0.01
1.63	-3382.82	4.33	0.90	0.98	0.11	0.01
1.64	-3382.82	4.55	0.91	0.98	0.10	0.01
1.65	-3382.82	4.51	0.91	0.98	0.10	0.01
1.66	-3382.82	5.58	0.92	0.97	0.10	0.01
1.67	-3382.82	5.48	0.93	0.97	0.09	0.01
1.68	-3382.82	5.71	0.94	0.97	0.09	0.01
1.69	-3382.82	5.80	0.95	0.97	0.08	0.01
1.70	-3382.82	6.14	0.96	0.97	0.07	0.01
1.71	-3382.82	6.34	0.97	0.97	0.06	0.00

a^{5}[(H$_8$Cz)Mn(O)-Zn(OTf)$_2$] was optimized at RIJCOSX-B3LYP/LANLDZ/6-31G.

Table 4.12. Absolute energies (E, in Eh) and relative energy[a] (ΔE, in kcal·mol^{-1}) and Mulliken group spin densities of the quintet (hs-Mn^{IV}) ^{5}[Mn(O–Zn(OTf)$_2$)(H$_8$Cz)] at varying Mn–O distances at RIJCOSX-B3LYP/LANLDZ/6-31G

rMnO	E	ΔE[a]	ρ(Mn)	ρ(O)	ρ(H8Cz)	ρ(ZnOTf2)
1.61	-3163.27	4.33	2.58	0.36	1.05	0.00
1.62	-3163.27	3.71	2.58	0.36	1.05	0.00
1.63	-3163.27	3.02	2.59	0.36	1.05	0.00
1.64	-3163.27	2.40	2.60	0.35	1.04	0.00
1.65	-3163.28	1.91	2.61	0.34	1.04	0.00
1.66	-3163.28	1.41	2.62	0.34	1.04	0.00
1.67	-3163.28	1.11	2.63	0.33	1.04	0.00
1.68	-3163.28	0.23	2.63	0.32	1.04	0.00
1.69	-3163.28	0.10	2.64	0.31	1.04	0.00
1.70	-3163.28	0.00	2.65	0.31	1.04	0.00
1.71	-3163.28	0.00	2.66	0.30	1.03	0.00

[a]Relative energies were obtained by subtracting each energy by the lowest energy among both the ^{3}E and ^{5}A relaxed surface scan

Table 4.13. Absolute energies (E, in Eh) and relative energy[a] (ΔE, in kcal·mol^{-1}) and Mulliken group spin densities of the quintet (hs-Mn^{IV}) ^{5}[Mn(O–B(C$_6$F$_5$)$_3$)(H$_8$Cz)] at varying Mn–O distances at RIJCOSX-B3LYP/LANLDZ/6-31G

rMnO	E	ΔE[a]	ρ(Mn)	ρ(O)	ρ(H8Cz)	ρ(BCF)
1.61	-3382.82	3.57	2.53	0.44	1.03	0.00
1.62	-3382.82	3.13	2.54	0.43	1.03	0.00
1.63	-3382.82	2.18	2.55	0.42	1.03	0.00
1.64	-3382.82	2.06	2.56	0.41	1.03	0.00
1.65	-3382.82	1.20	2.56	0.41	1.02	0.00
1.66	-3382.82	1.69	2.58	0.40	1.02	0.00
1.67	-3382.82	1.03	2.58	0.41	1.01	0.00
1.68	-3382.82	0.77	2.59	0.40	1.01	0.00
1.69	-3382.82	0.37	2.60	0.40	1.01	0.00
1.70	-3382.82	0.24	2.61	0.39	1.00	0.00
1.71	-3382.82	0.00	2.62	0.39	1.00	0.00

[a]Relative energies were obtained by subtracting each energy by the lowest energy among both the ^{3}E and ^{5}A relaxed surface scan

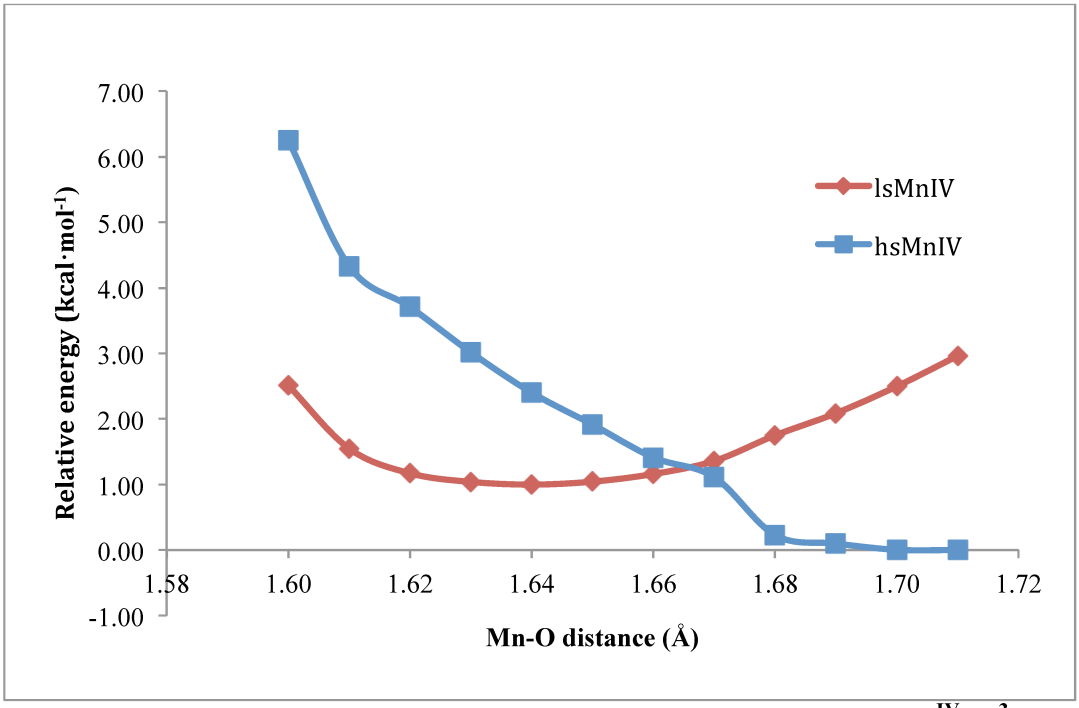

Figure 4.17. Energies from relaxed surface scans for (ls-Mn^{IV}) ^{3}[Mn(O–Zn(OTf)$_2$)(H$_8$Cz)] (red) and quintet ^{5}[Mn(O–Zn(OTf)$_2$)(H$_8$Cz)] (blue). The single

point energies at different Mn–O distances were compared to that of the optimized ^{5}[Mn(O–Zn(OTf)$_2$)(H$_8$Cz)].

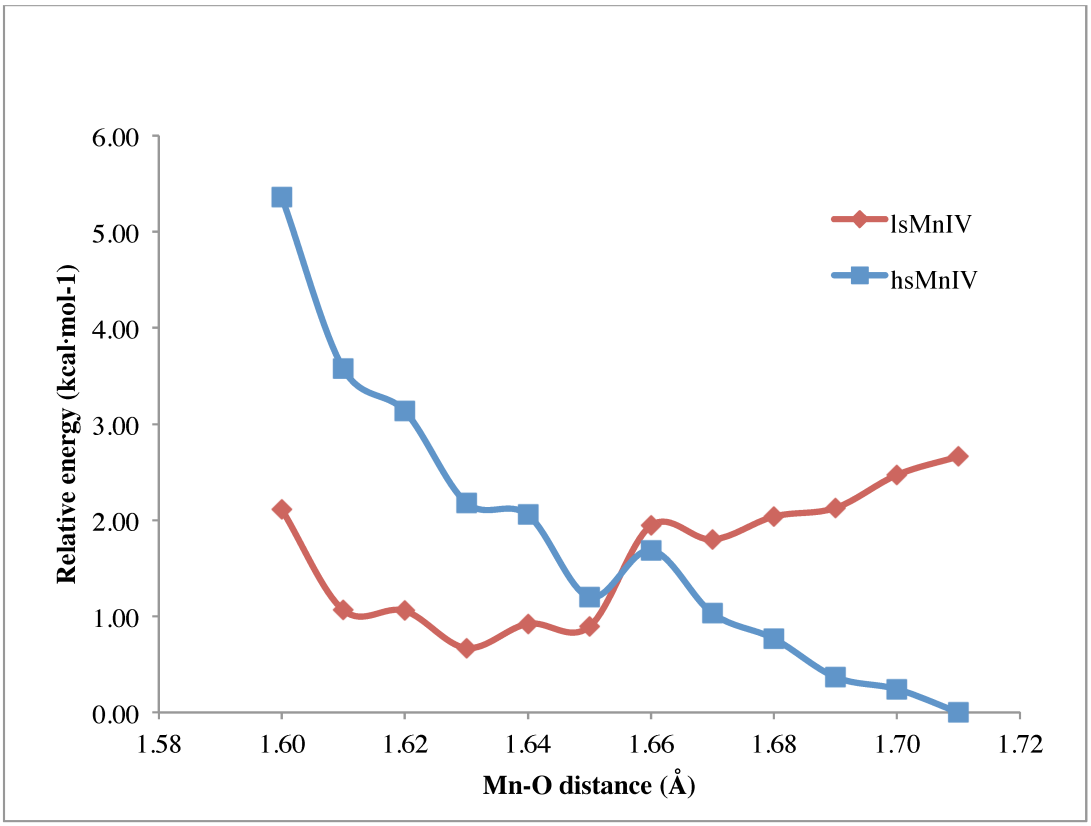

Figure 4.18. Energies from relaxed surface scans for (ls-Mn^{IV}) ^{3}[Mn(O–B(C$_6$F$_5$)$_3$)(H$_8$Cz)] (red) and quintet (hs-Mn^{IV}) ^{5}[Mn(O–B(C$_6$F$_5$)$_3$)(H$_8$Cz)] (blue). The single point energies at different Mn–O distances were compared to that of the optimized ^{5}[Mn(O– B(C$_6$F$_5$)$_3$)(H$_8$Cz)].

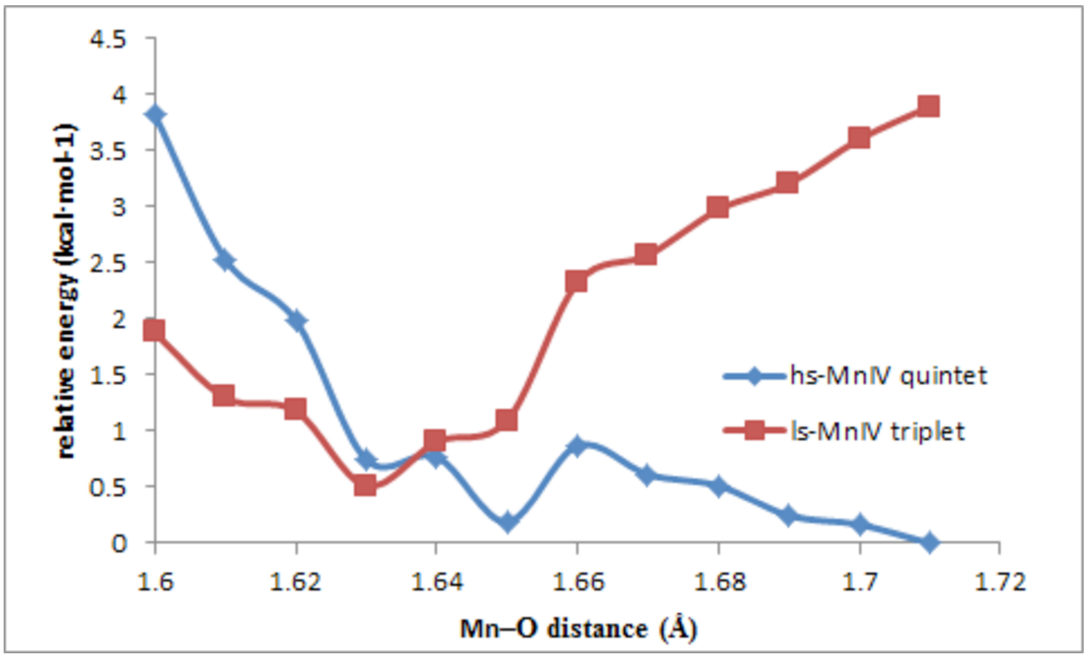

Figure 4.19. Relative energies in this plot are from the same relaxed surface scans as Figure S16 but with RIJCOSX-B3LYP-D3/def2-TZVPP/def2-TZVP/ZORA (i.e. def2-TZVPP on Mn and def2-TZVP on the rest of atoms, both of the def2 basis sets are full valence basis sets of triple zeta qualities). These energies were recalculated to determine if the choice of split basis set in Figure S16 affected the relative energies; however, the trend in relative energies depicted in Figure S16 was reproduced.

4.9. Appendix D. Cartesian Coordinates of All Optimized Structures

^{1}[Mn(O–Zn^{2+})(H_8Cz)]

Mn	-0.689146	-0.354553	0.347447
N	-0.699833	0.381425	2.121610
N	1.126140	-0.827494	0.547558
N	-0.316615	-0.224485	-1.535091
N	-1.786738	1.079158	-0.134287
C	-1.640725	1.269102	2.655258
C	-1.384389	1.387840	4.095171
C	-0.289671	0.629349	4.384842
C	0.163960	0.017677	3.133786
C	1.721156	-1.090351	1.781038
C	2.956697	-1.832977	1.549883
C	3.101270	-1.999155	0.205069
C	1.959470	-1.368135	-0.458124
C	0.724349	-0.643294	-2.290146
C	0.512653	-0.172174	-3.658479
C	-0.634855	0.586280	-3.665798
C	-1.143179	0.607086	-2.305654
C	-2.011680	1.333353	-1.499221
C	-3.026006	2.357613	-1.580531
C	-3.376151	2.702233	-0.289093
C	-2.575969	1.903544	0.621749
N	-2.534891	1.976648	1.972835
N	1.275583	-0.714876	2.983021
N	1.800941	-1.287245	-1.771405
H	-1.971972	2.008805	4.753549
H	0.206920	0.487686	5.332092
H	3.607319	-2.157198	2.346451
H	3.898698	-2.484276	-0.336012
H	1.164423	-0.397069	-4.487940
H	-1.087916	1.083544	-4.507193
H	-3.436295	2.760917	-2.493171
H	-4.106174	3.431071	0.029343
O	-1.600274	-1.724653	0.458108
Zn	-2.626640	-2.915421	-0.745640
S	-4.093071	-1.648092	-3.494336
C	-5.769581	-0.640452	-3.232739
F	-6.606106	-1.354633	-2.422978
F	-5.478361	0.573242	-2.660167
F	-6.351779	-0.435400	-4.455237
O	-3.598772	-1.646588	-1.870472
O	-4.480551	-3.134838	-4.023397
O	-3.166738	-0.675939	-4.424974
S	-2.549498	-5.711717	-0.679959

O	-1.498142	-4.582644	-1.387306
O	-3.263797	-6.816069	-1.615264
O	-3.511117	-4.627438	0.207073
C	-1.425329	-6.746239	0.602864
F	-0.610099	-7.546073	-0.146270
F	-0.686495	-5.888748	1.366818
F	-2.245054	-7.501601	1.391614

^{3}[Mn(O–Zn^{2+})(H_8Cz)] (^{3}A)

Mn	-0.515616	-0.230794	0.380169
N	-0.508560	0.482951	2.139093
N	1.257589	-0.887369	0.570066
N	-0.203134	-0.114439	-1.481228
N	-1.757146	1.122486	-0.086744
C	-1.471578	1.341348	2.693046
C	-1.218266	1.397150	4.137434
C	-0.136791	0.611439	4.409726
C	0.332262	0.036689	3.146392
C	1.853506	-1.148387	1.789910
C	3.077857	-1.912751	1.538707
C	3.194948	-2.085390	0.190243
C	2.048659	-1.432902	-0.455903
C	0.772283	-0.648257	-2.259492
C	0.472469	-0.272182	-3.637565
C	-0.661291	0.516649	-3.631153
C	-1.090000	0.654905	-2.253316
C	-1.979246	1.372176	-1.448287
C	-2.985342	2.415655	-1.519100
C	-3.298028	2.781512	-0.226436
C	-2.495339	1.964181	0.681279
N	-2.394928	2.034651	2.034502
N	1.413072	-0.739236	2.989535
N	1.840559	-1.329868	-1.763020
H	-1.805929	1.993799	4.817751
H	0.341022	0.424272	5.358831
H	3.740298	-2.247482	2.321283
H	3.977353	-2.585953	-0.358771
H	1.053216	-0.585054	-4.490949
H	-1.166202	0.948446	-4.480257
H	-3.408137	2.802363	-2.431659
H	-4.000660	3.534406	0.096883
O	-1.454145	-1.655131	0.488632
Zn	-2.683560	-2.632023	-0.669828
S	-4.031510	-1.120021	-3.385558
C	-5.931666	-1.638497	-3.565118
F	-6.068952	-2.942688	-3.181739

F	-6.696599	-0.829142	-2.771373
F	-6.299669	-1.490639	-4.875569
O	-3.847651	-1.448439	-1.734867
O	-3.126158	-2.092289	-4.330627
O	-3.993424	0.485311	-3.697687
S	-2.868979	-5.431958	-0.654308
O	-1.814561	-4.405875	-1.496684
O	-3.801858	-6.459991	-1.484043
O	-3.618020	-4.275586	0.334339
C	-1.712287	-6.531050	0.548886
F	-0.918451	-7.320950	-0.235070
F	-0.946683	-5.699208	1.316556
F	-2.518754	-7.300092	1.339385

^{3}[Mn(O–Zn^{2+})(H_8Cz)] (^{3}E)

Mn	0.06015714129562	-0.06720611724940	-0.12985120238842
N	1.97634580002008	0.05318073509513	-0.10157225741435
N	-0.06590311154177	1.81746993047427	-0.06837576644008
N	-1.62397137761018	-0.08191400802559	0.77112897746563
N	0.24083493768134	-1.58494619668048	0.93835165628215
C	2.86640836772639	-0.98790427320114	0.19504603264440
C	4.22839122442172	-0.49921718301200	-0.05619527670285
C	4.13959196669204	0.80853931593183	-0.42902465059887
C	2.71944749180798	1.16819642179597	-0.43486345159327
C	0.93589410787314	2.68704962816098	-0.49211692599893
C	0.34659310157358	4.00950788154326	-0.69429493565391
C	-0.97778872602778	3.92851642334044	-0.38562489009880
C	-1.26826400092537	2.55310085275580	0.02858846920296
C	-2.59811577437282	0.84689278530735	0.88994544937071
C	-3.71323911332473	0.23318599419598	1.60960722645822
C	-3.34246520883419	-1.05271490894258	1.93857026380297
C	-1.99283743082565	-1.25294177118303	1.43736116886416
C	-0.92062300225259	-2.13770362979547	1.50994779058547
C	-0.56346361776361	-3.44013370735424	2.02234056487264
C	0.77951256039132	-3.63338838339058	1.76806108069694
C	1.28849389708551	-2.44988540060469	1.09162941765428
N	2.55946782671532	-2.17237227336991	0.71594734101059
N	2.22894853241402	2.39436584257974	-0.66463444038851
N	-2.44695273952900	2.12927772013944	0.46396146409682
H	5.11001304443751	-1.10539888927328	0.08365685830079
H	4.93141583454145	1.50172369904125	-0.66559708054312
H	0.91422883114402	4.86434175033705	-1.02668160303047
H	-1.72694018304279	4.70489869473699	-0.40769611272416
H	-4.64448355557859	0.72975021771531	1.83344231879028
H	-3.93017723139460	-1.79641081276340	2.45117225375128
H	-1.24988732697915	-4.13038173535757	2.48578402602308

H	1.37860379460464	-4.49733425669057	2.01086450253538
O	-0.40502112400902	-0.60162730160897	-1.61489196496072
Zn	-1.64883769280645	-1.73151208491184	-2.66380695408117
S	-3.61757809783984	-3.75241962277224	-0.94008727353044
C	-3.66405731971722	-5.63271975923621	-1.55082835464604
F	-3.28395069375260	-5.69550300904168	-2.86101447304768
F	-2.82086559112046	-6.37889826652197	-0.77475969557594
F	-4.94941536924037	-6.07972981036433	-1.40739498171850
O	-2.11171548138934	-3.28520729225709	-1.56336904960450
O	-4.83006591355612	-2.95765628033830	-1.68261210271207
O	-3.60665906282469	-3.84885747397762	0.69107113940859
S	-1.98330019864196	-1.05056262625653	-5.36344135822244
O	-2.74027252782501	-0.45057292600983	-3.96578794340925
O	-2.86453092850184	-1.53528350701602	-6.62653500725019
O	-0.92261107114504	-2.14987120080306	-4.62916909131204
C	-0.83051945169848	0.44412504547579	-5.99693405613932
F	-1.56508859193285	1.59368895727086	-6.03270777537278
F	0.20923774163104	0.56970153477440	-5.12143177595729
F	-0.37541732651959	0.13100512333605	-7.24277765515283

^{5}[Mn(O–Zn^{2+})(H_8Cz)]

Mn	-0.42231672006366	-0.27310304856008	0.21950852895314
N	-0.57441347680963	0.29984190158255	2.02716015637614
N	1.38806040879722	-0.79881678659612	0.47064915054416
N	0.00248349628291	0.04662697316727	-1.59702737744582
N	-1.73412911211183	1.02389113824022	-0.21779204418431
C	-1.63375770316502	1.03631618124204	2.58010176839938
C	-1.45636987046318	1.01667121679210	4.03773706890918
C	-0.32331412919246	0.31143978607166	4.31924087569989
C	0.25543392710014	-0.13530587384871	3.04934085179907
C	1.95179072694712	-1.07285519858673	1.70461556312972
C	3.26952472023079	-1.66993065146742	1.47559298075943
C	3.47388573564283	-1.72751461855169	0.12811925677015
C	2.29090996783154	-1.16733640770593	-0.53907774559881
C	1.04669304024223	-0.37023050621579	-2.35813391259785
C	0.77214656717966	0.05300938087442	-3.72765440954246
C	-0.42398426611581	0.74283906093942	-3.73021074494118
C	-0.91763735096056	0.76848450341619	-2.36625718744543
C	-1.91385658795023	1.34055056187469	-1.56788620456196
C	-3.02455380244890	2.27287094730621	-1.62914566674832
C	-3.44169561600930	2.51132488136617	-0.33559381806481
C	-2.60320923377609	1.72003547059985	0.56064532601957
N	-2.58089263825628	1.69519799842331	1.91908175975896
N	1.41553866177503	-0.79033774234161	2.90212085484943
N	2.14535681039697	-0.98750715039139	-1.84755223782011
H	-2.12863077381624	1.51249210745551	4.72052316565384

H	0.12456858698483	0.10592259692849	5.27902552253683
H	3.92966515287007	-1.97479629021824	2.27205256639870
H	4.33802433944429	-2.09032442693570	-0.40647452849573
H	1.41560643465313	-0.15559894547151	-4.56809674167528
H	-0.93010688374970	1.17461175420016	-4.57833025006871
H	-3.43998752189645	2.67891321518255	-2.53701059405161
H	-4.23851099993113	3.16058447977251	-0.00653507221513
O	-1.26767407512509	-1.75129165292415	0.11913456391335
Zn	-2.64499442358197	-2.80979528028428	-0.74955368989589
S	-4.04405640304547	-1.30715967930963	-3.40595928668931
C	-6.01248525037170	-1.20406148864823	-3.38862491908903
F	-6.52275189070341	-2.42511498722660	-3.05527418216381
F	-6.39223043753364	-0.26119684659501	-2.47123910146825
F	-6.44505712180451	-0.83753749084849	-4.63477478579916
O	-3.82920808311735	-1.59768622058683	-1.75400691306347
O	-3.56921784164793	-2.56946511676661	-4.31544219895349
O	-3.57026609610542	0.19171233050782	-3.85811273067271
S	-3.09814073956256	-5.55010085488524	-0.27294271932531
O	-2.06386242366706	-4.78093724675250	-1.37378310895406
O	-4.21741420824141	-6.58890108622322	-0.80793877330683
O	-3.60093597824875	-4.18185181070380	0.59243749577466
C	-1.89536125548369	-6.61196221199334	0.91823689176461
F	-1.10501363082189	-7.40008302457407	0.12932810168387
F	-1.12618891083537	-5.76393586070504	1.66419973061742
F	-2.68149211976509	-7.38184898002520	1.72787376452736

^{1}[Mn(O–B(C_6F_5)$_3$)(H_8Cz)]

Mn	0.007382	-0.092390	0.050963
N	-0.338460	0.396066	-1.746818
C	0.604964	0.444220	-2.795975
N	1.932322	0.557350	-2.668664
C	2.471091	0.651543	-1.457582
N	1.728262	0.548931	-0.280713
C	2.555324	0.831984	0.799362
C	1.812162	0.864941	1.983441
N	0.471907	0.593741	1.722989
C	-0.266775	0.817206	2.886502
N	-1.592551	0.779651	2.930666
C	-2.283060	0.594996	1.801317
N	-1.749723	0.452478	0.503982
C	-2.845330	0.459678	-0.382319
N	-2.771135	0.436810	-1.707923
C	-1.608856	0.422042	-2.349440
C	-1.447917	0.449663	-3.776687
C	-0.102096	0.452528	-4.048454
H	0.393028	0.487465	-5.006431

H	-2.276866	0.459617	-4.466705
F	4.972936	-2.162559	-1.398991
C	3.814265	-2.875716	-1.621902
C	3.673118	-3.629130	-2.783705
C	2.493421	-4.334144	-2.993243
C	1.468819	-4.267150	-2.047799
C	1.553814	-3.515007	-0.869427
B	0.363047	-3.338117	0.224226
C	-1.067449	-4.007845	-0.139114
C	-1.861484	-3.540523	-1.191183
C	-3.088853	-4.087956	-1.543982
C	-3.575225	-5.179362	-0.829341
C	-2.813722	-5.704587	0.208118
C	-1.591621	-5.117752	0.534383
F	-0.889949	-5.712659	1.571454
F	-3.266086	-6.805187	0.899639
F	-4.793327	-5.733451	-1.140392
F	-3.807897	-3.571899	-2.598605
F	-1.413695	-2.480819	-1.972074
C	0.796743	-3.511676	1.778551
C	0.050474	-2.915771	2.800046
C	0.398958	-2.963146	4.145616
C	1.528639	-3.676821	4.530825
C	2.282677	-4.325717	3.558322
C	1.908433	-4.237270	2.219983
F	2.708066	-4.924399	1.320593
F	3.399033	-5.043944	3.918555
F	1.895520	-3.738672	5.854467
F	-0.363100	-2.307156	5.085678
F	-1.115184	-2.219185	2.492726
C	2.771965	-2.840136	-0.705299
F	2.987221	-2.076032	0.437784
F	0.338140	-5.010481	-2.338737
F	2.336595	-5.085702	-4.135385
F	4.689436	-3.670281	-3.706463
C	-4.059758	0.547934	0.381427
C	-3.717123	0.623794	1.709056
H	-4.361214	0.724025	2.568334
H	-5.041308	0.557307	-0.066527
C	0.665687	1.160695	3.924994
C	1.937249	1.194266	3.371421
H	2.856942	1.445631	3.877412
H	0.378456	1.363646	4.945100
C	3.878011	1.062321	0.299639
C	3.829169	0.941717	-1.080369
H	4.642024	1.046536	-1.781903

H	4.745113	1.294299	0.898762
O	0.086968	-1.701533	0.116348

^{3}[Mn(O–B(C_6F_5)$_3$)(H_8Cz)] (^{3}A)

Mn	-0.065407	-0.006080	0.068711
N	0.278780	0.319771	-1.771577
C	1.514780	0.672569	-2.349502
N	2.585996	1.129691	-1.717909
C	2.580196	1.300707	-0.373015
N	1.546975	0.942652	0.430396
C	1.762108	1.400173	1.735255
C	0.626815	1.239721	2.532823
N	-0.430673	0.677328	1.813734
C	-1.569155	0.692477	2.549018
N	-2.788706	0.362185	2.051588
C	-2.952935	0.081938	0.764242
N	-1.952113	0.030208	-0.226216
C	-2.565343	-0.097091	-1.464176
N	-1.954485	-0.074547	-2.653122
C	-0.641092	0.120616	-2.795403
C	0.059465	0.268139	-4.072387
C	1.355894	0.591064	-3.804252
H	2.156101	0.801685	-4.496246
H	-0.425203	0.149961	-5.029059
F	4.009925	-2.140837	-3.170682
C	2.984234	-2.967647	-2.758861
C	2.594179	-4.039563	-3.552153
C	1.565812	-4.865837	-3.111806
C	0.925752	-4.592322	-1.903963
C	1.259180	-3.509924	-1.080904
B	0.540365	-3.155114	0.357873
C	-0.984479	-3.757006	0.513289
C	-1.940950	-3.466979	-0.466351
C	-3.287735	-3.796263	-0.376234
C	-3.741453	-4.490043	0.741551
C	-2.835550	-4.820264	1.742185
C	-1.494713	-4.448519	1.616285
F	-0.677175	-4.800812	2.678702
F	-3.271861	-5.488754	2.865258
F	-5.069267	-4.834655	0.852189
F	-4.178171	-3.413388	-1.361691
F	-1.556496	-2.779785	-1.619037
C	1.575264	-3.598170	1.563168
C	2.071007	-2.775893	2.578338
C	2.981231	-3.208599	3.544857
C	3.431315	-4.521592	3.535006

C	2.952995	-5.389631	2.558152
C	2.051747	-4.916012	1.610236
F	1.590175	-5.837117	0.677940
F	3.371188	-6.702379	2.544607
F	4.334022	-4.957220	4.479787
F	3.432983	-2.336660	4.516459
F	1.678944	-1.446400	2.709284
C	2.329488	-2.742391	-1.550382
F	2.800535	-1.666650	-0.797182
F	-0.082037	-5.471208	-1.543439
F	1.192198	-5.950469	-3.872863
F	3.213796	-4.272693	-4.759677
C	-4.010870	-0.185835	-1.252062
C	-4.243460	-0.089932	0.087281
H	-5.188051	-0.094470	0.608894
H	-4.721406	-0.303726	-2.054600
C	-1.230890	1.243872	3.859434
C	0.106786	1.581190	3.843622
H	0.671163	2.032528	4.645301
H	-1.935673	1.373445	4.666172
C	3.062614	2.039520	1.745863
C	3.564176	1.981627	0.462062
H	4.500657	2.373114	0.096586
H	3.531350	2.495710	2.604146
O	0.322779	-1.630508	0.454991

^{3}[Mn(O–B(C_6F_5)$_3$)(H_8Cz)] (^{3}E)

Mn	-0.03424733045954	-0.05438306469219	0.07548763000539
N	0.32836733020929	0.28918385200817	-1.78376226209889
C	1.55336369197747	0.67610251836876	-2.34354936887671
N	2.60833526068133	1.14436642339672	-1.68742060282755
C	2.55191044700474	1.31433622195535	-0.35060076852761
N	1.47428952003909	0.98723849678057	0.43033554131621
C	1.71061952608607	1.40470801578710	1.75124657985435
C	0.59871228771814	1.20162648901197	2.56221573440027
N	-0.43599544273889	0.60605686086411	1.84413444598014
C	-1.57982716574282	0.66806761168113	2.55523204824805
N	-2.79458533018513	0.37923469575737	2.01928490363621
C	-2.90893147138265	0.15802089801624	0.71790766548508
N	-1.88150685115989	0.14610605770722	-0.25977846855486
C	-2.49580477457161	-0.00089930454902	-1.50651762878886
N	-1.89533416770421	-0.00850485115333	-2.69620222124333
C	-0.57488732280676	0.15071359733475	-2.82494281272433
C	0.12852290502894	0.33060588160336	-4.09639308970511
C	1.42093518284897	0.64377172746567	-3.80464047127220
H	2.23072939880000	0.87822614101066	-4.47748506287884

H	-0.35230043041593	0.24934159177100	-5.05882379189608
F	3.99720293507958	-2.24558909396393	-3.19778661556768
C	2.95872011723775	-3.04897484028850	-2.77534911775735
C	2.55426609926345	-4.12757246124744	-3.55253385131223
C	1.51679124913220	-4.93588707756953	-3.10038614588589
C	0.88359170489582	-4.63865218022860	-1.89490161497767
C	1.23547427501451	-3.55186933086009	-1.08632286376270
B	0.54059038523111	-3.18874773977388	0.35655277360013
C	-0.99599489529797	-3.74061490269208	0.52999878707639
C	-1.95369683358859	-3.43973430056007	-0.44635907196435
C	-3.30207964076581	-3.75976364036974	-0.34764372233360
C	-3.75434706737626	-4.44852579843080	0.77370108805597
C	-2.84708933418584	-4.78546203005739	1.77068648411450
C	-1.50397678639053	-4.42646490884241	1.63782515337815
F	-0.68115120438093	-4.78851495573785	2.69186891619292
F	-3.28410275464210	-5.44979648013155	2.89488584365429
F	-5.08265817038446	-4.78401756859672	0.89158936803338
F	-4.19401320903098	-3.37682762542595	-1.32982609992598
F	-1.56893353563800	-2.75878776156462	-1.60053503449567
C	1.57511422435201	-3.61869798982993	1.55657714426726
C	2.07345357159718	-2.78786177992513	2.56252297382543
C	2.98008023850151	-3.21223891675153	3.53506765295363
C	3.42806315530298	-4.52600156390011	3.53668607032430
C	2.95099795505081	-5.40171987546183	2.56587447403854
C	2.05008190519387	-4.93679922425956	1.61346791695764
F	1.58822707586544	-5.86508257893210	0.68871861100031
F	3.36996898002404	-6.71377767816180	2.56191666206654
F	4.32810647506061	-4.95478762445665	4.48623986891442
F	3.43033821356586	-2.33217467677827	4.49896073147013
F	1.68567623994169	-1.45636774911697	2.66767869075454
C	2.30918476768478	-2.79864551765737	-1.56973448100008
F	2.78715065461468	-1.71632072364637	-0.83102953871477
F	-0.13485383387599	-5.49755641040435	-1.51776653402368
F	1.12980960520598	-6.02765346547176	-3.84456833006273
F	3.17149392208933	-4.38359810306688	-4.75596197404436
C	-3.93717205485803	-0.11294850971034	-1.31139184259660
C	-4.18568887160014	-0.02635594600914	0.02399462382922
H	-5.13361278420588	-0.05699290173783	0.53895318265423
H	-4.63358879306492	-0.24560804642391	-2.12393018687627
C	-1.26887883014950	1.23976612326966	3.86511451571733
C	0.06908371410131	1.56989708261526	3.86391965937172
H	0.62361770827003	2.04242805092549	4.66034201196667
H	-1.99015691997096	1.39726800220844	4.65201394158261
C	3.02455835666110	2.00162315185035	1.78473145064074
C	3.54172464069341	1.94217607062385	0.50656392818711
H	4.50034615176986	2.29473760886850	0.15935348130918

H	3.50251436709595	2.41752589163732	2.65843100847026
O	0.31102256768294	-1.64344386408157	0.40659601136284

^{5}[Mn(O–B(C_6F_5)$_3$)(H_8Cz)]

Mn	-0.072158	-0.009367	0.063990
N	0.256756	0.313099	-1.778876
C	1.483530	0.672107	-2.366976
N	2.564005	1.125328	-1.745042
C	2.573636	1.290903	-0.400552
N	1.540397	0.945821	0.410437
C	1.768704	1.397701	1.712265
C	0.639797	1.237403	2.521246
N	-0.423957	0.679082	1.811500
C	-1.554111	0.684670	2.561321
N	-2.777334	0.354374	2.073312
C	-2.952641	0.075711	0.786804
N	-1.961488	0.024232	-0.212684
C	-2.586846	-0.106154	-1.445136
N	-1.986483	-0.077753	-2.640521
C	-0.675241	0.117998	-2.795892
C	0.011521	0.274361	-4.079021
C	1.308901	0.600973	-3.821772
H	2.102028	0.816799	-4.520348
H	-0.482693	0.161019	-5.031312
F	4.034940	-2.126715	-3.146092
C	3.012098	-2.959113	-2.738557
C	2.631824	-4.033598	-3.533124
C	1.605075	-4.864475	-3.097828
C	0.957422	-4.593903	-1.893318
C	1.280833	-3.509087	-1.069316
B	0.548497	-3.154940	0.363524
C	-0.980470	-3.751060	0.500821
C	-1.921248	-3.463216	-0.494373
C	-3.270961	-3.782918	-0.419582
C	-3.744878	-4.464007	0.697581
C	-2.855623	-4.790716	1.714028
C	-1.510720	-4.427961	1.603628
F	-0.710125	-4.770801	2.681589
F	-3.314314	-5.444461	2.837036
F	-5.076480	-4.798626	0.791967
F	-4.145882	-3.401106	-1.418873
F	-1.517356	-2.784841	-1.646092
C	1.570612	-3.601139	1.577685
C	2.065062	-2.778296	2.593147
C	2.970016	-3.212167	3.564074
C	3.415136	-4.526937	3.559086

C	2.937307	-5.395623	2.582636
C	2.041359	-4.920855	1.630185
F	1.581405	-5.841800	0.696942
F	3.351425	-6.709765	2.573346
F	4.312996	-4.963502	4.507994
F	3.421974	-2.339662	4.535026
F	1.677403	-1.447292	2.719082
C	2.349811	-2.736688	-1.533632
F	2.810780	-1.657166	-0.779705
F	-0.049107	-5.476426	-1.538446
F	1.239105	-5.949519	-3.861900
F	3.259353	-4.264989	-4.736900
C	-4.029598	-0.199172	-1.219933
C	-4.249665	-0.098684	0.121191
H	-5.189309	-0.104635	0.651696
H	-4.747254	-0.318661	-2.015776
C	-1.202605	1.228686	3.869912
C	0.134236	1.570473	3.839578
H	0.707223	2.016732	4.637995
H	-1.898326	1.354451	4.685034
C	3.076112	2.025039	1.714415
C	3.570457	1.960411	0.428191
H	4.507511	2.344703	0.056634
H	3.555241	2.475196	2.570181
O	0.330005	-1.630569	0.457034

5. Chapter 5. Site-Selective Protonation of a Terminal Imido Manganese Porphyrinoid Complex Using Relative Basicities

5.1. Introduction

Transforming inert C–H bonds to useful C-heteratom functionalities remains a difficult challenge in organic synthesis.[1,2] Much effort has been focused on the development of simple synthetic methods for the formation of C–N bonds using metal-based catalysts. Metal-nitrene species have been invoked as intermediates in these catalytic cycles, although the direct characterization or isolation of the intermediates during catalysis is rare.[3,4] Recently, a manganese-phthalocyanine complex was found to be an extremely fast and chemoselective catalyst for the intramolecular C–H amination of an sp^3 C–H substrate, and a putative high-valent metallonitrene intermediate was proposed to be the key C–H bond cleaving intermediate.[5]

The corrolazine (Cz) ligand is able to stabilize metal ions in high-oxidation states, which has allowed for the synthesis and characterization of isolable high-valent metal-oxo and -imido species. The stability of these compounds gave us the opportunity to study the factors that determine their reactivity in a controlled environment. A high-valent manganese-imido corrolazine complex, Mn^{V}(NMes)(TBP_8Cz) (NMes = 2,4,6-trimethylphenylimido^{2-}) (TBP_8Cz = octakis(*p-tert*-butylphenyl)corrolazinato^{3-}), was synthesized and characterized previously.[6] The Mn^{V}(NMes)(TBP_8Cz) complex was found to be completely unreactive with all substrates added, including TEMPOH, a common H-atom donor with a very weak O–H bond (BDFE(O–H) = 67 kcal/mol), as well as strong reductants such as Cp_2Co ($E_{1/2}$ = −1.33 V vs Fc^{+}/Fc^{0}). The electrochemical

properties of $Mn^{V}(NMes)(TBP_8Cz)$ revealed no accessible redox process until at least −1.7 V vs Fc^{+}/Fc^{0} consistent with the "non-reducible" reactivity of the complex. The oxo analogue of this complex, manganese(V)-oxo corrolazine, was first reported in 2002.[7] This complex was stable enough to be isolated and characterized by NMR, resonance Raman, LDI-MS, and XAS but also reactive enough to oxidize triphenylphosphine and the O–H bonds of phenol substrates.[8] Just recently, an X-ray crystal structure of the $Mn^{V}(O)(TBP_8Cz)$ was obtained, which was the first reported crystal structure of a $Mn^{V}(O)$ in any porphyrinoid ligand system.[9] The effects of various modifications including ligand oxidation[10] and addition of axial ligands[11-13] or Lewis acids[14-17] on the H-atom transfer (HAT) and oxygen atom transfer (OAT) reactivity of $Mn^{V}(O)(TBP_8Cz)$ have been studied.

In addition to the aforementioned modifications, the influence of proton (H^{+}) sources on metallocorrolazines showed that protonation at the remote *meso*-nitrogen positions of complexes could be achieved. The redox-inert $Re^{V}(O)(TBP_8Cz)$ complex could be protonated at the *meso*-nitrogen position by $HBAr^{F}$, which is a strong acid with a non-coordinating counterion.[18] The addition of $HBAr^{F}$ to $Mn^{III}(TBP_8Cz)$ resulted in protonation of the *meso*-nitrogens on the corrolazine ring, and allowed for the isolation of mono- and di- protonated $[Mn^{III}(TBP_8CzH_n)]^{n+}$ species. The site of protonation could be controlled in the high-valent complex $Mn^{V}(O)(TBP_8Cz)$ by addition of $HBAr^{F}$ at certain temperatures (Scheme 5.1). At -60 °C, the $Mn^{V}(O)(TBP_8Cz)$ was protonated at a *meso*-N site, whereas at room temperature, the oxo ligand was protonated, resulting in the valence tautomer of $Mn^{V}(O)$, $Mn^{IV}(O)(TBP_8Cz^{\bullet+})$, in which an electron was transferred from the Cz ring to the metal center.[14,19] Because the two protic tautomers, $[Mn^{V}(O)(TBP_8CzH)]^{+}$

and $[Mn^{IV}(O–H)(TBP_8Cz^{\bullet+})]^+$, were not reversibly interconvertible, their comparative reactivity could not be studied.

Scheme 5.1. Temperature dependence of protonation sites for $Mn^{V}(O)(TBP_8Cz)$ with $HBAr^F$.

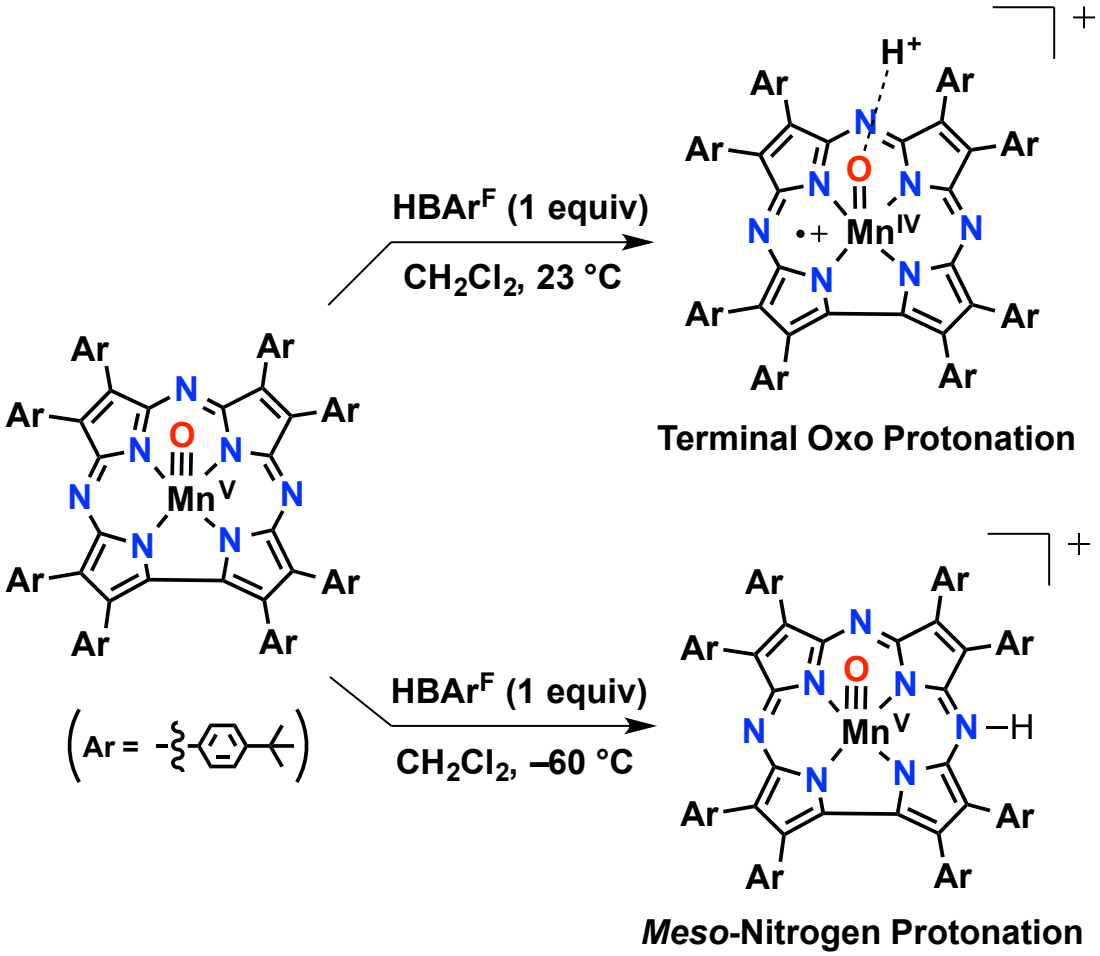

Here we show the synthesis and characterization of a novel, electron-deficient high-valent Mn^{V}-imido corrolazine complex, $Mn^{V}(NC_6Cl_3H_2)(TBP_8Cz)$ ($NC_6Cl_3H_2$ = 2,4,6-trichlorophenylimido^{2-}), from $Mn^{III}(TBP_8Cz)$ and photolysis of an electron-deficient azide precursor. Controlled addition of proton sources results in protonation of either the terminal imido ligand or the basic *meso*-nitrogen positions, depending on the strength of the acid.

5.2. Experimental Methods

5.2.1. General methods and materials

The compound $Mn^{III}(TBP_8Cz)$ was synthesized according to a published procedure.[8] The imide source 2,4,6-trichlorophenylazide was synthesized according to a published procedure.[20] All other reagents were commercially available and were purchased at the highest level of purity and used as received unless otherwise specified here. The oxonium acid $[H(OEt_2)_2]^+[B(C_6F_5)_4]^-$ ($HBAr^F$) was synthesized according to a published procedure.[21] Deuterated solvent ($CDCl_3$) for NMR was purchased from Cambridge Isotopes, Inc.

5.2.2. Analytical methods

UV-vis spectroscopy was performed on a Hewlett-Packard 8453 diode-array spectrophotometer equipped with HPChemstation software. A UV filter was used for UV-vis experiments to block light < 400 nm to protect the reaction mixtures from photoreduction. The light source for azide photolysis was a Cole–Parmer Illuminator equipped with a halogen lamp (150 W). ^{1}H-NMR spectra were recorded on a Bruker Avance 400 MHz NMR spectrometer at room temperature. Cyclic voltammetry measurements were undertaken in methylene chloride using a BAS 100B electrochemical analyzer with a glassy carbon working electrode and a platinum wire auxiliary electrode. Potentials were recorded versus an $Ag/AgNO_3$ electrode. Scans were run at 50 mV/s under Ar atmosphere using $[Bu_4N][PF_6]$ (0.1 M) as the supporting electrolyte.

5.2.3. Single Crystal X-ray Crystallography

All reflection intensities were measured at 110(2) K using a SuperNova diffractometer (equipped with Atlas detector) with Cu *K*α radiation (λ = 1.54178 Å)

under the program CrysAlisPro (Version 1.171.36.32 Agilent Technologies, 2013). The same program was used to refine the cell dimensions and for data reduction. The structure was solved with the program SHELXS-2014/7 (Sheldrick, 2008) and was refined on F^2 with SHELXL-2014/7 (Sheldrick, 2008). Analytical numeric absorption correction based on a multifaceted crystal model was applied using CrysAlisPro. The temperature of the data collection was controlled using the system Cryojet (manufactured by Oxford Instruments). The H atoms were placed at calculated positions (unless otherwise specified) using the instructions AFIX 43 or AFIX 137 with isotropic displacement parameters having values 1.2 or 1.5 *U*eq of the attached C atoms.

Additional notes:

(i) When taking out the crystals from the mother liquor, the crystals were protected in Paratone oil on a microscope slide under a cold N_2(g) stream to prevent crystal damage (as lattice solvent molecules are likely to escape the crystal lattice).

(ii) The final data-to-parameter ratio is 10.

5.2.4. Structure of $Mn^{V}(NC_6Cl_3H_2)(TBP_8Cz)$

Table 5.1. Crystal data for $Mn^{V}(NC_6Cl_3H_2)(TBP_8Cz)$

	xs0701a
Crystal data	
Chemical formula	$C_{102}H_{106}Cl_3MnN_8$
M_r	1605.23
Crystal system, space group	Triclinic, *P*-1
Temperature (K)	110
a, *b*, *c* (Å)	14.5261 (3), 17.4547 (3), 21.8456 (5)
α, β, γ (°)	100.4665 (18), 92.5595 (18), 100.3396 (16)
V (Å^3)	5341.20 (19)
Z	2
Radiation type	Cu *K*α
μ (mm^{-1})	2.02

Crystal size (mm)	0.35 × 0.28 × 0.18
Data collection	
Diffractometer	SuperNova, Dual, Cu at zero, Atlas diffractometer
Absorption correction	Analytical *CrysAlis PRO*, Agilent Technologies, Version 1.171.36.32 (release 02-08-2013 CrysAlis171 .NET) (compiled Aug 2 2013,16:46:58) Analytical numeric absorption correction using a multifaceted crystal model based on expressions derived by R.C. Clark & J.S. Reid. (Clark, R. C. & Reid, J. S. (1995). Acta Cryst. A51, 887-897)
T_{min}, T_{max}	0.581, 0.756
No. of measured, independent and observed [$I > 2\sigma(I)$] reflections	63233, 20851, 17333
R_{int}	0.030
$(\sin \theta/\lambda)_{max}$ (Å^{-1})	0.616
Refinement	
$R[F^2 > 2\sigma(F^2)]$, $wR(F^2)$, S	0.071, 0.215, 1.03
No. of reflections	20851
No. of parameters	2084
No. of restraints	4174
H-atom treatment	H-atom parameters constrained
$\Delta\rho_{max}$, $\Delta\rho_{min}$ (e Å^{-3})	0.63, -0.52

The corrolazine Mn complex is found to be wholly disordered over two orientations, and the occupancy factor of the major component of the disorder refines to 0.7325(16). The crystal lattice also contains a fair amount of disordered lattice solvent molecules (toluene) that are most likely not fully occupied. In order to keep the data-to-parameter ratio to an acceptable level (10), the contribution of those solvent molecules has been taken out in the final refinement (SQUEEZE details are provided in the CIF file, Spek, 2009).

5.2.5. Synthesis of $Mn^{IV}(NC_6Cl_3H_3)(TBP_8Cz)$

To an amount of $Mn^{III}(TBP_8Cz)$ (15 mg, 11 μmol) in degassed toluene under argon was added excess 2,4,6-trichlorophenylazide (47 mg, 0.21 mmol) in a schlenk flask. The mixture was irradiated using a white light source for ~40 min, followed by solvent evaporation to yield a green solid. After purification on silica gel (eluent: DCM, $R_f = 0.99$), the material was washed at least three times with acetonitrile to yield 16 mg of pure $Mn^{V}(NC_6Cl_3H_2)(TBP_8Cz)$ as a dark green solid (96 % yield). ^{1}H NMR (400 MHz, Methylene Chloride-d_2) δ 8.34 (dd, J = 8.6, 3.0 Hz, 8H), 8.00 (d, $^3J_{HH}$ = 8.7 Hz, 4H), 7.67 (dd, J = 8.6, 6.3 Hz, 8H), 7.52 (dd, J = 14.1, 8.6 Hz, 8H), 7.22 (d, $^3J_{HH}$ = 8.6 Hz, 4H), 6.26 (s, 2H), 1.51 (s, 42H), 1.43 (s, 15H), 1.39 (s, 15H). CV (CH_2Cl_2, 25 mV)): $E_{1/2}$ = 0.92 V, $E_{1/2}$ = 0.34 V, $E_{1/2}$ = -0.70V, $E_{1/2}$ = -1.75 V. UV-Vis (CH_2Cl_2) λ_{max} [nm] 429, 646.

5.2.6. Reaction of $Mn^{V}(NC_6Cl_3H_2)(TBP_8Cz)$ with $HBAr^F$

To an amount of $Mn^{V}(NC_6Cl_3H_2)(TBP_8Cz)$ (3.2 mM) was added $HBAr^F$ (3.2 mM, 1 equiv) in CD_2Cl_2 (500 μL) in an NMR tube. A color change from green to brown was observed. A ^{1}H-NMR spectrum was obtained of the starting material, followed by a spectrum after addition of the acid source. After initial spectral measurement, more $HBAr^F$ (4 equiv) was added and the spectrum was remeasured.

5.2.7. UV-vis Titration of $Mn^{V}(NC_6Cl_3H_2)(TBP_8Cz)$ with $HBAr^F$

To an amount of $Mn^{V}(NC_6Cl_3H_2)(TBP_8Cz)$ (11 μM) (λ_{max} = 429, 646 nm) in CH_2Cl_2 was titrated $HBAr^F$ in increments of 0.2 equiv (up to 1.0 and 2.0 equivalents), and the reaction was monitored by UV-vis spectroscopy. The formation of the mono-

(λ_{max} = 435, 713 nm) and di- (λ_{max} = 470, 759 nm) protonated complexes were observed after 1 and 2 equivalents of $HBAr^F$ were added, respectively.

5.2.8. Reaction of $Mn^V(NC_6Cl_3H_2)(TBP_8Cz)$ with the weak acids TCA or TFA

To an amount of $Mn^V(NC_6Cl_3H_2)(TBP_8Cz)$ (11 μM) was added TFA or TCA (11 μM, 1 equiv) in CH_2Cl_2 and a color change from green to brown was observed. Monitoring of this reaction by UV-vis showed isosbestic conversion from the spectrum for $Mn^V(NC_6Cl_3H_2)(TBP_8Cz)$ to a new spectrum with peaks at λ_{max} = 428 and 780 nm, which we have assigned to a $Mn^{IV}(NC_6Cl_3H_2)(TBP_8Cz^{\bullet+})$ species. Allowing this species to sit in solution for ~1 hr in air results in hydrolysis to the $Mn^{IV}(O)(TBP_8Cz^{\bullet+})$ species, which has features at λ_{max} = 419 and 789 nm, as shown in previous work.

5.3. Results and Discussion

5.3.1. Synthesis and characterization of $Mn^{IV}(NC_6Cl_3H_2)(TBP_8Cz)$

The synthesis of the high-valent $Mn^V(NC_6Cl_3H_2)(TBP_8Cz)$ was achieved through a photo-irradiation process (Scheme 5.2). We showed previously that $Mn^{III}(TBP_8Cz)$ achieves an open-shell excited state capable of reaction with dioxygen upon photoirradation to form $Mn^V(O)$, and we hypothesized that a similar process would allow for the synthesis of other high-valent species.[19,22] Addition of the electron-deficient aryl azide precursor, 2,4,6-trichlorophenyl azide, to a degassed solution of $Mn^{III}(TBP_8Cz)$ in toluene, followed by visible light irradiation for 20-40 min, resulted in a new species as seen by UV-vis. The spectrum for the starting complex $Mn^{III}(TBP_8Cz)$ (λ_{max} = 435, 685 nm) converted to a new spectrum with a Soret band at λ_{max} = 429 nm and a Q band at λ_{max} = 646 nm (Figure 5.1). These features resembled those obtained for the previously reported $Mn^V(NMes)(TBP_8Cz)$ complex (λ_{max} = 419, 659 nm), but are significantly

shifted.[6] This new species was purified by flash chromatography on silica gel (eluent: CH_2Cl_2), and washed several times with acetonitrile to remove the excess azide. ^{1}H-NMR spectroscopy of the purified material revealed a diamagnetic spectrum, indicative of a low-spin Mn^V (d^2) complex (Figure 5.2). The singlet phenyl peak for the trichlorophenylimido ligand ($NC_6Cl_3H_2$) is shifted significantly downfield (6.26 ppm) relative to the NMes ligand in the Mn^V(NMes)(TBP_8Cz) complex (5.74), consistent with the trichlorophenylimido being a more electron-withdrawing ligand. However, ring current effects for this shift cannot be ruled out. The aryl protons on the corrolazine ring appear in a series of 8 doublets in an 8:4:8:8:4 integration ratio, as found with both Mn^V(NMes)(TBP_8Cz) and Mn^V(O)(TBP_8Cz) complexes. The aliphatic region of the ^{1}H-NMR spectrum for Mn^V($NC_6Cl_3H_2$)(TBP_8Cz) exhibits 3 singlets with an integration ratio of 36:18:18 due to the *para-tert*-butyl methyl groups. This spectrum is almost identical in integration ratio and chemical shift to the Mn^V(NMes)(TBP_8Cz), aside from the imido-aryl protons.

Scheme 5.2. Synthesis of the high-valent Mn-imido complex, $Mn^V(NC_6Cl_3H_2)(TBP_8Cz)$ using visible light.

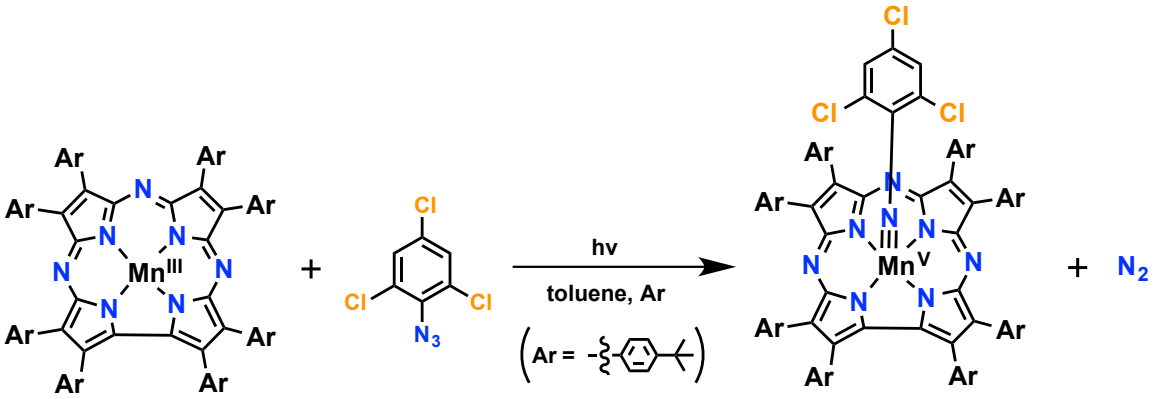

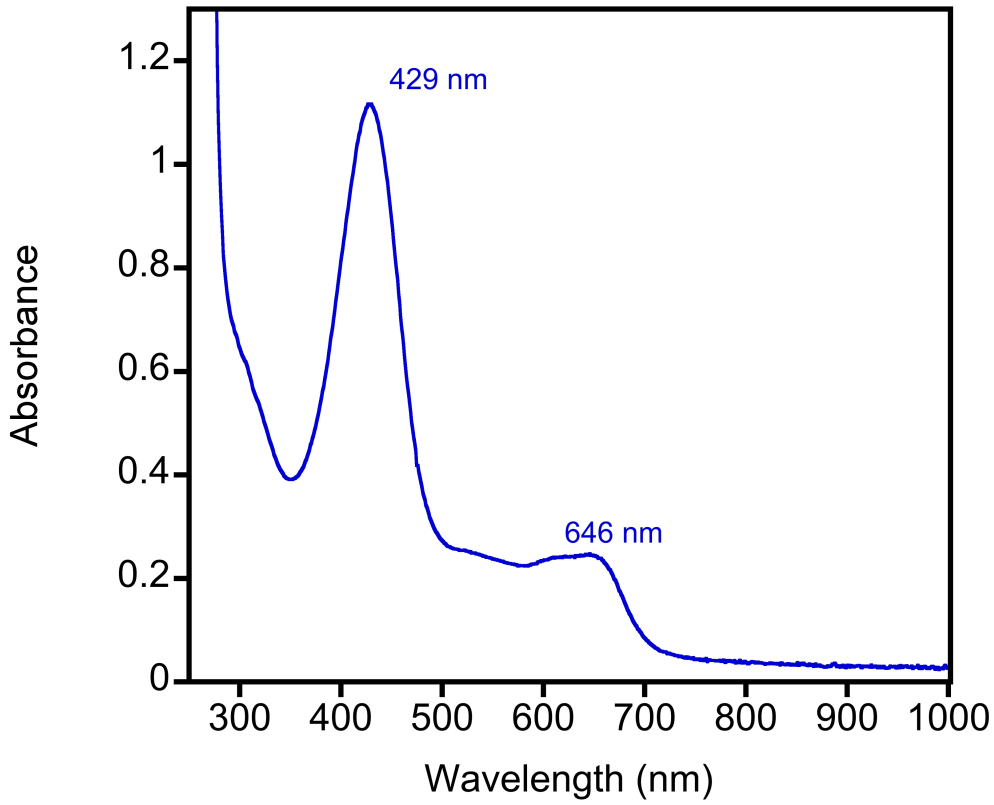

Figure 5.1. UV-visible spectrum of $Mn^{V}(NC_6Cl_3H_2)(TBP_8Cz)$ in CH_2Cl_2.

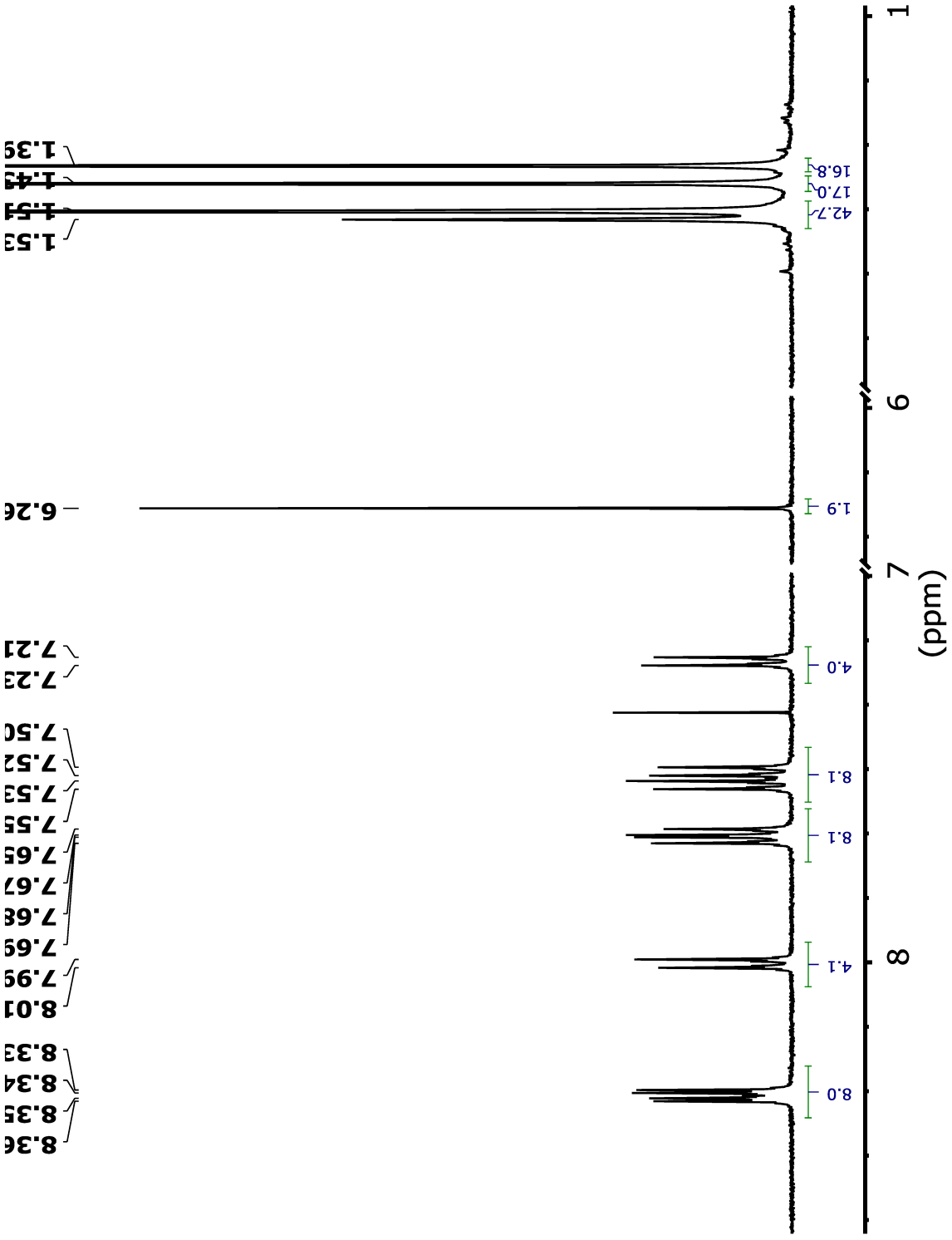

Figure 5.2. ^{1}H-NMR spectrum of $Mn^{V}(NC_6Cl_3H_2)(TBP_8Cz)$ in CD_2Cl_2.

The Mn^{V}-imido complex was crystallized by vapor diffusion of acetonitrile into a toluene solution of $Mn^{V}(NC_6Cl_3H_2)(TBP_8Cz)$, which yielded crystals suitable for analysis by X-ray diffraction (XRD). The structure is shown in Figure 5.3. The structure revealed a short Mn-imido distance of $d(Mn–N_{imido})$ = 1.617(5) Å, consistent with a triply-bonded terminal imido ligand, and $Mn–N_{pyrrole}$ distances ranging from 1.865(6) Å – 1.898(5) Å. The $Mn^{V}(NMes)(TBP_8Cz)$ had $Mn–N_{imido}$ distances of 1.595(4) Å and 1.611(4) Å for the two molecules in the asymmetric units, both of which are comparable to the $Mn–N_{imido}$ distance found here. The Mn ion in $Mn^{V}(NC_6Cl_3H_2)(TBP_8Cz)$ was displaced out of the plane of the four pyrrole nitrogens by 0.57 Å, which is slightly more out of the plane relative to both $Mn^{V}(NMes)(TBP_8Cz)$ and $Mn^{V}(O)(TBP_8Cz)$, $d(Mn–N_{4plane})$ = 0.55 Å. This may be due to the electron-withdrawing nature of the trichlorophenyl group. The $Mn–N_{imido}–C$ angle is linear (177.8°), and this value lies directly in between the two angles reported for $Mn^{V}(NMes)(TBP_8Cz)$ (179.7° and 176.9°). As shown in Table 5.2, the structural differences between the $Mn^{V}(NMes)(TBP_8Cz)$ and the $Mn^{V}(NC_6Cl_3H_2)(TBP_8Cz)$ complexes are subtle, despite the large difference in electronics between the two phenylimido substituents ($-CH_3$ versus –Cl).

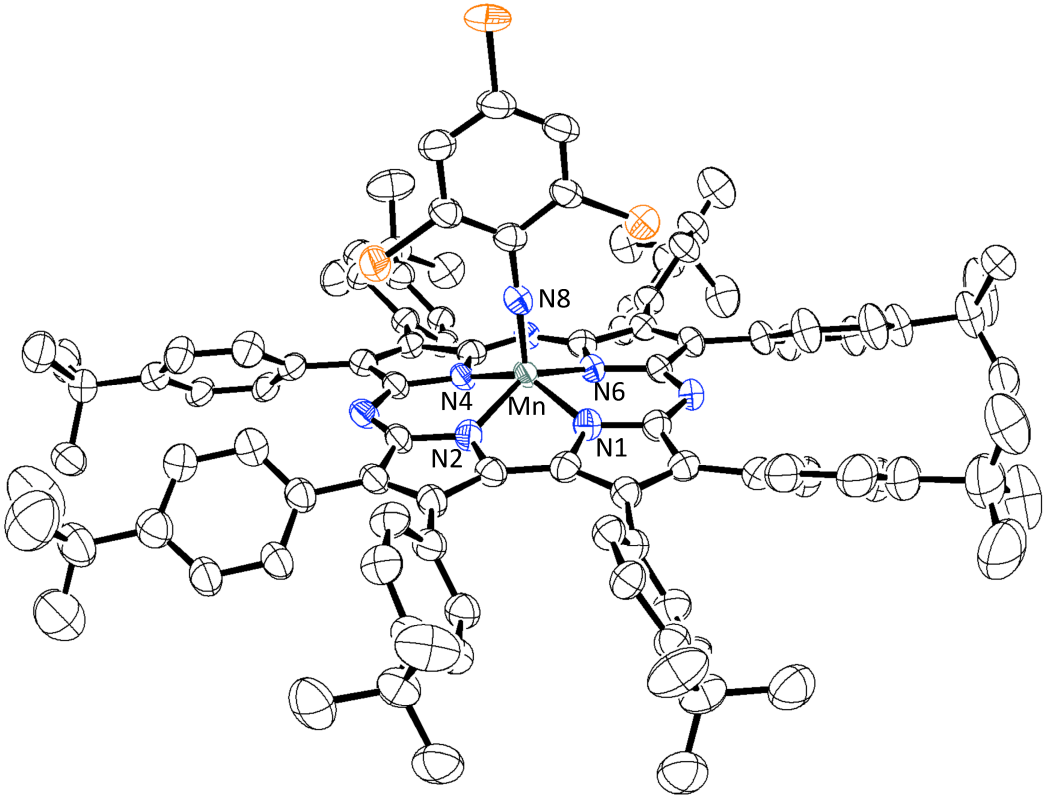

Figure 5.3. Displacement ellipsoid plot of $Mn^{V}(NC_6Cl_3H_2)(TBP_8Cz)$ (50% probability level) at 110 K. H atoms and disorder are omitted for clarity.

Table 5.2. Comparison of atomic distances from X-ray diffraction for the first coordination sphere of $Mn^{V}(NC_6H_2Cl_3)(TBP_8Cz)$ and $Mn^{V}(NMes)(TBP_8Cz)$.

Structural Parameters (Å)	$Mn^{V}(NC_6H_2Cl_3)(TBP_8Cz)$	$Mn^{V}(NMes)(TBP_8Cz)^{a}$	$Mn^{V}(NMes)(TBP_8Cz)^{b}$
Mn-N8	1.617(5)	1.595(4)	1.611(4)
Mn-N1	1.865(6)	1.885(3)	1.877(5)
Mn-N2	1.876(4)	1.886(5)	1.869(4)
Mn-N4	1.898(5)	1.907(4)	1.892(4)
Mn-N6	1.894(5)	1.893(4)	1.899(4)
Mn-N_4 plane	0.57	0.55	0.55

[a,b]Two independent molecules of $Mn^{V}(NMes)(TBP_8Cz)$ were found in the unit cell.

To gain some insight into the electronic influence of the imido substituent, the electrochemical properties of the complex were studied. The cyclic voltammogram (CV) of $Mn^{V}(NC_6Cl_3H_2)(TBP_8Cz)$ is shown in Figure 5.4. The CV of $Mn^{V}(NC_6Cl_3H_2)(TBP_8Cz)$ revealed three reversible waves, $E_{1/2}$ = 0.92 V, 0.34 V, and −1.75 V vs Fc^{+}/Fc, and one quasi-reversible wave at $E_{1/2}$ = -0.70 V vs Fc^{+}/Fc. The quasi-reversible wave at $E_{1/2}$ = -0.70 V vs Fc^{+}/Fc is close to metal-centered reduction waves for other high-valent metal corrolazine complexes such as $Mn^{V}(O)(TBP_8Cz)$ ($E_{1/2}$ = -0.55 V) and $Cr^{V}(O)(TBP_8Cz)$ ($E_{1/2}$ = -0.43 V).[9] However, $Mn^{V}(NMes)(TBP_8Cz)$, which is considered non-reducible, has no reversible wave in that region and is featureless in the CV until the potential is pushed to less than -1.7 V vs Fc^{+}/Fc. These data suggest that, by replacing the mesityl substituent with the more-electron deficient trichlorophenyl group, the Mn^{V}/Mn^{IV} potential is dramatically shifted in the positive direction by at least 1 V. Therefore, despite the lack of structural changes in the imido complexes relative to each other found by XRD, the *electronic* influence at the metal center is drastic.

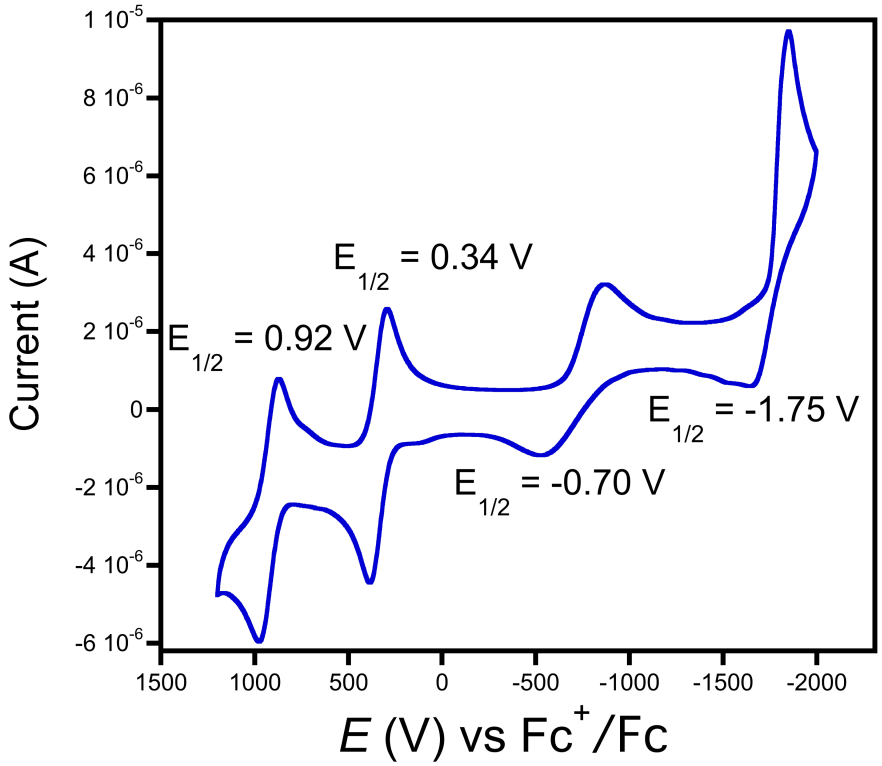

Figure 5.4. Cyclic voltammogram of $Mn^{V}(NC_6Cl_3H_2)(TBP_8Cz)$ (0.25 mM) in CH_2Cl_2 with 0.1 M $TBAPF_6$ added as a supporting electrolyte (scan rate = 50 mV/s).

5.3.2. Reactivity of $Mn^{V}(NC_6Cl_3H_2)(TBP_8Cz)$ with Brönsted Acids

The reaction of $Mn^{V}(NC_6Cl_3H_2)(TBP_8Cz)$ with one equivalent of $HBAr^{F}$ caused a red shift in the UV-vis spectrum to a new species with Soret and Q bands at λ_{max} = 437 and 699 nm (Figure 5.5). This process could be reversed quantitatively by the addition of "proton sponge" (1,8-bis(dimethylamino)naphthalene), a strong base, restoring the initial $Mn^{V}(NC_6Cl_3H_2)(TBP_8Cz)$ spectrum. These spectral changes are consistent with those observed upon reversible *meso*-N mono-protonation of other metal-corrolazines.[18,19,23] Titration of $HBAr^{F}$ (0-1.0 equivalents, 0.2 equiv aliquots) into $Mn^{V}(NC_6Cl_3H_2)(TBP_8Cz)$ showed isosbestic conversion from the initial spectrum to the final mono-protonated species (Figure 5.6). Further titration of $HBAr^{F}$ (1.2-2.0 equivalents) resulted in the

formation of a new species with features at λ_{max} = 470, 759 nm (Figure 5.7), consistent with the red-shift observed upon di-protonation of other metallocorrolazine complexes.

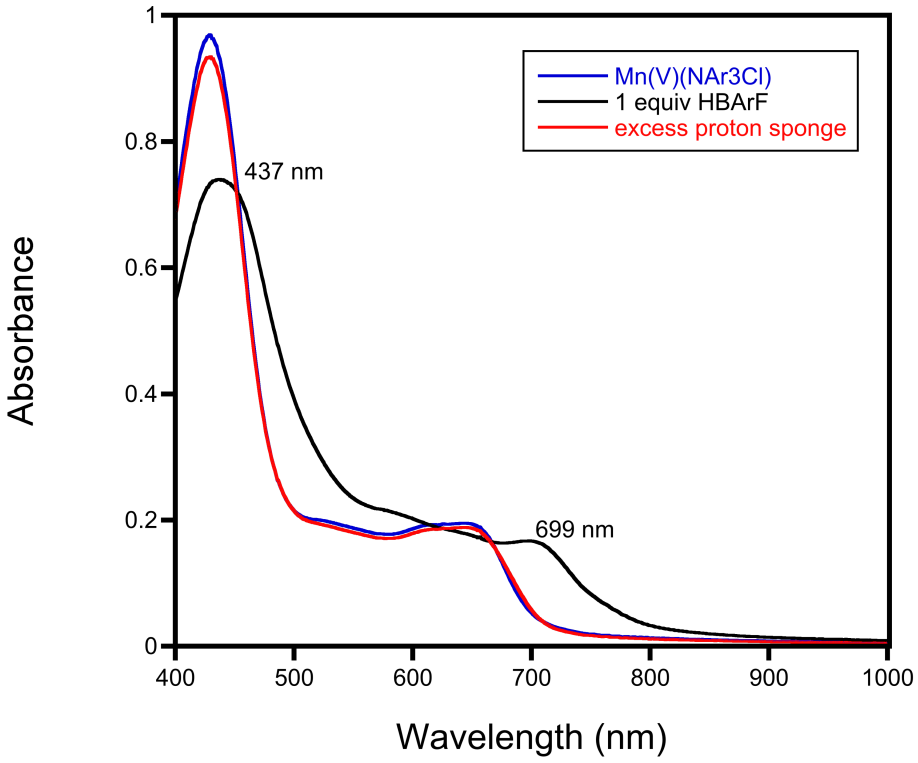

Figure 5.5. UV-vis spectral changes for the reaction between $Mn^{V}(NC_6Cl_3H_2)(TBP_8Cz)$ (11 µM) (blue spectrum) with $HBAr^{F}$ (1 equiv) (black spectrum), followed by the addition of proton sponge (excess) (red spectrum) all in CH_2Cl_2.

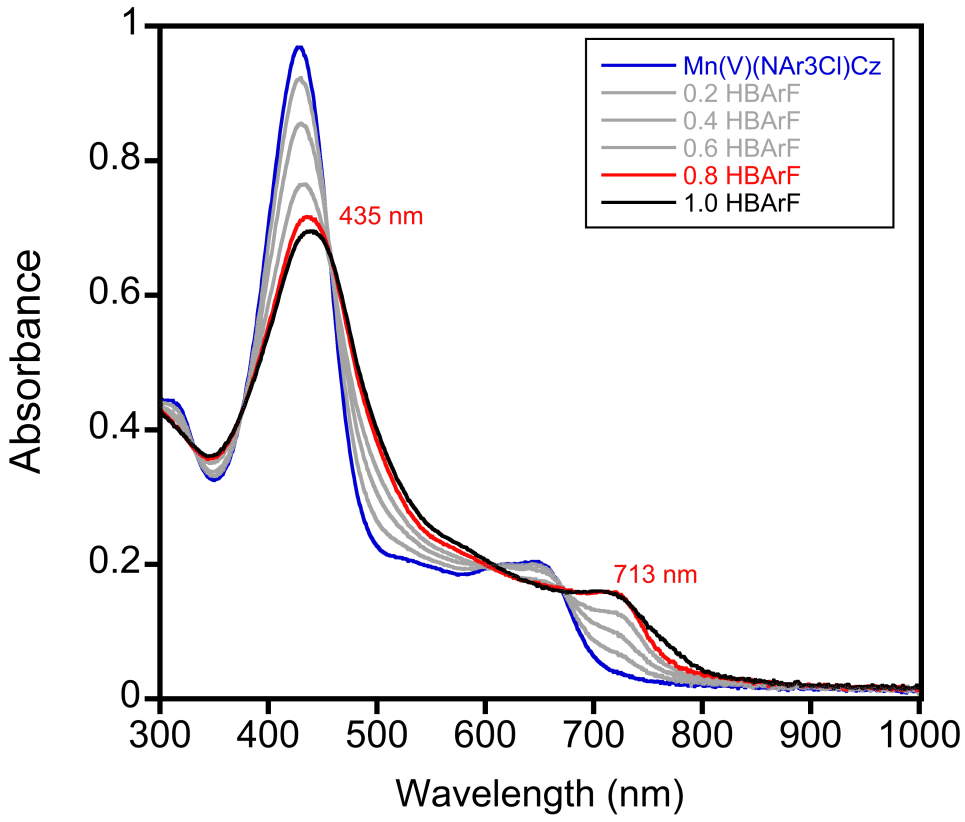

Figure 5.6. UV-vis titration of $Mn^{V}(NC_6Cl_3H_2)(TBP_8Cz)$ (11 µM) (blue spectrum) with $HBAr^{F}$ (0-1.0 equiv) in CH_2Cl_2 to give the monoprotonated $[Mn^{V}(NC_6Cl_3H_2)(TBP_8CzH)]^{+}$ complex (red spectrum).

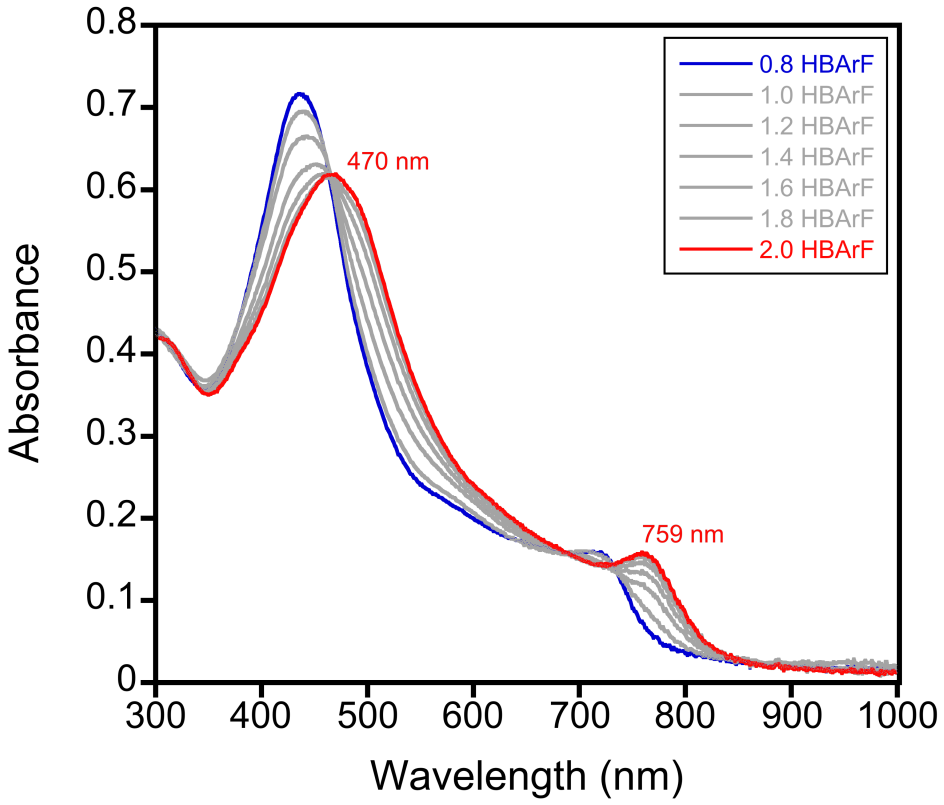

Figure 5.7. UV-vis titration of the monoprotonated $[Mn^{V}(NC_6Cl_3H_2)(TBP_8CzH)]^{+}$ (11 µM) (blue spectrum) with $HBAr^{F}$ (1.0-2.0 equiv) in CH_2Cl_2 to give the diprotonated $[Mn^{V}(NC_6Cl_3H_2)(TBP_8CzH_2)]^{2+}$ complex (red spectrum).

A ^{1}H-NMR spectrum at 23 °C of a 1:1 mixture of $Mn^{V}(NC_6Cl_3H_2)(TBP_8Cz)$ and $HBAr^{F}$ in CD_2Cl_2 is shown in Figure 5.8. It reveals a diamagnetic spectrum, indicating that valence tautomerization to a $Mn^{IV}(NR)(TBP_8Cz^{\bullet+})$ complex does not occur under these conditions. Spectra for the starting $Mn^{V}(NC_6Cl_3H_2)(TBP_8Cz)$ and the $Mn^{V}(NC_6Cl_3H_2)(TBP_8Cz)$ with excess $HBAr^{F}$ are shown for comparison. The new spectrum is complex, indicating a desymmetrization of the pattern which results from protonation of one of the *meso*-nitrogens that does not lie on the mirror plane that bisects the pyrrole-pyrrole linkage (Figure 5.8). The phenyl H peak for the imido ligand is shifted downfield by 0.12 ppm, suggesting that the *meso*-protonation is pulling electron

density away from the metal center. A new peak at 13.51 ppm that integrates to 1H is observed, which is consistent with protonation at a *meso*-nitrogen position, as seen for other metallocorrolazines.[18,19] Addition of excess $HBAr^F$ to this reaction mixture results in a re-symmetrization of the ^{1}H-NMR spectrum, which shows distinct chemical shifts from the starting $Mn^V(NC_6Cl_3H_2)(TBP_8Cz)$ spectrum. This return to a symmetric pattern indicates further protonation, possibly at the other *meso*-nitrogen that does not lie on the mirror plane that bisects the pyrrole-pyrrole linkage. The peak at 13.51 ppm disappears, which may be due exchange broadening from the excess acid present in solution. The phenyl H peak for the imido ligand is shifted further downfield from either the mono- or un-protonated complexes giving an overall change of 0.17 ppm. Based on the UV-vis and NMR data, the Mn^V oxidation state is maintained and protonation occurs at a meso-nitrogen (rather than the terminal imido ligand). Furthermore, with each sequential protonation, the terminal imido phenyl peaks shift downfield in the ^{1}H-NMR, indicating an increase in electrophilicity of the terminal imido ligand, which may result in an increase in reactivity with N-atom accepting substrates. A summary of the data and results with $HBAr^F$ is shown in Scheme 5.3.

Scheme 5.3.

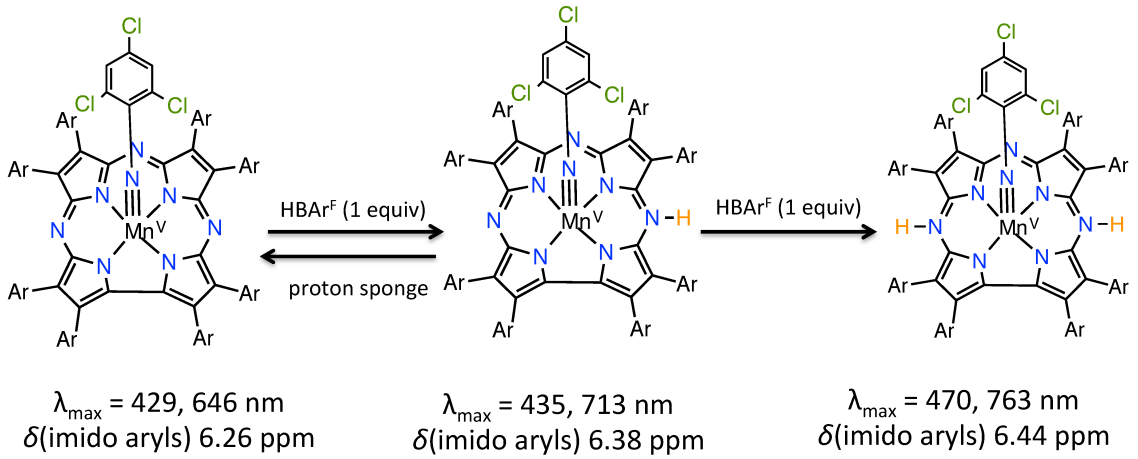

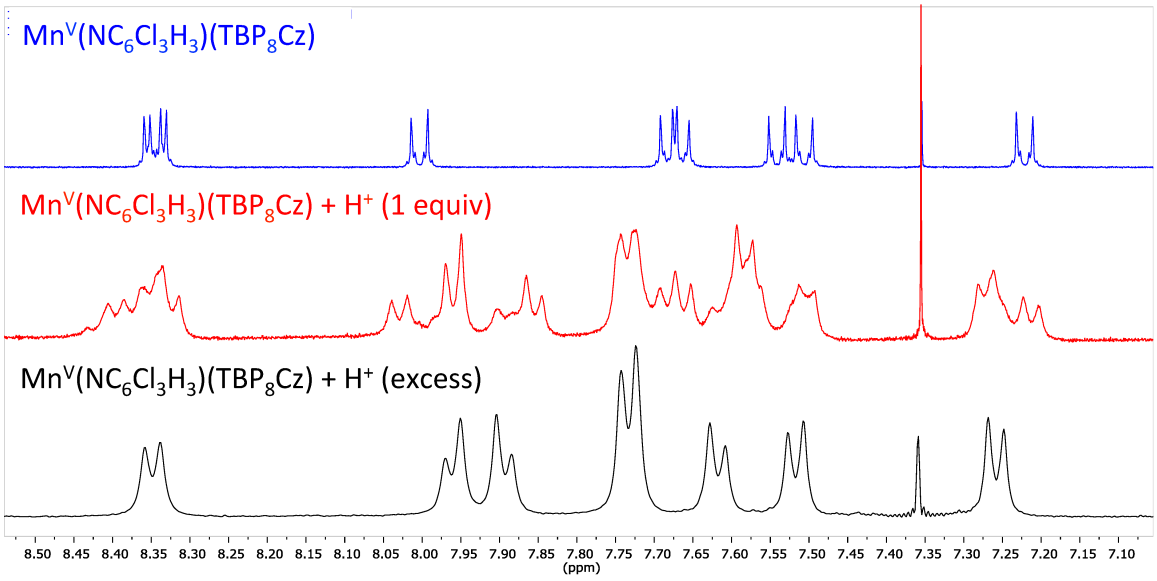

Figure 5.8. Comparison of ^{1}H-NMR spectra (400 MHz) near the aryl region of $Mn^V(NC_6Cl_3H_2)(TBP_8Cz)$, the monoprotonated $[Mn^V(NC_6Cl_3H_2)(TBP_8CzH)]^+$ complex, and the deprotonated $[Mn^V(NC_6Cl_3H_2)(TBP_8CzH_2)]^{2+}$ complex (3.2 mM) in CD_2Cl_2 at 23 °C.

While the Mn^V oxidation state was maintained in the presence of the strong acid HBAr^F, the $[Mn^V(NC_6Cl_3H_2)(TBP_8CzH)]^+$ complex underwent a surprising proton and valence tautomerization in the presence of a weak base. The addition of acetonitrile to

$[Mn^{V}(NC_6Cl_3H_2)(TBP_8CzH)]^{+}$ formed from the reaction with $Mn^{V}(NC_6Cl_3H_2)(TBP_8Cz)$ and $HBAr^{F}$, resulted in the formation of a spectrum with features at λ_{max} = 424, 780 nm and resembles the spectra seen for other π-cation-radical corrolazine species.[14-17,19] As seen in Figure 5.9, however, this reaction is not isosbestic, and appears to involve initial deprotonation of the *meso*-N to give the $Mn^{V}(NC_6Cl_3H_2)(TBP_8Cz)$ before the π-cation-radical species can be observed. This indicates that only one type of basic site on the complex (imido or *meso*-N(s)) can be protonated at a time, and that the electronic structures of the two protic tautomers mutually exclude each other. We tentatively assign the new species as an $Mn^{IV}(NC_6Cl_3H_2)(TBP_8Cz^{\bullet+})$ complex.

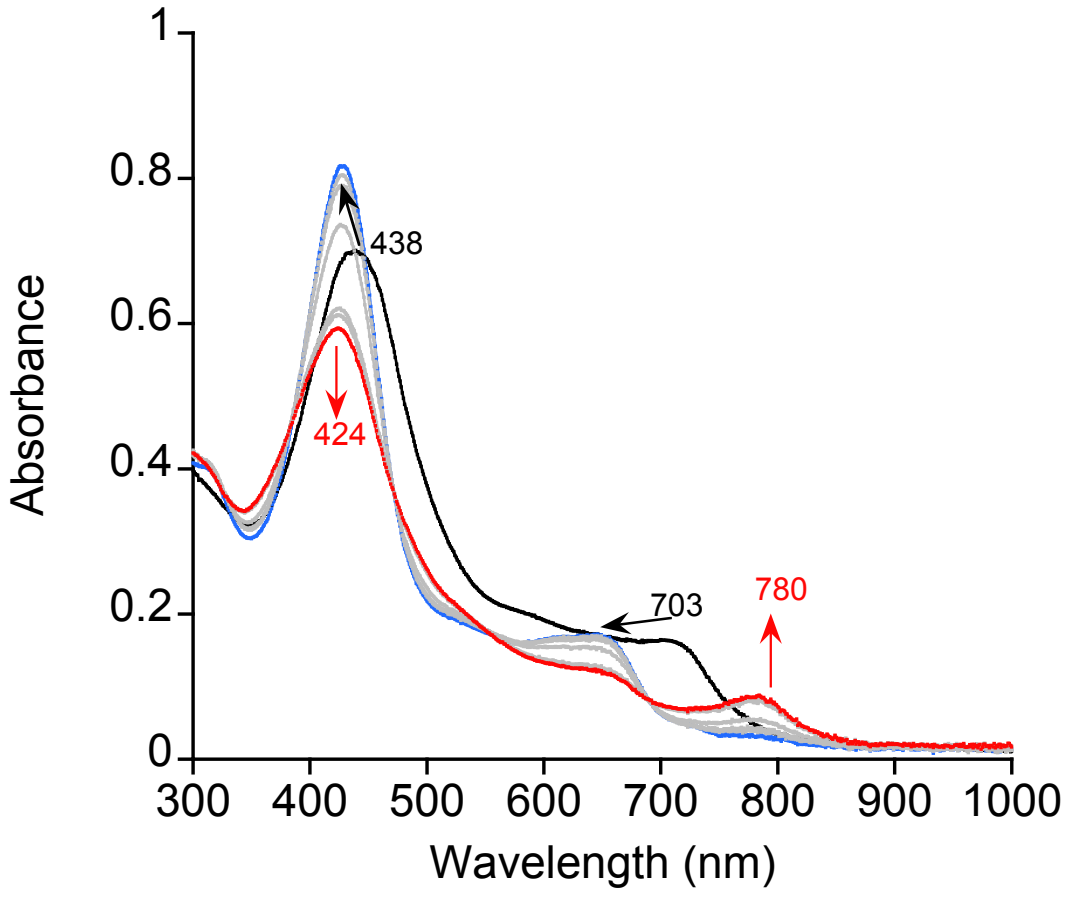

Figure 5.9. UV-vis spectral changes upon addition of CH_3CN to $[Mn^{V}(NC_6Cl_3H_2)(TBP_8CzH)]^{+}$ (black spectrum) in CH_2Cl_2 to give initial formation

of the $Mn^{V}(NC_6Cl_3H_2)(TBP_8Cz)$ (blue spectrum) with isosbestic conversion to the new π-cation-radical complex $Mn^{IV}(NC_6Cl_3H_2)(TBP_8Cz^{\bullet+})$ (red spectrum).

This new species could also be observed by addition of a weak acid, either trifluoroacetic acid (TFA) or trichloroacetic acid (TCA), to $Mn^{V}(NC_6Cl_3H_2)(TBP_8Cz)$ as shown in Figure 5.10. The formation of the $Mn^{IV}(NC_6Cl_3H_2)(TBP_8Cz^{\bullet+})$ species with these weak acids was partially reversible, and the extent of reversibility depended on how long the reaction between $Mn^{V}(NC_6Cl_3H_2)(TBP_8Cz)$ and TCA was allowed to sit open to air. When the $Mn^{IV}(NC_6Cl_3H_2)(TBP_8Cz^{\bullet+})$ complex was allowed to sit open to air for ~20 minutes, followed by addition of excess triethylamine (NEt_3), a weak base, the UV-vis spectrum showed peaks corresponding to a mixture of $Mn^{V}(O)(TBP_8Cz)$ (λ_{max}(Q band) = 630 nm) and Mn^{III} (λ_{max}(Q band) = 682 nm) (Figure 5.11). When excess triethylamine (NEt_3) was added to a reaction in which the $Mn^{IV}(NC_6Cl_3H_2)(TBP_8Cz^{\bullet+})$ complex was not fully formed (i.e. ~3 minutes), the UV-vis spectrum showed peaks corresponding to a mixture of $Mn^{V}(NC_6Cl_3H_2)(TBP_8Cz)$ (λ_{max}(Soret band) = 428 nm) and $Mn^{III}(TBP_8Cz)$ (λ_{max}(Q band) = 678 nm) (Figure 5.12). The presence of the $Mn^{V}(NC_6Cl_3H_2)(TBP_8Cz)$ in the latter experiment indicates that the imido ligand is still bound in the $Mn^{IV}(NC_6Cl_3H_2)(TBP_8Cz^{\bullet+})$ complex, but it is incredibly susceptible to hydrolysis as evidenced by the presence of $Mn^{V}(O)(TBP_8Cz)$ in the former experiment (Scheme 5.5). A summary of the reactivity of the $Mn^{V}(NC_6Cl_3H_2)(TBP_8Cz)$ complex with proton sources is shown in Scheme 5.4.

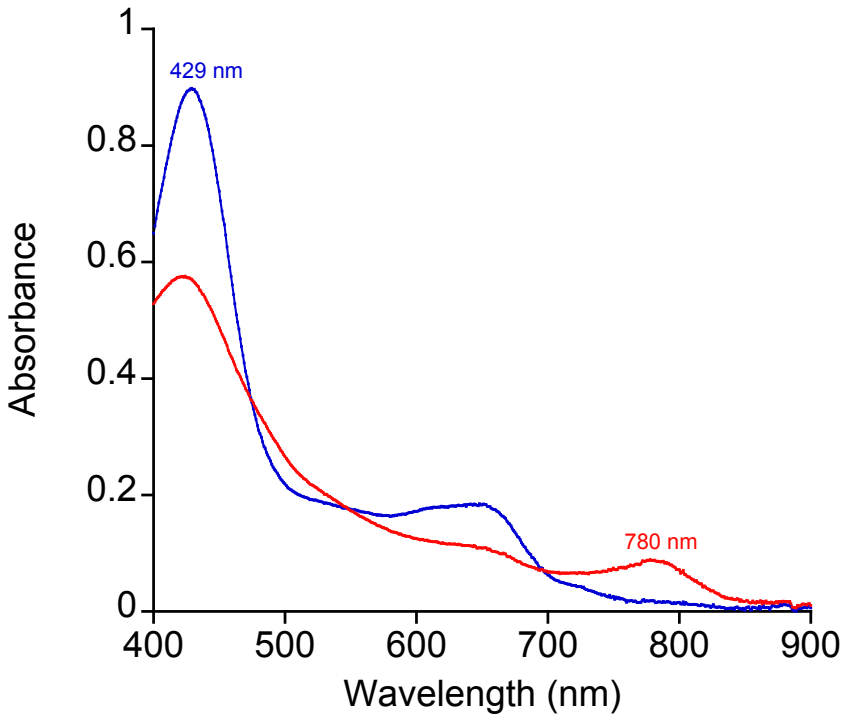

Figure 5.10. UV-vis spectra before (blue) and after (red) addition of TCA (1 equiv) to $Mn^{V}(NC_6Cl_3H_2)(TBP_8Cz)$ in CH_2Cl_2.

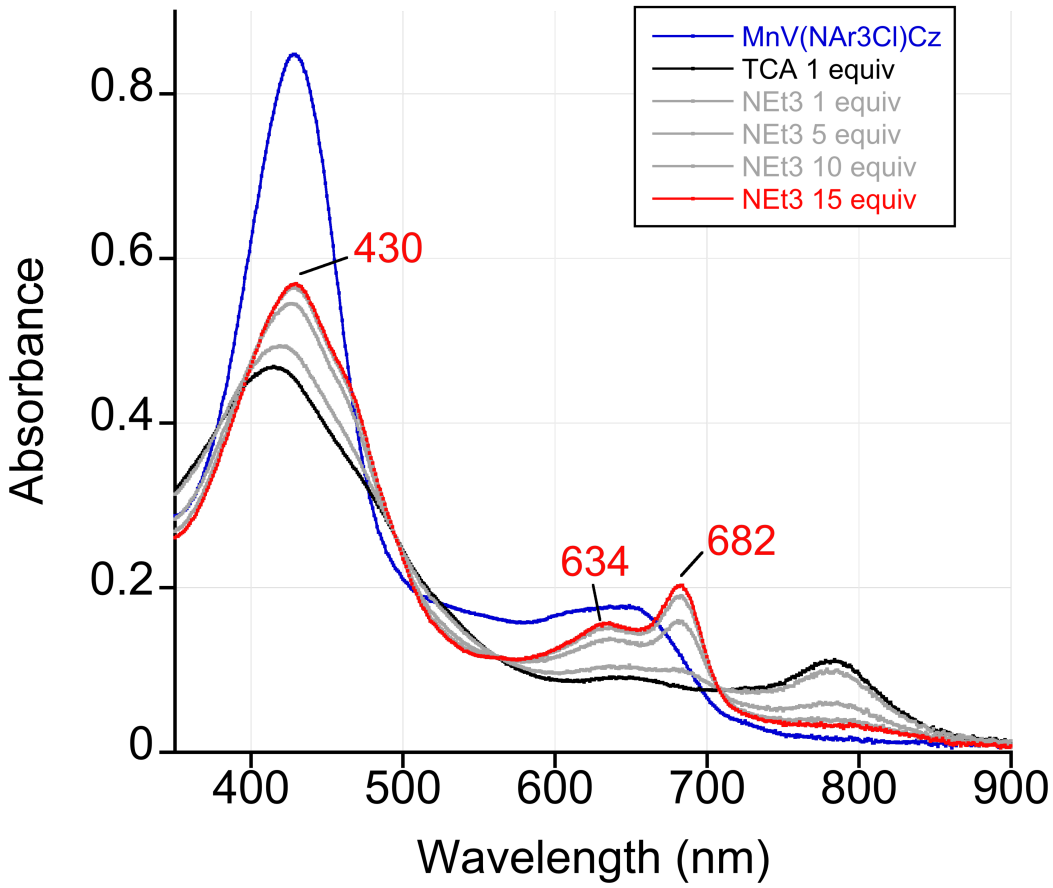

Figure 5.11. UV-vis spectral changes after the addition of NEt_3 to a 20 minute-old solution of the $Mn^{IV}(NC_6Cl_3H_2)(TBP_8Cz^{\bullet+})$ species formed from TCA.

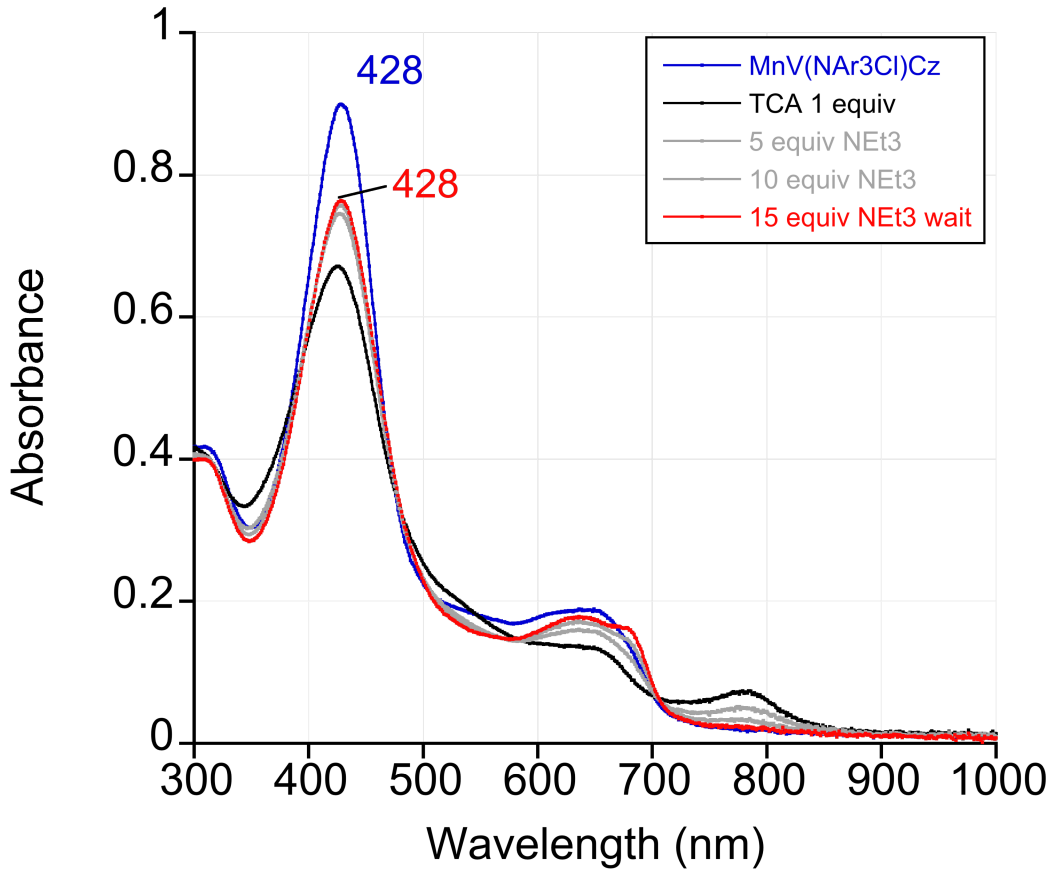

Figure 5.12. UV-vis spectral changes after the addition of NEt_3 to a freshly prepared solution of the $Mn^{IV}(NC_6Cl_3H_2)(TBP_8Cz^{\bullet+})$ species formed from TCA.

Scheme 5.4. Summary of reactivity of $Mn^{V}(NC_6Cl_3H_2)(TBP_8Cz)$ with proton sources.

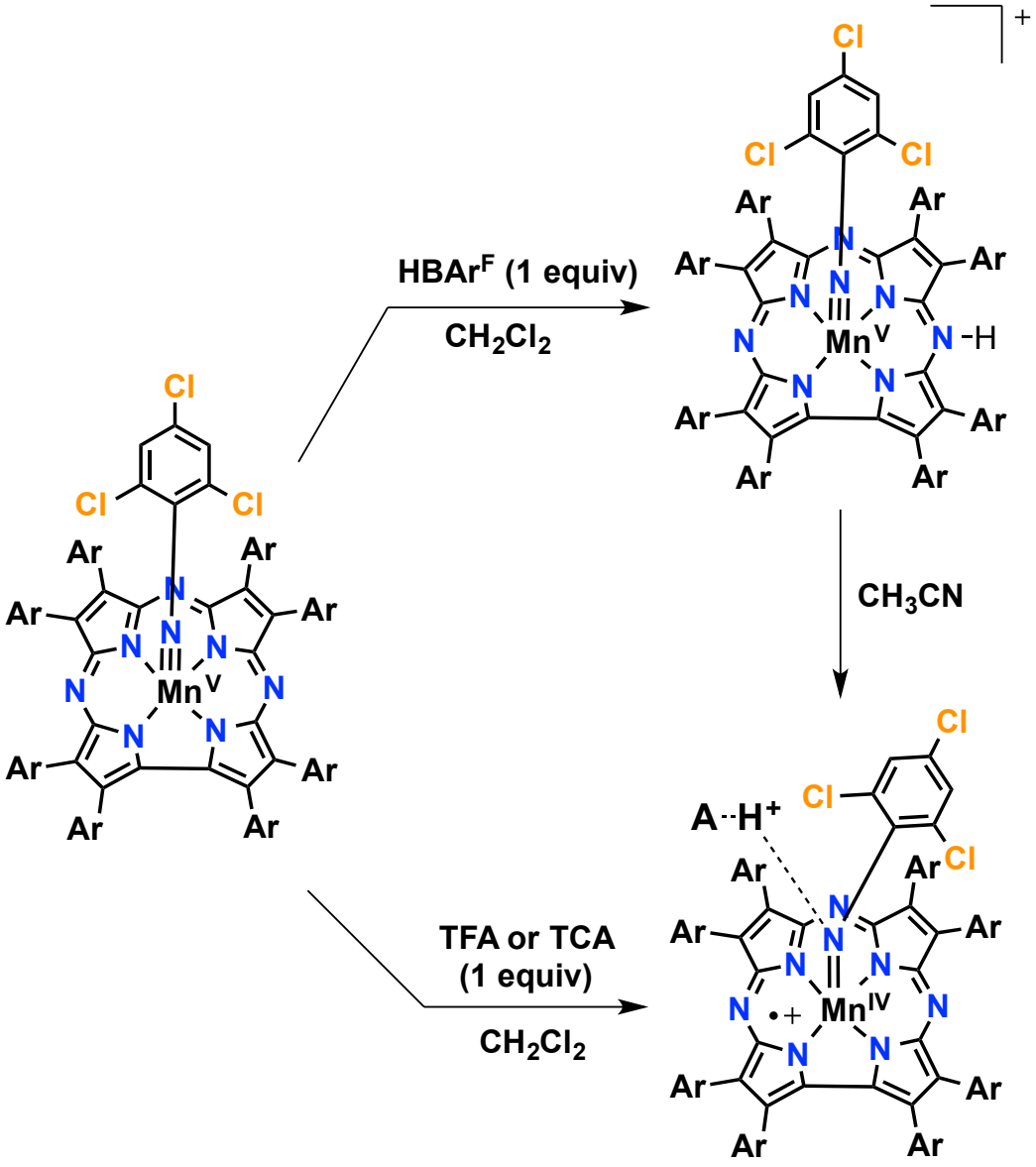

Scheme 5.5. Summary of Chemical Reversibility of Valence Tautomerization

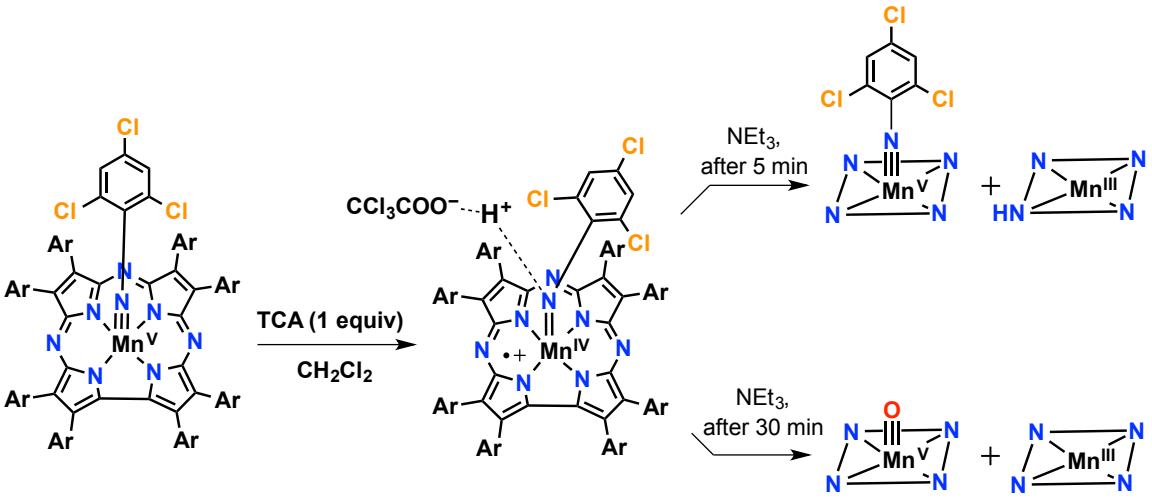

5.3.3. Preliminary Reactivity of Imido Complexes

In order to determine the effects of the trichlorophenylimido substituent on the reactivity of the $Mn^{V}(NC_6Cl_3H_2)(TBP_8Cz)$ complex and its protonated analogues, we attempted preliminary reactions with various model substrates. Unlike $Mn^{V}(NMes)(TBP_8Cz)$, $Mn^{V}(NC_6Cl_3H_2)(TBP_8Cz)$ was able to undergo both nitrogen atom transfer and hydrogen atom abstraction reactions. Monitoring the reaction of excess triphenylphosphine with $Mn^{V}(NC_6Cl_3H_2)(TBP_8Cz)$ by UV-vis resulted in a spectral change to features assigned to a reduced complex containing an axial ligand, $Mn^{III}(X)(TBP_8Cz)$ (λ_{max} = 448, 697 nm) (Figure 5.13). The addition of 2,2,6,6-tetramethylpiperidine hydroxylamine (TEMPOH), an H-atom donor with a weak O–H bond (BDFE(O–H) = 67 kcal/mol), to $Mn^{V}(NC_6Cl_3H_2)(TBP_8Cz)$ also resulted in conversion to a spectrum with features consistent with $Mn^{III}(TBP_8Cz)$ (λ_{max} = 435, 683 nm) (Figure 5.14). The $Mn^{V}(NMes)(TBP_8Cz)$ complex was incapable of oxidizing either of these substrates. However, addition of a huge excess of the weak C–H bond substrate xanthene (BDFE(C–H) = 73 kcal/mol) to both $Mn^{V}(NC_6Cl_3H_2)(TBP_8Cz)$ and

$Mn^{V}(NMes)(TBP_8Cz)$ gave no measurable change in the UV-vis over several hours. The enhanced reactivity of $Mn^{V}(NC_6Cl_3H_2)(TBP_8Cz)$ compared to $Mn^{V}(NMes)(TBP_8Cz)$ is consistent with the electrochemical data, where $Mn^{V}(NMes)(TBP_8Cz)$ is non-reducible in the presence of added substrates, but $Mn^{V}(NC_6Cl_3H_2)(TBP_8Cz)$ has accessible reduction potentials, allowing for oxidation of substrates.

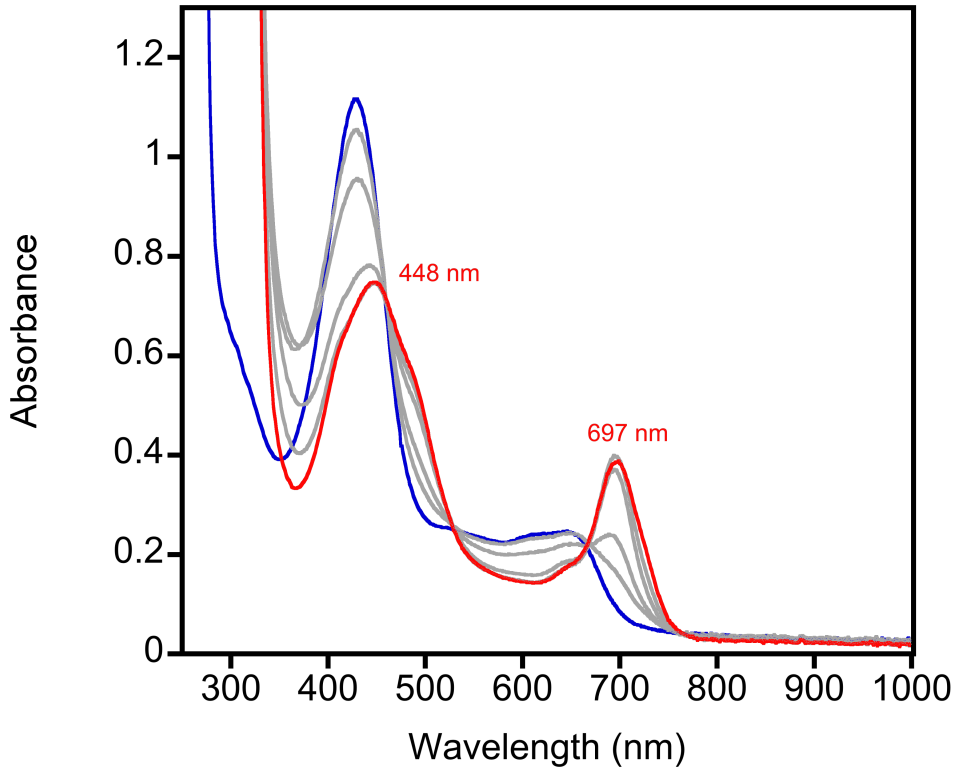

Figure 5.13. UV-vis spectral changes for the reaction of $Mn^{V}(NC_6Cl_3H_2)(TBP_8Cz)$ with excess PPh_3 in CH_2Cl_2.

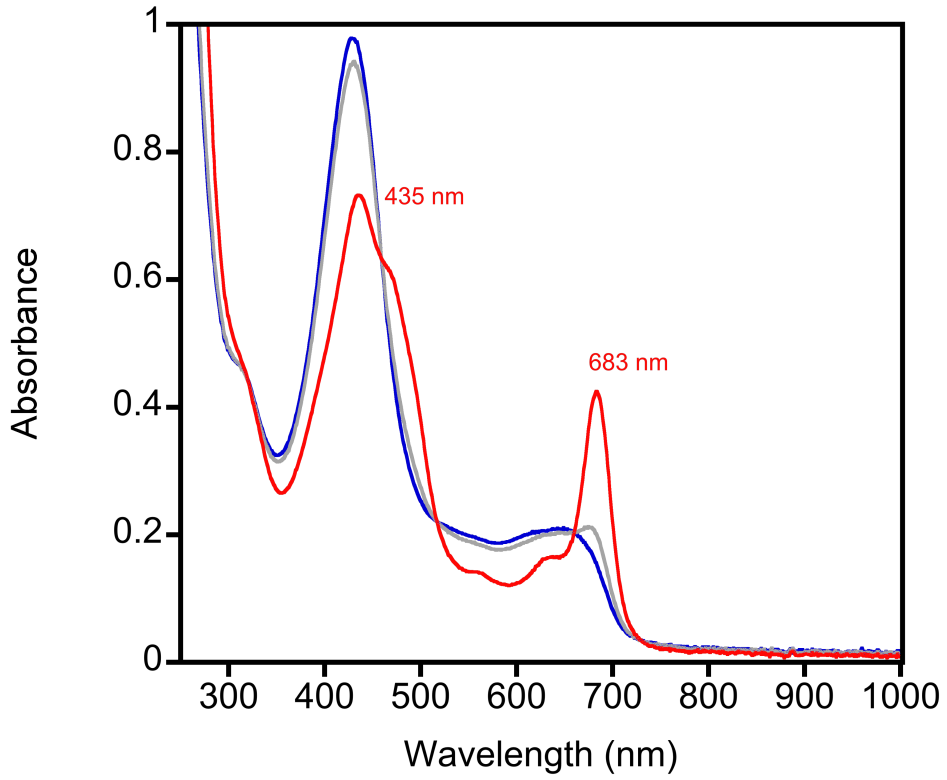

Figure 5.14. UV-vis spectral changes for the reaction of $Mn^{V}(NC_6Cl_3H_2)(TBP_8Cz)$ with excess TEMPOH in CH_2Cl_2.

The reaction between the mono-protonated $[Mn^{V}(NC_6Cl_3H_2)(TBP_8CzH)]^{+}$ complex and excess PPh_3 (50 equiv) was monitored by UV-vis (Figure 5.15). A rapid change in the UV-vis for the mono-protonated Mn^{V}-imido species (λ_{max} = 435, 713 nm) to a new spectrum with features at λ_{max} = 468 and 723 nm was observed. This new spectrum resembles that observed for the product of OAT from $Mn^{IV}(OH)(TBP_8Cz^{\bullet+})$, which was characterized as a *meso*-N-protonated $[Mn^{III}(TBP_8CzH)]^{+}$ complex. Qualitatively, the rate of the reaction between PPh_3 and the $[Mn^{V}(NC_6Cl_3H_2)(TBP_8CzH)]^{+}$ (over in <100 seconds) is much faster compared to that of PPh_3 and the starting $Mn^{V}(NC_6Cl_3H_2)(TBP_8Cz)$ complex (90 minutes). This rate enhancement for the *meso*-N-protonated imido can be attributed to the enhanced

electrophilicity of the imido ligand, which is expected based on the downfield-shifted phenyl-imido protons in the ^{1}H-NMR.

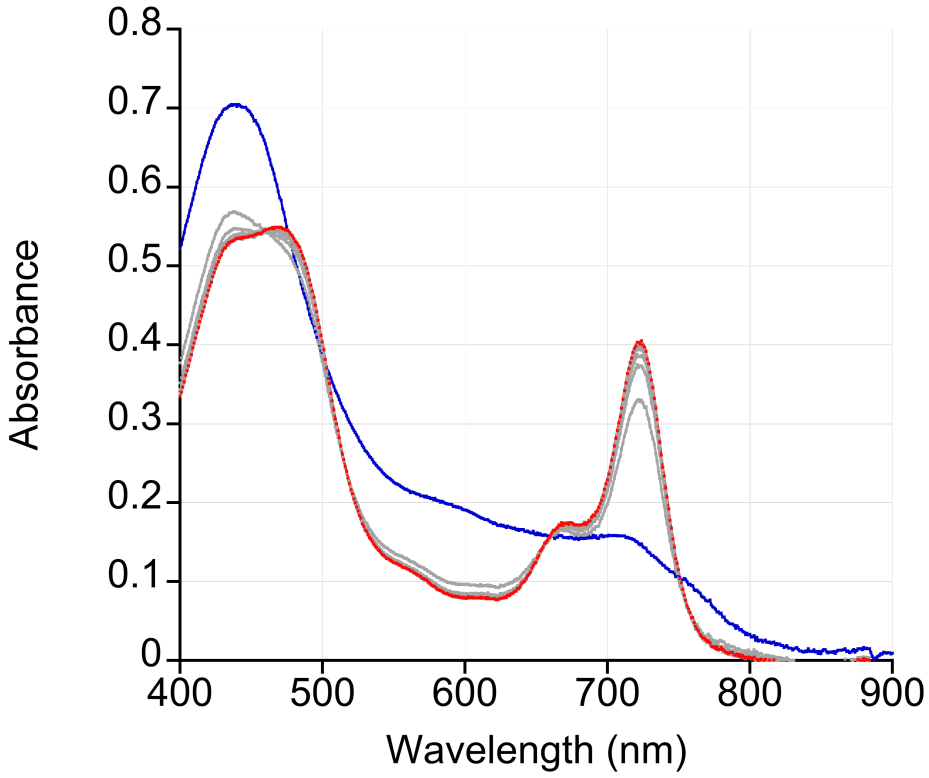

Figure 5.15. UV-vis spectral changes for the reaction between the mono-protonated $[Mn^{V}(NC_6Cl_3H_2)(TBP_8CzH)]^{+}$ complex (11 μM) (blue spectrum) and PPh_3 (50 equiv) in CH_2Cl_2

While the starting $Mn^{V}(NC_6Cl_3H_2)(TBP_8Cz)$ complex is unreactive with xanthene, the mono-protonated $[Mn^{V}(NC_6Cl_3H_2)(TBP_8CzH)]^{+}$ complex is capable of oxidation of this substrate. As seen in Figure 5.16, upon addition of xanthene (1500 equiv) the UV-vis features for $[Mn^{V}(NC_6Cl_3H_2)(TBP_8CzH)]^{+}$ isosbestically convert to a new spectrum with λ_{max} = 445 and 728 nm. This new spectrum is similar to that observed when C–H substrates are added to $Mn^{IV}(O)(TBP_8Cz^{\bullet+})$, with either an $Mn^{IV}(X)(TBP_8Cz)$ or $[Mn^{III}(TBP_8CzH)]^{+}$, depending on the substrate. By UV-vis, these two species are

indistinguishable, and further spectroscopic characterization is needed to determine the oxidation products. More work is needed to determine the underlying factors that control the difference in reactivity between the un- and mono-protonated manganese-imido species.

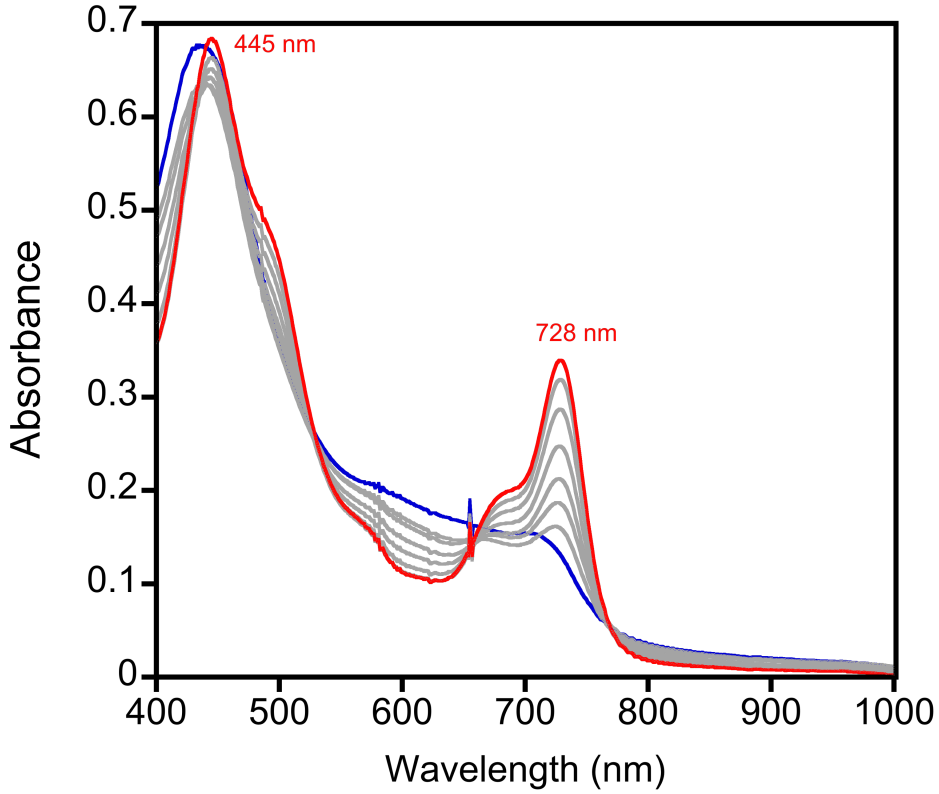

Figure 5.16. UV-vis spectral changes (0 – 6 hrs) observed upon addition of xanthene (1500 equiv) to $[Mn^{V}(NC_6Cl_3H_2)(TBP_8CzH)]^{+}$ (11 µM) in CH_2Cl_2.

5.4. Conclusions and Future Directions

Here we have shown the synthesis and characterization of a new Mn^{V}-imido corrolazine complex, $Mn^{V}(NC_6Cl_3H_2)(TBP_8Cz)$. Unlike the previously reported "non-reducible" $Mn^{V}(NMes)(TBP_8Cz)$ complex, this new electron-deficient complex is capable of nitrene transfer to PPh_3 and HAT from TEMPOH. Addition of the strong

proton source $HBAr^F$ to $Mn^V(NC_6Cl_3H_2)(TBP_8Cz)$ resulted in protonation at the *meso*-nitrogen positions to give mono- and di-protonated Mn^V-imido complexes. In contrast, addition of a weak acid (TCA or TFA) or a combination of $HBAr^F$ and acetonitrile as leveling agent gave the valence tautomer $Mn^{IV}(NC_6Cl_3H_2)(TBP_8Cz^{\bullet+})$ complex, which we propose is protonated at the imido nitrogen. Thus, the two types of protonation sites in the Mn-imido corrolazine complex are mutually exclusive, and can be controlled by the strength of the acid. More work is needed to full characterize the valence tautomer $Mn^{IV}(NC_6Cl_3H_2)(TBP_8Cz^{\bullet+})$, including a crystal structure and determination of magnetic properties. Comparative reactivity between this species and the *meso*-N protonated $Mn^V(NC_6Cl_3H_2)(TBP_8Cz)$ complex towards the oxidation of organic substrates is also needed.

5.5. References

(1) Wolfe, J. P.; Wagaw, S.; Marcoux, J.-F.; Buchwald, S. L. Rational Development of Practical Catalysts for Aromatic Carbon‚àíNitrogen Bond Formation. *Acc. Chem. Res.* **1998**, *31*, 805-818.

(2) Müller, P.; Fruit, C. Enantioselective Catalytic Aziridinations and Asymmetric Nitrene Insertions into CH Bonds. *Chem. Rev.* **2003**, *103*, 2905-2920.

(3) King, E. R.; Hennessy, E. T.; Betley, T. A. Catalytic C‚àíH Bond Amination from High-Spin Iron Imido Complexes. *J. Am. Chem. Soc.* **2011**, *133*, 4917-4923.

(4) Au, S.-M.; Huang, J.-S.; Yu, W.-Y.; Fung, W.-H.; Che, C.-M. Aziridination of Alkenes and Amidation of Alkanes by Bis(tosylimido)ruthenium(VI) Porphyrins. A Mechanistic Study. *J. Am. Chem. Soc.* **1999**, *121*, 9120-9132.

(5) Paradine, S. M.; Griffin, J. R.; Zhao, J.; Petronico, A. L.; Miller, S. M.; Christina White, M. A manganese catalyst for highly reactive yet chemoselective intramolecular C(sp3)–H amination. *Nat Chem* **2015**, *7*, 987-994.

(6) Lansky, D. E.; Kosack, J. R.; Narducci Sarjeant, A. A.; Goldberg, D. P. An Isolable, Nonreducible High-Valent Manganese(V) Imido Corrolazine Complex. *Inorg. Chem.* **2006**, *45*, 8477-8479.

(7) Mandimutsira, B. S.; Ramdhanie, B.; Todd, R. C.; Wang, H.; Zareba, A. A.; Czernuszewicz, R. S.; Goldberg, D. P. A Stable Manganese(V)-Oxo Corrolazine Complex. *J. Am. Chem. Soc.* **2002**, *124*, 15170-15171.

(8) Lansky, D. E.; Mandimutsira, B.; Ramdhanie, B.; Clausén, M.; Penner-Hahn, J.; Zvyagin, S. A.; Telser, J.; Krzystek, J.; Zhan, R.; Ou, Z.; Kadish, K. M.; Zakharov, L.; Rheingold, A. L.; Goldberg, D. P. Synthesis, Characterization, and Physicochemical Properties of Manganese(III) and Manganese(V)-Oxo Corrolazines. *Inorg. Chem.* **2005**, *44*, 4485-4498.

(9) Baglia, R. A.; Prokop-Prigge, K. A.; Neu, H. M.; Siegler, M. A.; Goldberg, D. P. Mn(V)(O) versus Cr(V)(O) Porphyrinoid Complexes: Structural Characterization and Implications for Basicity Controlling H-Atom Abstraction. *J. Am. Chem. Soc.* **2015**, *137*, 10874-10877.

(10) Prokop, K. A.; Neu, H. M.; de Visser, S. P.; Goldberg, D. P. A Manganese(V)–Oxo π-Cation Radical Complex: Influence of One-Electron Oxidation on Oxygen-Atom Transfer. *J. Am. Chem. Soc.* **2011**, *133*, 15874-15877.

(11) Prokop, K. A.; de Visser, S. P.; Goldberg, D. P. Unprecedented Rate Enhancements of Hydrogen-Atom Transfer to a Manganese(V)–Oxo Corrolazine Complex. *Angew. Chem., Int. Ed.* **2010**, *49*, 5091-5095.

(12) Neu, H. M.; Quesne, M. G.; Yang, T.; Prokop-Prigge, K. A.; Lancaster, K. M.; Donohoe, J.; DeBeer, S.; de Visser, S. P.; Goldberg, D. P. Dramatic Influence of an Anionic Donor on the Oxygen-Atom Transfer Reactivity of a MnV–Oxo Complex. *Chem. - Eur. J.* **2014**, *20*, 14584-14588.

(13) Neu, H. M.; Yang, T.; Baglia, R. A.; Yosca, T. H.; Green, M. T.; Quesne, M. G.; de Visser, S. P.; Goldberg, D. P. Oxygen-Atom Transfer Reactivity of Axially Ligated Mn(V)–Oxo Complexes: Evidence for Enhanced Electrophilic and Nucleophilic Pathways. *J. Am. Chem. Soc.* **2014**, *136*, 13845-13852.

(14) Leeladee, P.; Baglia, R. A.; Prokop, K. A.; Latifi, R.; de Visser, S. P.; Goldberg, D. P. Valence Tautomerism in a High-Valent Manganese-Oxo Porphyrinoid Complex Induced by a Lewis Acid. *J. Am. Chem. Soc.* **2012**, *134*, 10397-10400.

(15) Baglia, R. A.; Dürr, M.; Ivanović-Burmazović, I.; Goldberg, D. P. Activation of a High-Valent Manganese-Oxo Complex by a Nonmetallic Lewis Acid. *Inorg. Chem.* **2014**, *53*, 5893-5895.

(16) Baglia, R. A.; Krest, C. M.; Yang, T.; Leeladee, P.; Goldberg, D. P. High-Valent Manganese–Oxo Valence Tautomers and the Influence of Lewis/Br√ ∂ nsted Acids on C–H Bond Cleavage. *Inorg. Chem.* **2016**, *55*, 10800-10809.

(17) Zaragoza, J. P. T.; Baglia, R. A.; Siegler, M. A.; Goldberg, D. P. Strong Inhibition of O-Atom Transfer Reactivity for MnIV(O)(π-Radical-Cation)(Lewis Acid) versus MnV(O) Porphyrinoid Complexes. *J. Am. Chem. Soc.* **2015**, *137*, 6531-6540.

(18) Zaragoza, J. P. T.; Siegler, M. A.; Goldberg, D. P. Rhenium(v)-oxo corrolazines: isolating redox-active ligand reactivity. *Chemical Communications* **2016**, *52*, 167-170.

(19) Neu, H. M.; Jung, J.; Baglia, R. A.; Siegler, M. A.; Ohkubo, K.; Fukuzumi, S.; Goldberg, D. P. Light-Driven, Proton-Controlled, Catalytic Aerobic C-H Oxidation Mediated by a Mn(III) Porphyrinoid Complex. *J. Am. Chem. Soc.* **2015**, *137*, 4614-4617.

(20) Leyva, E.; Munoz, D.; Platz, M. S. Photochemistry of fluorinated aryl azides in toluene solution and in frozen polycrystals. *J. Org. Chem.* **1989**, *54*, 5938-5945.

(21) Jutzi, P.; Müller, C.; Stammler, A.; Stammler, H.-G. Synthesis, Crystal Structure, and Application of the Oxonium Acid [H(OEt2)2]+[B(C6F5)4]. *Organometallics* **2000**, *19*, 1442-1444.

(22) Prokop, K. A.; Goldberg, D. P. Generation of an Isolable, Monomeric Manganese(V)–Oxo Complex from O2 and Visible Light. *J. Am. Chem. Soc.* **2012**, *134*, 8014-8017.

(23) Jung, J.; Neu, H. M.; Leeladee, P.; Siegler, M. A.; Ohkubo, K.; Goldberg, D. P.; Fukuzumi, S. Photocatalytic Oxygenation of Substrates by Dioxygen with Protonated Manganese(III) Corrolazine. *Inorg. Chem.* **2016**, *55*, 3218-3228.

A. Appendix A. Synthesis of a New Corrolazine Ligand

Part of this chapter was co-written with the following authors and was published under the following title and citation:

Joslin, E. E.; Zaragoza, J. P. T.; **Baglia, R. A.;** Siegler, M. A.; Goldberg, D. P. "The Influence of Peripheral Substituent Modification on P^V, Mn^{III}, and $Mn^V(O)$ Corrolazines: X-ray Crystallography, Electrochemical and Spectroscopic Properties, and HAT and OAT Reactivities" *Inorg. Chem.,* **2016**, *55*, 8646.

A.1. Introduction

The synthesis of the corrolazine ligand framework was first published in 2001, starting from a β-substituted tetraazaporphyrin (porphyrazine) precursor.[1] Ring contraction of the porphyrazine compound (TBP_8PzH_2) was achieved through an oxidative metallation using phosphorous tribromide to give the phosphorous(V) corrolazine, $P^V(OH)_2(TBP_8Cz)$ (TBP_8Cz = octakis(*p*-tert-butylphenyl)corrolazinato^{3-}). The metal-free corrolazine (TBP_8CzH_3) was synthesized using sodium/liquid ammonia, through reductive demetallation of the P^V ion. The TBP_8CzH_3 ligand is able to coordinate a range of transition metals in various oxidation states, including Mn,[2,3] Fe,[4] and Cr[5]. Just recently, we have been able to derivatize the corrolazine ligand at the β-positions (Chart A.1). Synthesis of the $MeOP_8CzH_3$ ligand was achieved by a modified preparation of the original TBP_8CzH_3 procedure.[6] In this appendix, we present the synthesis and characterization of a novel corrolazine ligand with *para-iso*-propylphenyl substituents on the β-carbons from the octakis(*p*-isopropylphenyl)porphyrazine compound. This

isopropyl-substituted corrolazine ($iPrP_8CzH_3$) is capable of coordinating to Mn to give the $Mn^{III}(iPrP_8Cz)$ complex, and further oxidation to $Mn^{V}(O)(TBP_8Cz)$.

Chart A.1. Corrolazine ligand derivatives

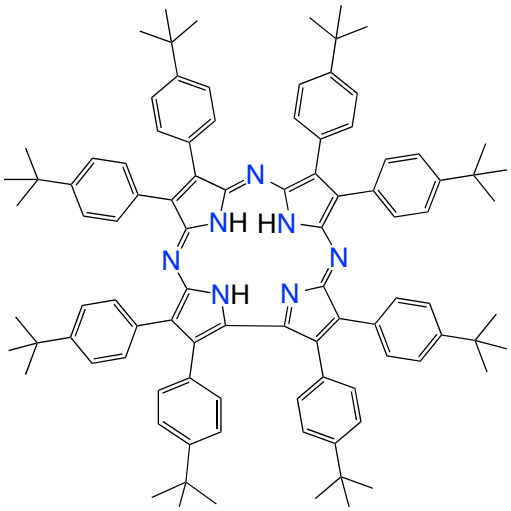

TBP_8CzH_3

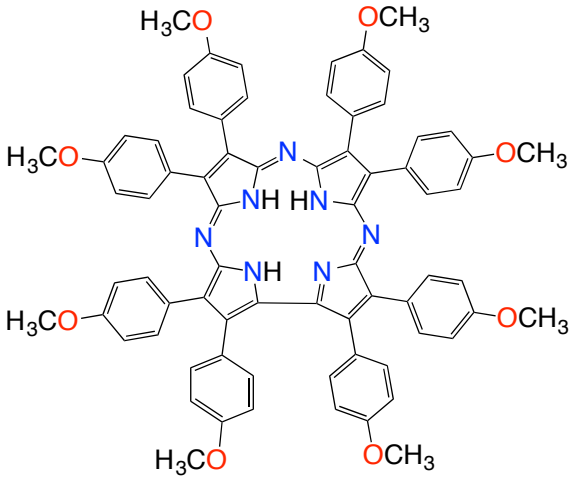

$MeOP_8CzH_3$

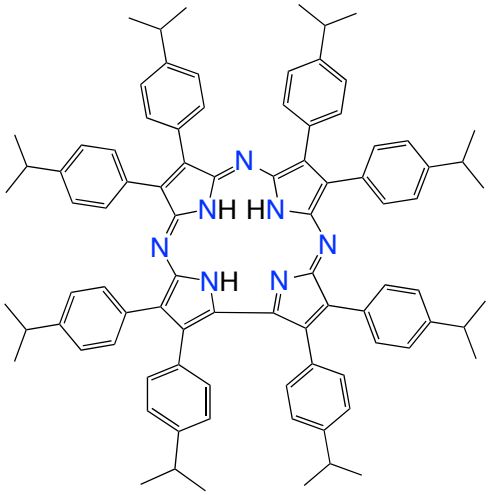

$iPrP_8CzH_3$

A.2.Experimental Methods

A.2.1. General methods and materials

All reagents were purchased commercially at the best available purity from Sigma-Aldrich at the best available purity and were used as received. Deuterated chloroform ($CDCl_3$, 0.03% v/v TMS) for NMR was purchased from Cambridge Isotopes, Inc. Toluene was purified via a Pure-Solv solvent purification system from Innovative Technologies, Inc, and all other solvents were purchased and used as received.

A.2.2. Analytical methods

UV-vis spectroscopy was performed on a Hewlett-Packard 8452 diode-array spectrophotometer equipped with HPChemstation software. ^{1}H-NMR spectra were recorded on a Bruker Avance 400 NMR instrument at 400 MHz. ^{13}C NMR spectra were recorded on a Bruker 300 MHz or a Bruker 400 MHz spectrometer (operating frequency 101 MHz or 151 MHz, respectively). All ^{1}H and ^{13}C NMR spectra are referenced against residual proton signals (^{1}H NMR) or the ^{13}C resonances of the deuterated solvent (^{13}C NMR). LDI-MS was collected on a Bruker Autoflex III/TOF/TOF instrument equipped with a nitrogen laser at 335 nm using an MTP 384 ground steel target plate. Cyclic voltammetry measurements were undertaken in methylene chloride using a BAS 100B electrochemical analyzer with a glassy carbon working electrode and a platinum wire auxiliary electrode. Potentials were recorded versus an $Ag/AgNO_3$ electrode. Scans were run at 25 mV/s under Ar atmosphere using $[Bu_4N][PF_6]$ (0.1 M) as the supporting electrolyte.

A.2.3. Synthesis of Bis(4-isopropylphenyl)fumaronitrile

The new dintrile precursor, bis(4-isopropylphenyl)fumaronitrile, was prepared as shown in Scheme A.1, below.

Scheme A.1. Synthesis of the dinitrile precursor, bis(4-isopropylphenyl)fumaronitrile

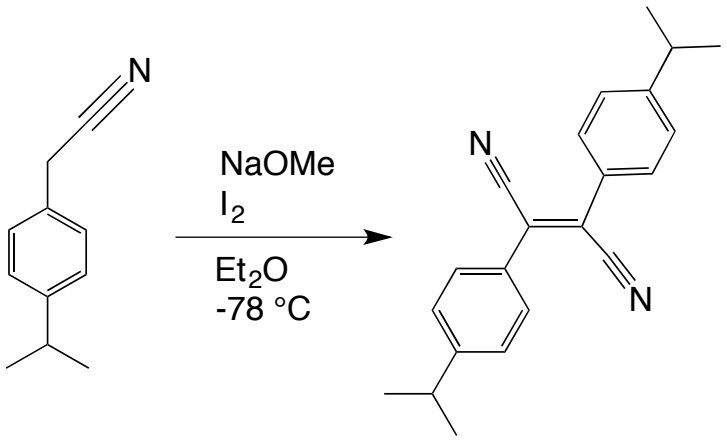

An amount of (4-isopropylphenyl)acetonitrile (10 g, 0.063 mol) and I_2 (16 g, 0.063 mol) was dissolved in 250 mL of Et_2O. NaOMe in MeOH (80 mL, 1.6 M) was slowly added by an addition funnel to the stirring solution at 0 °C. The reaction was stirred at -78 °C and a solid immediately precipitated out. The white solid was collected by filtration through a Büchner funnel, washed with MeOH and dried under vacuum to yield a white solid. A second batch of product could be isolated by placing the filtrate in the freezer for 12 h (7.3 g, 74%). ^{1}H NMR (400 MHz, $CDCl_3$) δ 7.77 (d, $^3J_{HH}$ = 8 Hz, 4H, Ar-*H*), 7.38 (d, $^3J_{HH}$ = 8 Hz, 4H, Ar-*H*), 2.99 (hept, $^3J_{HH}$ = 7 Hz, 2H, C*H*$(CH_3)_2$), 1.29 (d, $^3J_{HH}$ = 7 Hz, 12H, CH(C*H*$_3)_2$). ^{13}C NMR (101 MHz, $CDCl_3$) δ 153.15, 129.79, 128.89, 127.46 (Ar-*C*), 124.61 (alkene-*C*), 117.19 (*C*N), 34.29 (*C*H$(CH_3)_2$), 23.80 (CH(*C*H$_3)_2$).

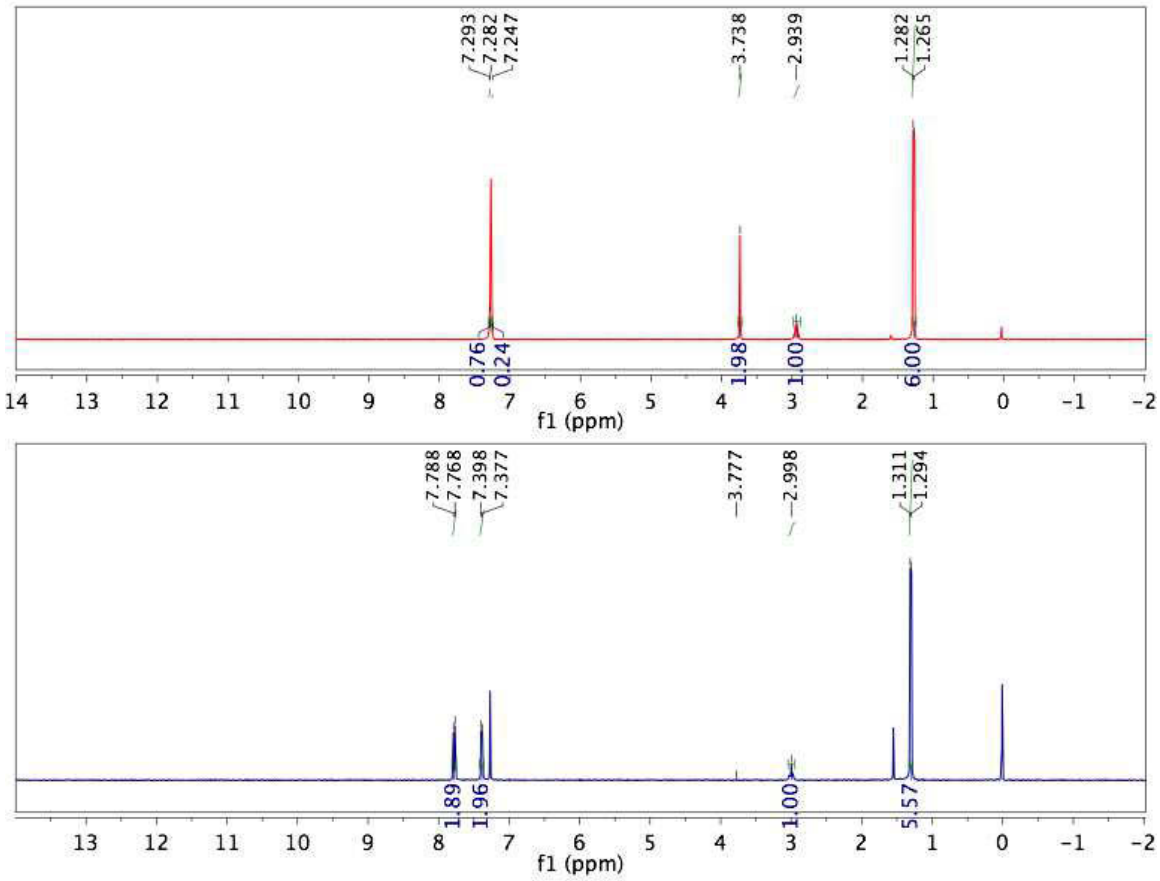

Figure A.1. Top: 4-isopropylphenylacetonitrile in $CDCl_3$. Bottom: bis(4-isopropylphenyl)fumaronitrile.

A.2.4. Synthesis of 2,3,7,8,12,13,17,18-octakis(4-isopropylphenyl) porphyrazine ($iPrP_8PzH_2$)

The new porphyrazine ligand $iPrP_8PzH_2$ was synthesized according to the procedure in Scheme A.2**Error! Reference source not found.**, below.

Scheme A.2. Synthesis of the porphyrazine ligand $iPrP_8PzH_2$.

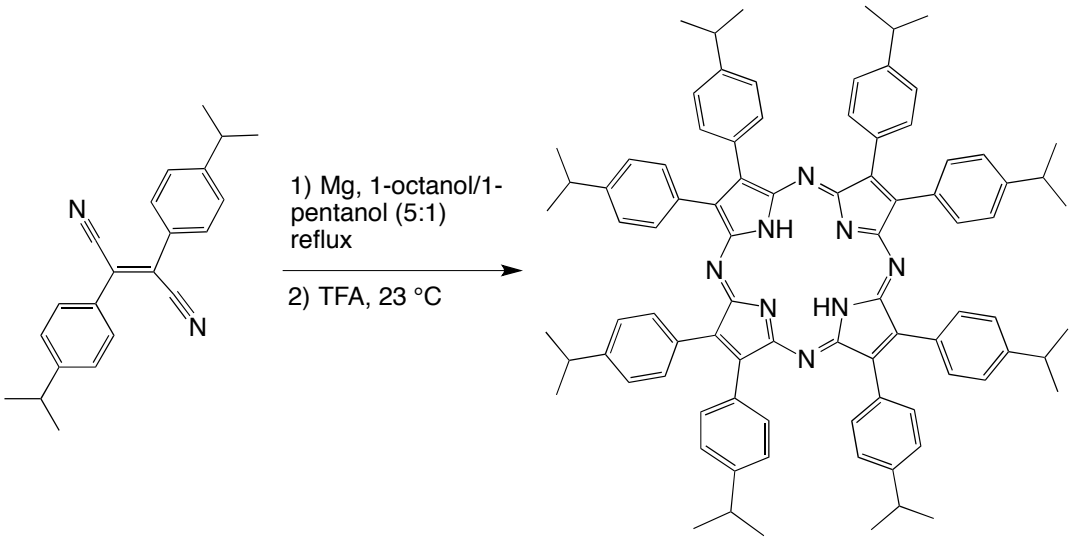

Magnesium metal (0.153 g, 0.00637 mol) was added to 13 mL of a 5:1 1-octanol:1-pentanol solution. The reaction mixture was refluxed until all the metal had reacted, yielding a viscous grey suspension. Bis(4-isopropylphenyl)fumaronitrile (2.00 g, 0.00636 mol) was added and the reaction mixture was refluxed for 2 h, in which time the solution turned dark green-blue. The solvent was removed via vacuum distillation to yield a blue-green solid (UV-vis (CH_2Cl_2) λ_{max} [nm] 379, 640; LDI-MS [M^+] m/z = 1281.97 Calc'd for $C_{88}H_{88}N_8Mg$ 1282.30). The solid was dissolved in CH_2Cl_2 (20 mL) and TFA (10 mL) and the solution immediately turned to a dark blue and was left to stir in the dark for 12 h. The CH_2Cl_2 was evaporated and the blue solution was poured on ice and neutralized with NH_4OH. The reaction mixture was filtered through a Büchner funnel and washed with copious amounts of MeOH. The solid was dried under vacuum to yield $iPrP_8PzH_2$ as a dark blue green solid. (1.6 g, 82%). UV-vis (CH_2Cl_2) λ_{max} [nm] 371, 454, 604, 670. LDI-MS $[M]^+$ *m/z* = 1259.74 Calc'd for $C_{88}H_{90}N_8$ 1259.74.

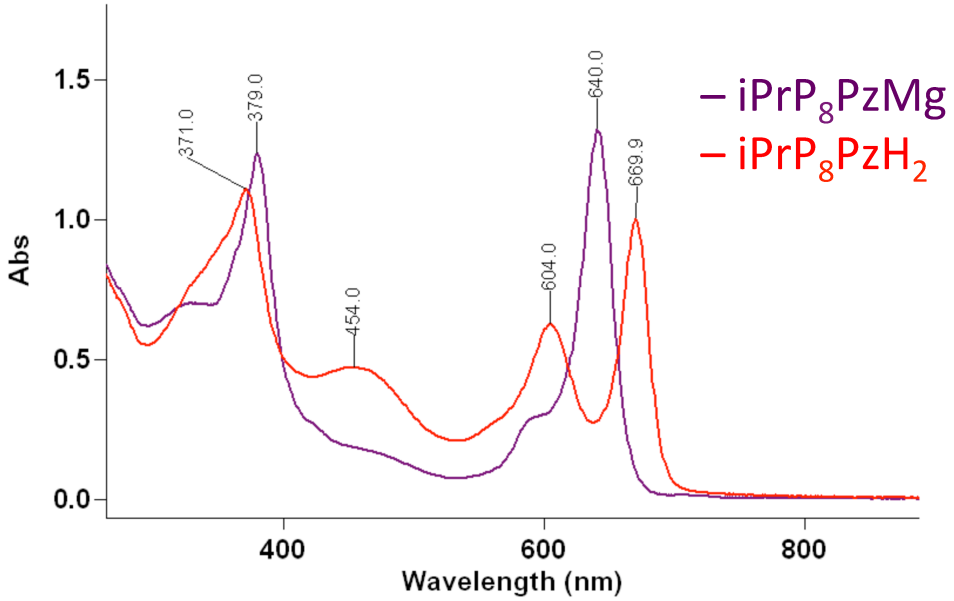

Figure A.2. UV-vis spectra of $iPrP_8PzMg$ (purple spectrum) and the metal-free $iPrP_8PzH_2$ (red spectrum) in CH_2Cl_2.

A.2.5. Synthesis and Characterization of $[P^V(OH)_2(iPrP_8Cz)]$

The synthesis of the phosphorous corrolazine $P^V(OH)_2(iPrP_8Cz)$ was achieved according to the procedure shown in Scheme A.3 below.

Scheme A.3. Synthesis of the phosphorous corrolazine $P^V(OH)_2(iPrP_8Cz)$.

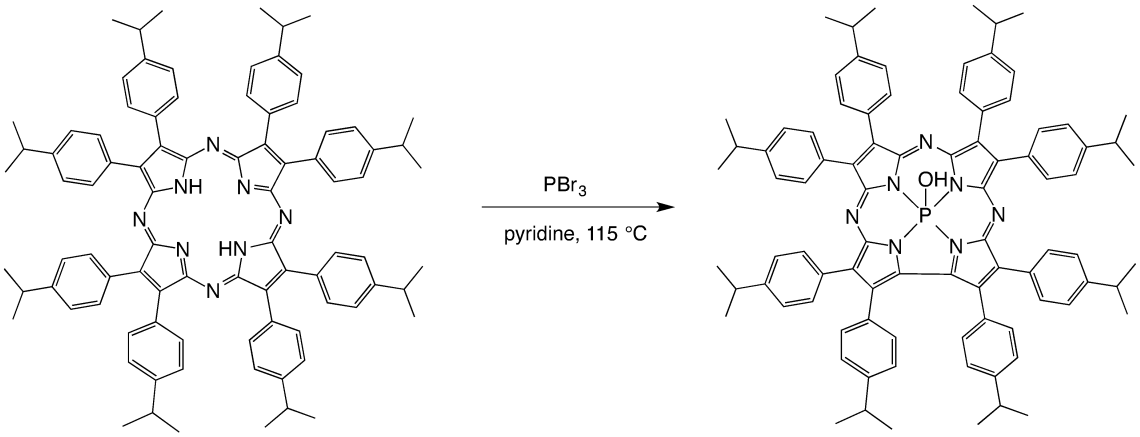

$iPrP_8PzH_2$ (1.0 g, 0.79 mmol) was dissolved in pyridine (150 mL) and heated to reflux and then PBr_3 (2 mL, 31.6 mmol) was added by syringe directly into the refluxing reaction. The reaction was refluxed for 24 h, in which time the solution turned from dark green to dark red. An additional 52 equiv of PBr_3 (3 mL, 41.1 mmol) was added and the reaction was refluxed for an additional 24 h, followed by a final addition of 100 equiv of PBr_3 (6 mL, 79 mmol) and reflux of the reaction for another 24 h. The reaction mixture was cooled to room temperature and methanol was added via syringe to quench the reaction, and the solution became dark green. The reaction mixture was reduced under vacuum to dryness and the remaining dark brown-green solid was dissolved in CH_2Cl_2, and filtered to obtain a green filtrate. The filtrate was reduced to dryness and was purified on silica gel with 95:5 CH_2Cl_2:EtOAc (Rf = 0.75). The solid was collected and dried under vacuum to yield a dark green solid (30 mg, 3%). ^{1}H NMR (400 MHz, CD_2Cl_2) ^{1}H NMR (400 MHz, chloroform-*d*) δ 8.34 (dd, $^3J_{HH}$ = 8.2, 2.6 Hz, 8H, Ar-*H*), 8.04 (d, $^3J_{HH}$ = 8.3 Hz, 4H, Ar-*H*), 7.50 (dd, J = 11.1, 8.2 Hz, 8H, Ar-*H*), 7.42 (d, $^3J_{HH}$ = 7.7 Hz, 4H, Ar-*H*), 7.33 (d, $^3J_{HH}$ = 8.2 Hz, 4H, Ar-*H*), 7.00 (d, $^3J_{HH}$ = 8.4 Hz, 4H, Ar-*H*), 3.27 – 2.78 (m, 8H, C*H*(CH_3)$_2$), 1.52 – 1.42 (m, 24H, CH(C*H*$_3$)$_2$), 1.42 – 1.31 (m, 24H, CH(C*H*$_3$)$_2$). ^{31}P NMR (162 MHz, $CDCl_3$) δ −110.75. CV (CH_2Cl_2, 50 mV)): $E_{1/2}$ = 0.71 V, $E_{1/2}$ = -1.24 V, $E_{1/2}$ = -1.76 V. UV-Vis (CH_2Cl_2) λ_{max} [nm] 439, 636. LDI-MS *m/z* = $[M\text{-}OH]^+$ 1292.7 (Calc'd: 1291.7)

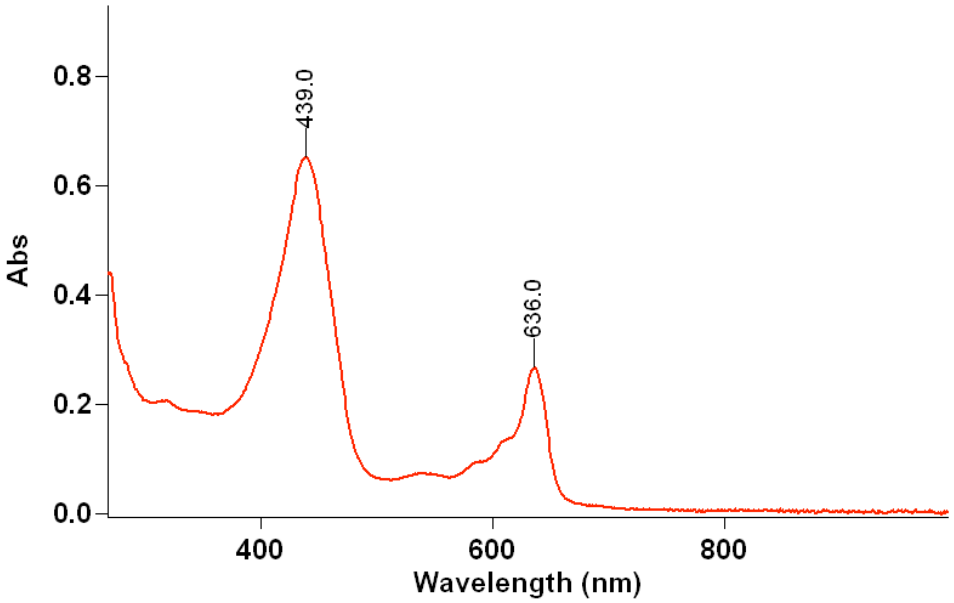

Figure A.3. UV-vis spectrum for the phosphorous corrolazine [$P^{V}(OH)_2$(iPrP$_8$Cz)] in CH_2Cl_2.

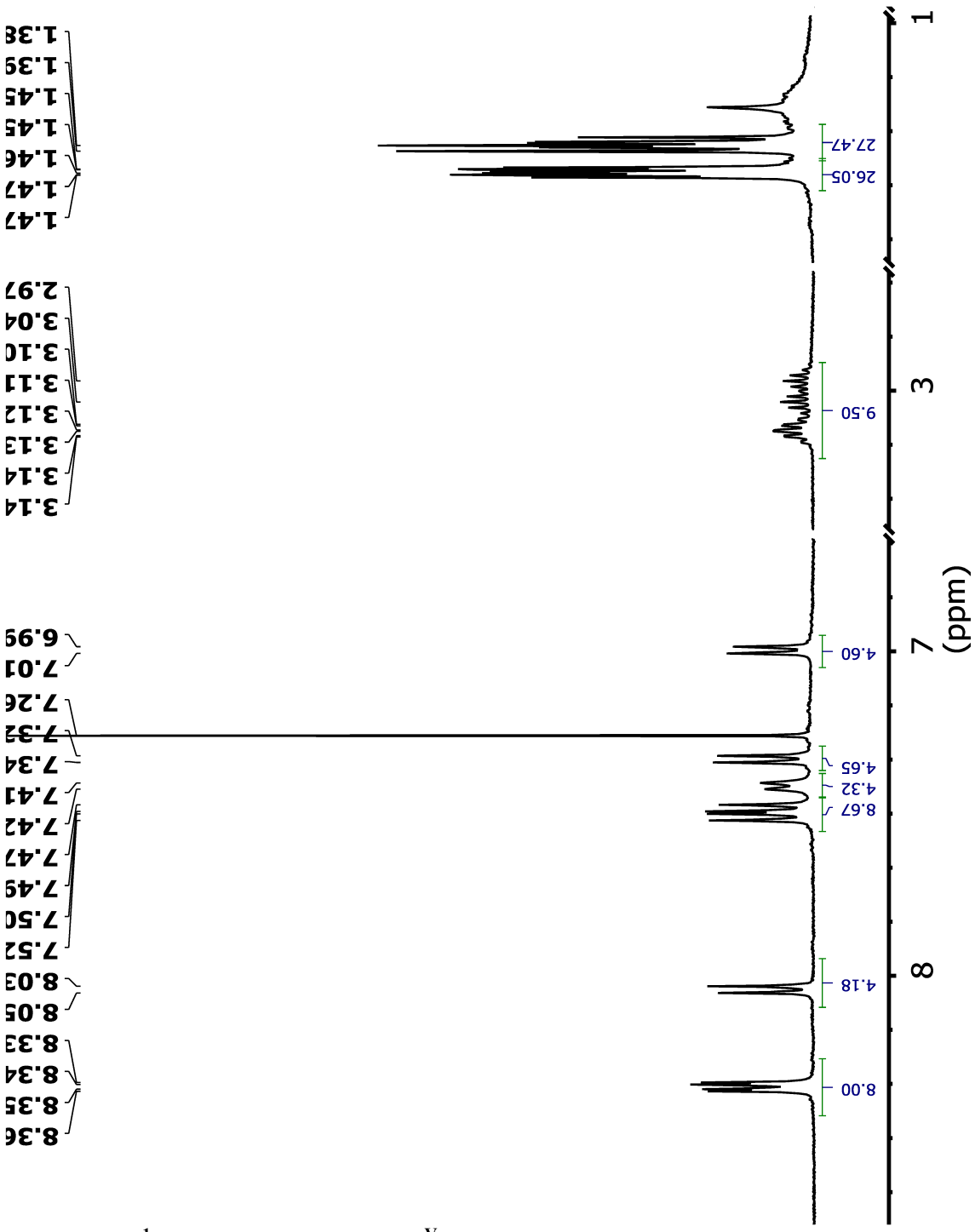

Figure A.4. ^{1}H-NMR spectrum of [$P^{V}(OH)_2$(iPrP_8Cz)] in $CDCl_3$.

A.2.6. Synthesis and Characterization of $iPrP_8CzH_3$

The metal-free corrolazine $iPrP_8CzH_3$ was synthesized according to the procedure shown in Scheme A.4 below.

Scheme A.4. Synthesis of the metal free corrolazine $iPrP_8CzH_3$.

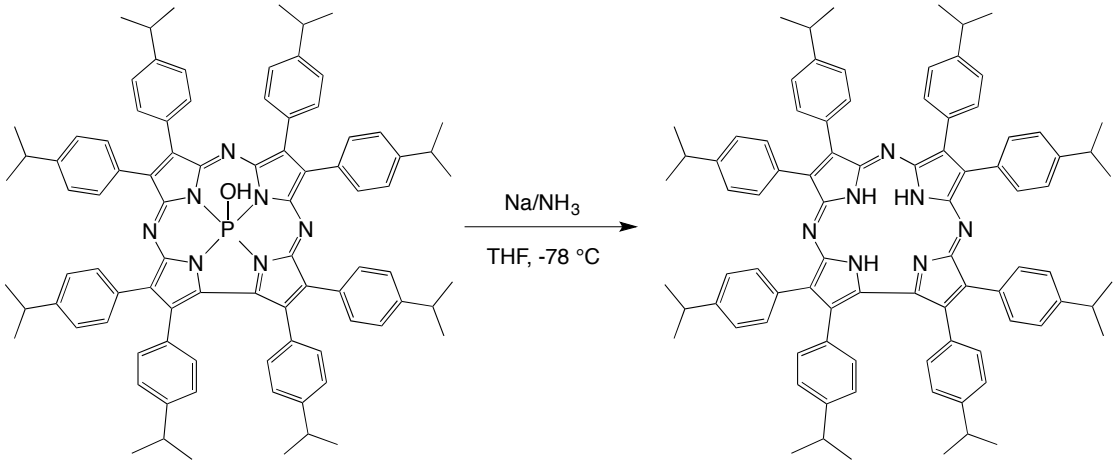

To a mixture of [P($iPrP_8Cz$)(OH)][(OH)] (30 mg, 0.023 mmol) in 5 mL of liquid ammonia cooled to –78 ^{o}C was added sodium metal (31 mg, 1.3 mmol) and the mixture was stirred for 30 min under argon. An amount of THF (8 mL) was added and the mixture was stirred for an additional 30 min at -78 ºC. The reaction mixture turned from dark green to a red-brown. An amount of NH_4Cl (0.500 g, 9.3 mmol) was added to the reaction mixture and the solution was allowed to slowly warm to room temperature to remove the ammonia. The reaction mixture was filtered through a Büchner funnel, and the filtrate was removed *in vacuo*. A flash silica column was run with 60:40 CH_2Cl_2:hexanes (R*f* = 0.60) to yield a flat green solid (6.5 mg, 22%). UV-Vis λ_{max} [nm] 458, 681. LDI-MS *m/z* = $[M]^+$ 1246.74 (Calc'd: 1247.12)

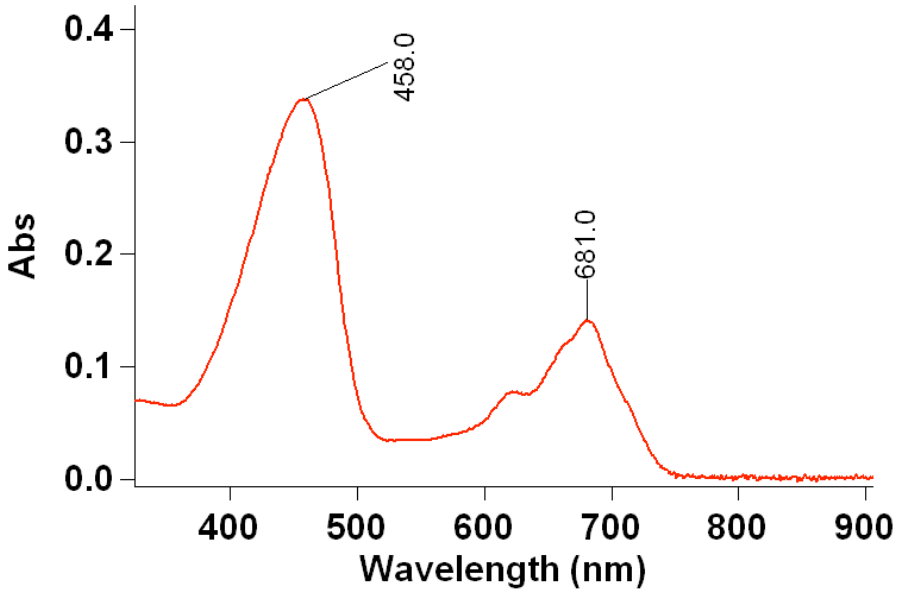

Figure A.5. UV-vis spectrum of $iPrP_8CzH_3$ in CH_2Cl_2.

A.2.7. Synthesis and Characterization of $Mn^{III}(iPrP_8Cz)$

The manganese corrolazine $Mn^{III}(iPrP_8Cz)$ was prepared according to the procedure in Scheme A.5 below.

Scheme A.5. Synthesis of the manganese corrolazine complex $Mn^{III}(iPrP_8Cz)$.

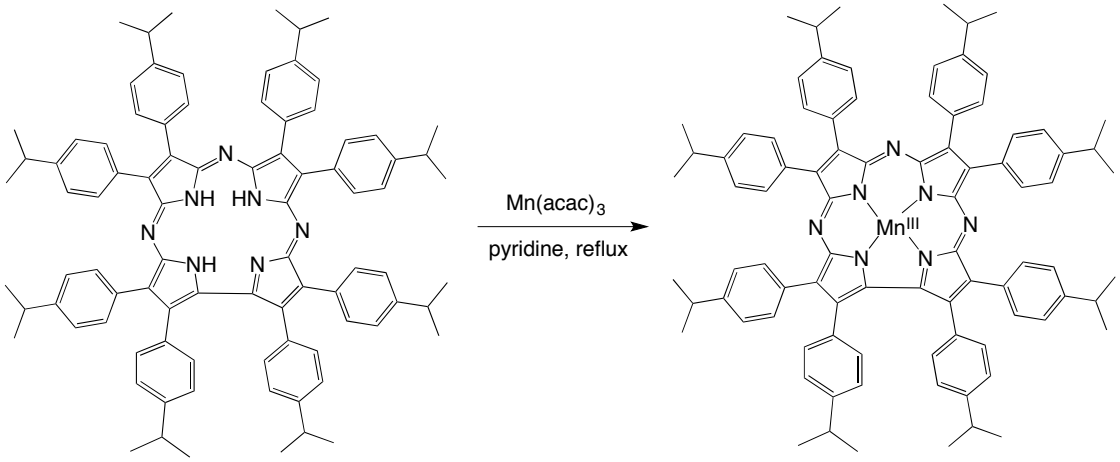

$iPrP_8CzH_3$ (6.5 mg, 0.0052 mmol) was dissolved in 7 mL of CH_2Cl_2 and 1 mL of pyridine. $Mn(acac)_3$ (88 mg, 0.25 mmol) was added to the reaction mixture, and was stirred for 12 h in the dark under air. The solvent was removed *in vacuo* to yield a brown solid. The crude brown solid was purified by flash chromatography on silica gel with 99:1 CH_2Cl_2:MeOH (R*f* = 0.61) (2.7 mg, 40% yield). UV-Vis (CH_2Cl_2) λ_{max} [nm] 438, 687. LDI-MS *m/z* = $[M]^+$ 1298.67 (Calc'd: 1298.66).

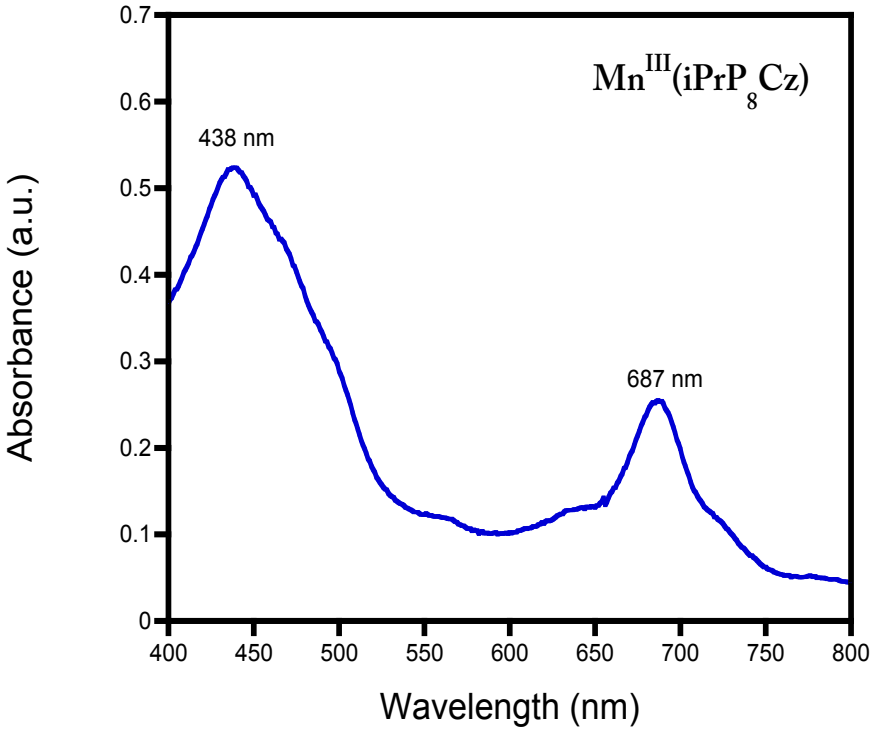

Figure A.6. UV-vis spectrum of $Mn^{III}(iPrP_8Cz)$ in CH_2Cl_2.

A.2.8. Synthesis and Characterization of $Mn^V(O)(iPrP_8Cz)$

The synthesis of the manganese-oxo corrolazine complex $Mn^V(O)(iPrP_8Cz)$ was performed according to the procedure shown in Scheme A.6 below.

Scheme A.6. Synthesis of Mn^{V}(O)(iPrP_8Cz).

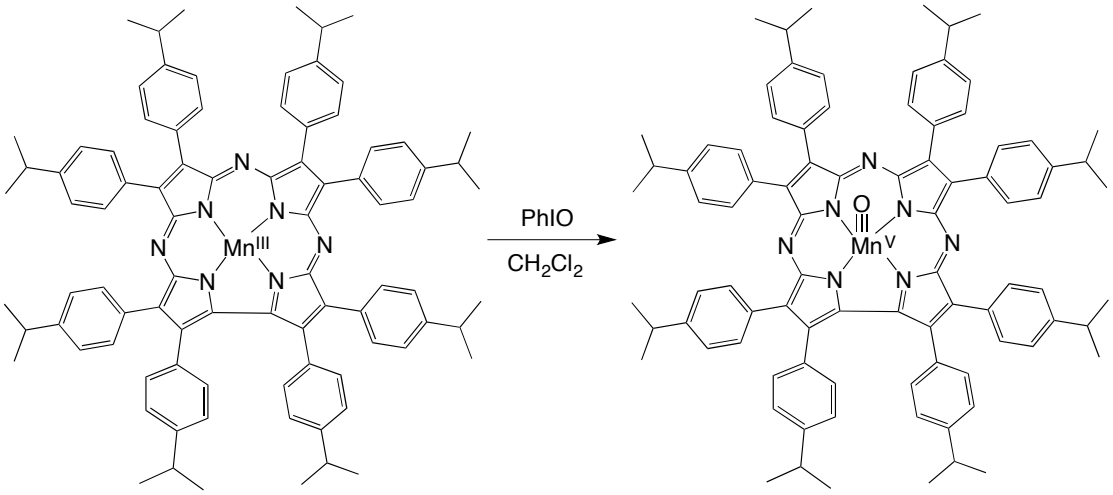

Mn^{III}(iPrP_8Cz) (2.7 mg, 2.1 μ mol) was dissolved in 1 mL of CH_2Cl_2. PhIO (10 mg, 42 μ mol) was added and the reaction mixture quickly turned from a dark brown to a lustrous green. The solution was filtered through a cotton plug and was purified by flash chromatography on silica column with CH_2Cl_2 as eluent (R*f* = 0.99). The product was dried under vacuum to yield a dark green solid (1 mg, 37% yield). ^{1}H NMR (400 MHz, methylene chloride-d_2) δ 8.38 (dd, *J* = 13.2, 8.3 Hz, 8H, Ar-*H*), 8.11 (d, $^3J_{HH}$ = 8.4 Hz, 4H, Ar-*H*), 7.54 (dd, *J* = 8.0, 4.0 Hz, 8H, Ar-*H*), 7.48 (d, $^3J_{HH}$ = 8.0 Hz, 4H, Ar-*H*), 7.39 (d, $^3J_{HH}$ = 8.1 Hz, 4H, Ar-*H*), 7.02 (d, $^3J_{HH}$ = 7.9 Hz, 4H, Ar-*H*), 3.25 – 2.82 (m, 8H, C*H*(CH_3)$_2$), 1.47 – 1.41 (m, 24H, CH(C*H*$_3$)$_{22}$), 1.41 – 1.32 (m, 24H, CH(C*H*$_3$)$_2$). CV (CH_2Cl_2, 25 mV) $E_{1/2}$ = 0.52 V, $E_{1/2}$ = 0.10 V, $E_{1/2}$ = -0.54 V, $E_{1/2}$ = -1.36 V. UV-Vis (CH_2Cl_2) λ_{max} [nm] 417, 634. LDI-MS *m/z* = 1313.26 (Calc'd: 1313.64).

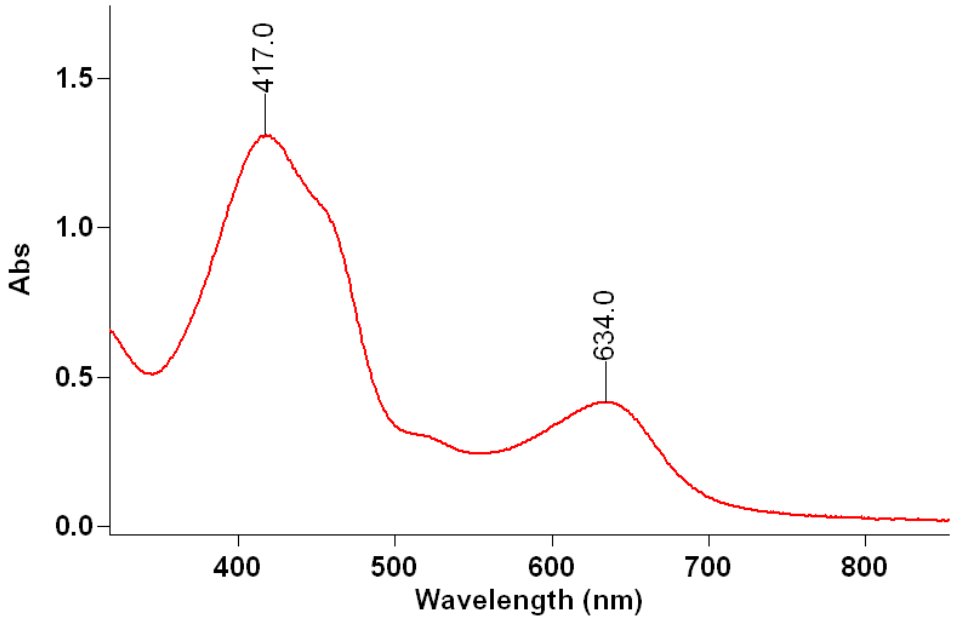

Figure A.7. UV-vis spectrum of $Mn^{V}(O)(iPrP_8Cz)$ in CH_2Cl_2.

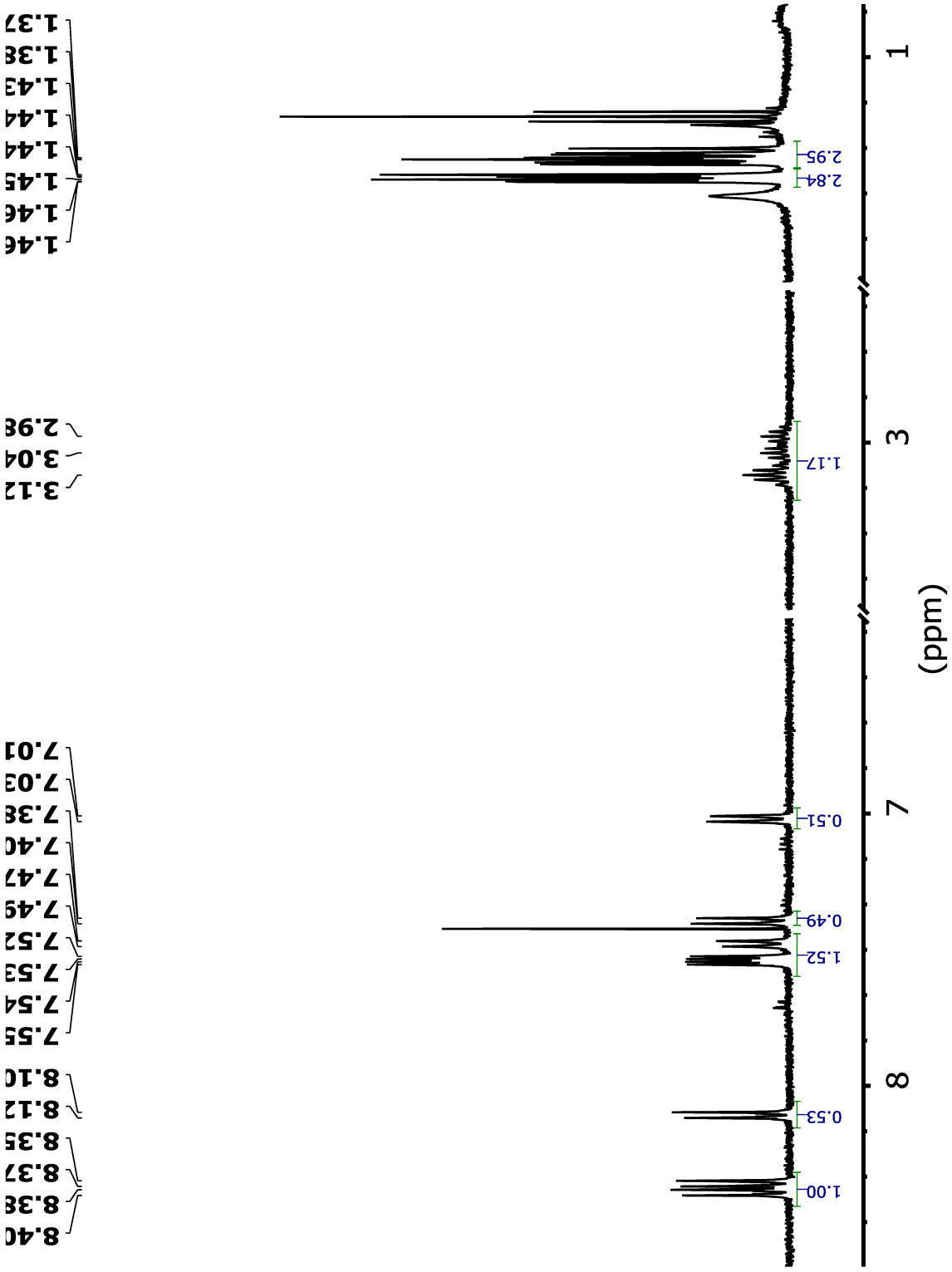

Figure A.8. ^{1}H-NMR spectrum of $Mn^{V}(O)(iPrP_8Cz)$ in CD_2Cl_2.

A.3.Conclusions

Here we have shown the synthesis of the isopropyl derivative of the corrolazine ligand ($iPrP_8CzH_3$) as well as the synthesis of the high-valent manganese-oxo complex, $Mn^V(O)(iPrP_8Cz)$. While the synthetic details need some optimization in future work, the synthesis of $Mn^V(O)(iPrP_8Cz)$ provides a proof of concept. However, the preliminary CV data for $Mn^V(O)(iPrP_8Cz)$ indicates that there may be little electronic difference between the isopropyl and tert-butyl corrolazine derivatives. This is consistent with the results from a reactivity comparison between the tert-butyl and methoxy corrolazine deriviatives, $Mn^V(O)(TBP_8Cz)$ and $Mn^V(O)(MeOP_8Cz)$, in which subtle but measurable differences in HAT and OAT reaction rates with these two metal-oxo complexes were found.

A.4. References

(1) Ramdhanie, B.; Stern, C. L.; Goldberg, D. P. Synthesis of the First Corrolazine: A New Member of the Porphyrinoid Family. *J. Am. Chem. Soc.* **2001**, *123*, 9447-9448.

(2) Lansky, D. E.; Mandimutsira, B.; Ramdhanie, B.; Clausén, M.; Penner-Hahn, J.; Zvyagin, S. A.; Telser, J.; Krzystek, J.; Zhan, R.; Ou, Z.; Kadish, K. M.; Zakharov, L.; Rheingold, A. L.; Goldberg, D. P. Synthesis, Characterization, and Physicochemical Properties of Manganese(III) and Manganese(V)-Oxo Corrolazines. *Inorg. Chem.* **2005**, *44*, 4485-4498.

(3) Mandimutsira, B. S.; Ramdhanie, B.; Todd, R. C.; Wang, H.; Zareba, A. A.; Czernuszewicz, R. S.; Goldberg, D. P. A Stable Manganese(V)-Oxo Corrolazine Complex. *J. Am. Chem. Soc.* **2002**, *124*, 15170-15171.

(4) Kerber, W. D.; Ramdhanie, B.; Goldberg, D. P. H2O2 Oxidations Catalyzed by an Iron(III) Corrolazine: Avoiding High-Valent Iron–Oxido Species? *Angew. Chem., Int. Ed.* **2007**, *46*, 3718-3721.

(5) Baglia, R. A.; Prokop-Prigge, K. A.; Neu, H. M.; Siegler, M. A.; Goldberg, D. P. Mn(V)(O) versus Cr(V)(O) Porphyrinoid Complexes: Structural Characterization and

Implications for Basicity Controlling H-Atom Abstraction. *J. Am. Chem. Soc.* **2015**, *137*, 10874-10877.

(6) Joslin, E. E.; Zaragoza, J. P. T.; Baglia, R. A.; Siegler, M. A.; Goldberg, D. P. The Influence of Peripheral Substituent Modification on PV, MnIII, and MnV(O) Corrolazines: X-ray Crystallography, Electrochemical and Spectroscopic Properties, and HAT and OAT Reactivities. *Inorg. Chem.* **2016**, *55*, 8646-8660.

Regina A. Baglia

Department of Chemistry, Johns Hopkins University
3400 N. Charles St, Baltimore, MD 21218

Education

The Johns Hopkins University 2016, Baltimore, MD
Ph.D., Chemistry
Advisor: Professor David P. Goldberg

Temple University 2011, Philadelphia, PA
B.S., Biochemistry, Distinction in Major, Magna Cum Laude
University Honors Program, Dean's List.

Professional Experience

Research
Research Assistant, Chemistry Graduate Program
The Johns Hopkins University, Baltimore, MD Dec. 2011 - Present

Research Assistant, Undergraduate Research Program and Diamond Research Scholar Program
Temple University, Philadelphia, PA Jan. 2010 - Aug. 2011

Teaching - The Johns Hopkins University
Introductory Chemistry Lecture Teaching Assistant Sept. 2011 – May 2013
Head TA – Fall 2012, Spring 2013
Introductory Chemistry Laboratory Teaching Assistant Sept. 2012 – May 2013

Honors/Awards

The Johns Hopkins University

ACS Division of Inorganic Chemistry (DIC) Student Travel Grant	2016
Harry and Cleio Greer Fellowship	2015
Shepard Memorial Travel Award	2015
E^2SHI Fellowship	2012-2013
NSF-GRFP Honorable Mention	2011-2012
George E. Owen Graduate Fellowship	2011-2013

Temple University

ACS Undergraduate Research Award in Inorganic Chemistry	2011
Creative Arts, Research, and Scholarship Travel Grant	2011
Diamond Research Scholar	2010
Conwell Undergraduate Research Award	2010

Publications (in reverse chronological order)

1. Baglia, R. A.; Krest, C. M.; Yang, T.; Leeladee, P.; Goldberg, D. P. "High-Valent Mnaganese–Oxo Valence Tautomers and the Influence of Lewis/Brönsted Acids on C–H Bond Cleavage" *Inorg. Chem.*, **2016**, *55*, 10800.

2. Joslin, E. E.; Zaragoza, J. P. T.; Baglia, R. A.; Siegler, M. A.; Goldberg, D. P. "The Influence of Peripheral Substituent Modification on P^{V}, Mn^{III}, and $Mn^{V}(O)$ Corrolazines: X-ray Crystallography, Electrochemical and Spectroscopic Properties, and HAT and OAT Reactivities" *Inorg. Chem.,* **2016**, *55*, 8646.

3. Neu, H. M.; Baglia, R. A.; Goldberg, D. P. "A Balancing Act: Stability versus Reactivity of Mn(O) Complexes" *Acc. Chem. Res.,* **2015**, *48*, 2754.

4. Baglia, R. A.; Prokop-Prigge, K. A.; Neu, H. M.; Siegler, M. A.; Goldberg, D. P. "Mn(V)(O) versus Cr(V)(O) Porphyrinoid Complexes: Structural Characterization and Implications for Basicity Controlling H-Atom Abstraction" *J. Am. Chem. Soc.*, **2015**, *137*, 10874.

5. Zaragoza, J. P.; Baglia, R. A.; Siegler, M. A.; Goldberg, D. P. "Strong Inhibition of O-Atom Transfer Reactivity for $Mn^{IV}(O)$(π-radical-cation)(Lewis acid) Versus $Mn^{V}(O)$ Porphyrinoid Complexes" *J. Am. Chem. Soc.,* **2015**, *137*, 6531.

6. Neu, H. M.; Jung, J.; Baglia, R. A.; Siegler, M. A.; Ohkubo, K.; Fukuzumi, S.; Goldberg, D. P. "Light-Driven, Proton-Controlled, Catalytic Aerobic C–H Oxidation Mediated by a Mn(III) Porphyrinoid Complex" *J. Am. Chem. Soc.,* **2015**, *137*, 4614.

7. Hamilton, C. R.; Gau, M. R.; Baglia, R. A.; McWilliams, S. F.; Zdilla, M. J. "Mechanistic Elucidation of the Stepwise Formation of a Tetranuclear Manganese Pinned Butterfly Cluster via N-N Bond Cleavage, Hydrogen Atom Transfer, and Cluster Rearrangement" *J. Am. Chem. Soc.* **2014**, *136*, 17974.

8. Neu, H. M.; Yang, T.; Baglia, R. A.; Yosca, T. H.; Green, M. T.; Quesne, M. G.; deVisser, S. P.; Goldberg, D. P. "Oxygen-Atom Transfer Reactivity of Axially Ligated Mn(V)-Oxo Complexes: Evidence for Enhanced Electrophilic and Nucleophilic Pathways" *J. Am. Chem. Soc.*, **2014**, *136*, 13845.

9. Baglia, R. A.; Dürr, M.; Ivanović-Burmazović, I.; Goldberg, D. P. "Activation of a High-Valent Manganese–Oxo Complex by a Nonmetallic Lewis Acid" *Inorg. Chem*., **2014**, *53*, 5893.

10. Leeladee, P.; Baglia, R. A.; Prokop, K. A.; Latifi, R.; de Visser, S. P.; Goldberg, D. P. "Valence Tautomerism in a High-Valent Manganese–Oxo Porphyrinoid Complex Induced by a Lewis Acid" *J. Am. Chem. Soc.,* **2012**, *134*, 10397.

11. Hamilton, C. R.; Baglia, R. A.; Gordon, A. D.; Zdilla, M. J. "Synthesis of Tetranuclear, Four-Coordinate Manganese Clusters with 'Pinned Butterfly' Geometry Formed by Redox Bond-Breaking and Hydrogen Atom Transfer Reactions" *J. Am. Chem. Soc*., **2011**, *133*, 4208.

Presentations

251st ACS National Meeting, **2016**, INOR, Paper 714. "Comparison of $Mn^{V}(O)$ and $Cr^{V}(O)$ complexes in HAT and PCET reactivity" San Diego, CA. *Oral Presentation*.

International Symposium on Activation of Dioxygen and Homogeneous Oxidation Catalysis (ADHOC), **2015**, "Crystallographic Characterization of *M*(V)-Oxo Porphyrinoid Complexes (*M* = Mn, Cr) and Comparison of HAT Reactivity" Madison, Wisconsin. *Oral and Poster Presentation.*

Bioinorganic Chemistry Gordon Research Seminar (GRS), **2015**, "Activation of a Manganese-Oxo Complex by Lewis Acids." Ventura, CA. *Oral Presentation.*

Metals in Biology Gordon Research Conference (GRC), **2015**, "Activation of a Manganese-Oxo Complex by Lewis Acids." Ventura, CA. *Poster Presentation.*

5th Mid-Atlantic Seaboard Inorganic Symposium (MASIS), **2014**, "Activation of a Manganese-Oxo Complex by a Nonmetallic Lewis Acid." Temple University, Philadelphia, PA. *Oral Presentation.*

33rd Summer Symposium in Molecular Biology at The Pennsylvania State University, "Frontiers in Metallobiochemistry III," **2014**, "Activation of a High-Valent Manganese-Oxo Complex by a Nonmetallic Lewis Acid." The Pennsylvania State University, State College, PA. *Poster Presentation.*

18th Annual Temple Undergraduate Research Forum and Creative Works Symposium, **2011**, "Synthesis of Novel Analogs of the Oxygen Evolving Complex." Temple University, Philadelphia, PA. *Oral Presentation.*

Temple Undergraduate Research Day, **2011**, "Building Molecular Models of the Oxygen Evolving Complex." East Rotunda of PA Capitol in Harrisburg, PA. *Poster Presentation.*

241st ACS National Meeting, **2011**, INOR, Paper 133. Symposium on Undergraduate Research at the Frontiers of Inorganic Chemistry. "Synthesis of Novel Analogs of the Oxygen Evolving Complex." Anaheim, CA. *Oral Presentation.*

Service Activities

Barclay Summer Program Volunteer (Inventor's Camp)	2016
SABES Classroom Mentor	2015-present
Research mentor for undergraduates in Goldberg lab	2013-present

High school visitation (Baltimore City Charter)
JHU Student Safety Committee 2014-present
JHU Graduate Chemistry Recruitment Weekend 2012-present

Professional Memberships

American Chemical Society Member 2010-present

References

1. **Prof. David Goldberg**, Department of Chemistry, The Johns Hopkins University, Baltimore, MD, 21218. *Email*: dpg@jhu.edu *Phone*: 410-516-6658
2. **Prof. Kenneth Karlin**, Department of Chemistry, The Johns Hopkins University, Baltimore, MD, 21218. *Email*: kkarlin1@jhu.edu *Phone*: 410-516-8027
3. **Prof. Michael Zdilla**, Department of Chemistry, Temple University, Philadelphia, PA, 19122. *Email*: mzdilla@temple.edu *Phone*: 215-204-7886